Color vision simulation through ophthalmic filters

Aiman Raza

N° d'ordre NNT : 2021LYSET008

THESE de DOCTORAT DE L'UNIVERSITE DE LYON
opérée au sein de
ENTPE, Lyon
En partenariat industrielle CIFRE n° 2017/1176 avec
Essilor International, Paris

Ecole Doctorale N° 162
MÉCANIQUE, ÉNERGÉTIQUE, GÉNIE CIVIL, ACOUSTIQUE
Spécialité / discipline de doctorat :

Génie Civil

Soutenue le 09/09/2021, par :
Aiman RAZA

Simulation de la vision colorée au travers des filtres ophtalmiques

---

Devant le jury composé de :

ANDRAUD Christine Professeure, Muséum National d'Histoire Naturelle, Paris, France	Présidente
KWAK Youngshin Professeure, Ulsan National Institute of Science and Technology, Corée du sud	Rapporteur
HEBERT Mathieu Maître de conférences, HDR, Laboratoire Hubert Curien -UJM, St Etienne	Rapporteur
HANSELAER Peter Professeur KU Leuven, Belgique	Examinateur
DUMORTIER Dominique ENTPE, Lyon, France	Directeur de thèse
JOST Sophie ENTPE, Lyon, France	Co-directrice de thèse
DUBAIL Marie Essilor International, Paris, France	Encadrante thèse (entreprise)

Thesis National Number: 2021LYSET008

A THESIS OF THE UNIVERSITY OF LYON

Prepared at

ENTPE, Lyon

Under an industrial partnership : CIFRE n° 2017/1176 with

Essilor International, Paris

Doctoral school N° 162

MEGA (Mechanics, Energy, Civil Engineering and Acoustics)

Spécialité / discipline de doctorat :

Civil Engineering

Defended on 09/09/2021, by :

Aiman RAZA

Color Vision Simulation through Ophthalmic Filters

In front of the following examination committee:

ANDRAUD Christine Professor, Muséum National d'Histoire Naturelle, Paris, France	Committee chair
KWAK Youngshin Professor, Ulsan National Institute of Science and Technology, South Korea	Reviewer
HEBERT Mathieu Lecturer, HDR, Laboratoire Hubert Curien -UJM, St Etienne	Reviewer
HANSELAER Peter Professor KU Leuven, Belgique	Examiner
DUMORTIER Dominique ENTPE, Lyon, France	Thesis director
JOST Sophie ENTPE, Lyon, France	Thesis co-director
DUBAIL Marie Essilor International, Paris, France	Supervisor (private partner)

Abstract

Sunglasses today not only offer protection against glare and harmful sun rays but may also improve visual experience, modifying color contrasts for wavelengths that matter as per specific activities (sports, driving, etc.). Currently, the industry today does not have standardized methods of characterization and valorization of these innovations in sunglass-filtered vision for real 2D scenes. This thesis work establishes a streamlined process to visualize and assess sunglass filtered vision on natural/urban images via color corrected simulations.

The major innovation in the PhD concerns the use of hyperspectral images that offer color information not just for the broad wavelengths (RGB) but for the entire spectrum (UV, visual, or IR). These, more detailed images contain information that offer non-invasive methods to analyze object properties, ranging from their color content, color appearances and reflective properties. These hyperspectral images, when combined with sunglasses, offer the possibility to simulate sunglass filtered vision on real scenes with a high precision.

The use of hyperspectral imaging in this PhD is combined with yet another technology, image color appearance modelling. Color appearance models (CAMs) ensure that the final rendered colors of objects resemble closely to that of the real object and take in account various visual phenomena and visual properties of the target object. Though, standard CAMs treat objects as points without taking in consideration the spatial aspects of human vision. Image CAMs remove this barrier and provide an opportunity to simulate color vision on a 2D scale and take in account the spatial aspect of human vision, thus bringing the images much closer to reality. Image CAMs also include techniques that enable simulating scenes with a large dynamic of light levels on display devices with a limited range of light levels, by compressing the variations and creating a perceptually closer version of the real scene. This further brings the images closer to reality by respecting the perceptual accuracy of colors and light levels.

This unique combination of hyperspectral imaging and color corrected image modelling ensures that the simulation of sunglasses is accurate and can reproduce the vision improvements/modifications brought in by sunglasses faithfully. The accuracy of these simulated sunglasses was validated by the means of psycho-visual experiments, firstly on color science experts, followed by experiments involving a general population. The thesis also proposes metrics to quantify the impact of sunglasses on specific scenes, and provides synthesized information regarding the color shifts brought by the sunglasses. These metrics further help the manufacturer to characterize the impact of sunglasses on scenes where they will be worn (beach, mountains, ski stations, urban landscape etc.). This adds in an aspect of contextualization for the users also as they can make an informed choice while assessing scenes other than the sunglass outlet, which is not the best representation of situations where the sunglass will be worn.

The work done during this thesis thus created, implemented and characterized a robust methodology to produce high fidelity images for a variety of sunglasses (neutral, colored, highly colored, with low to high opacity etc.) on a diverse range of scenes.

Résumé

Aujourd'hui, les lunettes solaires ne protègent pas seulement contre l'éblouissement et les rayons nocifs du soleil, elles améliorent aussi l'expérience visuelle en modifiant la contraste des couleurs aux longueurs d'onde essentielles à certaines activités : conduite automobile, pratiques sportives... Actuellement, l'industrie ne dispose pas de méthodes standardisées de caractérisation et de valorisation de ces innovations pour des scènes réelles 2D. Ce travail de thèse propose une méthodologie validée permettant de quantifier et d'illustrer l'impact de lunettes de soleil sur des images naturelles/urbaines par le biais de simulations.

L'innovation majeure de cette thèse concerne l'utilisation d'images hyperspectrales qui offrent des informations couvrant un grand nombre de longueurs d'onde de l'UV, du visible et du proche IR, contrairement aux images habituelles en RVB. Ces informations plus riches permettent de manière non invasive, d'analyser les propriétés des objets, allant de leur contenu en couleurs, à leur apparence colorée et à leurs propriétés de réflexion. Lorsqu'elles sont combinées avec la transmission spectrale des verres, les images hyperspectrales permettent de simuler avec une grande précision, la vision de scènes réelles filtrée par des lunettes de soleil.

Cette thèse associe l'imagerie hyperspectrale à la modélisation de l'apparence colorée avec des « image CAMs ». Les modèles d'apparence des couleurs (CAMs) garantissent que le rendu final d'un objet ressemble étroitement à celui de l'objet réel. Pour cela, ils prennent en compte plusieurs phénomènes liés à la vision humaine des couleurs ainsi que les propriétés de l'objet considéré. Les « standard CAMs » traitent les objets comme des points sans prendre en compte les aspects spatiaux de la vision humaine. Les « image CAMs » lèvent cette barrière en simulant la vision des couleurs à l'échelle 2D, ils produisent ainsi des images beaucoup plus proches de la réalité. Les « images CAMs » incluent aussi des techniques qui permettent de simuler des scènes avec une grande dynamique de niveaux de luminance sur des dispositifs d'affichage avec une dynamique beaucoup plus réduite. Ils le font en compressant ces variations tout en respectant au mieux la perception des couleurs et des luminosités pour être au plus proche de la scène réelle. Cette combinaison unique entre l'imagerie hyperspectrale et la modélisation de l'apparence colorée permet de s'assurer que la simulation des lunettes de soleil est précise et peut reproduire fidèlement les améliorations/modifications de la vision apportées par les lunettes de soleil. Pour cette thèse, une large gamme de verres a été simulée : neutres, colorés, fortement colorés avec des opacités variables, etc... La précision des simulations a été validée par le biais d'expériences psycho-visuelles, d'abord sur des experts en science des couleurs, puis sur une population générale.

Pour finir, la thèse propose une métrique permettant de quantifier l'impact des lunettes de soleil sur une scène spécifique ainsi qu'une représentation graphique permettant d'interpréter facilement les changements de couleur qu'elles apporteront sur cette scène. Ces informations aideront ainsi le fabricant à caractériser l'impact des lunettes de soleil sur les scènes où elles seront portées (plages, montagnes, stations de ski, paysages urbains, etc.). Les acheteurs potentiels pourront ainsi effectuer un choix plus pertinent que celui basé sur la vision de l'intérieur du magasin. Le travail effectué au cours de cette thèse a ainsi implémenté, testé et validé une méthodologie robuste permettant de produire des images simulant avec une grande fidélité la vision de scènes réelles au travers de lunettes de soleil.

Acknowledgements

This thesis work has been made possible with the help and support of various individuals and their kind-heartedness. I want to thank everyone, not only the people that directly contributed to this PhD project, but also the people who indirectly helped me to become the person I am today.

To begin with, I would like to thank my Ph.D. directors at ENTPE: Sophie JOST, Dominique DUMORTIER, and my supervisor at Essilor: Marie DUBAIL. Without your support, this project would be unimaginable. You supervised me through every step pedagogically, your constant guidance and your kindness during these years were invaluable. I will always be obliged for your immense help during the highs and especially during the lows of this Ph.D. I would also like to extend my thanks to Pascale LACAN, the director of Essilor R&D-Paris Bastille. You have been a perpetually uplifting presence during these years, always there to support me, both emotionally and professionally. Thanks to the people mentioned above, my Ph.D. project was a thrilling adventure that culminated on very calm waters.

A special thanks to Coralie CAUWERTS, your professional guidance during the various steps of this Ph.D. was priceless. I would also like to thank Mathieu IODICE for introducing me to the world of research and for his kind solutions to all my petty problems as a beginner.

The amount of love and support I received from Haris SHAMSI, my childhood best-friend of more than 25 years is incomparable, you're the best. A big and heartfelt thanks to all my friends: Anna, Benjamin, Caroline, Charlotte, Claire, Emilie, Gabriel, Jean-Viannay, Marie, Mayank, Mouche, Nicolas, Quique, Samuel, Sandal, Saumya, Tangi and Thibault. I cannot express my gratitude to you in words, thanks for believing in me and being a part of this incredible journey.

I would also like to thank my colleagues (and friends ☺) from ENTPE: Carlos, Dorian, Eva, Francois, Joachim, Luna, Mike, Pascale, Phileas, Pierre-Augustin, Valentin, Yousra; and from Essilor: Camille, Elisa, Kantha, Lauriane, Mathias, Sarah, Susana, and Victoria. You guys have been wonderfully nice and supportive, I feel lucky to have worked alongside you all.

I would like to extend my sincere gratitude towards the jury of this Ph.D. defense who gave me their precious time and even more treasurable reviews. This Ph.D. relied heavily on psycho-visual experimenting which would not have been possible without the contribution of the diligent participants, thank you all for your help.

Who I am and where I am today, is all because of my family, my father: Dr. Sartaj Husain, my mother: Munawwar Begum, my brother and sister-in-law: Mairaj Raza and Nida Raza, my sister and my brother-in-law: Anamta Noorie and Farhan Ali. The immense belief and emotional support they provided, ensured that I achieved my goals. They helped and supported me during not just my Ph.D. but since forever. I will always be indebted to them for everything in my life. Special thanks to my father whom I lost during my Ph.D., his unconditional belief in me gave me the courage to choose this path. *Daddy, I hope I have made you proud*!

I shall be telling this with a sigh
Somewhere ages and ages hence:
Two roads diverged in a wood, and I—
I took the one less traveled by,
And that has made all the difference.

-Excerpt from 'The Road Not Taken' by Robert FROST

To you Mummy and Daddy

I carry your heart with me, I carry it in my heart!

Contents

List of Figures

List of Tables

1. Overview

1.1. Background

The ophthalmic lens industry has witnessed a significant reinvention in the past few decades. From the simple combination of refractive error correction and UV protection, which still remains their primary purpose, ophthalmic filters nowadays have multiple other utilities to adapt to the increasing consciousness around visual health and new studies. Nowadays ophthalmic filters are designed: to provide protection against glare (Essilor Xperio, 2009), to adapt to various human activities like driving (night and day) (Crizal Sapphire+, 2017; Varilux RoadPilot, 2017) or computing (Crizal Prevencia, 2013; Essilor Eyezen, 2015), with the impetus shifting towards visual health (Cohen-Tannoudji et al., 2014; Giraudet, 2010). There has been an increase in colorful and aesthetically pleasing designs with individually adapted parameters (like age) to suit the consumer's preferences or visual perception.

These developments are not restricted to clear ophthalmic filters but also to sunglasses, with or without correction. Colored ophthalmic filters are no longer restricted to traditional gray or brown tints but can be deeply colorful (Essilor SunSolution, 2018; Oakley Prizm, 2018). With colored tints on sunglasses, which are increasingly optimized for sports and outdoor recreational activities (Varilux Sport, 2008), color vision issues such as color fidelity (Baillet et al., 2008; Vienot et al., 2002), or color enhancement (Saylor, 2015) are raised.

All the above-mentioned developments and other related innovations in the field of sunglasses require a due valorization process once the demonstration of their benefits has been done at the manufacturer's and/or the designer's end. The end users in this case are the consumers who purchase sunglasses and correction eye glasses. Currently, there are very few techniques that allow the demonstration of the benefits directly to the end users. Certain standards (like Q Signals, (ISO 13666 Q Signals, 2019)) provide tests for ruling out any major color distortions but these tools are limited.

From the point of view of the end users, main attention is given to the aesthetics and the brand-value of the frame. Very little or no attention is given to the filter composition except the long-term durability of the filter material (Dubail et al., 2020). There are other characteristics that could impact directly the end users but are not well known among the general population (Black, 2018). For example, the end users generally are unaware of the effects of the spectral transmission range of their filter on colored vision, contrast sensitivity, visual acuity and visual perception of their environment. Store trials are quick and concentrate largely on the look and feel of the frame, in an environment which is not entirely representative of the real situations where the glasses will be worn.

The above mentioned lack of knowledge among the general users is related to the inability of the designers and manufacturers to be able to portray with the means of a visual tool, the impact a type of colored filter would have on their vision and perception of the environment. More and more stable and selective dyes are available in the market allowing the development of very specific spectral transmission, without being able to predict the resulting color vision. The prediction of such color vision requires collection of data relating to the wearer and their visual environment. Wearer data can include the wearer's activities or wearer's visual sensitivity. The data related to the visual environment of the wearer can include the measurement of colors present in the field of vision of the wearer. This collection of data is time consuming, expensive, and the data is often quite difficult to analyze. Apart from this, the physical development of various prototypes to be tested is a long and expensive process.

1.2. Research question and the required solution

The aim of this thesis is the study, modeling and simulation of color perception through ophthalmic filter lenses, in natural complex environments, see Figure 1.

Figure 1, A natural scene filtered through a sunglass (left) & reproduced on a display device (right)

An ophthalmic filter can be characterized with the help of its spectral transmittance. It can be used to deduce the filter global photopic transmission (T_v) or the spectral radiance of a light source seen through it. This information, though very useful, is still not directly comprehensible for the end user and is difficult for the manufacturer to portray.

Every color is interpreted by the brain in relation to its surrounding objects and colors, which impacts the visual perception of a certain object (Zheng et al., 2018). Traditional imaging provides scene information in a spatial context, which is essential for complex scene simulation but does not provide spectral information. Spectral measurements of colored objects seen through a filter may provide detailed information but capturing spectral information of a complex scene point by point is rather long. Furthermore, if all the captures are not done more or less simultaneously, there is a risk of adding distortions in the scene due to temporal variations of light and movement of non-stationary objects in natural scenes (Foster & Amano, 2019).

Thus, a simulation of ophthalmic filters on a complex scene that accurately reproduces the wearer's color perception requires:

- A spectral image of a real complex scene which is representative of real-life situations where sunglasses are worn.
- A proper mathematical function (called a Color Appearance Model or CAM) that calculates the color perception phenomenon associated with size, shape, color and many other properties that dictate the perception of colors by humans in complex scenarios.
- A set of metrics and tools that can evaluate these simulations in terms of color contrast, color difference etc., and relay this information to both end users and manufacturers or designers.

1.3. Objectives

Specifically, this thesis proposes to use hyperspectral imaging to capture natural scenes and to optimize a Color Appearance Model applied to these scenes viewed through different types of colored glasses. This in order to be able to compare, through a display device, the different types of sunglasses and to extract predictive characteristics of a quality of color rendering.

The sub-objectives are:

- Determine the color appearance model and its most appropriate settings to represent natural scenes on a digital display medium.
- Study the impact of the hyperspectral imaging capture parameters of the real scene to obtain the precision needed to simulate a filter.
- Optimize the chosen model in order to represent as accurately as possible the color phenomena associated with a filter.

- Simulate filter-induced color distortions and develop indicators (metrics) that predict the perception of wearers.

1.4. Driving force behind the project

Accurate reproduction of real scenes in digital images is strongly influenced by the characteristics of the photo-detectors used in the capturing instrument, by the display device and the color management profile (Bodrogi et al., 2013). In digital imaging, any colored pixel is characterized by its RGB value representative of the trichromatic coordinates. The use of spectral data (spectral reflectance for objects combined with spectral distribution for light sources) instead of RGB values would make it possible to determine, for all the elements of a scene, the modified spectral information reaching the eye. The spectral data of each pixel in the scene can be multiplied by the spectral transmittance of the filter to simulate the light information reaching the eye through a colored filter. Since the final tristimulus coordinates are calculated via the spectral information, the errors due to the trichromatic sensors of a capture device are also minimized. These more realistic stimuli make it possible to overcome gamut (range of producible colors) limitations of the acquisition system. Sometimes filters with a different spectral structure produce similar tristimulus values when seen under a particular light source: this is called metamerism. By taking in account the whole spectrum and not just the tristimulus values, the impact (or the absence thereof) of metamerism can also be taken in account. A few studies have addressed various issues of complex scene simulation under different light sources by using hyperspectral images (Linhares et al., 2008; Nascimento, 2011; Nascimento et al., 2016). With a continuous development of spectral measurement devices (speed and simplification of system use), a large-scale change for the study of visual perceptions can be obtained.

Furthermore, the spectral characteristics of any object, its size, shape, dimension (2D or 3D), as well as the background and the complexity of the scene in which it is observed, influence our perception (CIE 208, 2014; M. Fairchild, 2013). Existing color appearance models such as CIECAM02 (CIE 159, 2004) attempt to model how the human visual system perceives the color of an object according to the light source and the background of the object. Based on the tristimulus components of the stimuli, the color appearance models are used to extend the traditional colorimetry to predict the appearance of complex colored stimuli under different viewing conditions. These models are generally limited to two-dimensional uniform stimuli seen on neutral backgrounds (M. R. Luo et al., 2006) and designed for low light levels (indoor scenes, ~150-200 cd/m^2) with limited range of contrast variations (Kuang, Johnson, et al., 2007). Some of these models, albeit very complex and requiring a large number of input parameters, still do not address most of the color phenomenon required for accurate color vision (M. Fairchild, 2013). Only a few CAMs, specially designed for images (such as iCAM (Kuang et al., 2006)) have tried to integrate the effects of spatial context and viewing conditions on the appearance of colors.

The study of the impact of the light spectrum on the appearance of the color of the object - color rendering - and more generally, on the quality of color rendering, has been a subject of research particularly studied in recent years (Bodrogi et al., 2013; Davis & Ohno, 2005; Jost-Boissard et al., 2009a, 2015, 2016; Y. Lin et al., 2017; Smet et al., 2011; Smet & Hanselaer, 2016). Studies have shown that the Color Rendering Index (CRI, (CIE 13.3, 1995)) used in many international standards, cannot accurately predict the visual color rendering properties of many light sources, especially sources with narrow band spectral characteristics such as LEDs or those with colored filters (Bodrogi et al., 2004; CIE 177, 2007; Smet et al., 2016). The International Commission on Illumination (CIE) has recommended a new index that addresses the weaknesses of the CRI in terms of color fidelity, CIE Rf (CIE 224, 2017). The Illuminating Engineering Society (IES) has also recommended a gamut index responsible for the enhancement of colors (IES TM-30-18, 2018). However, there is still no consensus on how to interpret color changes in terms of overall color rendering quality. Some studies have examined the relationship between saturation and gamut increase with color quality (Linhares et al., 2008; M. Royer et al., 2017; Wei, Houser, et al., 2017), but the data in this area is quite limited. Similarly, little research has been done on how the spectral content of a light source and the related color shifts affect the overall mood/visual comfort. The characterization of the color distortions by adapted metrics would bring new elements in this field.

1.5. Benefits

These developments would bring several advantages to the domain of color appearance modelling and in particular to the ophthalmic filter industry, specifically the manufacturer, the consumer and also the intermediary, i.e. the retailer.

For the manufacturer, a specific color appearance model, that could accurately simulate complex colored scenes as seen through a colored filter on a display device, would reduce time and costs of prototyping. The manufacturer would only need the filter transmittance of a real/virtual colored filter to simulate the intricate color perception of a real-world scene. These simulations could help in identifying potential impact (positive or negative) on color vision of the prototype and thus create an additional quality control parameter in the production process. It would eliminate the costly and cumbersome loop of prototyping where the manufacturer has to produce prototypes, test them on human observers, create ideal conditions for the test, only to discard the prototype if it falls short of the desired outcome and start from scratch. A virtually simulated filter would save both time and financial resources while increasing the efficiency of the production process.

In an increasingly globalized industrial world, such a utility would also facilitate the process of design consulting. With the manufacturer R&D centers spread across different locations, the ability to simultaneously analyze the impact of a colored filter would accelerate the process of validation before a colored filter is launched for the general public. More importantly, such a tool would reduce the possibility of slight discrepancies which could arise in physical prototypes distributed to different actors, thus ensuring precision at the prototyping stage. The manufacturer can thus proceed with the fabrication of the prototype that is validated by all the actors and save resources.

For the consumer, the ability to assess a sunglass virtually would assure an informed choice based on industrial standards before purchasing a sunglass. Trials in stores, though irreplaceable, would be further optimized with the consumer being able to make a pre-selection based on a virtual simulation. This would add a new dimension to the choice of colored filters apart from the aesthetics.

With the advent of e-commerce sites that sell sunglasses online, this tool would considerably improve the online sales. Although online purchases of sunglasses save both time and money for the end-users, they do not have the possibility to test the visual perception of their environment as perceived through a sunglass. This tool would help the end-user in making a much more informed choice of buying the sunglasses that suits their needs and thus making e-commerce more attractive.

For the retailer, this tool would provide the possibility to market the product with interactive tools in addition to the industrial metrics that are sometimes complicated for a layman to understand. Many sunglasses are produced for specific purposes, for e.g. to enhance the ability to detect subtle differences in shading (contrast sensitivity) or to modify color content to render scenes more attractive (chroma enhancement) while ensuring a similar color perception of the scene (color fidelity). With this tool, the retailer would be able to demonstrate the benefits brought by a certain sunglass. The ability to simulate its impact using real-world situations like sunny beaches, streets and landscapes instead of the store itself would provide an impetus to the sales. The sale would depend mostly on the real qualities of the product rather than on the visual conditions of the store which are relatively uncontrolled.

1.6. Methodology

To attain the objective, various tasks were distributed for each of the sub-objectives, dividing them into four different sections which depend on each other. The approach is visualized in Figure 2 and detailed thereafter.

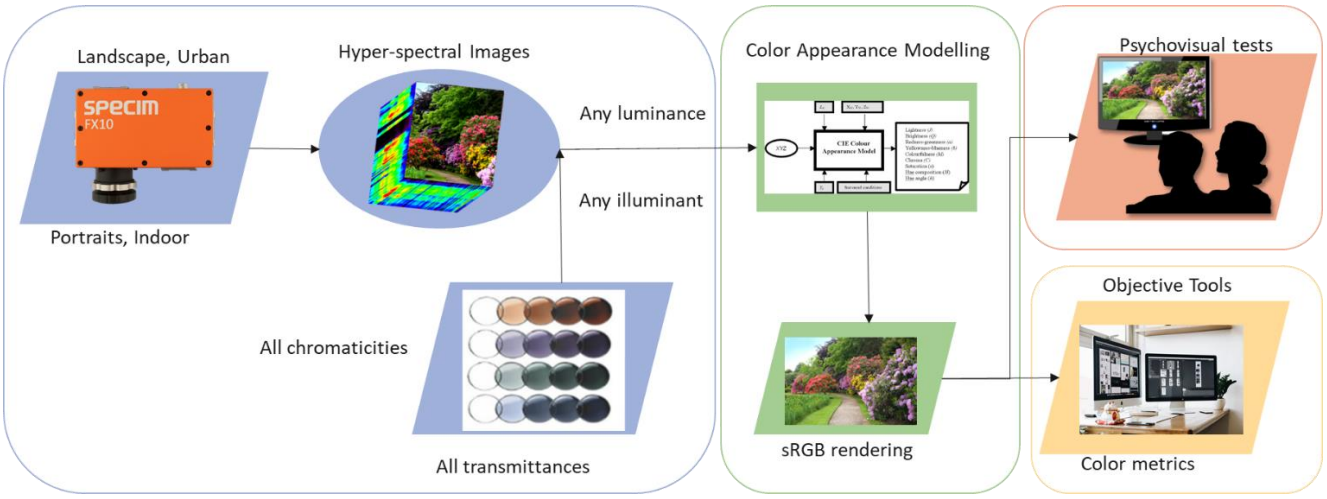

Figure 2, Project outline

The first section of the project outline will deal with the characterization and calibration of the hyperspectral camera. Optimum parameters will be determined for the hyperspectral camera for outdoor captures, indoor captures, portrait and landscapes, each with different luminance conditions. A set of colored filter transmittances will be applied to each hyperspectral image, with different chromaticities, ranging from the classic brown/grey and grey-green to chromatic red/green/yellow etc. A set of metameric filters will also be applied to the hyperspectral images. Tested filters will have spectral transmittances ranging from 15% to 85%.

The second and third section will describe the processing of the hyperspectral images related to their color appearance, when seen through colored filters under various illuminants. An image color appearance model, iCAM06 (Kuang et al., 2007), will be modified and applied to adapt to the vision through colored filters. Certain components of iCAM06 will be modified on the basis of bibliography, and each modification will be validated/rejected on the basis of psycho-visual experiments. The experiments will take place in laboratory conditions, where a complex scene will be compared against its hyperspectral reproduction processed through the modified iCAM06. Every modification done on iCAM06 will be validated on the basis of various properties like overall image accuracy, color reproduction accuracy and luminance.

The fourth section will be the valorization part where the impact of the applied sunglasses will be studied through objective means. In other words, this part will enable us to characterize the filtered scenes finalized during the second and third part of the pipeline. Tools and utilities will be developed to characterize the color shift induced by the application of glasses and the changes in hue and chroma. Complementary methods will be developed to analyze the color differences on complex scenes before and after sunglass application.

1.7. Manuscript outline

Each chapter of the manuscript deals with a topic of interest taken from the research bricks shown in Figure 2. Table 1 describes the complete chapter-wise breakdown of the manuscript. This chapter (Chapter 0) described an outline of the PhD topic and a streamlined methodology to accomplish the thesis.

Table 1, Chapter-wise manuscript outline

Chapter	Name	Description
1	Overview	Introduction, context and the need for the PhD thesis
2	Color Vision	Literature review of color vision
3	Hyperspectral Imaging for stimuli creation	Literature review, calibration and quantification protocol for hyperspectral imaging

4	iCAM06 for sunglass filtered vision	Application of sunglasses on hyperspectral images and color correction via iCAM06
5	Experimental validation: iCAM06	Literature review and testing of iCAM06 for sunglass filtered vision
6	Characterization of color shift induced by sunglasses	Literature review on graphic tools to assess color shift and tool creation for sunglass induced color shift
7	Summary and conclusion	Recap, achieved objectives and future work ideas

To go forward, chapter 2 will provide a brief literature review of the developments related to the physiological modelling of color vision. Chapter 3 will introduce hyperspectral imaging technology and its complexities with a literature review, while describing a simplified set of steps to follow when using a hyperspectral camera for stimuli creation (for psychophysical experimentation). Chapter 4 will combine the knowledge gained from chapters 2 and 3, and will describe the methodology to simulate a sunglass using hyperspectral cameras and color corrected images. Chapter 5 will re-introduce iCAM06 (initially introduced in chapter 2) with a literature review on its development. It will further detail the steps taken to experimentally validate the methodology described in chapter 4 and compare it with other state-of-the-art methods. Approaching the final phase of the topic, chapter 6 will describe ways to characterize and valorize the experimentally validated color images that simulate sunglasses. It will first provide a literature review on the existing methods to characterize color shifts followed by the development of a novel method of color shift identification. And to conclude the manuscript, chapter 7 will summarize the work done during the PhD and propose certain possibilities for future studies.

Certain chapters contain data that has been subject to publications. These publications and corresponding chapters are detailed in the Table 2.

Table 2, List of publications

S.No.	Publication Name	Authors	Journal/Conference	Year	Chapter
1	Simplified Hyperspectral Camera Calibration for accurate radiometric measurements	Aiman RAZA, Marie DUBAIL, Sophie JOST, Dominique DUMORTIER	CIE Quadrennial (C)	2019	3
2	Dominant color and Image color composition retrieval from complex images	Aiman RAZA, Sophie JOST, Marie DUBAIL	AIC (C)	2020	6
3	Categorizing color shifts due to tinted glazing via dominant colors of the scene	Aiman RAZA, Sophie JOST, Marie DUBAIL, Dominique DUMORTIER	CRA (J)	2021	6
4	Automatic colour segmentation and colour palette identification of complex images	Aiman RAZA, Sophie JOST, Marie DUBAIL, Dominique DUMORTIER	JAIC (J)	2021	6
5	Accuracy of hyperspectral imaging systems for in-situ measurements	Aiman RAZA, Sophie JOST, Coralie CAUWERTS, Marie DUBAIL, Dominique DUMORTIER	Submission in August 2021 (J)		3

2. Color Vision

Before undertaking the task to simulate colored images as seen through sunglasses, we need to first understand the complexities of color vision. This chapter will briefly discuss the various notions in the domain of color vision and detail some of them to give a better understanding of the global methodology.

Color in itself is a complex notion and not clearly understood by everyone. It is controlled by many factors such as the type of illuminant, luminance levels, angle of lighting, angle of vision, contours, surrounds, and the sensitivity of the eye among others. As per the Oxford dictionary, *the property possessed by an object of producing different sensations on the eye as a result of the way it reflects or emits light is called color*. Each individual's vision also plays an important role, for example two persons with a different sensitivity to colors will not visualize objects similarly. This suggests that color is not a fixed physical property of matter, but rather a sensation that changes as the interaction between the matter, light and the eyes evolve.

The human retina is sensitive to light because it is composed of photoreceptors among other cells. They are: cones (three types), rods (one type) and intrinsically photosensitive retinal ganglion cells (ipRGCs, one type). Together, these five types of photoreceptors interact to produce the sensation of vision, with the information of shape, size, motion and color through which humans are able to visualize and distinguish objects (Wyszecki & Stiles, 2000). It has been established that the spectral absorption functions of the three different types of cones compose the human color vision (Jacobs et al., 1996; Stockman & Sharpe, 2000). Rods are known to participate in color perception in the mesopic range (0.1 cd/m^2-3 cd/m^2), but their contribution to color vision is negligible for photopic vision (>3 cd/m^2) (Knight et al., 1998; Stabell & Stabell, 1974). The ipRGCs are known to regulate the circadian rhythm and control pupillary reflexes, with recent studies suggesting a participation in brightness perception (Brown et al., 2012; Graham & Wong, 1995; Viénot et al., 2012). Other studies have also suggested that ipRGCs might be responsible in ensuring the stability of color perception (color constancy) and the unique white perception by participating in the peripheral vision (Cao et al., 2018; Zele et al., 2018). Figure 3 shows the relative sensitivity of the five photoreceptors and the wavelengths corresponding to their peak sensitivities.

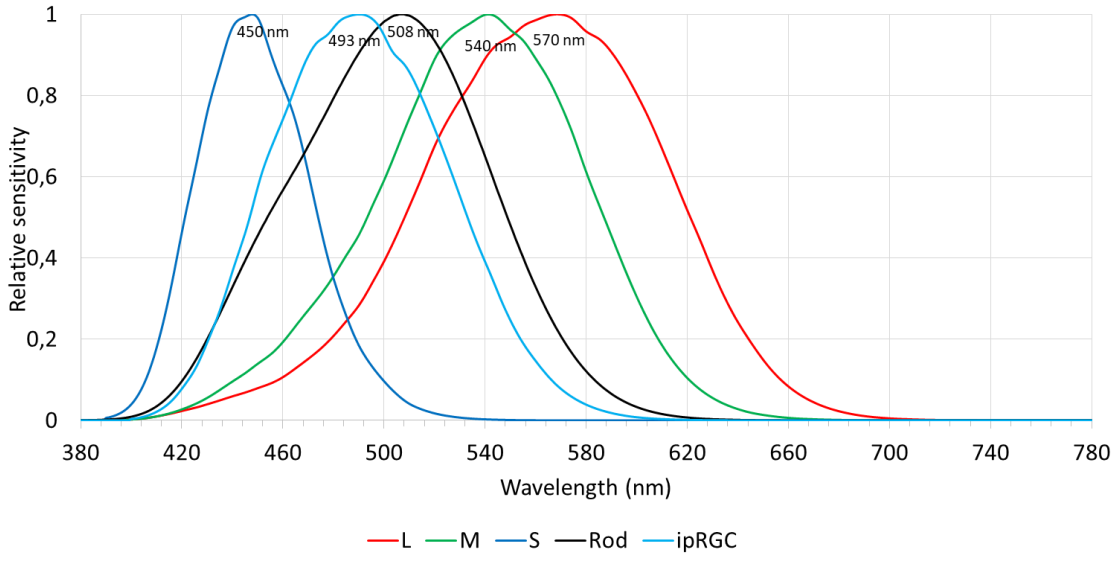

Figure 3, Relative sensitivity of photoreceptors across the visible spectrum

The three cones are identified as sensitive to Long, Medium and Short wavelengths and thus referred to as L, M and S cones. These retinal cone photoreceptors absorb light's electromagnetic energy and transduce it into electrophysiological voltages. A complex network of cells in the retina relays this information to the visual cortex in the brain which analyzes and controls our color vision (Gegenfurtner & Kiper, 2003).

2.1. Physiological mechanism

Human color vision follows an intricate process that starts at the eye level and continues up to the visual cortex where all the received information is processed. There are two theories which together explain human color vision: the trichromatic color theory (Young-Helmholtz color theory) and the opponent color theory (Ewald Hering color opponent theory) (Hall, 1999; Wyszecki & Stiles, 1982). The trichromatic theory suggests that the visual response of the human eye is a combination of differential responses of the three cone photoreceptors (Millington, 1942; Von Helmholtz, 1867; Young, 1802). It is supported by the fact that all visible colors can be expressed by mixing three colored lights of different wavelengths. The opponent color theory suggests that the trichromatic signals reaching the brain are further processed in neural stages. The perceived color is a combination of the differential responses of three opponent systems: red-green opponency, blue-yellow opponency and black-white opponency (Hering, 1920; Hurvich & Jameson, 1957). This theory is supported by the fact that we never see bluish-yellow or reddish-green colors. These two theories were considered at odds with each other for a long time but now are understood to be a part of a global process of color vision. The visual processing in the eye (retina) follows the trichromatic theory and once the signal goes past the retina (towards the brain), the opponent color theory holds true.

The visible stimulus received at the eye is a spectrum containing an infinite number of wavebands between 380 nm to 780 nm. The three cones found in the deepest layers of the retina relay this light information to the brain. This induces a reduction in the dimensionality of light information and is also the basis for the theory of trichromacy. A photochemical reaction, known as transduction, converts light into an electrical signal (potential difference) whose amplitude depends on the number of photons absorbed by the cones (Jindrova, 1998). Once light is absorbed, the only information left is the amplitude of the signal depending on photon count and not the wavelength from which the photon was absorbed (Rushton, 1972). The photoreceptor transfers this signal to the bipolar neurons in the second layer and further to the ganglion cells in the third layer. Apart from this direct transfer, the photoreceptors also send the information to the horizontal cells which relay further information to the surrounding bipolar cells. The bipolar cells also transfer the information to amacrine cells who send the information to the ganglion cells (Dubuc, 2013). Figure 4 describes this visual processing system at the retinal level.

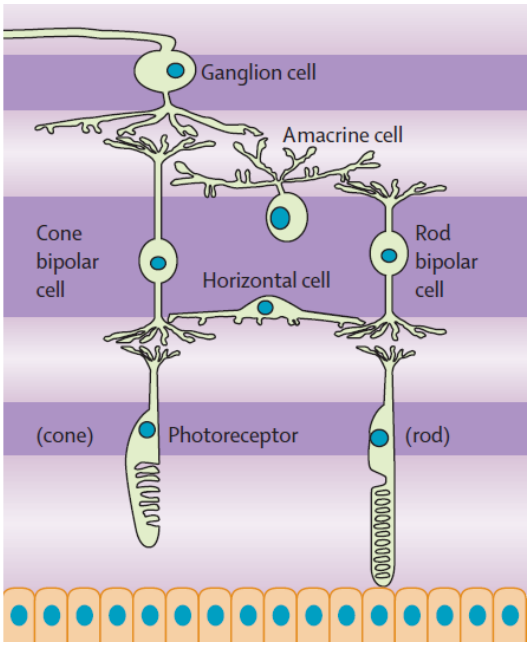

Figure 4, Structure of the retinal layers (Hartong et al., 2006)

Each ganglion cell is connected to several photoreceptors and has areas associated with each cell called receptive field (Wyszecki & Stiles, 2000). The information received at the ganglion cells travels to the

Lateral Geniculate Nucleus (LGN) in three separate color opponent channels (Gegenfurtner & Kiper, 2003). These ganglion cells can react differently depending on which area is stimulated with the incoming photons from a photoreceptor, either on-center or off-center (Wyszecki & Stiles, 2000). This gives rise to the color opponent channels which are characterized by three sets of logical channels. The first one is the luminance axis or the black and white axis, where the information from all the three cones is added. The second channel is the red-green opponent axis where the information from the L cones and M cones is subtracted, this is the reason why no color is said to be reddish-green. The third channel is the blue-yellow opponent axis, where the S cones information is subtracted from the sum of L and M cones. The third channel explains why there is no bluish-yellow color either. The logical channels were derived from purely computational methods but confirmed through electro-physiological and psychophysical experiments (De Valois et al., 1966; Derrington et al., 1984; Krauskopf et al., 1982; Lee et al., 1988). The color opponency is visualized below in Figure 5.

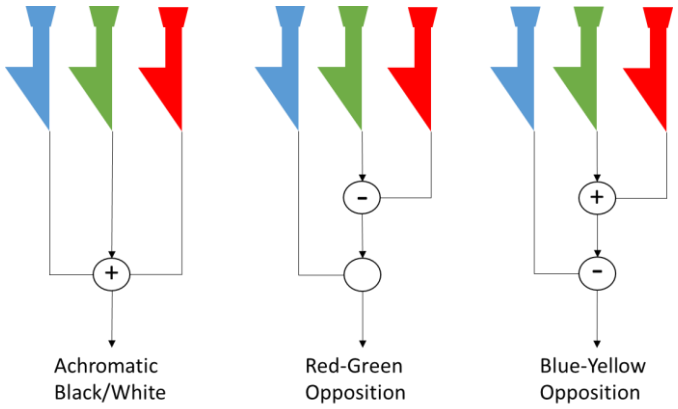

Figure 5, Color opponent system

The primary visual cortex (V1) processes information received from the retina according to the perceptive fields of the ganglion cells. The information from the three retino-geniculate channels is treated in the V1 visual cortex and relayed to the higher-level neurons (V2, V4 and IT (Inferior Temporal)) of the brain. The V1 codes basic information like detection of edges and lines while the higher level neurons are responsible for the detection of faces, objects and shapes (Herzog & Clarke, 2014). This hierarchical structure in the brain enables the final perception of the variety of colors and forms we can discern (Gegenfurtner & Kiper, 2003). These deep hierarchies in the visual cortex are visualized in Figure 6.

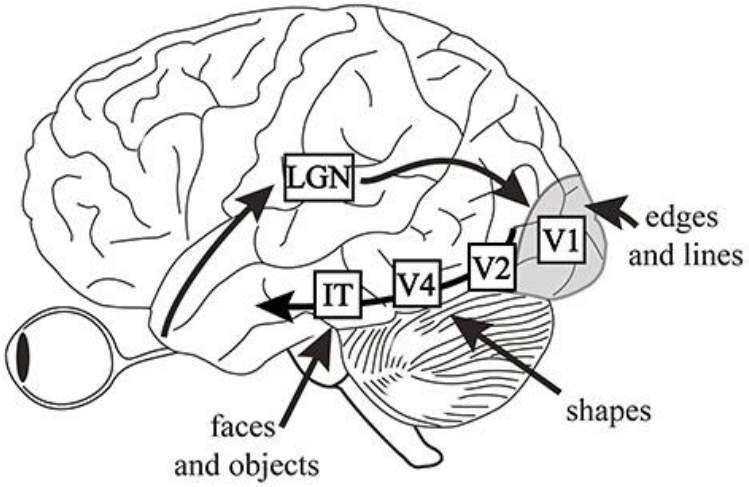

Figure 6, Hierarchical processing of vision in the human brain (Herzog & Clarke, 2014)

2.2. Modelling the physiological response of the eye

The process between the light entering our eyes and us being able to see colors needs to be modelled and understood on a quantified scale. This quantification process is important to understand in order to be able to reproduce the human color sensation (through mathematical models).

Photometric definitions and calculations have been developed to quantify the physiological sensation induced by a physical light stimulation. For e.g., spectral radiance ($W/m^2.sr.nm$) characterizes a light source in terms of its radiant energy across the visible spectrum. Light transmitting media like glass, window glazing, sunglasses etc. are quantified with the help of their light transmission percentage (%) across the visible spectrum. Opaque objects are characterized on the basis of how much light (in %) they reflect across the visible spectrum.

The aforementioned spectral quantities can be multiplied with each other to obtain the effective light reaching the human eye. For example, a complex sunny scene viewed through a pair of sunglasses would be characterized by the spectral radiance of the daylight reflected by the objects in the field of view finally transmitted through the sunglasses to the eyes.

The above physical and spectral properties can be used to calculate the relevant cone response of an average human eye. This has been made possible with the help of CIE Color Matching Functions (CMFs) calculated using the data of color matching experiments of Wright (10 observers) and Guild (7 observers) (Guild, 1931; Wright, 1929). CIE CMFs form a link between the human eye response and the spectral distribution of light. Despite such a small number of participant data, the CMFs hold true for most of the CIE's usage. Though rapidly changing lighting and display technology has led to the development of more accurate CMFs. The original CIE 1931 XYZ CMFs have been reported to occasionally produce visual color differences between colored objects, even though they have the same colorimetric values (LPR 60, 2017). Early CIE CMFs assume a single standard observer that represents an average observer with normal color vision. The differences arising due to the absence of observer variability in the CMFs are negligible for cross media color reproduction (Oicherman et al., 2008). But with the advent of modern wide-gamut displays that are lit by narrowband LEDs, these errors are no longer negligible (M. Fairchild & Wyble, 2007; Ramanath, 2009; Sarkar et al., 2010). Two different displays, with very different characteristics can have metameric colors that match for a certain observer and significantly differ for another (Sarkar et al., 2010). This is known as observer metamerism and this effect is much stronger when the displays have narrow-band primaries. The narrow and steep peaks in LEDs induce a noticeable shift in the chromaticities of the perceived colors, even with a negligible observer variability (Sarkar et al., 2010). These errors are also present when using new age LED lighting sources (Csuti & Schanda, 2008, 2010; J. Li et al., 2019; Petrulis et al., 2017).

Since the original experiments which established these CMFs, others have been developed. The most notable one being the CIE XYZ Cone Fundamental 10° color matching functions, see Figure 7, (CIE 170-1, 2006; CIE 170-2, 2015). These CMFs use the 10° CMFs of Stiles & Burch (47 observers) and the spectral sensitivities of the long, medium and short cones derived for the corneal plane at 10° viewing field (Stiles & Burch, 1959). These functions are further corrected for the absorption in ocular media, macular pigments and the optical densities of the cone visual pigments. These new cone fundamentals allow the calculation of CMFs anywhere between 1°-10° of the viewing field and for different ages. These CMFs have been shown to significantly improve the visual evaluation of light sources (compared with 1931 CMFs) for people under 40 years (Ohno et al., 2019), though the results are mixed for an older population.

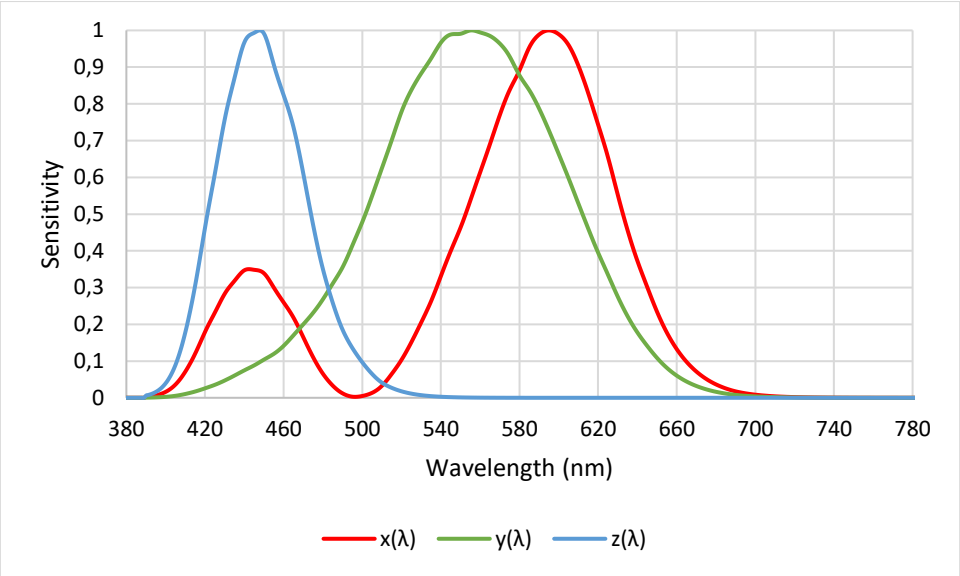

Figure 7, CIE XYZ fundamental 10° CMFs

With the help of these CMFs and the quantified light reaching the eye, the response of the three cones can be calculated with the help of tristimulus values (RGB, LMS (or LMS_{F10}), XYZ (or XYZ_{F10}) etc.). Their calculation is based on the principle of human trichromacy and is done through the following equations (for XYZ, irrespective of the chosen CMF):

$$X = k \int_{\lambda} \phi(\lambda)\bar{x}(\lambda)d\lambda \ldots(1)$$

$$Y = k \int_{\lambda} \phi(\lambda)\bar{y}(\lambda)d\lambda \ldots(2)$$

$$Z = k \int_{\lambda} \phi(\lambda)\bar{z}(\lambda)d\lambda \ldots(3)$$

Where, $\bar{x}, \bar{y}$ and $\bar{z}$ are the CIE color matching functions, $\phi(\lambda)$ is the product of the spectral radiance of the light source and the spectral reflectance of the target stimuli, k is the normalizing constant set to 683 lumens/watt for standard colorimetry and λ is the wavelength information.

2.3. Color appearance phenomena

CIE tristimulus values allow us to compare colors between stimuli given that they are seen under matching visual conditions. Their adapting fields, i.e. the limit of vision in all directions of the two stimuli should be the same. It comprises the proximal field (immediate environment subtending 2°), background (environment subtending 10° from the edge of proximal field) and the surround (the field outside the background (dim, dark and average)) (Hunt, 1991, 1995). Furthermore, they should have the same size, shape, surface characteristics, luminance levels and light source direction. Such conditions are hard to meet in everyday life and there are many situations that show that tristimulus values alone are not sufficient to describe color appearance (M. Fairchild, 2013; M. D. Fairchild, 2002; Schanda, 2007). Such phenomena are the main driving force behind the development of enhanced color metrics like chromatic adaptation transforms and color appearance models (M. Fairchild, 2013). Some of the major color appearance phenomena are discussed in this section.

Abney effect: Mixing of pure hues (monochromatic light) with white light does not produce constant hues (Purdy, 1931). The hue changes in a non-linear fashion with the change of colorimetric purity of the mixture and shows that the human visual system is not linear. The effect is demonstrated in Figure 8, where a gradual mixing (10% steps) of white in a pure blue hue takes a purplish hue in the center instead of producing a paler shade of blue.

Figure 8, Abney effect demonstration

Bezold-Brucke Hue shift: Hue is thought to be linked to the wavelength of the light source. But the experiments conducted by Purdy indicate that luminance levels impact the hue of monochromatic light sources (Purdy, 1931).

Helmholtz-Kohlrausch effect: Brightness is often considered to be directly defined by the luminance of the target object. This is not always true as objects with the same luminance levels but different chromaticities appear differently bright. Thus, brightness is a combined effect of both chromaticity and luminance level (Evans, 1974; Nayatani et al., 1994). The five patches in Figure 9 have similar luminance values but they appear differently bright.

Figure 9, Helmholtz-Kohlrausch effect demonstration

Hunt Effect: Colorfulness of objects is directly linked to the luminance levels. For e.g., objects appear more colorful when seen on a bright sunny afternoon in comparison to a rainy evening (Hunt, 1952).

Steven's effect: Contrast between objects increases with an increase in luminance levels. Contrast is the rate of change of brightness in function of the luminance levels. Higher levels of luminance will make the dark colors appear even darker while the light colors will appear even lighter (Stevens & Stevens, 1963).

In Figure 10, the original (hyperspectral) image on the left, was artificially adjusted to have 85% reduction in radiance to simulate the image on the right with a reduced luminance (by applying a constant filter of 15% transmittance on the hyperspectral radiance). Both the images were otherwise produced by using exactly the same parameters. The original image is more colorful and with higher contrasts, as compared to the image on the right with lower luminance levels, thus demonstrating both Hunt effect and Steven's effect.

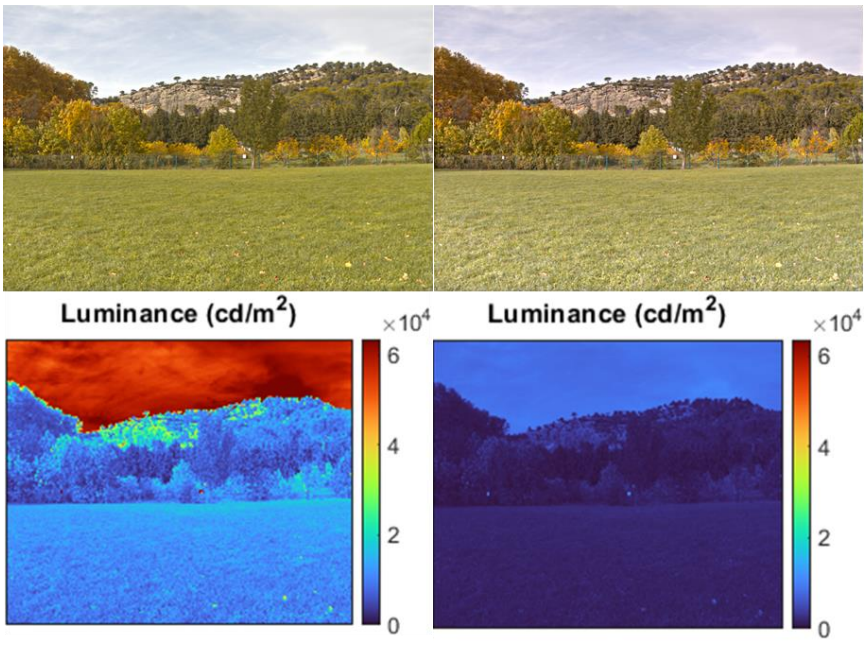

Figure 10, Hunt effect and Steven's effect demonstration

Bartleson-Breneman effect: This effect applies specifically to complex real world images. According to the Bartleson-Breneman effect, the perception of contrast in an image increases when the image surround is light, instead of dim or dark (Bartleson & Breneman, 1967).

Simultaneous Contrast: The color appearance of objects/stimuli changes when the background of the object is changed in accord with the opponent color system, for example from dark to light, red to green, blue to yellow and vice-versa (Albers, 1963). In Figure 11, the red and green squares appear differently when presented on a yellow background or on a blue background.

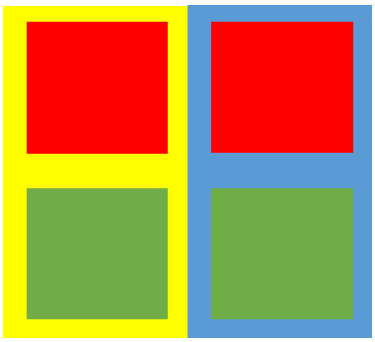

Figure 11, Simultaneous contrast demonstration

Crispening: The difference in colors and lightness of two stimuli change in perceptual magnitude with a change in the background (Semmelroth, 1970). The two blue blocks in Figure 12 appear different when seen on a black, blue or a white background.

Figure 12, Crispening demonstration

Spreading: Spreading is the apparent blending of stimuli with the surround when the stimuli appear frequently next to each other (Chevreul, 1839). The broad gray bars on the left in Figure 13 appear to have a pinkish tinge when the bars appear more frequently next to each other (center), this effect is amplified when the horizontal spacing between the bars is reduced further (extreme right).

Figure 13, Spreading demonstration

2.4. Chromatic adaptation

The CIE tristimulus values obtained for two similar objects match when they are seen in exactly the same visual conditions. Remarkably, many objects continue to match in colors even when viewed under different light sources and viewing conditions. For example, a piece of white clothing would continue to appear white when worn in interior space under a warm-yellow incandescent lighting or under sunlight. Chromatic adaptation ensures that the color appearance of objects remains largely unchanged even if the lighting conditions have changed.

Adaptation is the reaction of an organism to adjust its sensitivity according to different stimuli. In terms of the human vision system, there are three types of adaptations: light, dark and chromatic. Light adaptation is a uniform reduction in the sensitivity of the photoreceptors when the illumination levels are increased while dark adaptation is the overall increase in the visual sensitivity of rods when illumination levels are drastically reduced. The third kind of adaptation, i.e. the chromatic adaptation is the re-establishment of the sensory mechanisms of color vision. It is induced due to a change in type of illumination, precisely, a change in the color of a light source. A change in the color of the light source induces a regulation of the three cone photoreceptors which is independent for each cone photoreceptor. This is different from light adaptation where a single gain control is applied to all the photoreceptors. This independent change in the photoreceptors is known as the "receptor gain-control" (M. Fairchild, 2013).

While sensory mechanisms (pupil dilation and rod-to-cone transition) can explain light and dark adaptation to an extent, chromatic adaptation is thought to be caused by both sensory and cognitive mechanisms (M. Fairchild, 1992a, 1992b, 1993a). The "receptor gain-control" mechanism induces photo-pigment depletion at photopic luminance levels (>1 cd/m^2) (Smet et al., 2017). At mesopic and scotopic light levels, the site of adaptation shifts from the photoreceptors to the post-receptoral neural circuit involving a gain control in horizontal, bi-polar and ganglion cells (C. Li et al., 2002). There is also an evidence of interactions between the three cone photoreceptors (Delahunt & Brainard, 2000) and subtractive adjustments in the post-receptoral pathways to discount (subtract) the background signal (Shevell, 1978; Walraven, 1976; Walraven et al., 1990). Apart from these sensory mechanisms in the forefront of the visual system (photoreceptors and the retinal layers), cortical mechanisms i.e. activities in the visual cortex also participate in chromatic adaptation (M. A. Webster & Mollon, 1994). This presence of higher level interactions in the brain also suggests that a cognitive mechanism involving the human memory of colors may play a role in the chromatic adaptation process (Davidoff, 1991; Evans, 1943; M. Fairchild, 2013; Hering, 1920; Smet et al., 2017; Von Helmholtz, 1867).

Human eyes are able to achieve chromatic adaptation with the help of the above mechanisms but image capturing devices need an adjustment of colors to reproduce this chromatic adaptation. If light adaptation and dark adaptation are analogous to the automatic exposure (amount of light per unit area) control of imaging devices, chromatic adaptation is the automatic white-balance feature in imaging devices. If this feature is turned off, the image will not reproduce the scene as perceived, for example the image on the left in Figure 14 is without any chromatic adaptation while a complete chromatic adaptation has been applied on the image on the right.

Figure 14, Original un-adapted image (left) compared to its chromatically adapted version (right)

Chromatic adaptation is the most important step in color appearance calculations for faithful imaging. The hypothesis of Johannes von Kries forms the base for all the existing chromatic adaptation models (von Kries, 1902). A simplified translation of the hypothesis done by MacAdam states: "*This can be conceived in the sense that the individual components present in the organ of vision are completely independent of one another and each is fatigued or adapted exclusively according to its own function*" (MacAdam, 1993). Precisely, it means that each of the three cone photoreceptors works uniformly with the help of an independent gain control. The modern interpretation of this hypothesis is described below:

$$L_a = k_L L; M_a = k_M M;\ S_a = k_S S \quad ...(4)$$

Where, L, M and S are the initial cone responses, $k_{L,}\ k_{M,}\ k_S$ are the coefficients (gain-controls) and L_a, M_a and S_a are the post chromatic adaptation responses (M. Fairchild, 2013).

Since the von Kries hypothesis in 1902, many chromatic adaptation models have been developed that extrapolated the original hypothesis to achieve a mathematical equivalent of the physiological mechanism. Chromatic adaptation is achieved by applying a mathematical transformation matrix based on the von Kries hypothesis, on the CIE tristimulus XYZ or LMS values. Almost all chromatic adaptation models take into account the photoreceptor gain-control of the cones. Some of these can be modified to include a post-receptoral adjustment of subtractive mechanisms (M. Fairchild, 2013). Cognitive mechanisms being difficult to quantify do not form part of the physiological models of chromatic adaptation. This might explain the differences in the actual chromatic adaptation process and the different chromatic adaptation models.

Some major Chromatic Adaptation Transforms (CATs) proposed until today include MacAdam's Model (MacAdam, 1961), the Retinex models (Land, 1977, 1986; Land & McCann, 1971), Nayatani et al's Model (Nayatani et al., 1981), Guth's Model (Guth, 1991), Fairchild's Model (M. Fairchild & Reniff, 1995) followed by the CAT called CMCCAT97, developed by Luo and Hunt that became the first CIE standard CAT, included in the CIECAM97s (CIE 131, 1998; M. Luo & Hunt, 1998).

The CMCCAT97 uses a non-linear 'Bradford transformation matrix' similar to the modified Nayatani CAT model (Nayatani, 1997b, 1997a). It applies a non-linear compression on the S-cones but a linear transform on the L and M cones. The CMCCAT97s is described below:

$$\begin{pmatrix} R_c \\ G_c \\ B_c \end{pmatrix} = \left[D \begin{pmatrix} \alpha & 0 & 0 \\ 0 & \beta & 0 \\ 0 & 0 & \lambda^n \end{pmatrix} + 1 - D \right] \begin{pmatrix} R \\ G \\ B \end{pmatrix} ...(5)$$

$$\begin{pmatrix} R \\ G \\ B \end{pmatrix} = M_B \begin{pmatrix} X/Y_{max} \\ Y/Y_{max} \\ Z/Y_{max} \end{pmatrix} ...(5a)$$

$$M_B = \begin{pmatrix} 0{,}8951 & 0{,}2664 & -0{,}1614 \\ -0{,}7502 & 1{,}7135 & 0{,}0367 \\ 0{,}0389 & -0{,}0685 & 1{,}0296 \end{pmatrix} ...(5b)$$

$$\alpha = \frac{1}{R_w}; \beta = \frac{1}{G_w}; \lambda^n = \frac{1}{B_w^p} ...(5c)$$

$$p = \left(\frac{B_w}{B_{rw}}\right)^{0{,}0834} ...(5d)$$

$$D = F - F/[1 + 2(L_A^{1/4}/300)] ...(5e)$$

Where, R, G and B are the initial cone responses calculated from the CIE XYZ tristimulus values, D refers to the degree of chromatic adaptation and lies between 0 (no adaptation) and 1 (complete adaptation) while the subscript w refers to the test white (original source illuminant) and rw refers to the reference white

(adapting illuminant). For the calculation of the degree of chromatic adaptation D, F is a constant chosen according to the surround and L_A corresponds to the luminance of the adapting field. The chromatically adapted RGB_c is returned back to the original XYZ format using the following matrix transformation:

$$\begin{pmatrix} X_c \\ Y_c \\ Z_c \end{pmatrix} = M_B^{-1} \begin{pmatrix} R_c \\ G_c \\ B_c \end{pmatrix} \ldots (5f)$$

The CMCCAT97 is an adaptation of the original von-Kries model with an added exponential factor on the B channel. This non-linear structure of the transform posed problems in the calculations of the inverse CIECAM97s values (M. Fairchild, 2013). Thus, CIE created the TC8-01 committee to define a completely linear CAT, which eventually led to the development of the CAT02 transform used in CIECAM02 (CIE 159, 2004). CAT02 uses a linear von Kries linear transformation of cone responsivities (Calabria & Fairchild, 2001) and is described below:

$$\begin{pmatrix} R_c \\ G_c \\ B_c \end{pmatrix} = \left[D \begin{pmatrix} \alpha & 0 & 0 \\ 0 & \beta & 0 \\ 0 & 0 & \lambda \end{pmatrix} + 1 - D \right] \begin{pmatrix} R \\ G \\ B \end{pmatrix} \ldots (6)$$

$$\begin{pmatrix} R \\ G \\ B \end{pmatrix} = M_{02} \begin{pmatrix} X \\ Y \\ Z \end{pmatrix} \ldots (6a)$$

$$M_{02} = \begin{pmatrix} 0.7328 & 0.4296 & -0.1624 \\ -0.7036 & 1.6975 & 0.0061 \\ 0.0030 & 0.0136 & 0.9834 \end{pmatrix} \ldots (6b)$$

$$\alpha = \frac{1}{R_w}; \beta = \frac{1}{G_w}; \lambda = \frac{1}{B_w} \ldots (6c)$$

$$D = F \left[1 - \left(\frac{1}{3{,}6} \right) e^{\frac{(-L_A - 42)}{92}} \right] \ldots (6d)$$

$$\begin{pmatrix} X_c \\ Y_c \\ Z_c \end{pmatrix} = M_{02}^{-1} \begin{pmatrix} R_c \\ G_c \\ B_c \end{pmatrix} \ldots (6e)$$

Despite being currently the most used CAT, CIECAT02 when used within CIECAM02 causes certain computational errors. Since these errors are linked to the use of CAT02 within a CAM framework, they will be discussed in the next section. A more recent CAT, CAT16, which is bundled within the CAM16 color appearance model and the CAM16-UCS color space, has been shown to solve the computational errors of CAT02 (C. Li et al., 2017). The CAT16, when used within the CAM16 is considered to be more accurate or similar to that of CAT02 and at the same time less complex (M. R. Luo & Pointer, 2018). This will also be briefly discussed in the next section.

2.5. Color appearance modelling

The color appearance phenomena and the chromatic adaptation process discussed above show that the CIE tristimulus values in itself are not sufficient to faithfully reproduce color images. This is achieved by Color Appearance Models, or CAMs. A CAM is a set of mathematical functions that are applied on the CIE tristimulus values to take in account the various phenomena discussed above and more. As per the CIE TC 1-34 (M. Fairchild & Chair, 1995), a CAM needs to at least: predict the relative color appearance attributes like lightness, chroma and hue; include a form of chromatic adaptation transform; predict brightness and colorfulness or at least the Stevens effect and the Hunt effect.

Various CAMs have been developed since the development of the CIELAB color space which can be considered to be among the first CAMs, even though it is in reality a color space (and does not have any

CAT) (McLAREN, 1976). Major CAMs include : Nayatani et al Models (Nayatani, 1995; Nayatani et al., 1986, 1987), Hunt Models (Hunt, 1982, 1987, 1991, 1995), RLAB Model (M. Fairchild, 1993b) and LLAB among others (M. R. Luo, 1996). The first standardized CAM adopted by the CIE is the CIECAM97s (CIE 131, 1998) followed by CIECAM02 (CIE 159, 2004).

Both CIECAM97s and CIECAM02 follow a similar structure which is described below in Figure 15. Their major difference is the chromatic adaptation model, which is linear for CIECAM02 and non-linear for CIECAM97s (discussed in the section 2.4).

The input data includes: the XYZ tristimulus values of the stimuli in source conditions (under the test light source); L_A, which is the adapting luminance; XYZ_W, tristimulus values of the test illuminant and Y_b which is the relative luminance of the source background. The surround conditions consist of a group of constants: c (surround impact), Nc (chromatic induction factor), F_{LL} (lightness contrast factor) and F (degree of adaptation factor). Their fixed values depend on the viewing conditions.

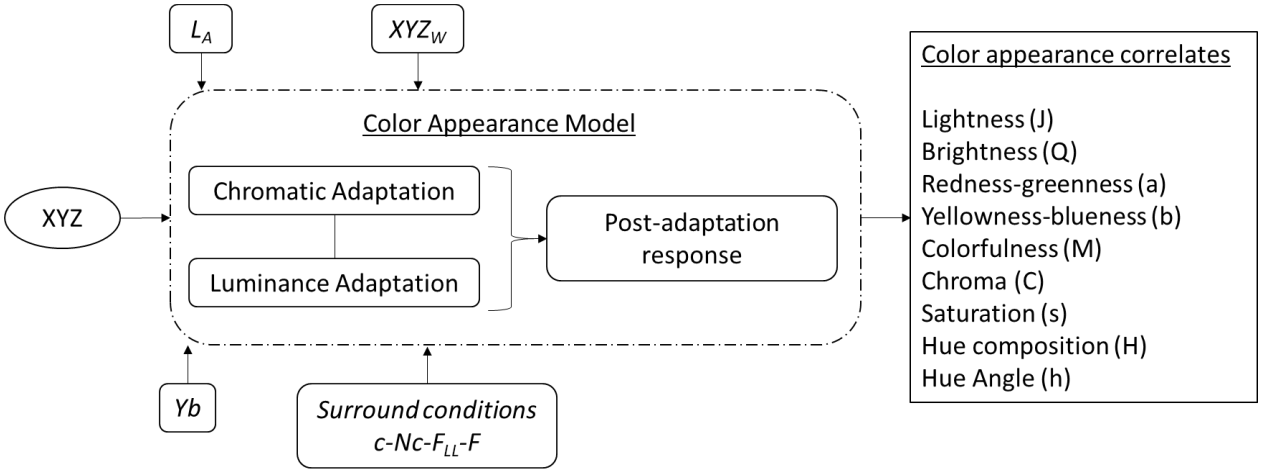

Figure 15, General structure of a Color Appearance Model

The next step is the calculation of various color correlates like lightness, brightness, chroma, hue etc. This includes *J*, *a* and *b*, which are equivalent to the CIELAB Cartesian coordinates, and form the CAM02-UCS (uniform color space).

CIECAM02, itself an improvement to the CIECAM97s, still has many defaults (Brill, 2006; Brill & Mahy, 2013; Brill & Süsstrunk, 2008; Z. Wang et al., 2016). For example, during cross-media image reproduction the lightness computation of CIECAM02 sometimes gives negative values (C. Li et al., 2013). This is mainly because of separate chromatic adaptation (via CAT02) and luminance adaptation (via Hunter-Pointer Estevez transform). Many modifications have been proposed to correct this and certain other problems of the CIECAM02 (Gill, 2008; J. Jiang et al., 2015; C. Li et al., 2013, 2014, 2015). Neither of these corrections try to alter the structure of CIECAM02. Most of them proposed modified matrix transforms of M_{02} to reduce errors. Recently, a simplified and improved CAM, CAM16, which includes the CAT16 and CAM16-UCS, was developed with coordinated efforts from a consortium of vision and color scientists (C. Li et al., 2017). The idea behind CAM16 is to simplify and combine the adaptation process, thus changing the structure of the original CAM02 alongside a new matrix transform M_{16}. It is accomplished by doing both the luminance and chromatic adaptation in a single space, thus maintaining the accuracy levels and at the same time solving the negative lightness value problem. The mathematical steps of CAT16 are shown below

$$\begin{pmatrix} R_c \\ G_c \\ B_c \end{pmatrix} = \begin{pmatrix} D_R.R \\ D_G.G \\ D_B.B \end{pmatrix} \ldots(7)$$

$$\begin{pmatrix} R \\ G \\ B \end{pmatrix} = M_{16} \begin{pmatrix} X \\ Y \\ Z \end{pmatrix} \ldots(7a)$$

$$M_{16} = \begin{pmatrix} 0.401288 & 0.650173 & -0.051461 \\ -0.250268 & 1.204414 & 0.045854 \\ 0.002079 & 0.048952 & 0.953127 \end{pmatrix} \ldots(7b)$$

$$D_R = D.\frac{Y_W}{R_w} + 1 - D; D_G = D.\frac{Y_W}{G_w} + 1 - D; D_B = D.\frac{Y_W}{B_W} + 1 - D \ldots(7c)$$

The relative luminance of the adapting white, Y_w is taken into account when doing the CAT16 calculations. The degree of adaptation D remains the same as that of CIECAM02. After the calculations of various color correlates (Figure 15), the RGBc values are reverted back to the XYZ color space.

$$\begin{pmatrix} R \\ G \\ B \end{pmatrix} = \begin{pmatrix} \frac{R_c}{D_R} \\ \frac{G_c}{D_G} \\ \frac{B_c}{D_B} \end{pmatrix} \ldots(7d)$$

$$\begin{pmatrix} X \\ Y \\ Z \end{pmatrix} = M_{16}^{-1} \begin{pmatrix} R \\ G \\ B \end{pmatrix} \ldots(7e)$$

The CAM16 is currently in the process to become the future CIE standard. Though the use of CAT16 as a stand-alone CAT has shown to bring certain inconsistencies due to the presence of the Y_w factor (Smet & Ma, 2020).

2.6. Image color appearance modelling: iCAM06

The accuracy of most CAMs is tested on the basis of the prediction of various color appearance datasets and color difference datasets (Juan & Luo, 2000; D.-H. Kim, 1997; M. R. Luo et al., 1991, 1993; M. R. Luo & Hunt, 1998; Newhall, 1940). Despite having quite accurate CAMs like CAM02, CAM16; the work on CAMs is not yet complete, especially for imaging applications. The various CAMs mentioned in the previous section have a point in common: they focus on the prediction of illuminant color, illumination level and the relative luminance of the illuminant. Mainly, they treat each pixel as a separate stimulus and predict various color appearance properties pixel-by-pixel. Human vision is spatial and temporal in nature. We do not see our surroundings as point objects but rather as a perceptual relationship of various objects (spatial vision). Our vision also has a temporal aspect, i.e. it changes with the passage of time, which is closely related to our ability to perceive notions. Such temporal and spatial impacts of vision are discounted in traditional CAMs.

S-CIELAB, a spatial extension to the CIELAB color space, is the first model to integrate spatial filtering to calculate perceptual differences between complex scenes (images). Nevertheless, the filtering computation of S-CIELAB is a complicated process, sometimes broken down into various channels. It has been found that such a level of complexity to predict image appearance attributes is not always required and can be discounted for a simpler process (M. Fairchild, 2004; M. Fairchild & Johnson, 2003, 2002). A spatial extension of CIECAM02 that takes in account the spatial frequencies of the environment was developed by Tulet et al by applying Fourier transforms on the image plane divided into various spatial frequency levels (Tulet et al., 2008). Albeit their approach remains directly inapplicable due to the loss of test images and a ready-to-go algorithm (due to a database crash) by the author (of the spatial extension of CIECAM02).

Fairchild simplified image CAMs by combining the color appearance calculations of CIECAM02 with the spatial characteristics of images with the introduction of iCAM (M. Fairchild & Johnson, 2002) and then a refined version known as iCAM06 (Kuang, Johnson, et al., 2007). iCAM06 is presented primarily as a HDR-

TMO (High Dynamic Range Tone-Mapping Operator) in the original publication, but can be successfully used as a CAM. Each step of iCAM06 is visualized in Figure 16 by applying the algorithm on a naturally day-lit scene.

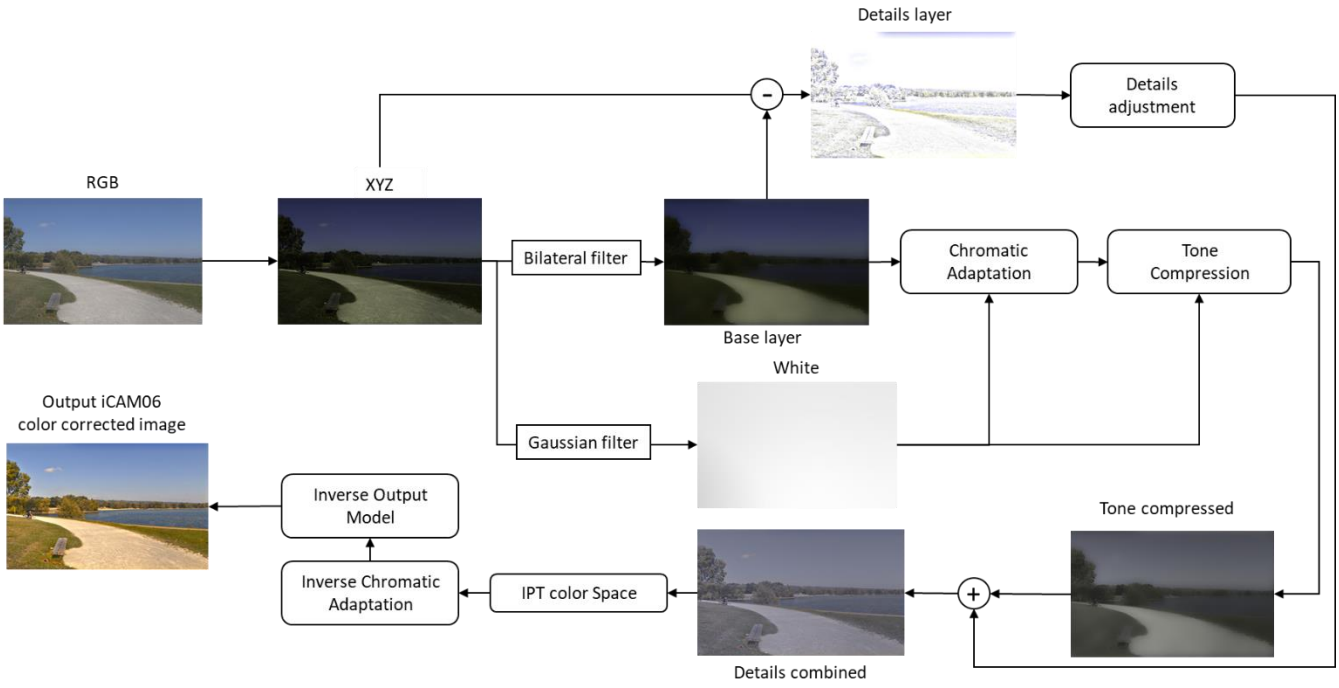

Figure 16, Framework of iCAM06 explained on a natural scene

The input for iCAM06 is the XYZ tristimulus values (or floating point RGB converted to XYZ). The processing begins by separating the image into two layers: base layer and details layer. A base layer contains the large scale variations and the rest of the image containing minute 'details' is stored in the details layer. These details are left untouched from most of the processing of iCAM06 and are re-combined with a color corrected base layer at the end of the module. The decomposition process is accomplished by using a 'fast' implementation of the piecewise bilateral filter (Durand & Dorsey, 2002). Bilateral filter is an edge-sensitive filter which applies a weighted Gaussian low pass filter taking into account both, the spatial and intensity domain of the image. It assigns a lower weight to the neighboring pixels having a large intensity difference, thus identifying edges. This avoids the formations of halos around the edges when applying a low-pass filter. The Piecewise Bilateral filter applies a 2-D fast Fourier transform on a log image. A log image compresses the dynamic range of an image by replacing each pixel with its logarithmic value. This log image is then down sampled before applying the Gaussian filter depending on the intensity difference of neighboring pixels. When the blurred image is normalized, the image is up-sampled to preserve the edges in the image. An interpolation is done on the image to have the same size as the input, which is the base layer of the original XYZ input.

The next step is the application of the CIECAM02 chromatic adaptation on the base layer of the image. A Gaussian filter is applied on the base layer to have a low pass version of the base layer as the RGB adapted white (RGB_W). The adapting luminance (L_A) is taken as the 20% of each pixel in the Y channel of RGB_W converted to XYZ (XYZ_w). The surround factor F is set at 1 for an average surround. The calculation of the degree of adaptation 'D' from CIECAM02 is modified in iCAM06 by applying a factor of 0.3 to the original formula in order to avoid image de-saturation. With all the necessary input data for applying the CAT02, the base layer is chromatically adapted with D65 illuminant as the illuminant of reference as shown below.

$$\begin{pmatrix} R_c \\ G_c \\ B_c \end{pmatrix} = \left[D \begin{pmatrix} \frac{R_{D65}}{R_w} & 0 & 0 \\ 0 & \frac{G_{D65}}{G_w} & 0 \\ 0 & 0 & \frac{B_{D65}}{B_w} \end{pmatrix} + 1 - D \right] \begin{pmatrix} R \\ G \\ B \end{pmatrix} \ldots(8)$$

$$D = 0.3F \left[1 - \left(\frac{1}{3.6} \right) e^{\left(\frac{-(L_A - 42)}{92} \right)} \right] \ldots(9)$$

The post chromatic adaptation process of iCAM06 is similar to that of CIECAM02, i.e. the application of a Hunter-Pointer-Estevez transform followed by the calculation of the cone-response and the rod-response.

$$\begin{bmatrix} R' \\ G' \\ B' \end{bmatrix} = M_{HPE} M_{CAT02}^{-1} \begin{bmatrix} R_c \\ G_c \\ B_c \end{bmatrix} \ldots(10)$$

$$M_{HPE} = \begin{bmatrix} 0.38971 & 0.68898 & -0.07868 \\ -0.22981 & 1.18340 & 0.04641 \\ 0 & 0 & 1 \end{bmatrix} \ldots(10a)$$

The cone response calculation of CIECAM02 is modified by adding a power factor 'p' ($\in$ [0,6-0,85]). This user-controlled power factor controls the steepness of the cone response curve and thus controls the image contrast. A higher value of p increases the overall contrast of the final output image.

$$k = 1/(5L_A + 1)) \ldots(11)$$

$$F_L = 0.2k^4(5L_A) + 0.1 * (1 - k^4)^2 (5L_A)^{1/3} \ldots(12)$$

$$RGB'_a = \frac{400(F_L RGB'/Y_W)^p}{27.13 + (F_L RGB'/Y_W)^p} + 0.1 \ldots(13)$$

The rod response calculation of iCAM06 is not taken from CIECAM02, but from Hunt's model (Hunt, 1995). The neutral rod response (A_s) is adjusted automatically to ensure that the luminance (S) of each pixel corresponds to the luminance value of the reference white (S_W). The rod-response becomes significantly small in comparison to the cone response for a bright scene. The Hunt's model includes the calculation of the scotopic luminance (L_{AS}), the saturation factor (or the rod-pigment bleaching factor B_s) and the scotopic luminance adaptation factor (F_{LS}). The final response (tone-compressed) is calculated by combining the cone response (RGB'_a) with the neutral rod response (A_s) and is detailed below.

$$L_{AS} = 2.26L_A \ldots(14)$$

$$j = 0.00001/[5L_{AS}/2.26)] + 0.00001] \ldots(15)$$

$$B_s = 0.5/\{1 + 0.3[(5L_{AS}/2.26) * (S/S_w)]^{0.3}\} \ldots(16)$$

$$A_s = 3.05 * B_s \left[\frac{400\left(\frac{F_{LS}S'}{S_W}\right)^p}{27.13 + \left(\frac{F_{LS}SB'}{S_W}\right)^p} \right] + 0.3 \ldots(17)$$

$$F_{LS} = 3800j^2(5L_{AS}/2.26) + 0.2(1 - j^2)^4(5L_{AS}/2.26) \ldots(18)$$

$$RGB_{TC} = RGB'_a + A_s \ldots(19)$$

Furthermore, the details layer is now merged back with the chromatically adapted and corrected for luminance RGB image, which is further reverted to XYZ. A details adjustment is done to predict Steven's effect by adding a non-linear factor to the details layer, as shown below.

$$Details_a = Details^{(F_L+0.8)^{0.25}} ...(20)$$

The next step in iCAM06 is the application of the IPT color space developed by Ebner and Fairchild (Ebner & Fairchild, 1998). It is a uniform color space known to make consistently accurate hue predictions. The I channel is the lightness channel, while P-T channels are similar to the red-green and blue-yellow color opponent channels. It operates in the LMS color space, thus the post-adaptation XYZ image is converted to the LMS color space and then to the IPT color space using the following matrix transformation:

$$\begin{pmatrix} L \\ M \\ S \end{pmatrix} = M_H^{D65} \begin{pmatrix} X_c \\ Y_c \\ Z_c \end{pmatrix} \ldots(21a)$$

$$\begin{pmatrix} I \\ P \\ T \end{pmatrix} = M_{IPT} \begin{pmatrix} L' \\ M' \\ S' \end{pmatrix} ...(22a)$$

$$M_H^{D65} = \begin{bmatrix} 0.4002 & 0.7075 & -0.0807 \\ -0.2280 & 1.1500 & 0.0612 \\ 0 & 0 & 0.9184 \end{bmatrix} ...(21b)$$

$$\mathrm{L}MS' = \mathrm{L}MS^{0,43} ...(22b)$$

$$M_{IPT} = \begin{bmatrix} 0.4000 & 0.4000 & 0.2000 \\ 4.4550 & 1.1500 & 0.3960 \\ 00.8056 & 0.3572 & -1.1628 \end{bmatrix} ...(22c)$$

The IPT space comes with the possibility to enhance the image by applying the Hunt's effect on the P-T channels and the Bartleson surround adjustment on the I channel as shown below.

$$I = I^{\gamma} ...(23)$$

$$P = P.[\,(F_L+1)^{0.2}\left(\frac{1.29C^2-0.27C+0.42}{C^2-0.31C+0.42}\right) ...(24)$$

$$T = T.[\,(F_L+1)^{0.2}\left(\frac{1.29C^2-0.27C+0.42}{C^2-0.31C+0.42}\right) ...(25)$$

Where, $\gamma_{dark} = 1.5$; $\gamma_{dim} = 1.25$; $\gamma_{average} = 1.0$ and $C = \sqrt{P^2+T^2}$

The IPT image is now reverted back to the LMS space and further back to the XYZ space. The application of the iCAM06 is completed by applying an inverse chromatic adaptation (using the inverse of CAT02 matrix: M_{02} and the chosen white-point (D65)). This tone-mapped XYZ image is converted back to the RGB space by taking into account the color profile (sRGB, Adobe etc.) and the type of operating system (Mac, Windows etc.).

3. Hyperspectral Imaging for stimuli creation

The previous chapter provided a general description of color vision, but to simulate color vision we also need to understand the data acquisitioning technologies that enable color vision modelling. This chapter will discuss the need for spectral imaging in the context of this thesis and detail the entire process of data acquisition using spectral imaging. This chapter contains text and data that has been the subject of two conference presentations, one conference article and one journal article (submitted for review in July 2021) (Cauwerts et al., 2019; Raza et al., 2019).

Spectral analysis holds a high importance in both, lighting engineering and optometry as it offers a non-invasive method to characterize object properties, such as their reflectance/transmittance and colorimetric appearance (Bullough et al., 2014; Fotios, 2006; Giannos et al., 2019; Sliney, 2001). A spectroradiometer captures the spectral radiances of a point target within the spectral range of the acquisition system. This methodology is efficient as long as we treat point objects. When a 2D object or an entire scene has to be analyzed, spectral measurement of every point, of every object in the scene becomes very time consuming.

For spatial analysis of scenes, imaging is frequently used by color and lighting researchers to obtain both qualitative and quantitative descriptors, and to investigate people's perception of their environments and day-lit spaces (Foster et al., 2006; F. Jiang et al., 2019; Ledda et al., 2004; Smet et al., 2014; Yoshida et al., 2005). As long as the perceptual attributes induced by the displayed pictures are faithful to reality, and the physical world is accurately captured by the camera, images can be used as visual stimuli in a psychophysical approach. One drawback of traditional imaging for our application is the absence of detailed spectral information in narrow wavelength regions of the objects. For each pixel (point target), the only information available is in the broad wavelength (RGB). Hyperspectral imaging provides a good solution for these concerns as it aptly combines spectroscopy and imaging.

3.1. Hyperspectral Imaging

Hyperspectral imaging combines conventional imaging sensors with spectroscopy and provides image data containing spatial and spectral information. For each pixel of the image, the spectral power distribution (SPD) is measured (or retrieved) to generate datasets with three dimensions (also called data-cubes). With spectral imaging, radiometric measurements are no more restricted to a limited number of points but can be applied to the entire surface of the object, or an entire visual scene, seen from a single point of observation. There is no standardized limit defined in spectral imaging to differentiate between multispectral and hyperspectral imaging (Foster & Amano, 2019; Westland et al., 2012). While it seems to be discipline dependent, the difference is always related to the number of spectral bands. In general, a system is called multispectral if it has strictly more than 3 spectral bands (to differentiate it with a conventional RGB camera) and hyperspectral if it has more than 20 bands. Even if some studies suggest that 10 bands are sufficient to recover the spectral information (Imai et al., 2003), for high spectral accuracy, a higher number of bands are required (Vilaseca et al., 2014). Particularly if one wants to measure the effect of narrow spectral peaks like those of LED sources. For lighting and color research, CIE recommends the calculation of chromatic coordinates from spectral data with a spectral resolution of 5 nm or less (CIE 15, 2004). This corresponds to 80 bands in the range of 380 nm - 780 nm.

Although spectral imaging technology was developed for remote sensing application (astrophysics, planetary science) (Goetz et al., 1985), it has become a useful tool in many other fields of research (agriculture, medicine, food engineering, cultural heritage etc.). For instance, spectral imaging is used on artworks, with applications on canvases and manuscripts for material identification, visualization of underdrawings (sketch before paint application), conservation monitoring and for color reproduction (Fischer & Kakoulli, 2006; Foster & Amano, 2019; Liang, 2012; MacDonald et al., 2017). This ability to reproduce relevant colors and to estimate the color appearance under different illuminants is of great interest for the color and lighting community. Contrary to conventional imaging, spectral imaging permits to predict the effect of any change in light source (artificial, daylight, daylight transmitted by sunglasses),

for any observer (CIE standard observers, color deficient observers or for any individual color matching functions). By determining the spectral radiance for each pixel, the acquired capture can be used to retrieve photometric and colorimetric properties and to generate the corresponding visual stimuli. Moreover, contrary to point-measurement spectrophotometers, spectral imaging allows both global rendering and local study of selected areas (Cauwerts & Jost-Boissard, 2018). Some teams have harnessed this ability and used spectral imaging as a decisive tool to select light sources for artwork by visually predicting the effect of illumination (Masuda & Nascimento, 2013; Nascimento & Masuda, 2014; Pinto et al., 2006, 2008) or by calculating colorimetric properties of simulated colored scenes (Liang, 2012; Martínez-Domingo et al., 2019).

A hyperspectral camera captures spectral information within a particular wavelength range (UV, NIR, VIS or a mix) for each spatial target in the scene which in turn depends on the spatial resolution of the camera. A hyperspectral image has three dimensions, [R C W]; where R and C denote the pixel array (row and columns) and W denotes the wavelength dimension, see Figure 17.

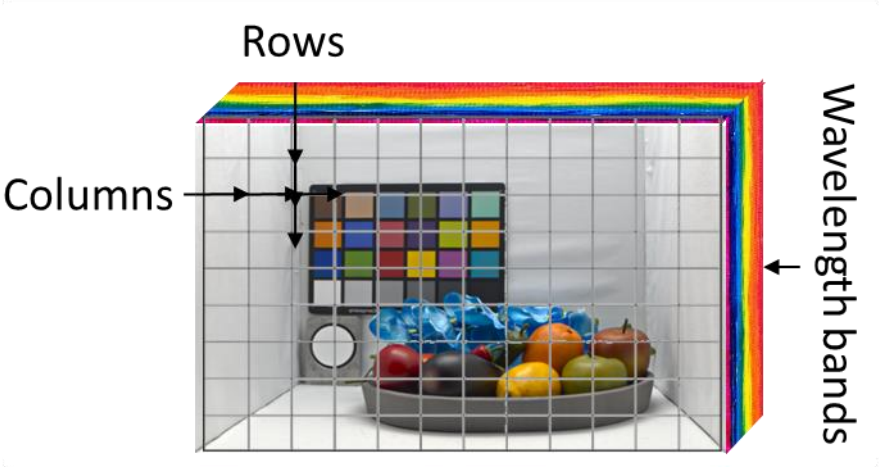

Figure 17, Hyperspectral image structure

Hardware development of spectral imaging has reached new heights with commercial availability on the market of good quality, portable and fast imaging systems. The earlier methodology of creating a hypercube involved taking quasi-monochromatic images of the same scene sequentially for changing wavelengths. Objects like Liquid Crystal Tunable Filters (LCTFs) and Acousto-optic Tunable Filters (AOTFs) were used to achieve this bandpass filtering (Lewis et al., 2008; X. Wang et al., 2018). This methodology provided a good spatial resolution and focused images but had a poor spectral resolution. Modern spectral imagers use the line-scanning push broom technology. They are equipped with an array (line) of spectral detectors that measure the scene line-by-line with a relative motion between the camera and the scene, through either a conveyer belt (moving sample) or rotary motor (moving camera) (Shi et al., 2018). These types of hyperspectral cameras are able to capture scenes with an improved spectral resolution (as high as every 1,3 nm) and have a good spatial resolution as well. Modern hyperspectral cameras also have increasingly improved lens *aperture* (opening through which light passes) which in turn ensures higher *exposure* and improved image sharpness. A high *exposure* ensures the ability to capture low light scenes with relatively less noise (Faris Belt, 2012; Mansurov, 2020). The focal length of available camera lenses is also improving with values as high as 150 mm ensuring the capture of larger fields of view (Faris Belt, 2012). These developments create a growing interest for hyperspectral imaging for in-situ acquisition with innovative research on indoor and outdoor scenes (Chakrabarti & Zickler, 2011; Foster et al., 2006; Foster & Amano, 2019; Montagner et al., 2016; Párraga et al., 1998). This opportunity to have on-site measurements is of great interest in the field of lighting and particularly for color rendering, to determine color properties of real scenes, to predict color appearance of a whole scene, or of specific objects, under different illuminants and to develop a comprehensive database of typical lighting environments.

3.2. Hyperspectral Camera Calibration

A typical Hyper-Spectral Imaging (HSI) device's output is in raw units which do not match real radiances (the peaks, shapes and magnitudes are different). This raw output defined by the camera manufacturer requires further calibration to produce radiances in SI units. Most manufacturers provide their own calibration at an additional cost. This calibration is valid for a limited time period ($\gtrsim$ 1 year) since the physical sensors in the device may depreciate over time. It is recommended to send the HSI system back to the manufacturer for re-calibration periodically to take into account any such depreciation in the sensors. The frequency of re-calibration is different for different devices and manufacturers. This process is not only expensive but also complicated. Despite the development of portable and relatively light-weight HSI devices, they still are bulky, heavy and at the same time quite delicate for frequent transport as compared to a traditional RGB camera. These concerns prompted us to identify a calibration protocol that can be used in-situ to assure the accuracy of the hyperspectral cameras in the long run.

This section describes a simplified protocol to **calibrate any push-broom hyperspectral camera**. The principal objective behind calibration is to bring the hyperspectral radiance closer to that of a reference spectral measurement device with the help of a correction factor (or a matrix of factors per waveband). This can be obtained by dividing the spectral radiance of hyperspectral data with that of the reference device (for e.g. spectroradiometer) for the same measurement area. The measurement area should be of a homogeneous and uniform spectral reflectance.

3.2.1. Material and setup

a) Instruments

Hyperspectral Camera

A commercial push broom hyperspectral camera manufactured by Specim (Specim FX10, S/N 1200061), was used to establish a generalized protocol for any HSI system calibration. It has a sCMOS (scientific Complementary Metal-Oxide-Semiconductor) detector and captures wavelengths from ~400 nm to 1000 nm. sCMOS detectors ensure low noise, high frame rates, a large field of view and a wide dynamic range as compared to traditional CMOS sensors (Grunsby, 2012). The camera can also apply binning on the spatial and spectral resolutions thus offering the possibility to reduce sampling intervals when needed. It can be mounted on a rotary scanner to capture the scene. Further technical information about the camera is detailed in Table 3.

Table 3, Characteristics of the Hyperspectral Imaging System

	Characteristics			Lens		Acquisition parameters				
HSI System	Aperture	Spectral resolution FWHM (nm)	Spatial resolution (pixels)	Manufacturer	Focal Length (mm)	Binning	Spectral resolution (nm)	Spatial resolution (pixels)	Exposure (ms)	Frame (sec^{-1})
Specim FX10	f/2,1	5,5	1024	Specim	15	2x1	2,7	1024*1232	40	15

Spectroradiometer

A JETI Specbos 1211-UV spectroradiometer (S/N 2011273) was used to measure the reference spectral radiance of various elements in the scene. Its spectral accuracy is 0.5nm, chromatic accuracy is $\pm$ 0.002 for the chromaticity coordinates under illuminant A and luminance accuracy is of 2% at 100 cd/m^2 under illuminant A. The instrument was calibrated by SCIENTEC less than six months prior to the study. It was mounted on a tripod at the same position as the camera.

Chromameter

A Konica Minolta CL-200A chromameter (S/N 80731014) was used to check the stability of the light sources during hyperspectral data acquisition. The chromameter took a few seconds to start measuring and had a $\pm$2% variation of illuminance (in lux).

b) Scene acquisition setup

To calibrate radiance from hyperspectral data, captures were taken in a white light booth covered with a cloth of a uniform reflectance (ρ=0.81), see Figure 18a. A Macbeth ColorChecker (MCC) with 24 colored patches and a Spectralon white standard (Gigahertz-Optik ref. BN-R986SQ2C) were added in the light booth for colorimetric measurements and white reference. Two configurations were set for the data acquisition. The first configuration named low radiance (see Figure 18a) used a polycarbonate diffuser placed on the ceiling of the light booth to uniformly distribute the light. This configuration was used for validating the obtained calibration. The second configuration named High radiance (see Figure 18b) did not use the diffuser and used a block inside the light booth to increase the available luminance levels. It was used for the calibration. The booth was lit either by a cold incandescent source or by three spectrally tunable 7-channel LED projectors (SourceFour LED, Lustr+ from ETC Company). A cold incandescent source has a higher energy contribution to the short and medium wavelength range of the visible spectrum than a classic incandescent lamp. This ensures a calibration curve achieved from a relatively more uniform light source while still using the conventional incandescent technology. The tunable LED source enables us to validate our calibration curve on the popular LED sources with different CCTs. The spectral radiance of the light source used for the calibration (Cold Incandescent) measured in the light booth on the Spectralon reference white standard is plotted in Figure 19.

To obtain an optimum focus, a sheet of black and white stripes was added temporally in the scene at the distance of ~80 cm from the camera lens (in front of the MCC chart). The focusing ring of the camera lens was adjusted to obtain the maximum amplitude difference in the peaks and troughs visible in the pixel view of the camera's software. This task is delicate as the focus ring has a very small margin of operation. Figure 20 shows the focusing target with examples of bad and good focusing on the camera software's pixel view window.

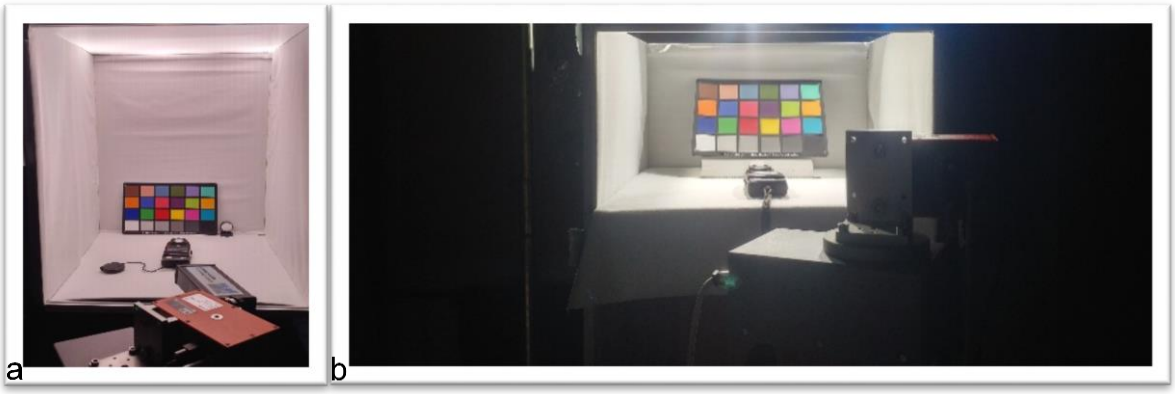

Figure 18, Low radiance level configuration (a); High radiance level configuration (b)

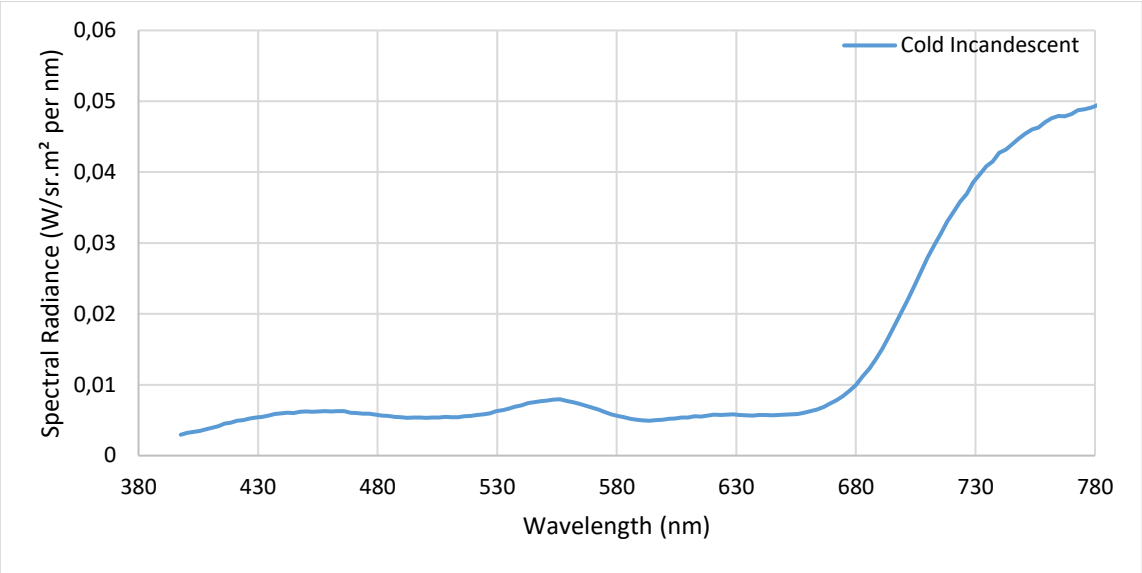

Figure 19, Spectral radiances of the Cold Incandescent source measured on the Spectralon

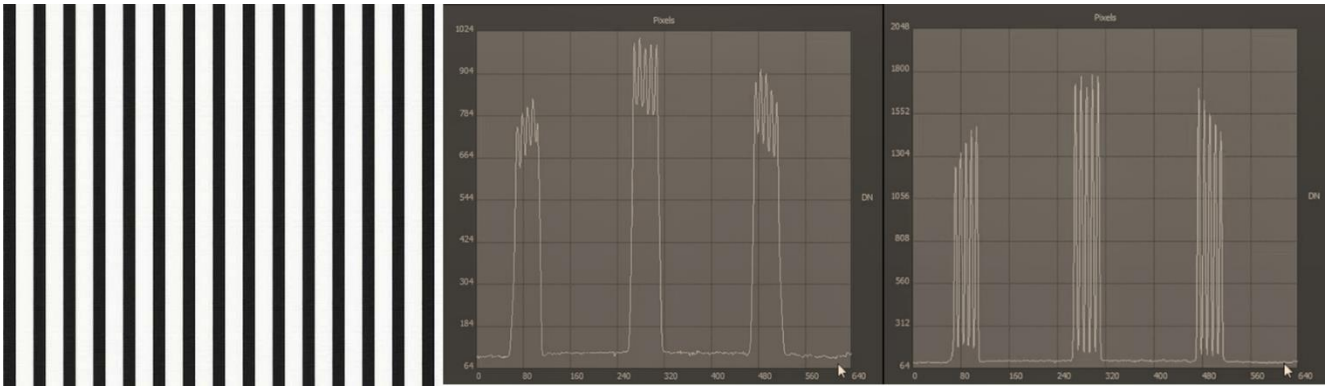

Figure 20, Focus target (left) with bad (middle) and good (right) focusing of the camera

c) Hyper spectral data extraction and processing

The first step of the capture was a dark reference (.raw). The hyperspectral camera recorded data with the shutter closed before capturing any scene (.raw). This dark capture was subtracted from the raw capture and the metadata for each hyperspectral capture was stored in a separate file (.hdr). The metadata consisted of information regarding the image size, spatial/spectral resolution, exposure time, frame rate, data type and various other essential information for image treatment and calibration. This dark subtraction was done with the help of a proprietary software of Specim. Each measurement also automatically generated a preview image without any color balancing or correction. The preview image was generated with (false) colors as per user-defined (false) RGB wavebands. The camera interface (integrated with the acquisitioning system as a software) monitors the chosen exposure time and shows bright red pixels if the exposure is too high (luminance saturation).

For processing the data, the metadata was extracted through the *textscan* command of Matlab and the raw radiance cube (.raw) was converted with the *multibandread* command into a hyperspectral cube readable in Matlab (.mat). This function reads the band-interleaved-by-line (BIL) data from the raw file. BIL is not an image format but rather a system developed for storing the actual pixel values of a multiband raster image file, band by band for each line.

3.2.2. Calibration Methodology

To calibrate the raw radiance output of the hyperspectral camera, the target scene was composed of the MCC and the Spectralon illuminated with a cold Incandescent lamp as a reference calibration source (L_v=550 cd/m^2). The capture was done in the High radiance configuration (b) of the light booth. An exposure of 40 ms was chosen for the HSI acquisition as it was sufficiently high to avoid any unwanted noise due to under-exposure and did not saturate the scene either (over-exposure).

The reference spectral radiance of the Spectralon was measured via the spectroradiometer. The laser pointer of the spectroradiometer was used to identify the area measured on the Spectralon. The spectral data associated with the Spectralon was also extracted from the uncalibrated output file. Using the Matlab circle ROI function, the pixel location was retrieved from the preview image to correspond to the measurement zone of the spectroradiometer (ensuring maximum coverage of the patch surface without touching the border). This corresponded to ~1250 pixels for a circle with a radius of 20 pixels. The uncalibrated spectral radiance values obtained from individual pixels were then averaged to obtain a single radiance curve for the Spectralon. This was done to prevent inhomogeneity linked errors arising due to the slightly non-uniform lighting (Vitorino et al., 2015).

The raw radiance values of the Spectralon retrieved from the hyperspectral image (.mat) were divided with the corresponding reference spectral radiance measured with the spectroradiometer. The spectroradiometer produced interpolated spectral data every 1 nm obtained from a FWHM spectral resolution of 4,9 nm. Thus the spectral data from the spectroradiometer was interpolated linearly to match the spectral resolution of the hyperspectral camera. A more robust cubic-spline interpolation method was avoided at this step as it produced negative spectral radiances at the extreme ends of the spectrum. The spectral radiance calibration curve was determined for the complete spectral range of the camera (~400 nm-1000 nm) and a (base) spectral resolution of 2,7 nm with an exposure of 40 ms. The calibration curve is shown in Figure 21 and the raw camera radiance is compared with the reference spectroradiometer radiance in Figure 22.

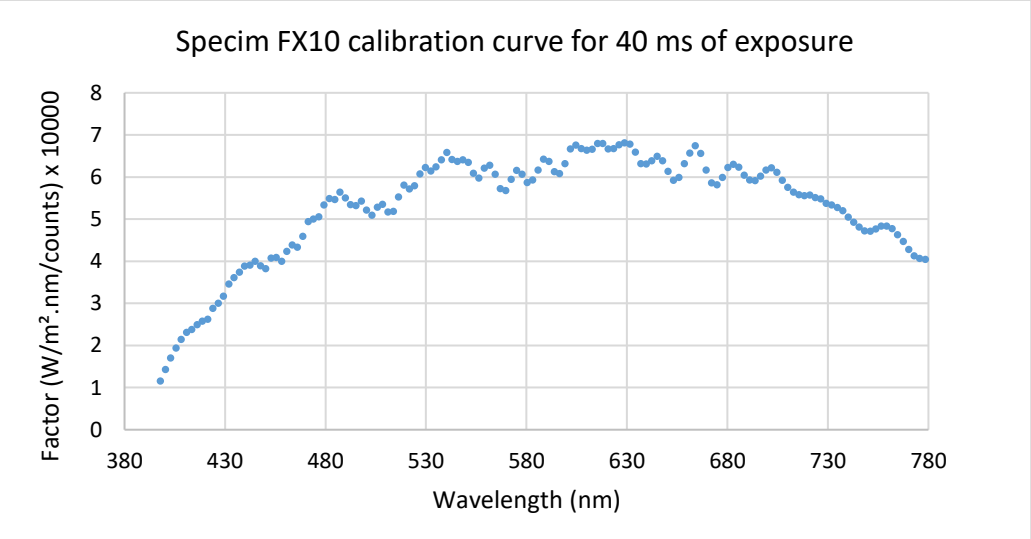

Figure 21, Radiance calibration curve obtained for Specim FX10

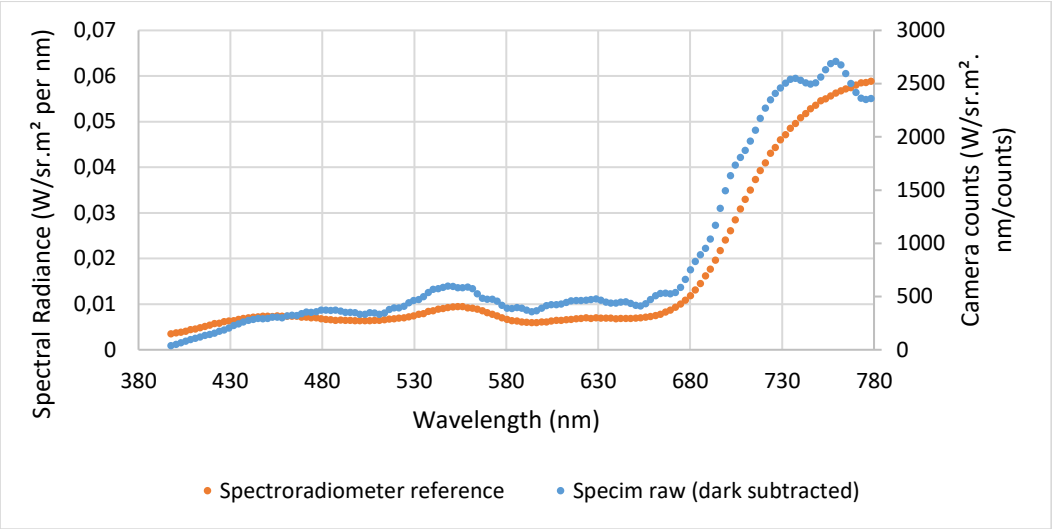

Figure 22, Comparison of raw spectral radiance vs reference spectral radiance: Cold Incandescent

Certain other methods of calibration were tested and subsequently rejected due to relatively less accurate results. The tested methods were: a unique averaged factor of the above calibration curve, a calibration curve with factors derived from monochromatic light sources and two calibration curves from less homogenous LED sources.

3.2.3. Validation

The spectral radiance calibration curve obtained with the cold Incandescent source was tested on a LED based approximation of the Equi-Energy Spectrum (EES) in the high radiance configuration of the light booth (Figure 18b), with hyperspectral capture taken at 40 ms, 20 ms and 10 ms of exposure. The calibration was determined for 40 ms of exposure, thus to see any impact of the choice of exposure, it was tested for 40 ms and 40 ms halved twice (20 ms and 10 ms). It is common practice as per the Exposure Value System to change the exposure by a factor of 2 to see any visible impact. As per the CIE definition, *EES is a spectrum of radiation whose spectral concentration of a radiometric quantity as a function of wavelength is constant throughout the visible region*. The EES approximation was produced using the 7-channel LED projectors. The mix of the channels was determined with the help of a constrained non-linear multivariable search algorithm of Matlab, *fmincon* function. The spectral radiances on the Spectralon obtained with the three captures were compared with the spectral radiance obtained from the spectroradiometer (spectral plots in Figure 23 and percentage errors in Figure 24). The percentage errors remain below 20% for most of the spectral range except for wavebands with negligible spectral energy distribution ($\lambda<413$ nm and $\lambda>756$ nm, $L_{e,\lambda}\sim0{,}0003$ W/m^2.sr per nm). The spectral radiance curves were also verified by taking captures of the MCC and the Spectralon in a room partially illuminated by daylight and a warm LED lamp. The spectral radiance curves of selected colored patches (MCC Red, MCC Green, MCC Blue) and a perfect white (Spectralon) are plotted in Figure 25.

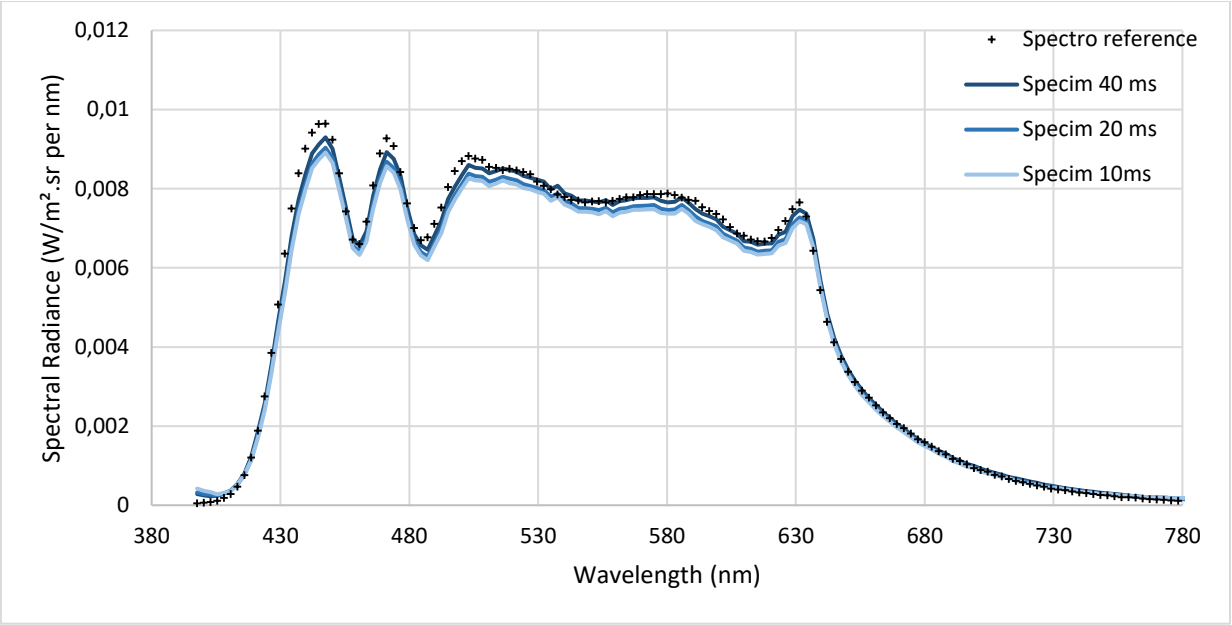

Figure 23, Validation of calibration curve on a LED based Equi-energy Source (EES)

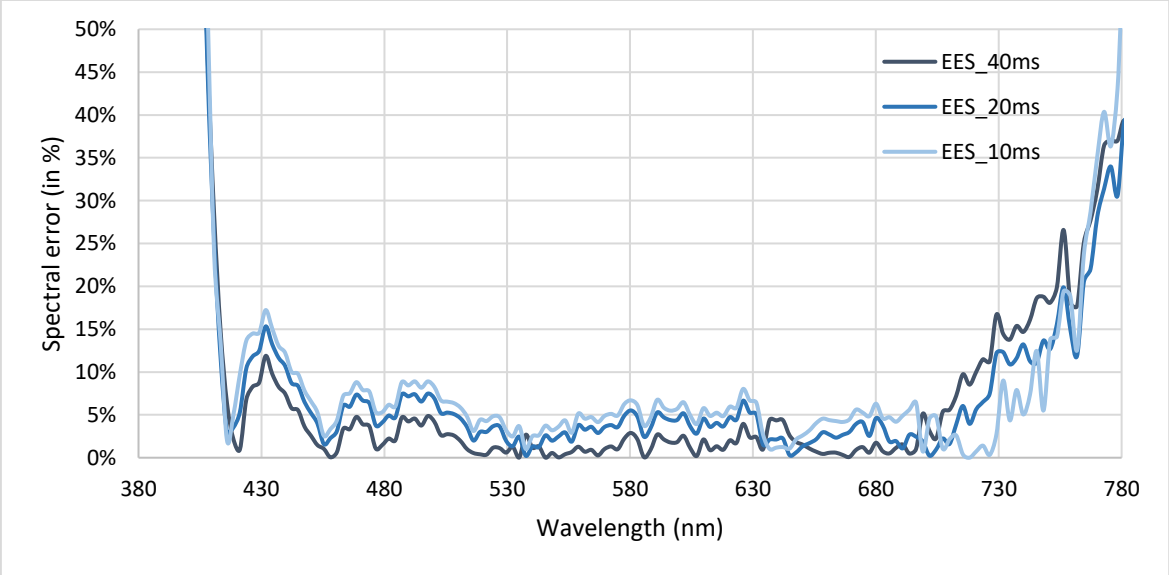

Figure 24, Symmetric mean absolute percentage error: spectroradiometer vs calibrated data

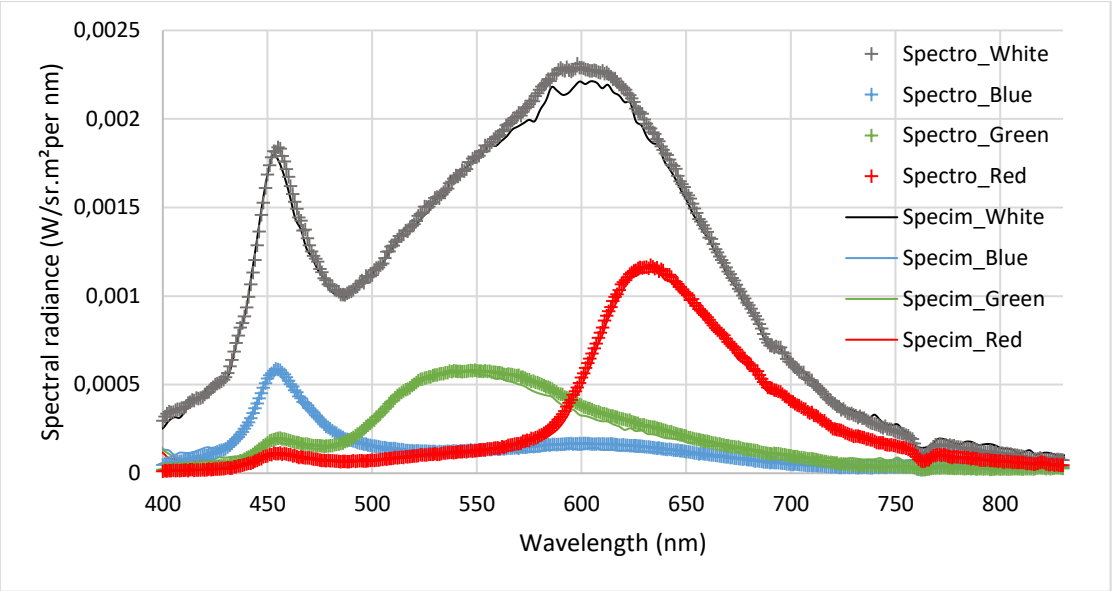

Figure 25, Validation of calibration curve on daylight mixed with a warm LED lamp

The calibration curve was further verified (for spectral errors and color differences) in nine identical light booths, illuminated with nine light sources of different Correlated Color Temperatures (CCTs) ranging from 2391 K to 5776 K. The light booths were equipped with three Incandescent sources, a mixed Fluorescent-Incandescent source and five Fluorescent sources, and are shown in Figure 26.

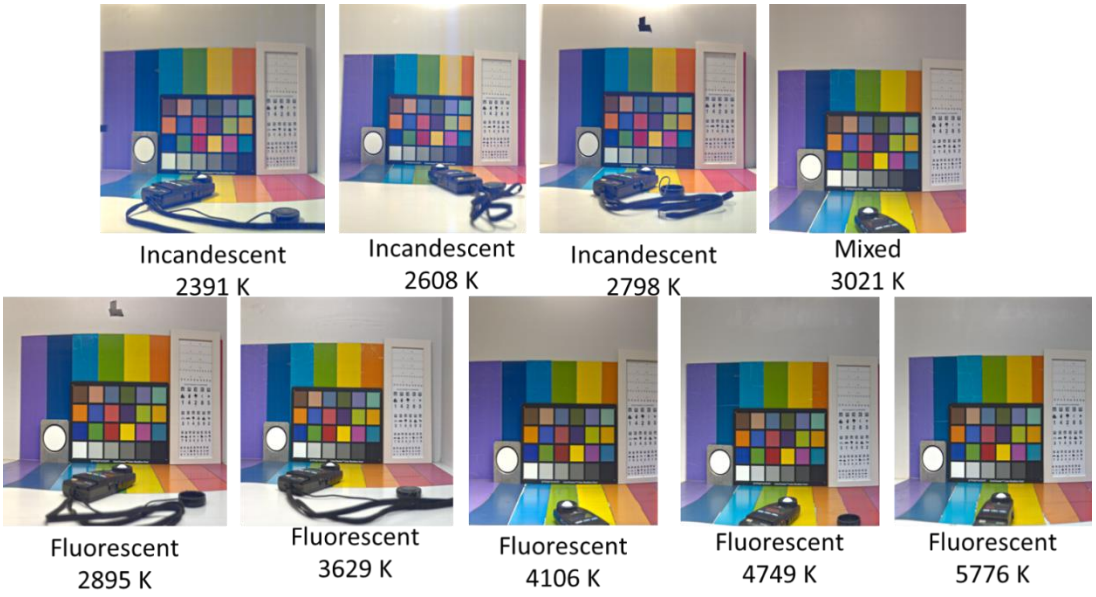

Figure 26, Nine identical light booths, each with a different light source

The calibration curve was also tested in the original light booth (Figure 18a) on nine different LED sources with CCTs ranging from 2316 K to 6589 K. The MCC (1-24) were used as targets for all these comparisons. The exposure time for the Fluorescent and Incandescent sources was 80 ms while for the LED sources it was 50 ms.

The differences of spectral radiances between the calibrated hyperspectral data and the spectroradiometer were evaluated with the Normalized Root Mean Square Deviation (NRMSD) (Foster & Amano, 2019).

NRMSD corresponds to the Root Mean Square Error (RMSE) normalized by the largest radiance value of the two spectra being compared, see equation below:

$$NRMSD\ (\%) = \frac{\sqrt{\frac{1}{N}\sum_{\lambda i}^{N}\left(s_{\lambda i,t} - s_{\lambda i,r}\right)^2}}{max(s_{\lambda i,t}\ ;\ s_{\lambda i,r})} \times 100 \ldots (26)$$

Where, $s_{\lambda i,t}$ and $s_{\lambda i,r}$ are the spectral radiances measured with the (calibrated) hyperspectral camera and with the spectroradiometer (reference) respectively, and N is the number of spectral samples (N_{Specim_FX10}=144).

Colorimetric accuracy was evaluated with the CIELAB color difference formula (ΔE*ab (CIE 15, 2004)) with the Spectralon chosen as the reference white (measured with the spectroradiometer). The formula is described below:

$$\Delta E^{*}ab\ = \sqrt{(L_{i,t} - L_{i,r})^2 + (a_{i,t} - a_{i,r})^2 + (b_{i,t} - b_{i,r})^2} \ldots (27)$$

Where $[Lab]_{i,t}$ and $[Lab]_{i,r}$ are the CIELAB values of the ith color patch measured with the (calibrated) hyperspectral camera and with the reference (spectroradiometer) respectively.

The mean spectral and color differences per source for the 24 color samples of MCC and Spectralon are given in Table 4.

Table 4, Average reproduction accuracy (on MCC 1-24 + Spectralon) of the calibration - summary

Lamp type	CCT (K)	Luminance (cd/m)²	Illuminance (Lux)	Mean NRMSD	Mean ΔE*ab
Incandescent	2391	54	381	9%	36,6
Incandescent	2608	41	371	11%	34,8
Incandescent	2798	68	730	11%	30,8
Mixed	3021	141	915	8%	12,8
Fluorescent	2895	160	910	3%	5,3
Fluorescent	3629	93	527	6%	5,1
Fluorescent	4106	159	1325	6%	5,2
Fluorescent	4749	97	558	7%	5,1
Fluorescent	5776	100	552	6%	5,1
LED	2316	550	1796	2%	6,9
LED	2535	552	1795	2%	3,9
LED	2704	545	1797	4%	4,1
LED	3009	548	1794	4%	3,6
LED	4009	552	1795	3%	2,2
LED	5017	553	1796	3%	2,0
LED	5108	848	4142	3%	2,7
LED	5896	500	2349	5%	2,5
LED	6589	555	1795	3%	1,9
Mean (LED and Fluorescent sources only)				4%	4,0
Mean (all sources)				5%	9,5

In the literature, normalized RMS errors lie between 1,9%-23% on radiances and up to 13% on reflectance measurements (Foster & Amano, 2019; Vilaseca et al., 2014). Thus, it can be said that the mean spectral

error for different light sources, obtained through our calibration method (max NRMSD 11% for Incandescent, 7% for fluorescent and 5% for LEDs) stay within the limits identified by other studies.

The calibration curve when applied on LED and fluorescent sources captures gave us a mean ΔE*ab of 4 units. For simple color patches, ΔE*ab less than 2 is deemed to be visually indistinguishable for non-expert observers (Mokrzycki & Tatol, 2011). It is to be noted that for a complex scene the color perception changes in relation to the surrounding environment, shape and size of the object in question (K. Shevell, 1982; M. Stone, 2012; Shevell & Humanski, 1988; M. Webster, 2015). It has been identified that a ΔE*ab less than 6 can be considered as non-perceivable difference for complex images (Hordley et al., 2004; Meyer, 1988).

The color differences were found to be unacceptable for Incandescent and mixed lamps. The LED source at 2316 K also had a mean color difference of more than 6 units, which is considered to be visually perceptible for images. These color differences were perhaps due to the inherent structure of Incandescent and other warm light sources. Warm light sources induce an unequal distribution of spectral energy across the visible spectrum on warm colored objects/patches. In such cases, even if the color spectrum is reproduced accurately, a non-uniform spectral distribution can perhaps introduce errors in the calculation of tristimulus color values. One such example is shown below in Figure 27, where the orange patch (MCC 7) and cyan patch (MCC 6) have a similar spectral reproduction accuracy but very different color reproduction accuracy. This could be due to the relatively unequal distribution of spectral radiance for the orange patch as compared to the cyan patch, see Figure 28.

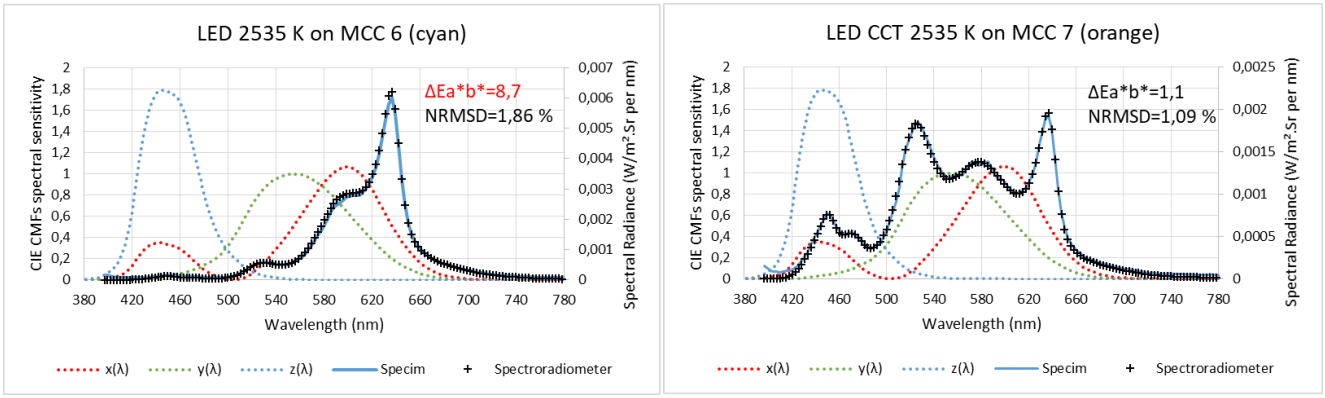

Figure 27, Impact of unequal spectral energy distribution on color differences

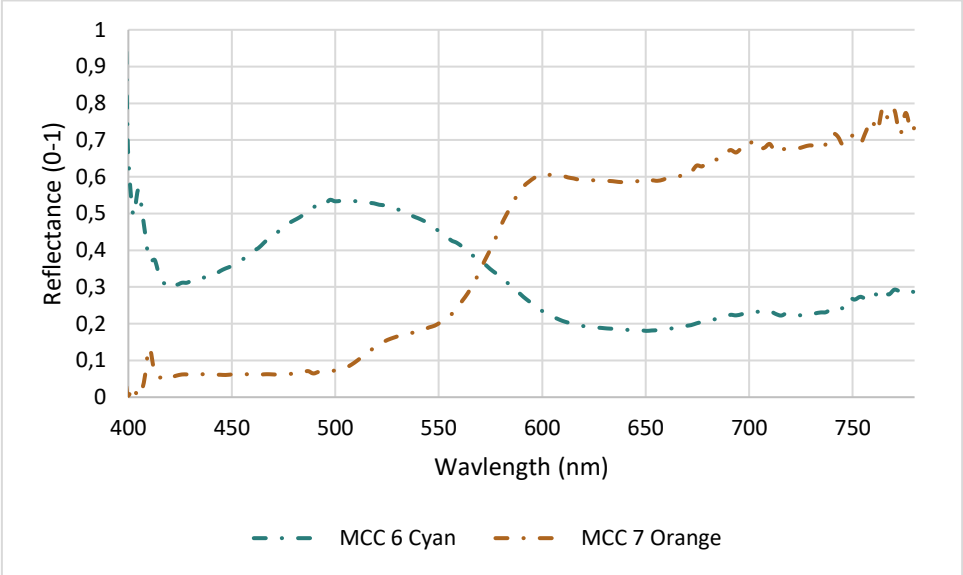

Figure 28, Reflectances of MCC 6 and MCC 7

Incandescent light sources not only have an unequal distribution of energy in the visible spectrum but it seems that they introduce a significant amount of stray light (a form of noise) that disturbs the normal functioning of the imaging device. This deteriorates the signal-to-noise (SNR) ratio of the capturing device, see Figure 29. These two factors together can perhaps explain why incandescent sources have very high reproduction errors.

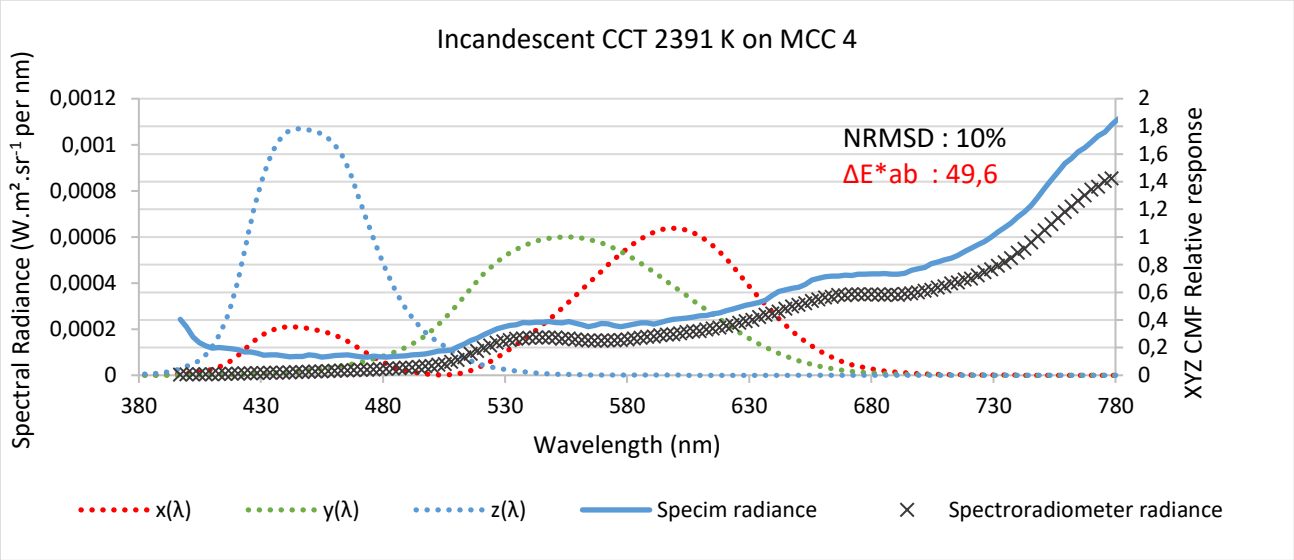

Figure 29, Spectral energy distribution of Incandescent on spectral/color differences

To ensure that these colorimetric errors were not due to our calibration method, hyperspectral captures were also done with the help of the manufacturer supplied calibration. The Specim FX10 came with a calibration plugin that provided both calibrated and non-calibrated radiance data. Such comparisons were done for the three Incandescent sources (Table 5) which had abnormally high ΔE*ab and also for the nine LED sources (Table 6) which covered a large range of CCTs.

Table 5, Calibration comparison-Incandescent sources

CCT (K)	Luminance (cd/m)²	Illuminance (Lux)	Mean ΔE*ab	
			Plugin	Our Method
2391	54	381	36,2	36,6
2608	41	371	34,0	34,8
2798	68	730	29,3	30,8
		Mean of means	33,2	34,1

Table 6, Calibration comparison-LED sources

CCT (K)	Luminance (cd/m)²	Illuminance (Lux)	Mean ΔE*ab	
			Plugin	Our Method
2316	550	1796	7,5	6,9
2535	552	1795	4,2	3,9
2704	545	1797	4,5	4,1
3009	548	1794	3,9	3,6
4009	552	1795	2,5	2,2
5017	553	1796	2,4	2,0
5108	848	2349	2,7	2,7

5896	500	4142	2,6	2,5
6589	555	1795	2,3	1,9
		Mean of means	3,6	3,3

The manufacturer's methodology yielded similar ΔE*ab values for Incandescent sources and LED sources. Thus, confirming that our calibration methodology is as efficient for calibrating HSI devices as the manufacturer's calibration.

Once the method was validated for indoor scenes illuminated by artificial light sources (max luminance on Spectralon=848 cd/m^2), a comparison was done for a sunlit indoor scene (filtered by a glass window, effective luminance on Spectralon=161 cd/m^2) and a sunlit outdoor scene (luminance on Spectralon=1554 cd/m^2), see Figure 30. An average ΔE*ab of 4,5 was obtained for the indoor sunlit scene on the 24 patches of MCC and Spectralon, and ΔE*ab of 4,7 was obtained on Spectralon for the sunlit outdoor scene. This ensured the efficiency of our calibration method on sunlit scenes. A comparison of the spectra produced by the spectroradiometer and the one obtained through our calibration method, for both the scenes, is shown in Figure 31. It is to be noted that outdoor scenes have rapidly changing luminance conditions (temporal variation of sunlight). Since the spectroradiometer measurement and the hyperspectral capture were not done exactly at the same time, a variation in the radiance magnitude was observed. A radiance correction factor of 1,12 (radiance/1,12) was applied to both the spectral radiance curves (Figure 31) to take in account the temporal variation of sunlight. Though no such correction was taken in account while calculating the colorimetric errors.

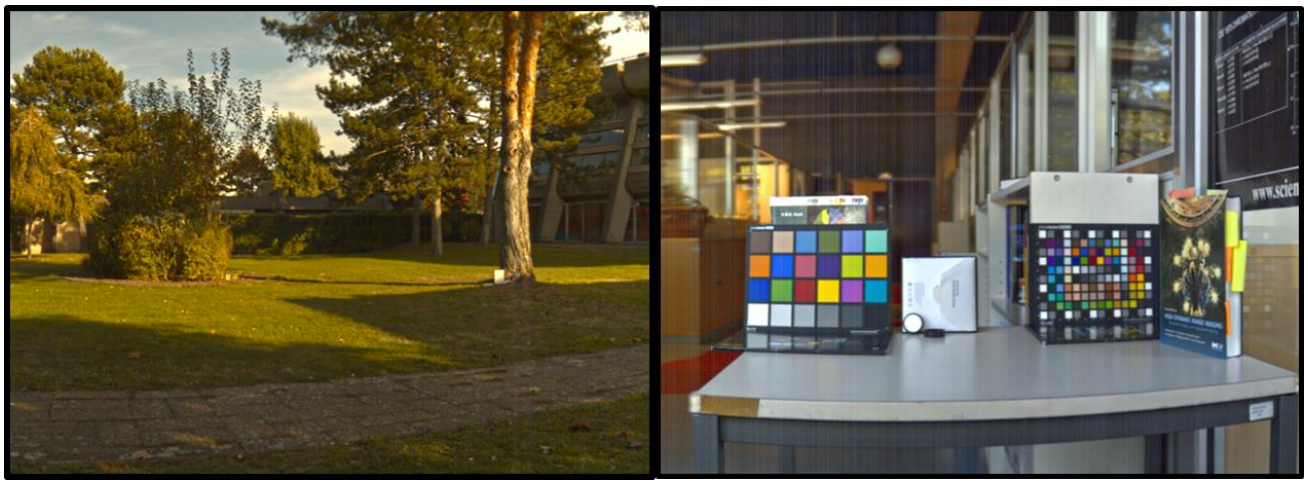

Figure 30, Sunlit outdoor scene (left) and sunlit indoor scene (right)

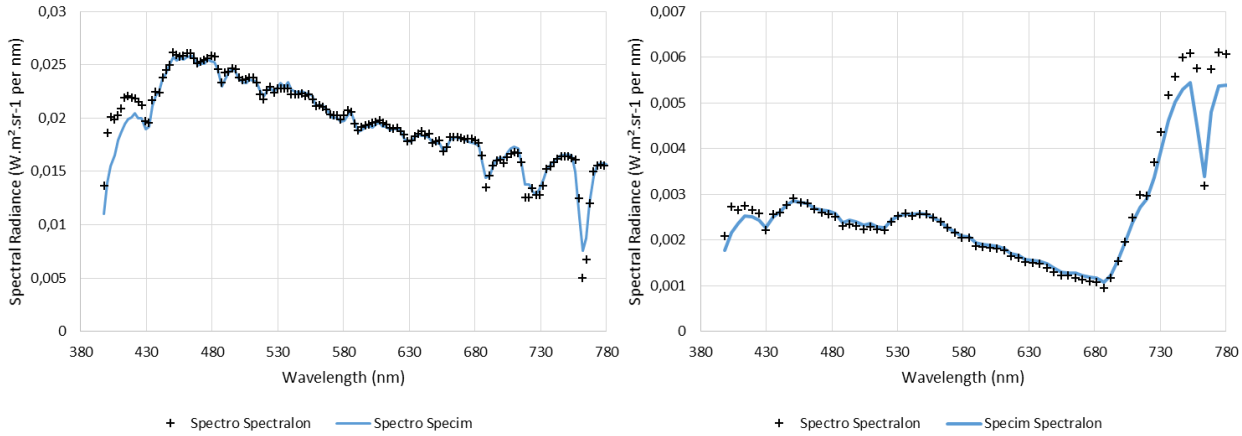

Figure 31, Radiance comparison (on Spectralon) spectroradiometer vs calibrated data: Sunlit outdoor scene (left) and Sunlit indoor scene (right)

The ΔE*ab on Spectralon for the outdoor scene came down to 1,7 (from 4,7) when the corrected radiances were used for calculating the colorimetric errors, thus emphasizing the impact of temporal sunlight variation on outdoor validation.

In view of the aforementioned analyses, it can be said that our calibration methodology is sufficiently credible and can be successfully used for calibrating push-broom hyperspectral cameras, for both, indoor and outdoor scenes. Moreover, the LED sources we used included the approximations of EES, D50 and D65, further ensuring the precision under various daylight spectrum.

3.3. Data acquisition: choice of data type

The calibration plugin of the manufacturer required a choice of data type for data storage to be made before the capture. By default, the data-type is *UINT16,* with the option of choosing Float data type as well. UINT16 was found to be a bad choice for outdoor captures as it cannot store data beyond ~5300 cd/m^2, which is inadequate for outdoor captures with luminance easily crossing 25000 cd/m^2. This was confirmed when outdoor captures done with the manufacturer's calibration and default UINT16 data type turned out to be saturated and clipped at 5326 cd/m^2. No such issue was found when the raw data calibrated with our method was saved in the *double* precision format, see Figure 32 and Figure 33.

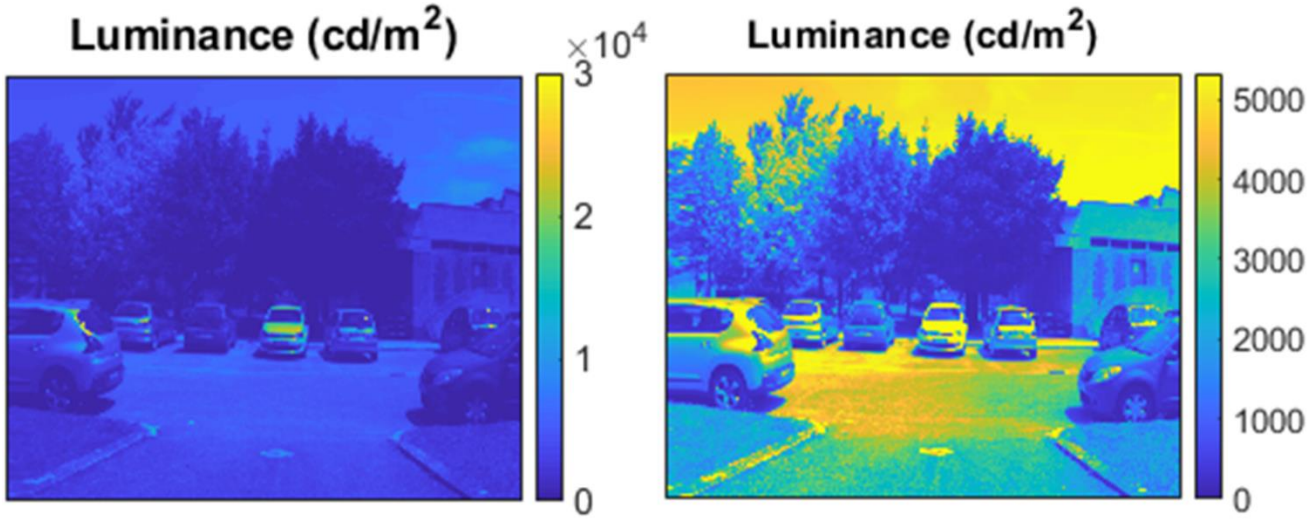

Figure 32, Luminance map comparison: double (left) vs UINT16 (right)

Figure 33, RGB images: Our method (double (left)) vs Manufacturer's method (UINT16 (right))

No such problems were found when the Float data type was used for outdoor captures. Instead, the issue now was that the Float data type tripled the data size as it contained the raw captures (.raw) plus the calibrated captures (.dat) that were twice the size of raw captures. With our calibration methodology only the raw data (.raw) is generated and required to calibrate and save the data in a Matlab readable format (.mat). Thus our methodology is less costly in terms of data storage. A comparison of our calibration and Float based manufacturer's calibration is shown in Figure 34 and the absence of any perceptible color difference between them is shown in Figure 35.

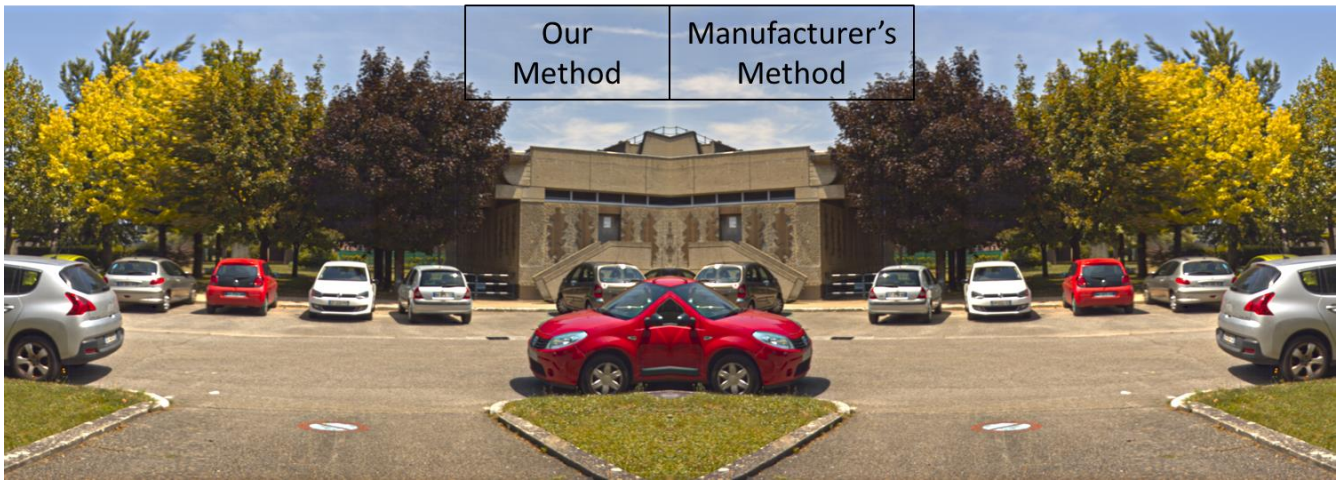

Figure 34, RGB images: Our method (double) vs Manufacturer's method (float)

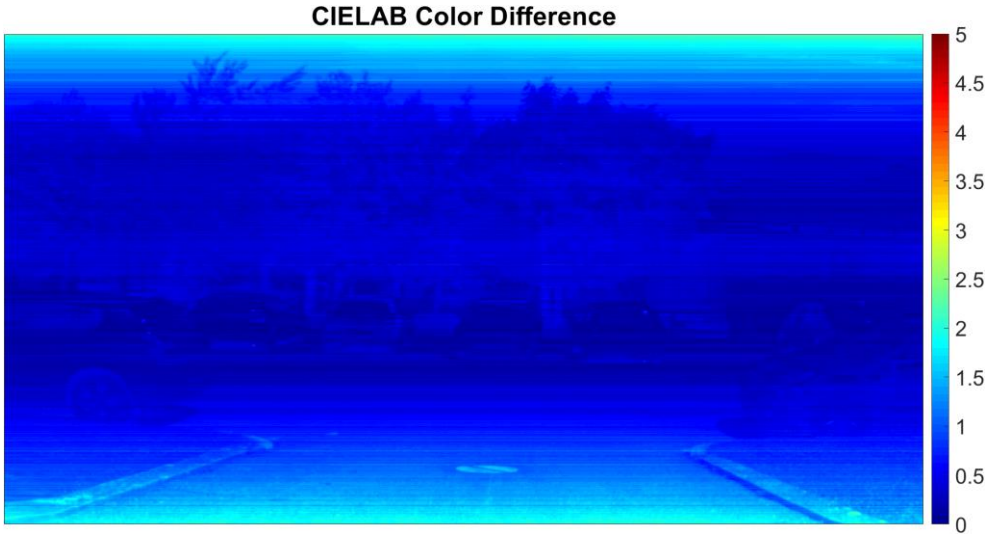

*Figure 35, ΔE*ab: Our method (double) vs Manufacturer's method (Float)*

In circumstances where the maximum luminance doesn't cross the threshold of UINT16 data capacity, the precision of the two data storage types is the same for colorimetric errors. A colorimetric precision study was done where the colorimetric data was obtained from two captures encoded differently (UINT16 & Float). This comparison was done for two light sources (Cold incandescent from Figure 22, and EES from Figure 23), and ΔE*ab was calculated for the 24 MCC patches. The obtained ΔE*ab was always less than 0,5 for Cold Incandescent (Figure 36: left) and 0,8 for EES (Figure 36: right), which is less than the perceptible threshold of color differences. Thus, for luminance levels below ~5300 cd/m^2, if the manufacturer calibration is to be used, the UINT16 data-type should be preferred to save storage space.

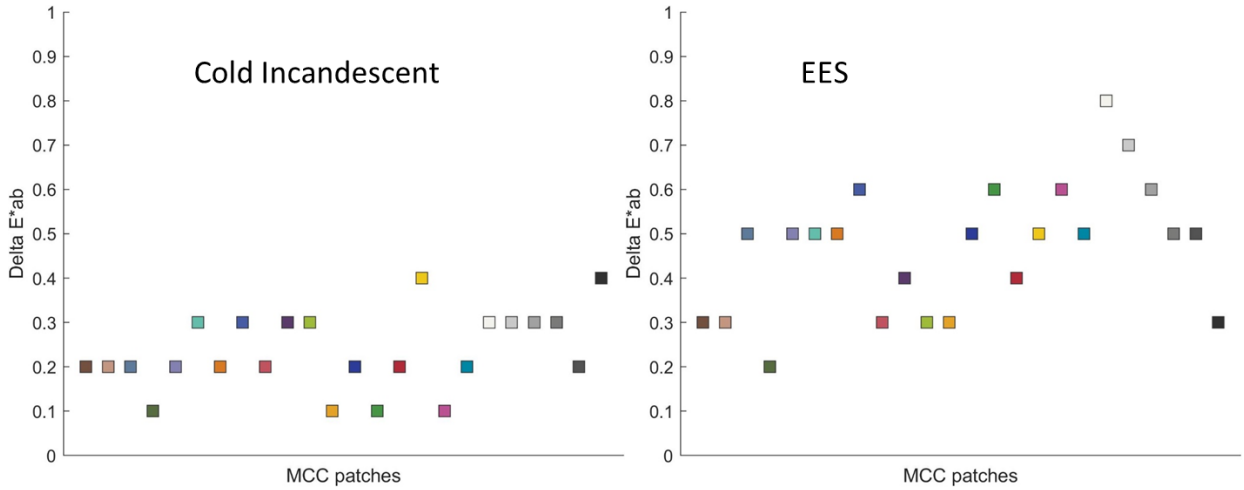

*Figure 36, ΔE*ab between data obtained from UINT16 and Float data storage type*

3.4. Appropriate exposure (ms) for different luminance levels

A spectroradiometer automatically adjusts the exposure for each spectral capture depending on the luminance conditions, unfortunately this is not the case with hyperspectral captures. With an HSI device there is a constant risk to over or under-expose the spectral sensors under extreme luminance conditions (too bright or too dark). The exposure needs to be adjusted for different luminance conditions and for a non-expert in photography this can be difficult.

To solve this problem, we designed a tool in MS Excel which predicted exposures that over/under expose the camera. To do this, we simulated raw spectral radiances of the camera for various exposures from the

spectral radiance of the test source (obtained via a spectroradiometer). To simulate the raw spectral radiances of the HSI device (Specim FX10), the radiance calibration curve (obtained at 40 ms of exposure) was multiplied with the spectroradiometer radiances. Thus we obtained values close to the raw radiances produced by the Specim FX10. To be able to simulate various exposures and not just 40 ms, we identified the relation between the raw radiance values obtained from the exposure used for calibration (40 ms) and various other exposures (starting from 1 ms). Then we identified the maximum and the minimum measurable raw radiances of the Specim FX10 by taking measures with increasing exposures (starting from 5 ms) and increasing luminance levels (starting from 0 cd/m^2).

To identify the raw radiance values of the Specim FX10 that over/under expose the camera optics, hyperspectral captures (with Specim FX10) were done under EES in the high radiance level configuration of the light booth (Figure 18b). The captures were done for luminance values of 0-546-1103-1656-2739-2791 $cd.m^{-2}$ (measured on Spectralon) with increasing exposures of 5-10-20-40-80 ms. For the measurements at 0 cd/m^2, the lens lid was kept on. These luminance levels were decided by keeping in mind the maximum possible luminance in the high radiance level configuration of the light booth using EES. We chose EES here because of its uniform distribution of spectral radiance and absence of peaks. With the help of these upper/lower limit of appropriate exposures, we were able to identify if the simulated raw radiance was within the measurable range of the HSI device or not.

To identify the relation between the raw radiance values obtained from 40 ms of exposure (used for calibration) and the raw radiance values obtained from other exposures, we did hyperspectral captures under a cold incandescent source (Figure 19). The luminance was fixed at 537 $cd.m^{-2}$, while exposures progressively increased (1-5-10-20-30-40-50-60-70-80 ms). A cold incandescent source was chosen here as it has a significant energy presence across the measuring spectrum of the device (400-1000 nm for us), unlike EES.

The mean raw radiance values for the Spectralon were extracted from all the above measurements for the measurable spectrum (400 nm-1000 nm). These measurements helped us in identifying:

a) The exposure which saturates the camera optics. Saturation is characterized by flat signals with raw radiances reaching the maximum storage value (3820 raw radiance units) for some wavelengths.

b) The exposure which under-exposes the camera optics. Under-exposure is characterized by unstable raw radiances with values comparable to noise (1,43 raw radiance units).

c) A linear relationship between the raw radiance values obtained at 40 ms and the raw radiance values obtained with other exposures (1-5-10-20-30-40-50-60-70-80 ms) for the incandescent source.

Using the linear relationship between the different exposures and the raw spectral radiance values (step (c)) and the radiance calibration coefficient established at the 40 ms exposure (see Section 3.2), we were able to model a raw hyperspectral radiance curve from a spectral curve measured with a spectroradiometer. The spectroradiometer radiance was simply multiplied by the radiance calibration curve. The magnitude of the radiance was amplified using the relationship between the various exposures identified in step (c) to simulate various exposures.

Using the upper and lower limits of the raw radiance values from steps (a) and (b), we were able to identify the possible exposures that could over/under expose the hyperspectral camera.

The EES source was chosen for the calculations (a)-(b) as the nearly flat structure of EES gave a clear and uniform upper/lower limit of exposures. Initially, measures were done with a fluorescent source, though the presence of sharp peaks in its spectral distribution curves, complicated this task. Incandescent sources do not have peaks either, but they have a relatively low distribution of energy in the short-medium

wavelengths of the spectrum, unlike EES, which has a more uniform energy distribution. Since the amount of energy didn't matter for identifying the relation between radiance values at different exposures, a cold Incandescent source was used for step (c).

As can be seen in Figure 37b, the saturation for the camera is clearly identifiable with a flat spectral radiance plot starting for 80 ms of exposure for the luminance level of 2791 cd.m^{-2}. This flat curve was also identified at the luminance level of 2739 cd/m^2 between 516 nm-566 nm. This saturating radiance value was identical for all over exposed captures and equal to 3820 raw radiance units. To be on the safe side, the upper limit was defined as 90% of the saturated raw radiance value, thus a capture leading to raw radiances higher than 3438 units was determined as over-exposed. From the spectral radiance plot of the dark capture Figure 37a, we identified the noise measured by the camera and set a value 10% higher than the highest noise value (1,43 raw units) as the lower limit (thus 1,58 raw units) for a properly exposed capture.

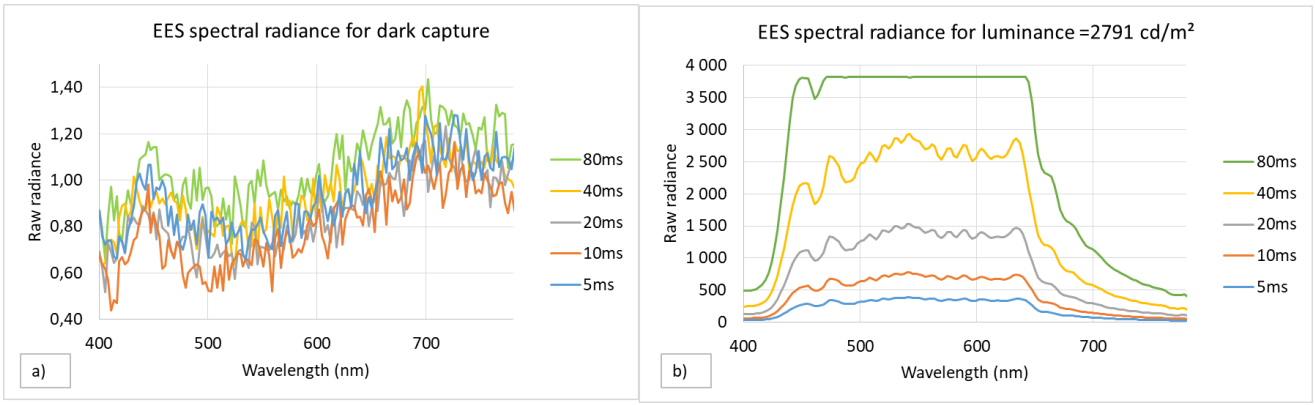

Figure 37, Dark (a) and saturated (b) raw radiances (Spectralon under EES at 2791 cd/m²)

From the hyperspectral captures under the incandescent source with a fixed luminance value of 537 cd.m^{-2} and increasing exposures (1 ms-80 ms), we identified a linear equation between the radiance values for different exposures while setting the radiance values from 40 ms of exposure as the base. The exposure of 40 ms was chosen as the base because our calibration curve was determined for 40 ms. These linear equations, the radiance calibration curve and the upper/lower limits of exposures enabled us to develop a utility tool in MS Excel to automatically identify correct exposures for the spectral radiances measured with a spectroradiometer.

With the help of the spectral radiance of the scene's illuminant (measured on white) as input, the tool simulates the raw spectral radiance of the HSI device. This is done by simply multiplying the spectral radiance of the illuminant with the spectral calibration curve of the HSI device. This will simulate the raw spectral radiance of the HSI device for the exposure of the calibration curve (40 ms). Furthermore, the tool also simulates the raw radiance for various other exposures as well (1-5-10-20-30-40-50-60-70-80 ms). If even a single raw radiance touches the upper/lower limit of raw radiance values (over/under exposure), the tool will identify that exposure as incorrect.

This tool was validated on HSI captures done under two LED sources and one Incandescent source with the help of NRMSD (Normalized Root Mean Square Deviation) scores, see Table 7. The superposed graphs of simulated vs measured HSI raw radiances are shown in Figure 38 for EES and a Cold Incandescent source for 10-20-40 ms of exposures. Once validated for indoor scenes, the tool can be assumed to have similar precisions for outdoor scenes.

Table 7, NRMSD errors between simulated and measured raw radiance values

Lamp Type	CCT (K)	Exposure (in ms)	NRMSD
LED	5108	40	1%
LED	5108	20	2%
LED	5108	10	2%
INC	5463	1	1%
INC	5463	5	1%
INC	5463	10	1%
INC	5463	20	1%
INC	5463	30	1%
INC	5463	40	1%
INC	5463	50	1%
INC	5463	60	1%
INC	5463	70	2%
INC	5463	80	4%
LED	5896	40	1%
LED	5896	20	2%
LED	5896	10	3%

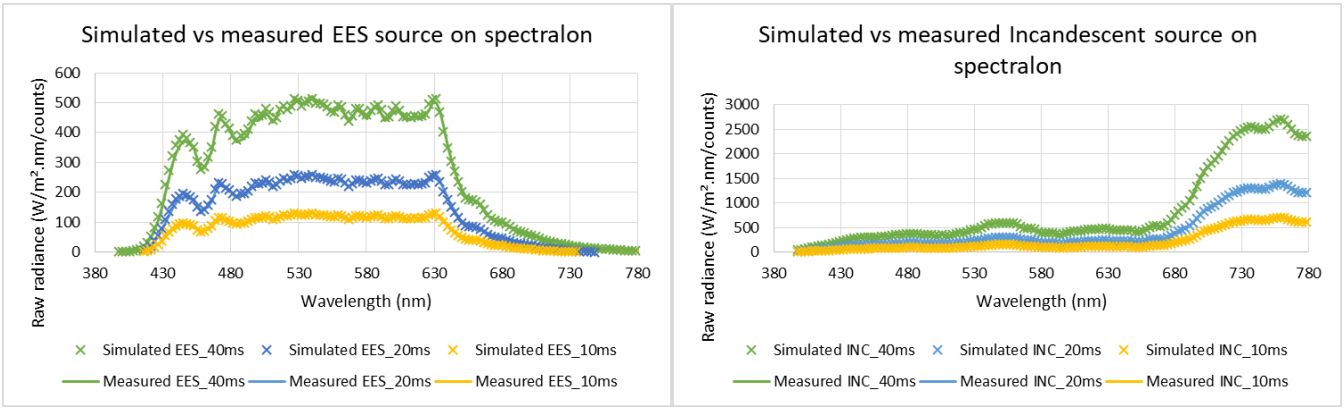

Figure 38, Validation of automatic exposure calculation tool: EES (left); Cold Incandescent (right)

3.5. Choice of Hyperspectral camera: Quantitative analysis

The data obtained from a Hyperspectral capture can be used to retrieve radiometric (radiance), photometric (XYZ tristimulus) and colorimetric (CIELAB) data in addition to the RGB image of the scene with a single capture. Naturally, the reproduction accuracy of such different datasets would be different as well. Furthermore, depending on the optical fixtures and sensors of the hyperspectral camera, this reproduction accuracy can vary from one device to another.

To investigate the opportunity to use HSI systems on indoor scenes (and by extrapolation on outdoor scenes) for lighting and color research, we compared spectral, photometric, colorimetric and image quality of two different commercially available HSI systems of the same manufacturer, under light sources with different SPDs and correlated color temperatures (CCTs). One of the two HSI systems was the Specim FX10 (S/N 1200061), used for creating the calibration protocol, while the other one was the Specim V10E (S/N 560009). The Specim FX10 is portable, relatively lightweight and less expensive (20K€) while the Specim V10E is bulky, heavy and very expensive (80K€). When comparing their technical specifications (provided in Table 8), we see a significant difference in the proposed spectral/spatial resolutions. With this study we

wanted to identify whether the portability advantages proposed by the Specim FX10 come at a significant cost of precision. The two hyperspectral cameras were calibrated using the same protocol described in section 3.2, the calibration curve for Specim V10E (with 15 ms of Exposure) is plotted in Figure 39. Initially, the Specim V10E's hyperspectral data was calibrated using the manufacturer's calibration methodology except that the spectral radiance was found to be shifted. This shift was calculated to be about 1,27 nm for LED sources for any color patch. This further amplified the already existing errors of the HSI device. With our calibration method, no such problem was found for any capture. For illustration, see the different spectral radiance plot comparisons for a warm LED based light source (CCT=2316 K) in Figure 40. The plot shows a comparison of the spectral radiances of the Red, Green and Blue MCC (Macbeth ColorChecker) patches, obtained with the spectroradiometer and the Specim V10E for both our calibration and the manufacturer's calibration.

Table 8, Characteristics of the compared Hyperspectral Imaging Systems

	Characteristics			Lens		Acquisition parameters				
HSI Systems	Aperture	Spectral resolution FWHM (nm)	Spatial resolution (pixels)	Manufacturer	Focal Length (mm)	Binning	Spectral resolution (nm)	Spatial resolution (pixels)	Exposure (ms)	Frame (sec^{-1})
Specim V10E	f/2,4	2,7	2184	Specim	18,5	2x2	1,3	1080*1437	50	15
Specim FX10	f/2,1	5,5	1024	Specim	15	2x1	2,7	1024*1232	50	15

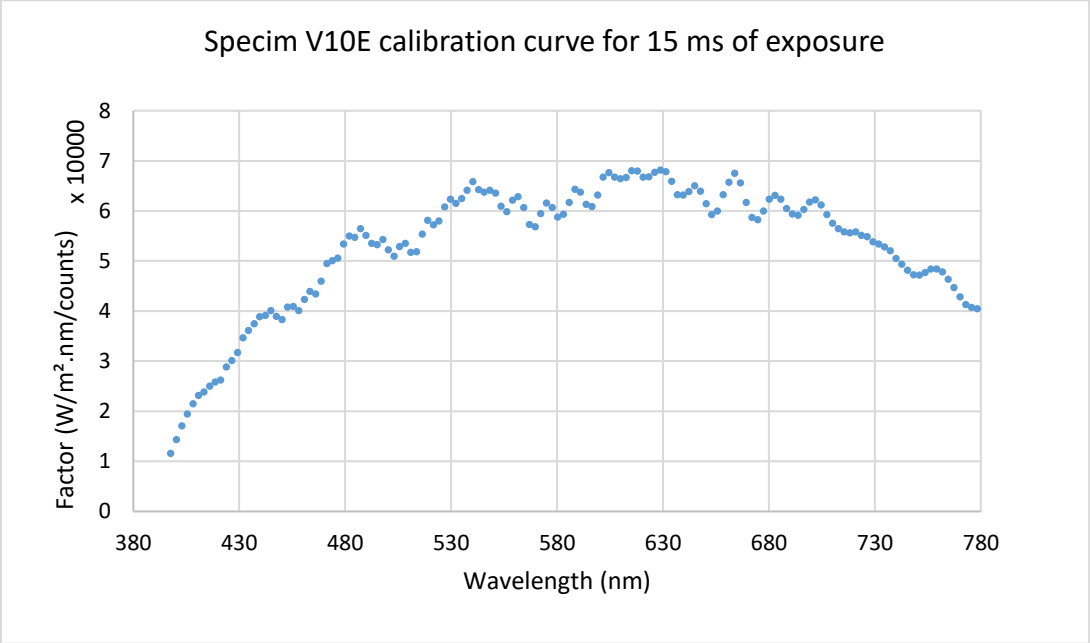

Figure 39, Radiance calibration curve obtained for the Specim V10E

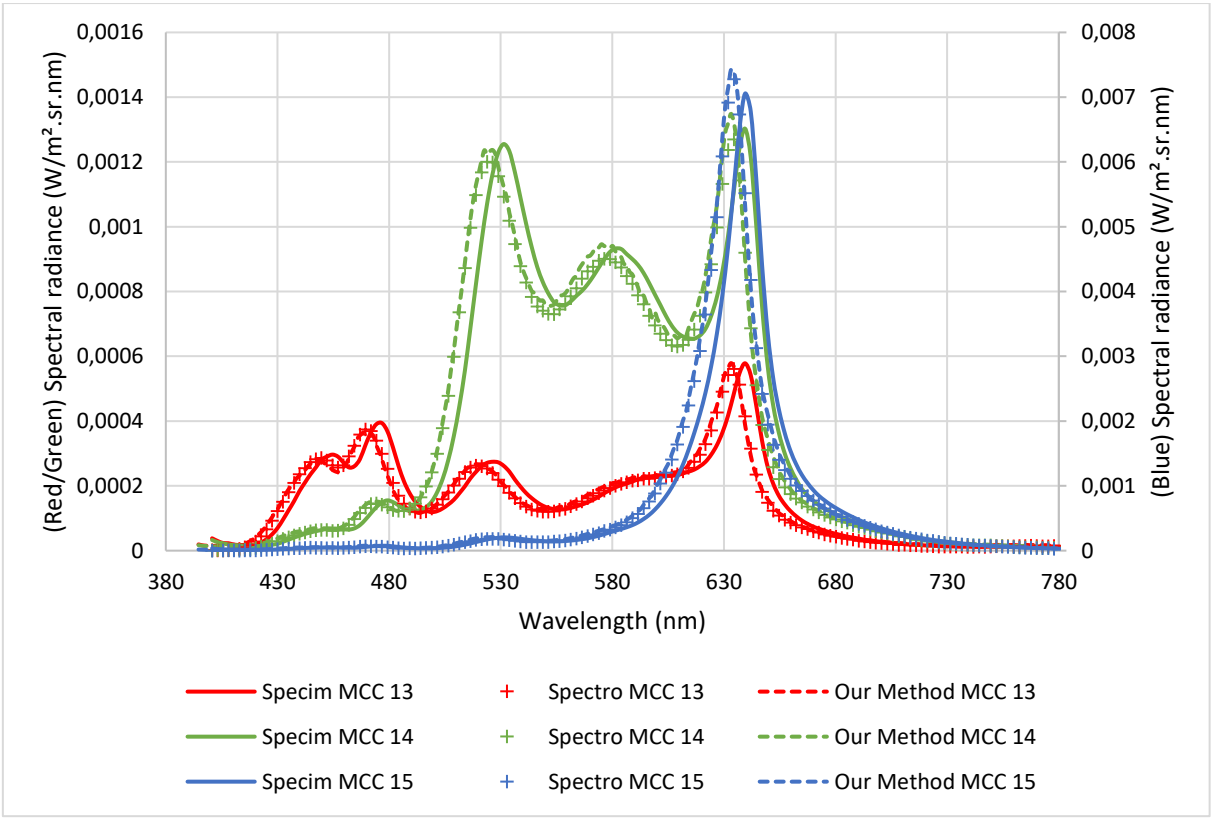

Figure 40, Comparison: Manufacturer's calibration vs our method-Specim V10E

Scene

To test image quality and sharpness, a light booth containing: a Macbeth ColorChecker Chart (MCC), 33 samples from the Munsell Book of Colors, a visual acuity chart (a chart with Landolt's rings and tumbling E's in the upper part, and a Rossano and Weiss-Inserm test) was used. The validation scene is presented in Figure 41.

Figure 41, HSI system quantitative comparison scene

Light Sources

Three spectrally tunable LED projectors (SourceFour LED, Lustr+, ETC Company) illuminated the light booth through a diffuser. Their seven LED channels were mixed to produce eight light sources: S1 to S7 - metameric to Planckian or Daylight illuminants (with 10° fundamental observer (CIE 170-2, 2015)) at different CCTs with the highest possible Color fidelity Index (Rf) (CIE 224, 2017), and S8 - a nearly flat spectrum (close to Equal Energy Spectrum). The sources were determined using the *fmincon* function in Matlab. The colorimetric and photometric properties of the light sources measured in the booth are given in Table 9. The chromaticity coordinates were measured on the Spectralon with the spectroradiometer, and the illuminance was measured with the chromameter positioned horizontally at the center of the booth. The spectral radiances of the light sources are shown in Figure 42.

Table 9. Characteristics of the light sources used in the experiment

Light sources	S1	S2	S3	S4	S5	S6	S7	S8
Illuminance (lux)	1796	1795	1797	1794	1795	1796	1765	2349
CCT (K)	2351	2574	2777	3084	4142	5217	6974	5400
Rf	89	93	94	95	96	95	89	84
x	0,4884	0,4605	0,4521	0,4292	0,3724	0,3380	0,3051	0,3231
y	0,4150	0,3996	0,4075	0,4006	0,3709	0,3519	0,3209	0,3509

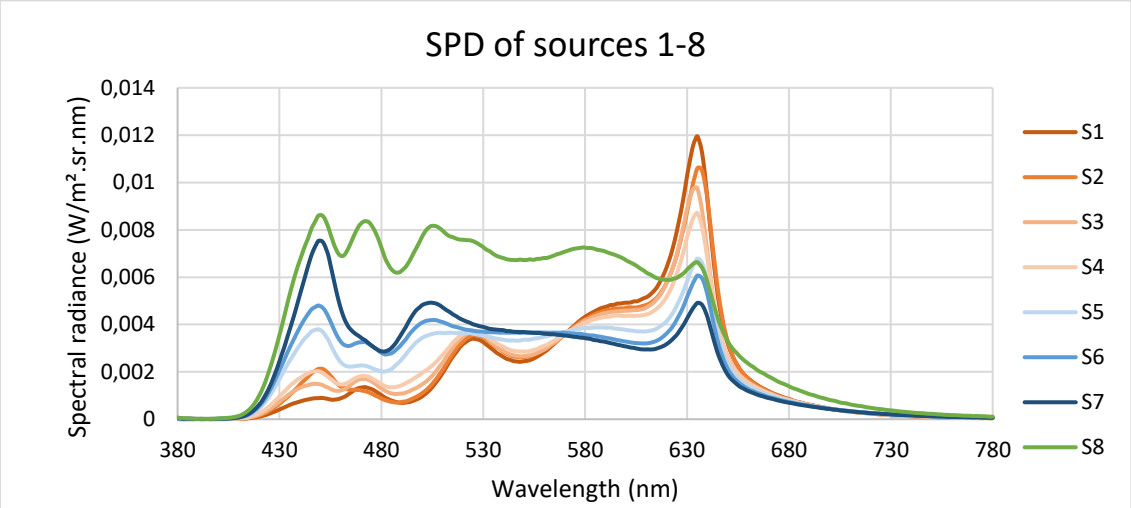

Figure 42, Spectral radiances of the comparison light sources

All measurements were acquired within a set of predefined protocol. To ensure maximum precision in reference measurements, spectroradiometer measurements were conducted twice, once before the hyperspectral capture and once after. Figure 43 illustrates the overall sequence for data acquisition. The light source heating of 2 minutes was done to ensure that the light sources had stabilized and emitted stable energy (verified with the help of the chromameter).

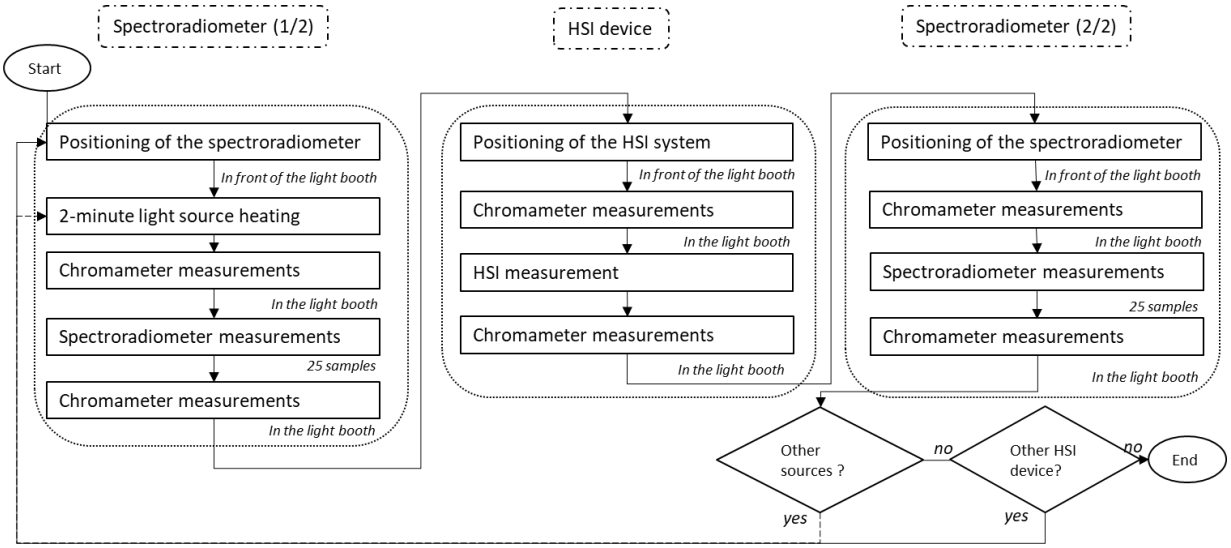

Figure 43, Complete HSI imaging sequence with reference measurements

3.5.1. Data processing

The data processing methodology and the contents of the extracted metadata remained similar to those described in 3.2.1. The metadata was extracted through the *textscan* command of Matlab and the raw radiance cube was converted with the *multibandread* command into a hyperspectral cube readable in Matlab (.mat). For the purpose of data analysis, the spectral data associated with the 24 colored patches of MCC and the Spectralon was extracted from the **calibrated** output files. Using the Matlab *circle ROI* function, the pixel location was retrieved from the preview sRGB image to correspond to the measurement zone of the spectroradiometer (ensuring maximum coverage of the patch surface without touching the border, ~1250 pixels). The spectral radiance values were then averaged to obtain a single radiance curve for each to prevent inhomogeneity linked errors. The spectral radiances were converted to tristimulus values (XYZ) with the CIE 2° standard observer CMFs interpolated to the measurement wavelengths of each HSI system. Furthermore, the CIE L*a*b* values were calculated using the diffuse white standard measured with the spectroradiometer as a reference (CIE 15, 2004).

Color images were reconstructed from the tristimulus values of each pixel using the iCAM06 image color appearance model (Kuang, Johnson, et al., 2007). The parameters were defined as per the default iCAM06 model (section 2.6) with gamma=1.5 (dark surround), p=0.75 (indoor scene) and F=1 (average adapting surround). The D value for chromatic adaptation was fixed at 0.9 for real-world perception (Smet et al., 2012). Figure 44 represents the rendered images under S8 where the close-up views illustrate sharpness.

Figure 44, Color images treated with iCAM06 of hyperspectral data obtained from Specim V10E (left) and Specim FX10 (right); (Kuang et al, 2007)

The sharpness of the images can be further quantified by the amplitude difference of the Y channel over the tumbling E's in the two images. The above images were converted to XYZ color space and the Y channel ($Y \in [0\text{-}1]$) data was extracted for both the images across the last two tumbling E, see Figure 45. A difference of more than twice can be observed between the amplitudes of the two curves indicating that the inherent optical sharpness of Specim FX10 is inferior to that of Specim V10E.

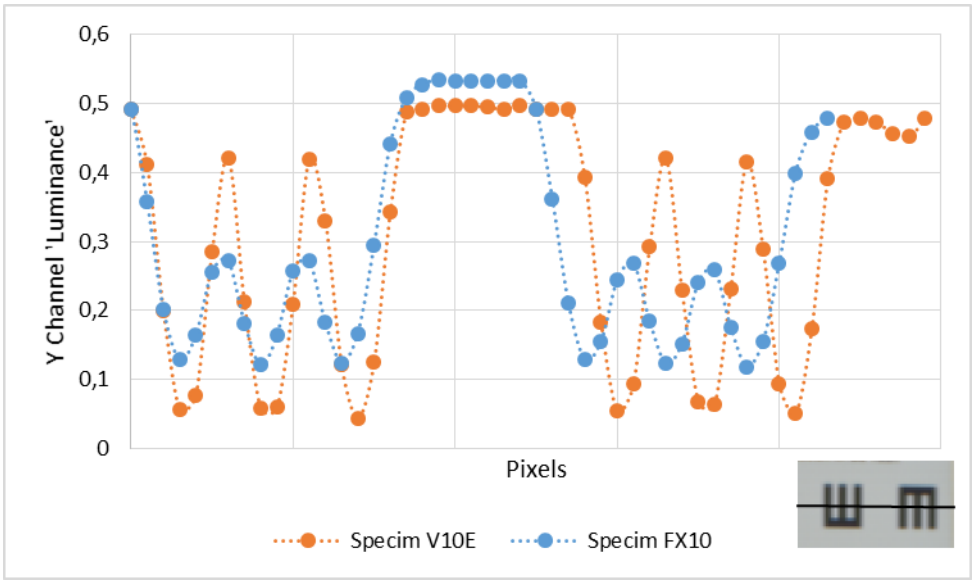

Figure 45, Spatial frequency curve of the luminance channel: Specim FX10 vs Specim V10E

3.5.2. Spectral Accuracy

The differences of spectral radiances between the HSI systems and the spectroradiometer were evaluated with the Normalized Root Mean Square Deviation (NRMSD), see equation below:

$$NRMSD\ (\%) = \frac{\sqrt{\frac{1}{N}\sum_{\lambda i}^{N}\left(s_{\lambda i,t} - s_{\lambda i,r}\right)^2}}{max(s_{\lambda i,t}\,;\, s_{\lambda i,r})} \times 100 \ldots (28)$$

Where, $s_{\lambda i,t}$ and $s_{\lambda i,r}$ are the spectral radiances measured with the tested HSI system and with the spectroradiometer (reference) respectively, and N is the number of spectral samples as per the chosen spectral resolution (base spectral resolutions: $N_{Specim\_V10E} = 307$ and $N_{Specim\_FX10} = 144$).

Figure 46 illustrates the distribution of errors in spectral radiance by representing the NRMSD (%) for both HSI systems calculated between the hyperspectral data and the reference spectroradiometer for the eight light sources and the 24 MCC patches (the face colors correspond to the RGB colors of the MCC patches).

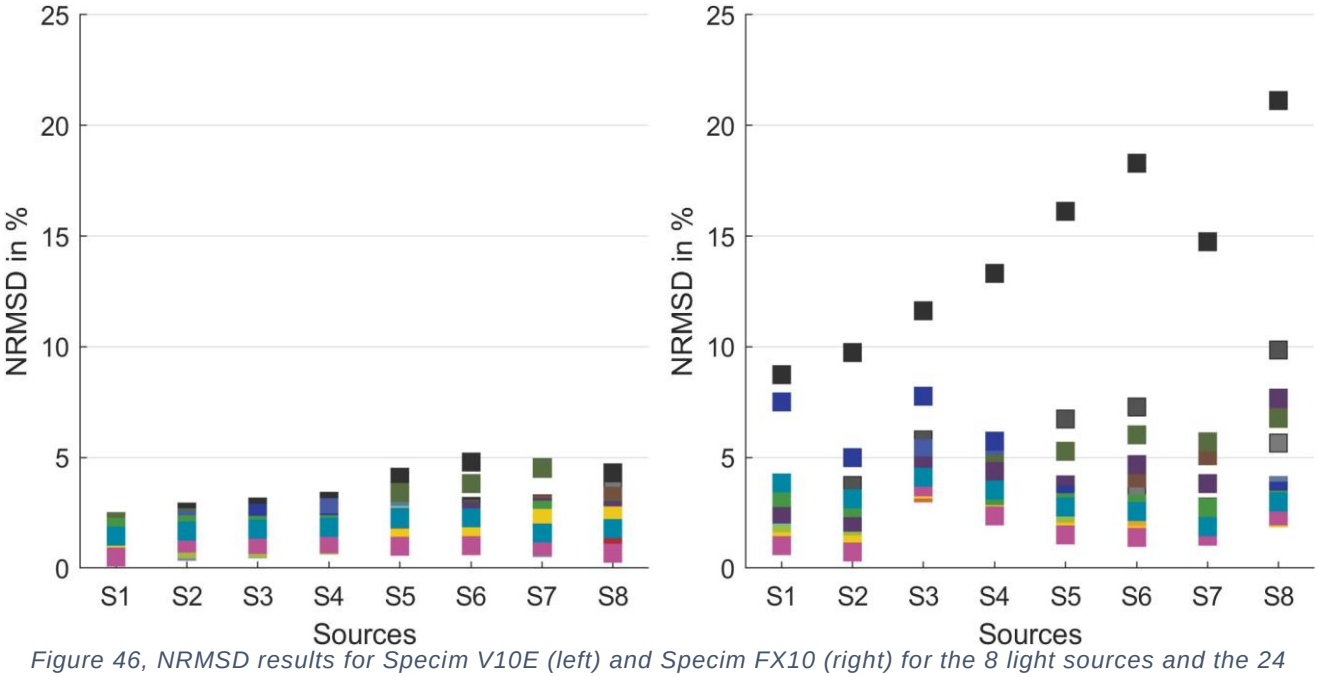

Figure 46, NRMSD results for Specim V10E (left) and Specim FX10 (right) for the 8 light sources and the 24 MCC color patches

For all sources and MCC patches, the maximum NRMSD is 5% for the Specim V10E and 23% for the Specim FX10. For each source, the maximum is always obtained for the dark MCCs. This is particularly obvious for MCC 24 (black) for the Specim FX10. The Specim V10E clearly provides the most accurate spectral radiances.

3.5.3. Photometric Accuracy

Photometric accuracy was quantified by the Mean Absolute Percentage Error (MAPE (Inanici & Galvin, 2004)) between luminance (Y) values captured with the HSI systems and luminance values measured with the spectroradiometer, as formulated below:

$$MAPE = \frac{100}{n}\sum_{i=1}^{n}\left|\frac{Y_{i,t}-Y_{i,r}}{Y_{i,r}}\right| (\%) \ldots(29)$$

Where $Y_{i,t}$ and $Y_{i,r}$ are the luminance values of the ith color sample measured with the tested HSI system and with the reference (spectroradiometer) respectively, and n is the number of patches (n=24).

Figure 47 illustrates the distribution of photometric errors by representing the MAPE (%) for both HSI systems calculated between the hyperspectral data and the reference spectroradiometer for the eight light sources and the 24 MCC patches. The upper limit of 20% MAPE was identified as per the luminance errors found in literature that lie between 2,8%-20% (Cai & Chung, 2011; Inanici & Galvin, 2004).

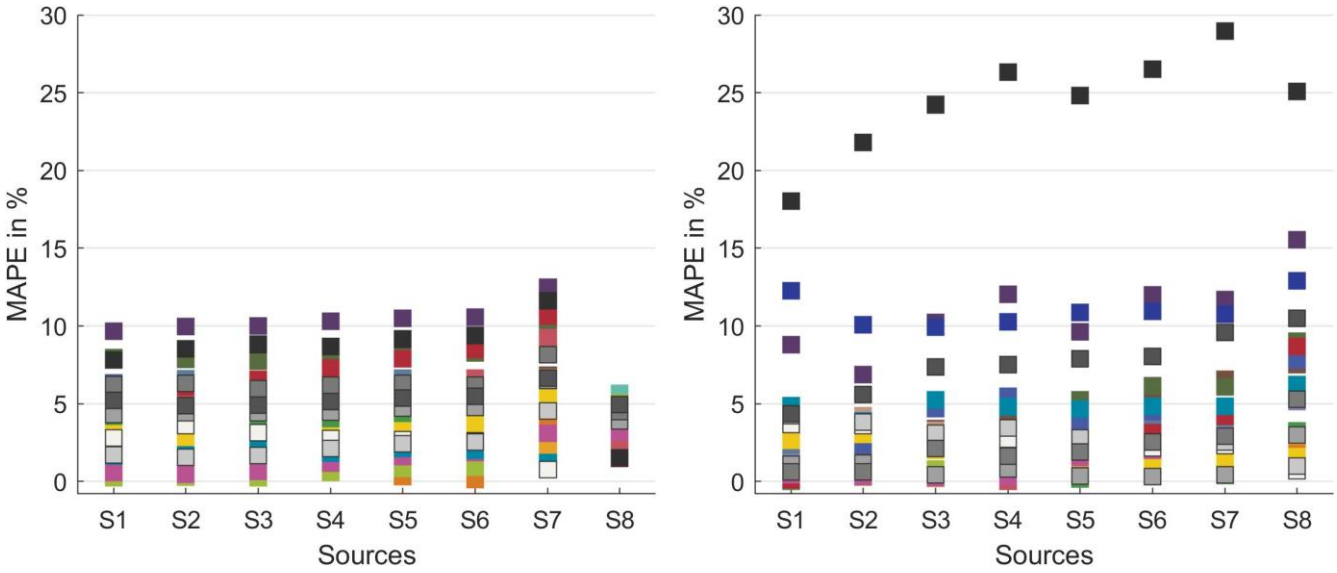

Figure 47, MAPE results for Specim V10E (left) and Specim FX10 (right) for the 8 light sources and the 24 MCC color patches

The Specim FX10 reproduces the luminance values for colored patches with sufficient precision but not so much for the Black MCC24 patches. Overall, the Specim V10E clearly produces lower photometric errors for any color patch or light source.

3.5.4. Colorimetric accuracy

Colorimetric accuracy was evaluated with the CIELAB color difference formula (ΔE*ab) with the Spectralon chosen as the reference white (measured with the spectroradiometer). The formula is described below:

$$\Delta E a^* b^* = \sqrt{(L_{i,t} - L_{i,r})^2 + (a_{i,t} - a_{i,r})^2 + (b_{i,t} - b_{i,r})^2} \ldots (30)$$

Where $[Lab]_{i,t}$ and $[Lab]_{i,r}$ are the CIELAB values of the ith color patch measured with the tested HSI system and with the reference (spectroradiometer) respectively. Figure 48 illustrates the distribution of color differences by representing the CIELAB color difference (ΔE*ab) for both HSI systems calculated between the hyperspectral data and the reference spectroradiometer for the eight light sources and the 24 MCC patches. The upper limit of ΔE*ab=6 was identified as per the perceptible limit of color difference for complex images (Hordley et al., 2004; Meyer, 1988).

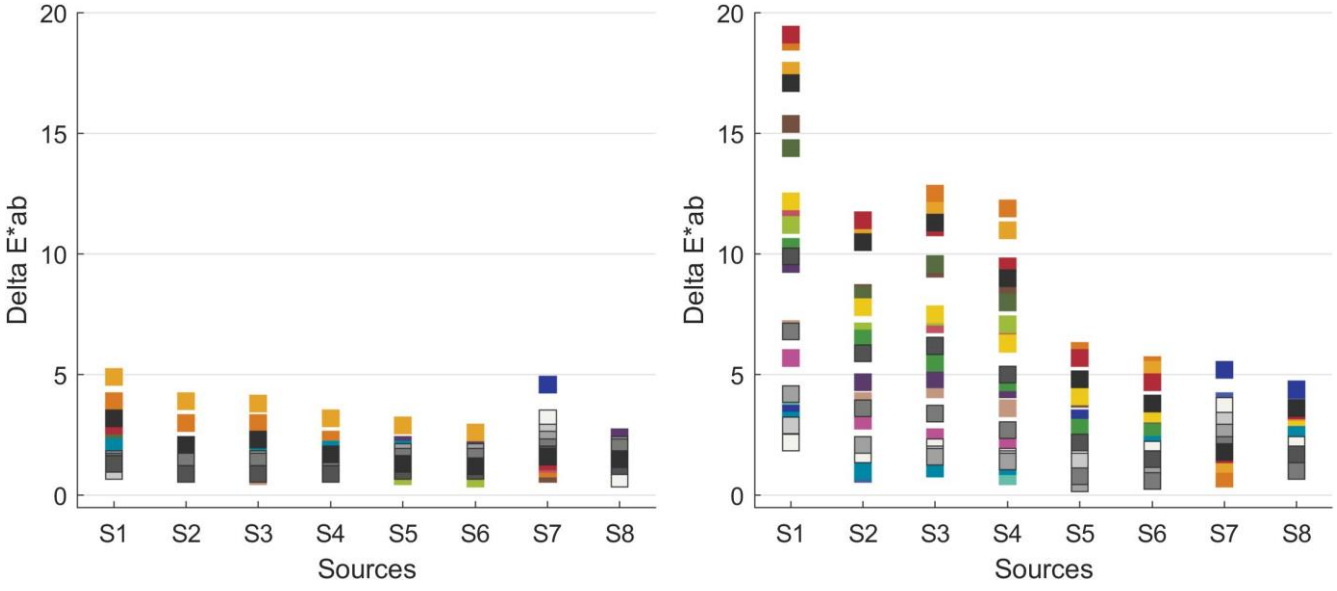

*Figure 48, ΔE*ab results for Specim V10E (left) and Specim FX10 (right) for the 8 light sources and the 24 MCC color patches*

The Specim V10E has the smallest range of colorimetric errors that stay below 6 units of ΔE*ab under all sources. The Specim FX10 has errors below 6 units of ΔE*ab only under cold light sources (S5 to S8). Under warmer sources errors go up to 12 units (S2 to S4) reaching even 19 units under S1. This behavior is similar to that in section 3.2.3. Warm light sources have a poor colorimetric reproduction accuracy due to unequal distribution of radiant energy, and which is amplified due to the hardware configuration of Specim FX10.

3.5.5. Image quality

Image quality depends on various preconceived notions of imaging that depend on the final objective. These notions include sharpness, vividness, image spatial resolution, naturalness etc. With the help of Image Quality Metrics (IQMs), one can quantify these subjective notions. For our application, we need metrics that do not necessarily use distortion-specific criterions but instead exploit the statistics of an image. Most of the IQMs are calculated with the purpose to test various compression algorithms and use a reference image that identifies the target image quality. We do not have any such reference image and thus a no-reference IQM is required for this comparison. We chose no-reference metrics that normalize the luminance coefficients locally to quantify a difference in Image Quality.

Two Image Quality Metrics (IQMs), without any reference requirements, were selected to objectively compute the quality of the final RGB image produced by each imaging instrument. The first is the Blind/Referenceless Image Spatial Quality Evaluator (BRISQUE) which relies on a previously trained SVM (Support Vector Machine) model of the LIVE IQA Image dataset (Ghadiyaram & Bovik, 2016). BRISQUE scores are opinion-aware, i.e. subjective image quality scores are taken into account while training the model. The smaller the score of the BRISQUE, the higher is the image quality (Mittal et al., 2011). The second is the Naturalness Image Quality Evaluator (NIQE) which has scores between 0-10 and works similarly to BRISQUE but estimates the naturalness of the image. NIQE was developed by training a Multivariate Gaussian model on 125 images retrieved from the Berkeley Image Segmentation database (Martin et al., 2001). *It makes use of measurable deviations from statistical regularities observed in "natural" images* (Mittal et al., 2013). In this context, natural images mean images that underwent no image enhancement. NIQE scores are opinion-unaware, i.e. no subjective image quality scores are taken into account. A smaller score is considered perceptually more natural (Mittal et al., 2013). They both are available in Matlab for direct application on images.

Figure 49 represents the BRISQUE and NIQE scores for the two HSI systems calculated for the iCAM06 processed images, for the 8 light sources. These scores depend not only on the HSI system but also on the precision of iCAM06, but since the data from both the HSI devices was treated similarly, the impact of iCAM06 can be excluded in a relative comparison.

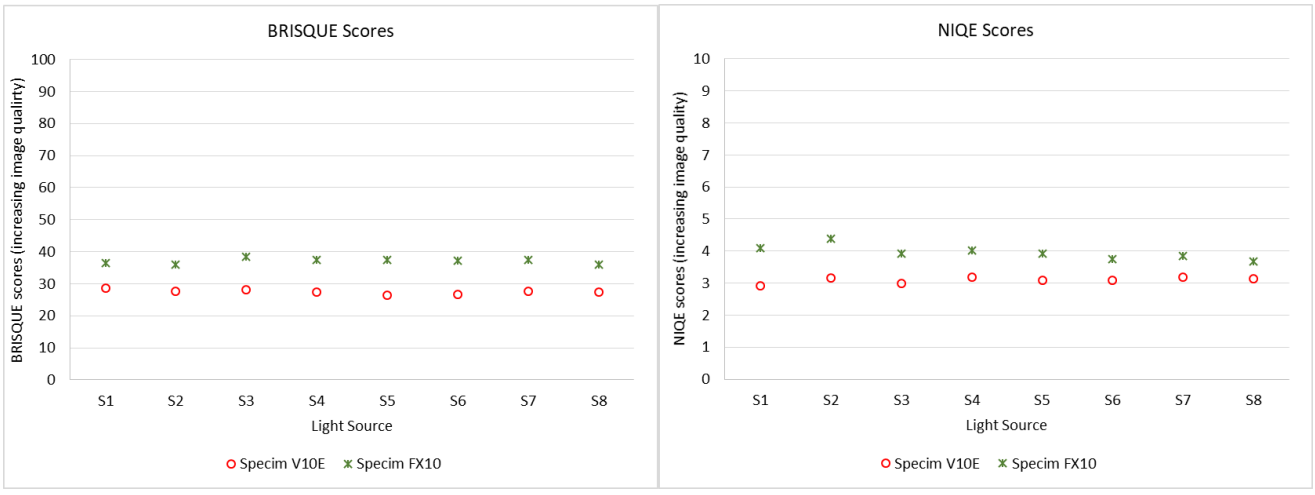

Figure 49, BRISQUE and NIQE Image Quality Metrics for the 2 HSI devices under the 8 sources

The maximum BRISQUE score is under 40 and the NIQE score under 5,2 for any HSI system and Sources. There is no existing use of BRISQUE or NIQE scores for hyperspectral imaging in the literature in the knowledge of the authors. Thus, to quantify the difference in these scores, statistical tests were conducted on the BRISQUE and NIQE scores.

A principal effect ANOVA found significant differences in the BRISQUE and NIQUE scores of the two cameras (BRISQUE, $F(1,7)=555,9$, $p=0,00$* and NIQE, $F(1,7)=98,4$, $p=0,00$*). A Tukey's HSD post hoc test revealed significantly lower (thus better) BRISQUE and NIQE scores for Specim V10E (mean BRISQUE=27,4, mean NIQE=3,1) relative to Specim FX10 (mean BRISQUE=37; mean NIQE=3,9). No effect of the light source was found for either camera. To give an idea of the impact of these scores, cropped images with the best and the worst NIQE scores are shown in Figure 50.

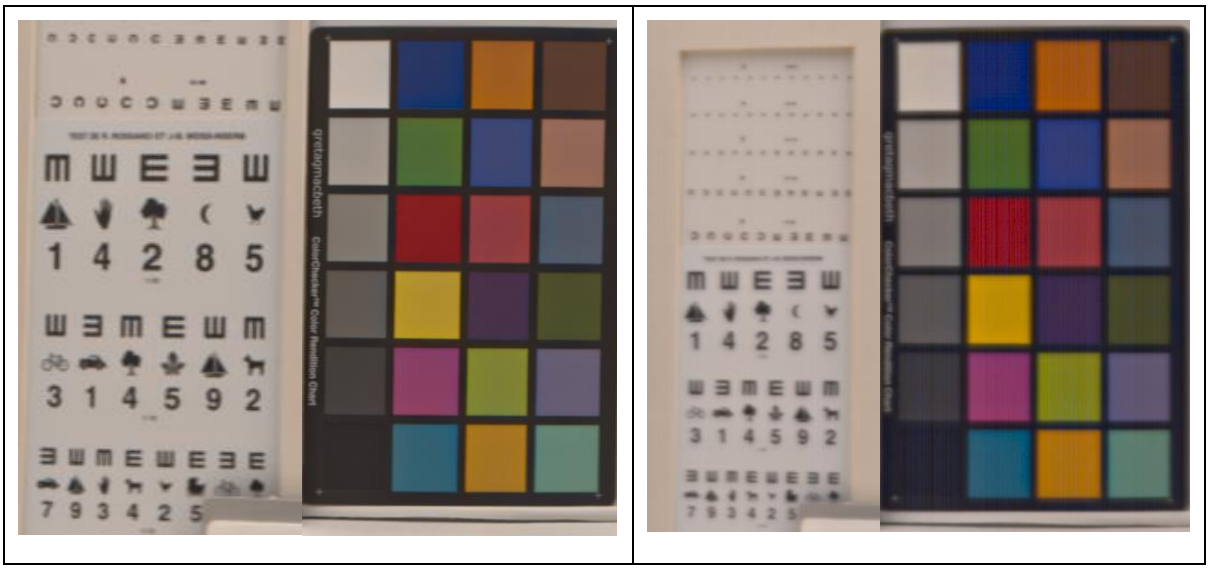

Figure 50, Cropped Images for the best NIQE score (Specim V10E under S1 = 2,9; left) and worst NIQE score (Specim FX10 under S2=3,16; right)

3.5.6. Conclusion

The Specim V10E can be said to be the system with the highest precision which is acceptable for any usage, be it spectral (mean NRMSD 1.8%), photometric (mean MAPE 4.3%), colorimetric (mean ΔE*ab 1.7) or for psychophysical experiments via RGB images treated through iCAM06 (mean BRISQUE 27, mean NIQE 3). The Specim FX10 is a good candidate for spectral (mean NRMSD 3.3%) and photometric (mean MAPE 4.5%) usage but for colorimetric reproduction it should be avoided for warm light sources (CCT $\leq$ 3000K) since individual ΔE*ab exceeds 6 units (which is the limit of unnoticeable color differences for complex images). One can also notice that the Specim FX10 does a poor spectral and photometric reproduction of black and dark colored patches. This indicates the presence of unwanted noise in the hyperspectral radiances. It could be due to a poor or outdated dark subtraction technique used in Specim FX10 combined with a poor SNR of Specim FX10. Dark subtraction for every image (for either of the cameras) was accomplished via a tool provided by Specim. Perhaps the algorithm behind this tool needs to be adjusted for the changes in the sensor sensitivity over time. In terms of RGB image quality, Specim V10E has significantly superior image quality indices in comparison to Specim FX10 as per the statistical tests done on the NIQE and BRISQUE scores.

The significantly different results for the different metrics tested in this section, for the two cameras, highlight the importance of quantifying each set of data, either produced or derived. The use of hyperspectral data is primarily to produce spectral images, thus mostly only the spectral data is quantified for accuracy. However, if one wishes to derive other forms of data from apparently precise hyperspectral data, it is imperative to quantify the respective derived data with pertinent metrics.

In view of the above metrics, it was decided to use the Specim V10E for testing the color appearance models. Nevertheless, the Specim FX10 can still be successfully used for indoor scenes (without fine details) under cold light sources with minimum illuminance around 1800 lux. The Specim FX10 is less heavy and easy to transport thus facilitating outdoor captures when compared to Specim V10E. By extrapolation it can be assumed that for outdoor scenes, the image metrics should improve with increasing radiant energy.

4. iCAM06 for vision through colored sunglasses

Once we have understood the technicalities of color vision and elaborated the imaging techniques to acquire spectral images, we need to combine them to create color corrected 2D images from spectral images. This section will describe the complete framework of stimuli creation for colored sunglasses simulation by using hyperspectral imaging technology and an image CAM.

The choice of the CAM in this section will be iCAM06 with default parameters and settings as described in chapter 2.6. Two different HSI devices will be used for this chapter as the section 4.1 requires the use of a HSI device with the best colorimetric precision (Specim V10E) and the section 4.2 demands moving the hyperspectral camera outside the laboratory (thus calling for the use of the portable Specim FX10).

4.1. Choice of spectral binning

Hyperspectral images are quite heavy in terms of size. A typical hyperspectral image of an outdoor scene (spatial resolution: 2327x1080, Figure 51), with spectral radiances measured every 1,3 nm between 400-780 nm takes up about 3 Gb. This creates issues not only for storing the hyperspectral image but also for processing it (time taken for the application of CAM, etc.). It is possible to reduce the size of a hyperspectral image by compromising on certain parameters, though the question is: will this impact the colorimetric accuracy of the hyperspectral data? For example, the base spectral resolution of Specim V10E is 1,3 nm. By taking spectral radiance measurements every 5,4 nm instead of 1.3 nm, the size of the hypercube can be reduced by 4 times (763 Mb) while staying within the optimal spectral resolution recommended by CIE of ~5 nm (CIE 15, 2004). This quantization of data is known as binning, and is known to improve up to 40% of the Peak Signal-to-Noise Ratio (PSNR) of the system, compared to non-binned data (Marmion, 2016). For Specim V10E, binning is a pre-acquisition parameter, and its proprietary acquisition system proposes binning of 1 (spectral resolution~0,7 nm), 2 (spectral resolution~1,3 nm), 4 (spectral resolution~2,7 nm) and 8 (spectral resolution~5,4 nm). Binning can be performed by averaging or interpolating the data to have a larger/smaller spectral sampling resolution, though the method used by Specim V10E seems to be interpolation. On a separate note, the spectral resolution of Specim V10 (and also of Specim FX10) is not fixed for every measured waveband (~~every 1,3 nm~~), but varies within a range of 0-0,8 nm for the chosen spectral resolution. For example, measurements at the base spectral resolution resemble: 1,22 nm- 1,23 nm- 1,24 nm…..1,3 nm).

Figure 51, Unfiltered Adobe RGB image of a typical hyperspectral capture (Specim V10E)

To ensure that no loss in colorimetric accuracy occurs when increasing the spectral resolution from ~1,3 nm to ~5,4 nm via binning, a study was undertaken. Colorimetric differences were calculated for the CIELAB values obtained through the spectral data of 24 MCC patches taken from a hyperspectral capture using Specim V10E under the EES light source (see Figure 23) in the light booth (see Table 18a). The color differences (ΔE*ab) were calculated between the radiances obtained from the spectroradiometer

(reference) and the radiances obtained from the hyperspectral cube with different spectral resolutions. The methodology of data extraction and processing remains the same as explained in chapter 3.2. The hyperspectral data was obtained directly for the selected binning options (binning 2~=1,3 nm, binning 4~=2,7 nm and binning 8~=5,4 nm).

A one-way ANOVA on the resulting colorimetric differences visualized in Figure 52 shows that increasing the spectral resolution from every 1,3 nm to every 5,4 nm did not significantly impact the colorimetric accuracy of the hyperspectral captures ($F(2,69)=0,0114$; $p=0,98$).

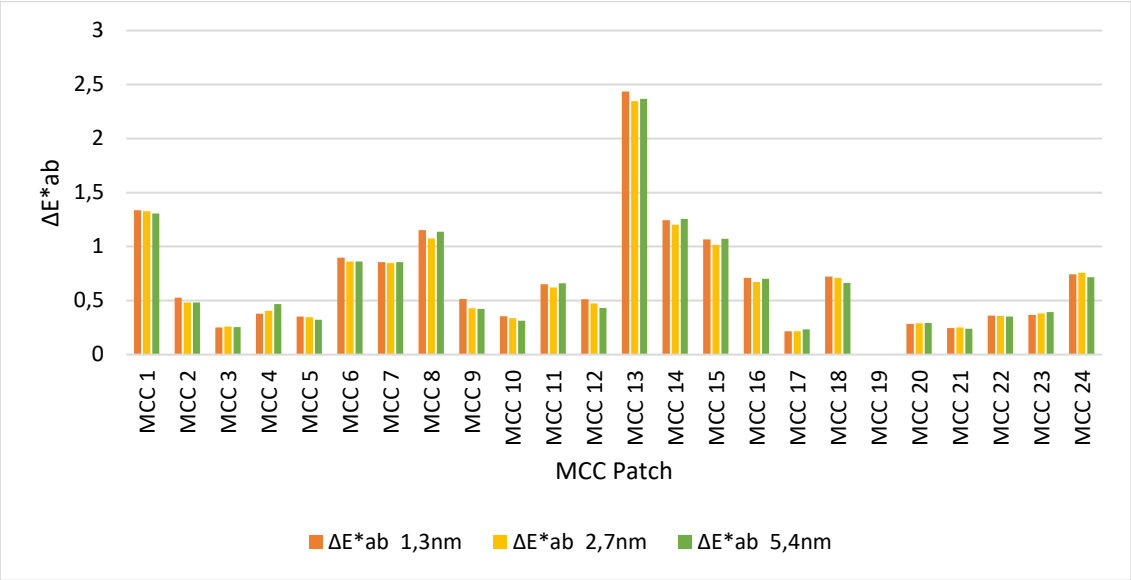

*Figure 52, ΔE*ab values for hypercube creation: spectral resolution comparison*

To ensure that we had all the data that could be measured, the hyperspectral captures were taken at the base spectral resolution (1,3 nm). But in the scope of this PhD, the hypercube spectral resolution was fixed at 5,4 nm as per the CIE guidelines and our own accuracy study. Since the original hypercube had a smaller spectral resolution (1,3 nm) than the desired resolution (5,4 nm), the image treatment algorithm skipped the intermediary radiance values from the hypercube. It was found that skipping intermediary radiance values significantly speeded up the process when compared to interpolating them, without any change in the accuracy (measured $\Delta E^*ab = 0,04$ for both interpolated data and skipped data).

4.2. Choice of spectral range

Apart from the spectral resolution, the spectral range of the capture can also impact the size of the hypercube. Both Specim V10E and Specim FX10 are capable of measuring radiance data in the spectral range of [400-1000] nm. Since the final goal is to produce images from the hyperspectral data, all the data outside the visible range of spectrum can be safely ignored. The CIE CMFs are available for the spectral range of [360-830] nm (from 380 nm for 10° fundamental CMFs). Though it is a common practice to use values between 380-780 nm since the sensitivity of the human eye (and the CIE CMFs) is negligible outside this range, see Figure 53.

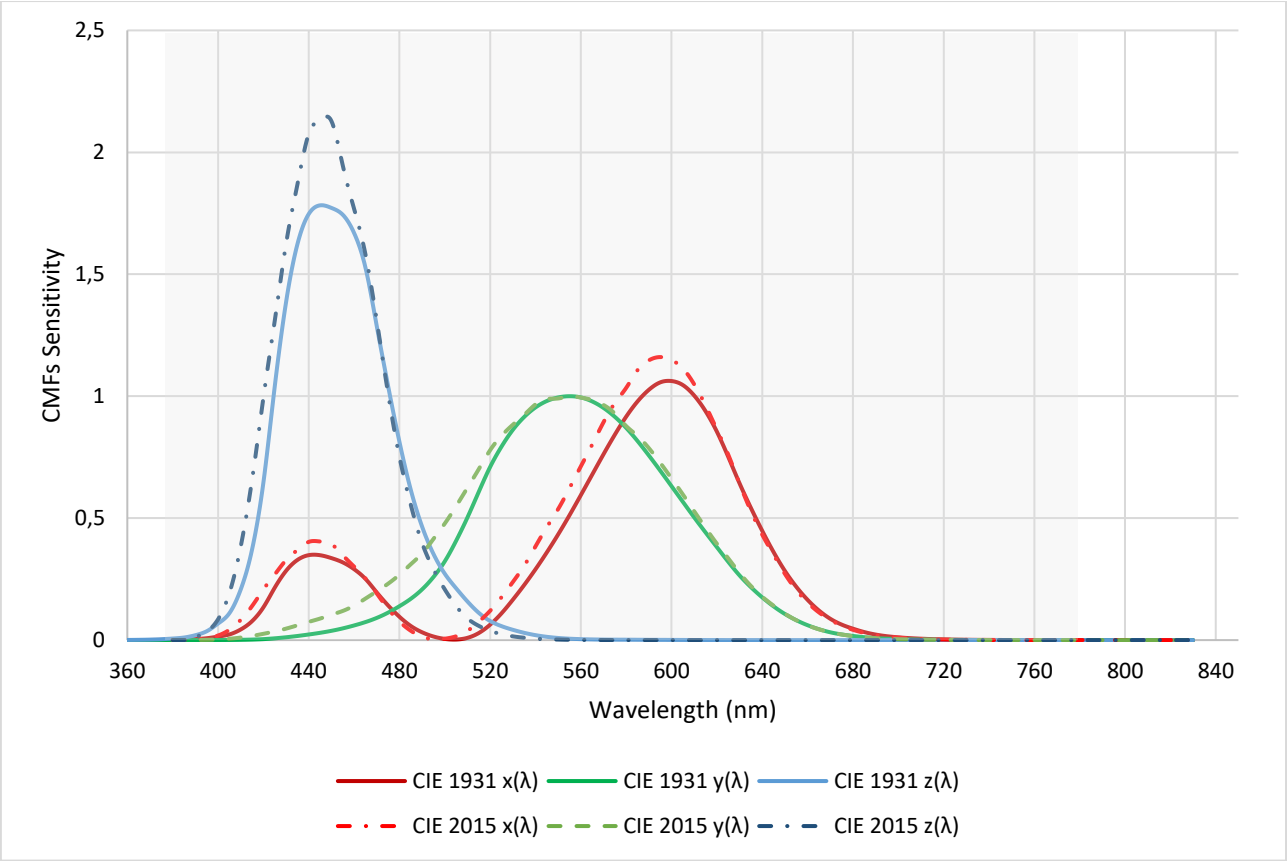

Figure 53, CIE CMFs: 1931 (solid lines) and 2015 (dashed lines)

Before deciding to use a smaller spectral range than the CIE CMFs (for e.g. [400-780] nm], it had to be verified that a smaller spectral range would not reduce the hypercube's accuracy. For this purpose, radiances of different spectral ranges were compared. The spectral ranges tested were: [400-830] nm (upper limit of CIE CMFs), [400-780] nm (upper-limit of effective visible spectrum), [400-720] nm and [400-650] nm (both are the upper-limit of existing hyperspectral databases in the literature). A sunlit indoor space (Figure 54) was captured (with Specim FX10) and reference measurements were done with the Spectroradiometer for MCC (1-24) and Spectralon. The spectral data captured (by the HSI device) for each MCC patch and the Spectralon was extracted, and CIELAB values were calculated for the radiance values for each of the tested spectral ranges. Color differences obtained from the reference spectroradiometer measurement for each spectral range are shown in Figure 55.

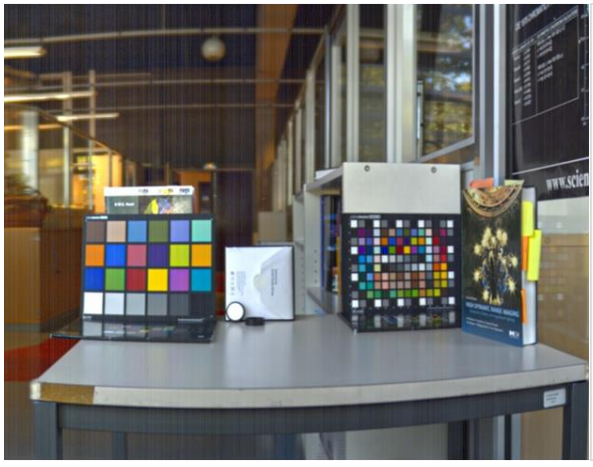

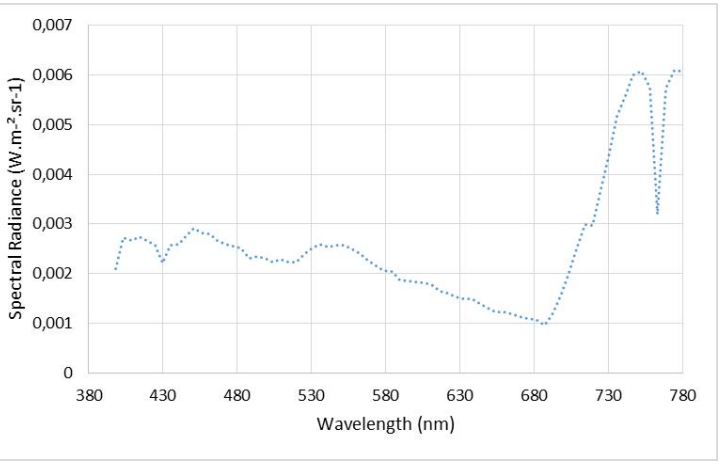

Figure 54, Sunlit indoor scene (left) with its spectral radiance measured on the Spectralon (right)

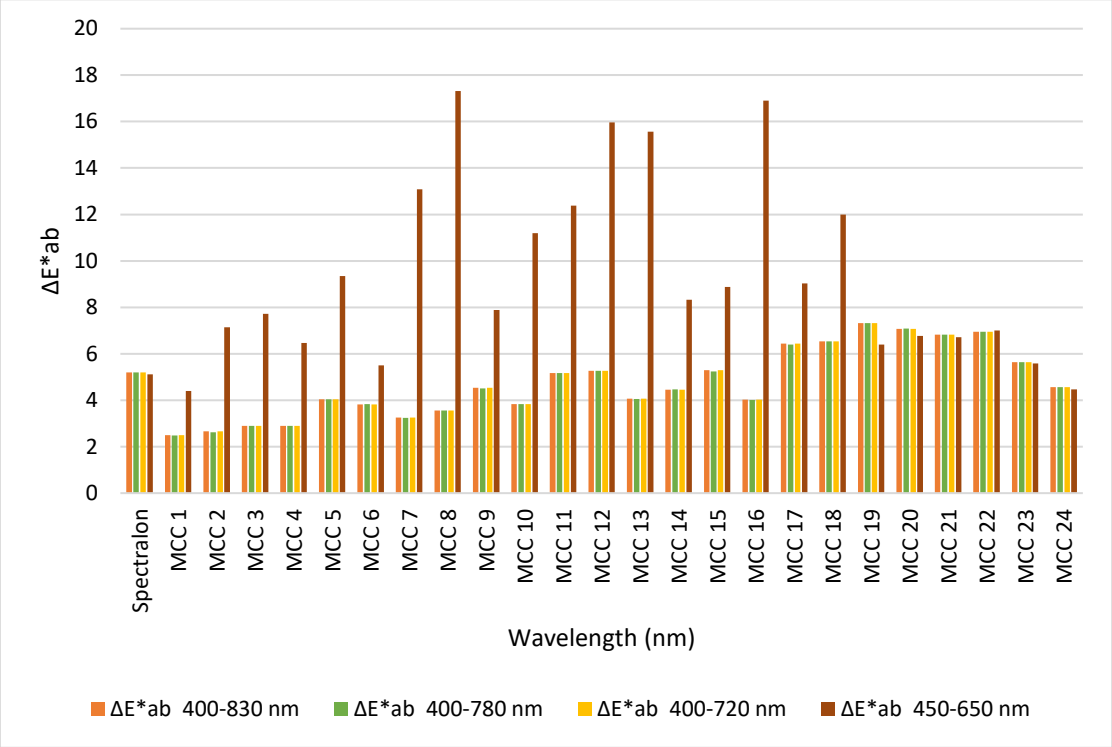

*Figure 55, ΔE*ab values for different spectral range*

This study confirmed that a reduction in spectral range from [400-830] nm to [400-780] nm or [400-720] nm did not impact the color reproduction accuracy of the hyperspectral data. Though the spectral range of [400-650] nm produced high color differences, suggesting a reduction in the color precision. To be on the safer side, in the scope of this PhD, the spectral range of the hypercubes was thus limited to [400-780] nm.

4.3. Creation of filtered stimuli

Once the hypercube is ready, the next step is to apply the sunglass (filter) on the hypercube and create an image (with iCAM06). The filter transmittances were measured between 380-780 nm (every 1 nm). Since the hyperspectral camera measured data between 400 nm-1000 nm, the data before 400 nm was deleted. The creation of the filtered radiance cube $\phi(\lambda)_f$ can be described with the help of the equation below:

$$\phi(\lambda)_{f(i,j)} = \phi(\lambda)_{o(i,j)} * \tau_v(\lambda) \ldots (31)$$

Where, $\phi(\lambda)_{o(i,j)}$ is the original unfiltered and calibrated hyperspectral radiance for pixel (i, j) and $\tau_v(\lambda)$ is the spectral transmittance of a particular sunglass. The transmittance is interpolated (cubic-spline) to have the wavelength dimension (λ) as the desired spectral resolution of the hypercube before multiplication (every 5,4 nm). A cubic spline method was chosen here since the original transmittance data was measured between 250 nm -1000 nm, thus reducing any possibility of errors at the extreme ends, as shown in section 3.2.

Once the filtered hypercube is ready, the spectral information is reduced to the CIE fundamental XYZ tristimulus values for 10° of viewing field using the equations below:

$$X_{f(i,j)} = k \int_\lambda \phi(\lambda)_{f(i,j)} \overline{x_{F10}}(\lambda) d\lambda \ldots (32)$$

$$Y_{f(i,j)} = k \int_\lambda \phi(\lambda)_{f(i,j)} \overline{y_{F10}}(\lambda) d\lambda \ldots (33)$$

$$Z_{f(i,j)} = k \int_{\lambda} \phi(\lambda)_{f(i,j)} \overline{z_{F10}}(\lambda) d\lambda \ldots (34)$$

To calculate the CIE XYZ tristimulus values for an entire 3-D image, the algorithm uses nested loops which slow down the processing. To speed up the algorithm, the calculations are done in 2-D space by resizing the filtered hypercube of dimensions [R C W] to [RxC W]. Once the tristimulus values have been calculated for the entire image, they are resized back to the original spatial resolution with three channels of information for each pixel, i.e. [R C 3].

The Y channel of the XYZ color space contains the absolute luminance information of the captured scene and is used to create a luminance map of the scene. This is done by creating a pseudo colored scalar image of the Y channel. A sample luminance map is shown in Figure 56.

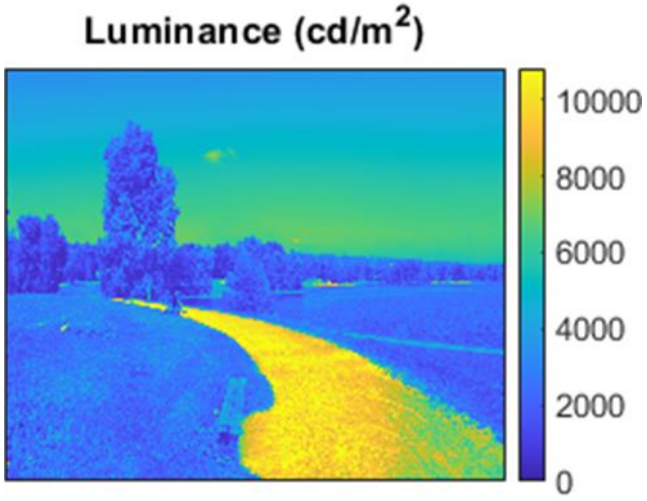

Figure 56, Sample Luminance map for an outdoor scene

The filtered XYZF10 data is now ready to be processed with iCAM06, using the default parameters of IPT power factor *pval* =0,75; gamma value for surround adjustment *gval*=1 and degree of adaptation factor D=0.9 for real world scenes. The complete framework for the simulation of colored vision through sunglasses is described in Figure 57.

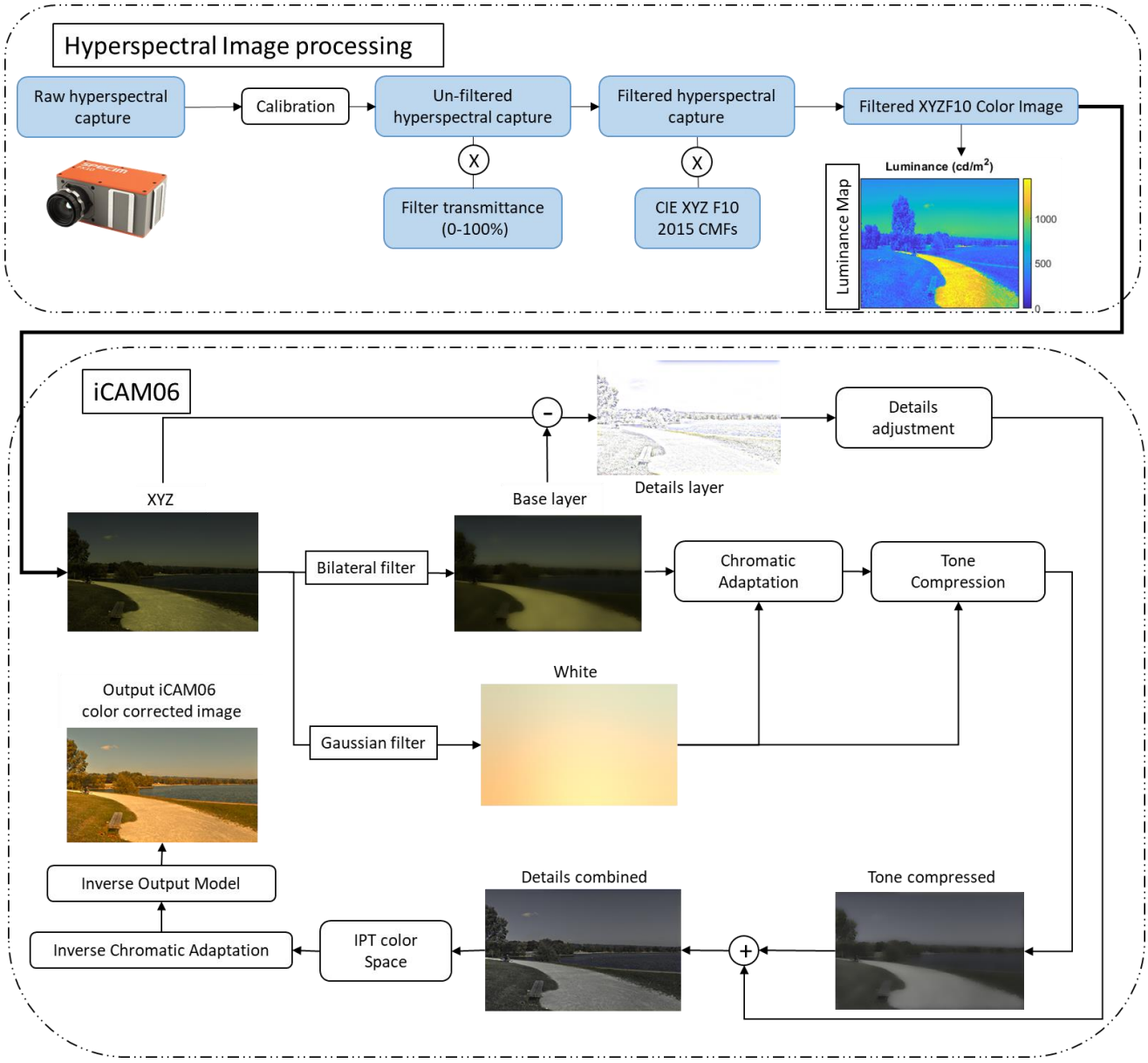

Figure 57, Framework for filtered image creation through hyperspectral imaging and iCAM06

4.4. Database of hyperspectral images

Sunglasses are worn in various environments where the ambient luminance and colors may vary. To optimally quantify colored vision through sunglasses, it is essential to have hyperspectral images of various possible scenes where sunglasses are worn.

For this reason, a database of hyperspectral images was needed with varying chromatic content and luminance conditions (sunlit outdoor, cloudy outdoor, interior spaces, portraits etc.). A substantial amount of outdoor hyperspectral images had already been captured during a previous project and certain of them are publically available (at https://www.entpe.fr/en/ressources-p2e), (Cauwerts & Jost-Boissard, 2019). Many others were captured during the course of the PhD. The current hyperspectral database contains 50 images. The outdoor images contain natural scenes with the landscapes of sea, lakes and mountains; and urban scenes, with the landscapes of city-skyline, streets, squares, buildings (with people) and gardens. The indoor images include typical waiting rooms, office spaces and meeting rooms, classrooms, work tables, corridors and light-booth setups. Except for the light-booth setups, the indoor scenes are either partially or fully illuminated by daylight, via skylights and windows. RGB image icons of certain images

from the hyperspectral database are presented in Figure 58, Figure 59 and Figure 60. Hyperspectral images available for the general public (for a non-profit use) have a green border.

Figure 58, Hyperspectral Database: Outdoor Natural/Urban

Figure 59, Hyperspectral Database: Outdoor Building

Figure 60, Hyperspectral Database: Indoor

The dynamic range of luminance for outdoor scenes is between 0:2000 and 0:25000 ($L_{v\_max} \in$ (2000 cd/m^2,25000 cd/m^2), see Figure 61). For indoor scenes, the luminance dynamic is less extreme but nevertheless important with a dynamic range between 0:300 and 0:5000 ($L_{v\_max} \in$ (300 cd/m^2,5000 cd/m^2), see Figure 62). The exposure for the captures of outdoor scenes is between 5 and 10 ms and for indoor scenes between 15 and 25 ms.

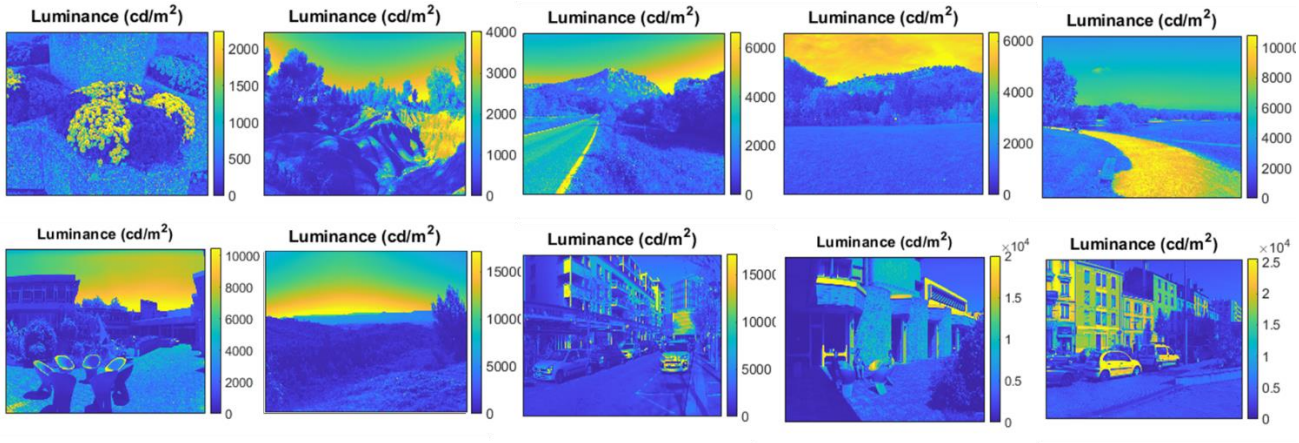

Figure 61, Sample luminance maps of outdoor scenes

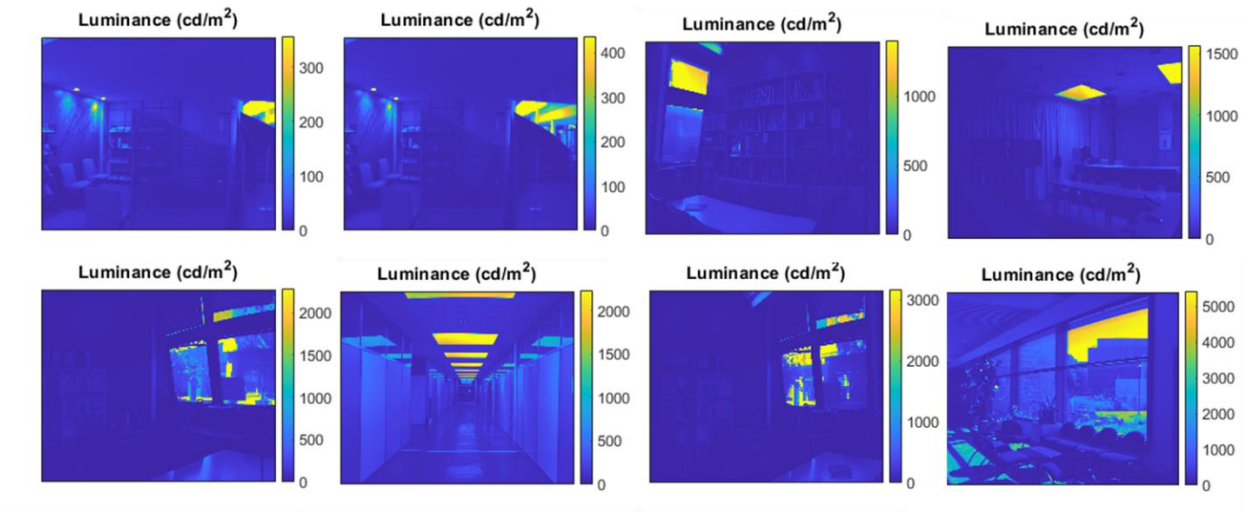

Figure 62, Sample luminance maps of indoor scenes

5. Experimental validation: iCAM06

The previous chapter (chapter 4) described the stimuli creation method to process hyperspectral images via iCAM06 to take into account the various color appearance changes induced by sunglasses. In this chapter, we will validate this stimuli creation method through psycho-visual experiments. At the same time, we will also compare the default iCAM06 with other versions of iCAM06 where certain components will be modified. The components modified will be: the color space (IPT (Ebner & Fairchild, 1998)), the edge-sensitive image segmentation method (bilateral filter (Paris & Durand, 2009)) and the chromatic adaptation transform (CAT02 (CIE 159, 2004)). The testing of a different color space and image segmentation method was encouraged by the availability of newer, more efficient alternatives (JzAzBz color space (Safdar et al., 2017b) and guided filter (Hutchison et al., 2010)). Whereas, the strong color shifts induced by sunglasses prompted the testing of a non-linear chromatic adaptation transform (CAT97) that might better reproduce non-white stimuli (CIE 131, 1998).

Apart from the above component modifications, we will also modify the values of certain parameters and test the changes in reproduction accuracy. We are interested in determining the accuracy for long term use of sunglasses. This corresponds to a complete chromatic adaptation controlled by D, the degree of chromatic adaptation, thus we will test different values of D. Since sunglasses induce strong color shifts, which render the scene visibly non-white, we will also modify and test the adapting white-point (WP) used for chromatic adaptation, which by default is D65 in iCAM06.

The axis of validation will be the achieved perception of color reproduction accuracy via iCAM06 when compared against the real scene for instances that concern specifically the use of sunglasses. These instances will include the simulation of sunglasses with different levels of transmission (category of sunglasses), sunglasses with different spectral repartition (metameric and colorful sunglasses) and light sources with different color temperatures (cold and warm scenes). A summary of the tested components in the experiments are presented in Table 10.

Table 10, Summary of the tested components in the experimental series

Exp.No.	Tested components	Original component	Proposed component	Nb. of Observers
1	Color Space and edge sensitive image decomposition method	IPT, bilateral filter	JzAzBz, guided filter	6
1A	Degree of chromatic adaptation	D=0,3 (iCAM06); D=0,9 (Smet et al)	D = 0,5; 0,7 and 0,9	4
2	Degree of chromatic adaptation and adapting white-point	D=0,3 (iCAM06); D=0,9 (Smet et al); WP=D65	D = 0,5; 0,7 and 0,9; WP=effective of light source & filter	6
3	Degree of chromatic adaptation and adapting white-point	D=0,3 (iCAM06); WP=D65	D = 0,5; WP=effective of light source & filter	34
4	Chromatic adaptation model and adapting white-point	CAT02; WP=D65	CAT97; Ma et al; WP=effective of light source & filter closer to D65	20

5.1. Background

The use of iCAM06 as a HDR-TMO (High Dynamic Range - Tone Mapping Operators) has been quantified with the help of psycho-physical experiments conducted by the developing team (Kuang, Johnson, et al., 2007). As described in the publication, twelve outdoor/indoor scenes (see Figure 63) treated with iCAM06 were compared against four TMOs: bilateral filter (Durand & Dorsey, 2002), photographic reproduction (Reinhard et al., 2002), iCAM (M. Fairchild & Johnson, 2002) and histogram equalization (Larson et al., 1997) along with two Photoshop CS2 HDR conversion methods: Exposure-Gamma and Local Adaptation.

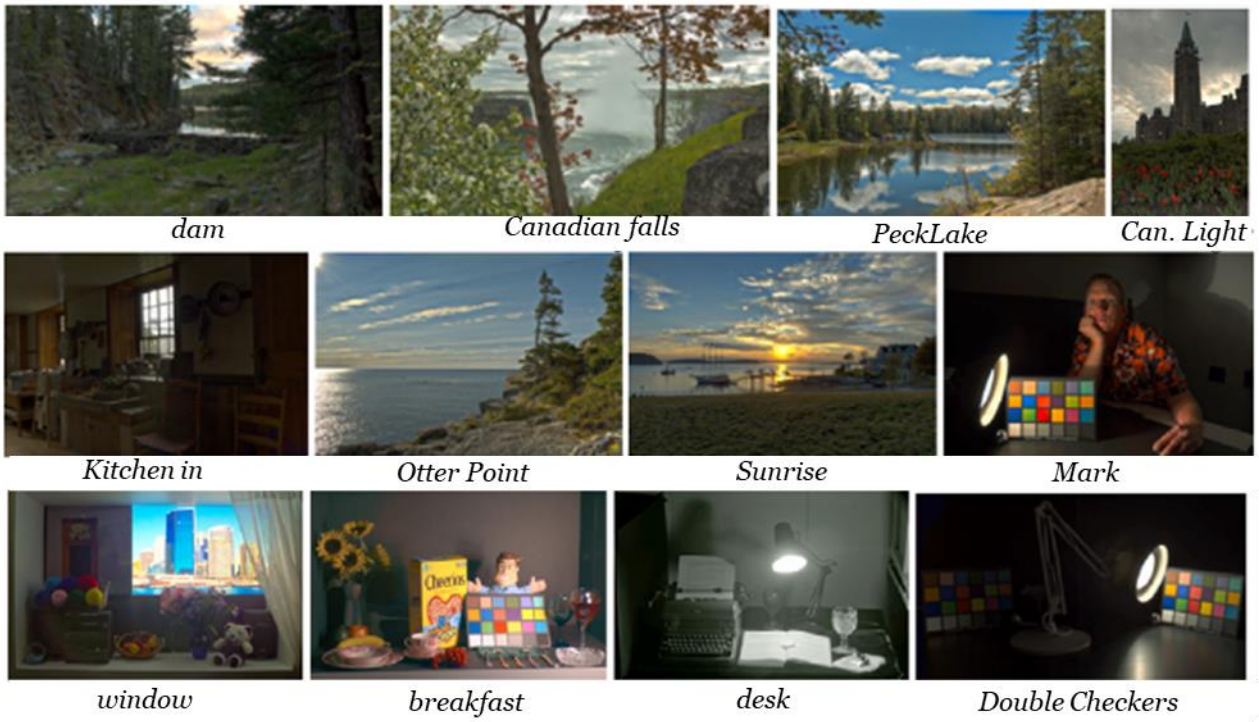

Figure 63, Test images used to validate iCAM06 as a TMO by Kuang et al 2007

The attributes tested by Kuang et al. were image rendering preference and the perceptual accuracy of the HDR reproduction. The images were shown on an Apple Cinema HD LCD Display (at 180 cd/m^2) using a paired-comparison method. For the preference scores, the observers were asked to compare the six versions of the twelve images for individual preference based on attributes like contrast, naturalness, sharpness etc. For perceptual accuracy, the observers compared the original scene with the reproduction presented on the computer for the four images in the last row of Figure 63. They were required to look at the original scene in a different room and then rate the accuracy of perceptual reproduction based on their memory (with an obligatory 30s chromatic adaptation). The results showed that iCAM06 was the most preferred TMO for image rendering, while for perceptual color accuracy, iCAM06 performed similarly to Photoshop methods but better than the four TMOs tested.

The use of iCAM06 as a TMO for representing indoor/outdoor HDR scenes was validated by Kuang et al through this study. However, this study does not validate the use of iCAM06 to represent the changes in color appearance of scenes seen through sunglasses. The more popular sunglasses of C3 (category 3) induce >80% reduction in luminance, sometimes accompanied by strong color shifts. Furthermore, little or no data is available for comparing non HDR scene reproduction accuracy of iCAM06, i.e. its use as an image CAM. For HDR imaging, Biggs modified the original iCAM (not iCAM06) framework to add the TMO of Reinhard and Devlin (Biggs, 2004; Reinhard & Devlin, 2005). Kuang et al found it (along with the Retinex model) to be the least accurate among the tested methods (Kuang, Yamaguchi, et al., 2007). Another study proposed modifications in the IPT color space after the application of iCAM06 to correct a possible de-saturation of colors caused by tone compression (Chae et al., 2013). We tested their implementation on a sunlit outdoor image of a person, Figure 64 (left). Indeed, the application did modify the saturation for many colors. But it seemed that it also modified the hues causing blue artefacts to appear in the images, see Figure 64 (right). Another study from the same group of authors proposed to combine a hue correction to the saturation correction (H.-G. Kim & Lee, 2013). They found that both objectively and subjectively, the color reproduction significantly improved with this new modification. For the subjective accuracy test, they showed three LDR images of the scene taken at different exposures as thumbnails. The participants were asked to compare these "*original images*" with iCAM06 and their method on the same screen, see Figure 65. Though it remains unclear how these three LDR images were processed (chromatically adapted or not,

choice of color space etc.). Even if the image processing method for reference images was known, the fact remains that the comparison was done with two out of three reference images being either partially saturated (over exposed) or partially dark (under-exposed). This in itself is quite difficult to apprehend as such incorrectly exposed images are not necessarily the best reference image for color reproduction accuracy tests. Furthermore, the pictures included in the publication also have the blue artefacts in the dark shadows, see Figure 65. This modification was thus not further tested due to doubts in the application of the modification.

Figure 64, Original iCAM06 (left) vs Saturation corrected iCAM06 (right)

Figure 65, Blue artefacts due to saturation compensation (H.-G. Kim & Lee, 2013)

The method of image comparison used by Kuang et al depends on memory matching. A series of experiments conducted by Wei et al (Y. Wang et al., 2019; Wei, Ma, et al., 2017) evaluated pair comparison methods based on memory matching and side by side comparison (haploscopic conditions). Haploscopic matching was found to be a more precise method for pair comparison.

Thus, to test the reproduction accuracy of hyperspectral images processed using iCAM06 to simulate color appearances as seen through sunglasses, a series of experiments were designed. The objective was to test

a large range of sunglasses and identify their reproduction accuracy. At the same time, various modifications were introduced in iCAM06 for certain components that have seen a major development since the launch of iCAM06. These modifications were compared against the original iCAM06 at each experimental step. To judiciously use time, it was decided to recruit a small panel of six experts in colorimetry for initial experiments. This way, for experiments that validated the testing protocol and the setup, we had expert opinion and at the same time this small but expert population ensured faster yet robust execution of experiments. The results of every experiment were analyzed via various statistical modules. These modules and other statistical terms are briefly defined in Annex I: Statistical Definitions.

5.2. Retrofitting iCAM06: recent techniques in colorimetry and image processing

The primary aim of this pilot experiment (Experiment 1) was to test the limits of the color space and the image segmentation technique used in the iCAM06 framework. Precisely to test the replacement of bilateral filter (Paris & Durand, 2009) used in iCAM06 by a guided filter (Hutchison et al., 2010); and the use of JzAzBz color space (Safdar et al., 2017b) instead of the IPT color space (Ebner & Fairchild, 1998).

As described in section 2.6, most of the manipulations of color appearances in iCAM06, including chromatic adaptation and tone compression, are applied only on the base layer obtained through the application of the bilateral filter. This makes the choice of image segmentation method to be something that will have a far-reaching impact on the final image. Thus, it is important to identify if the overall color precision of iCAM06 can be improved by using a newer edge-sensitive image segmentation technique.

The application of color space is the immediate next step once the color-adjusted base layer is merged back with the details layer (both layers obtained from edge-sensitive image segmentation). Thus, the choice of color space is the next important component that could significantly impact the color precision of the output image. Furthermore, certain color appearance phenomena in iCAM06, like Hunt effect, Steven's effect and Bartleson surround adjustment are applied on the IPT color space. If an improvement is possible in the color space, it will directly improve the overall color quality of the output image.

5.2.1. Choice of modifications

a) Color Space

The iCAM06 framework uses the IPT color space to bring back the tone compressed RGB signal into a device independent and homogenous colorimetric structure. Another alternative to IPT could be the JzAzBz color space that includes a wide color gamut and high dynamic range (Safdar et al., 2017b). The publication claims that JzAzBz performs second-best for small color difference data sets (after CAM16 UCS) and the best for large color differences (along with CAM16-UCS) (C. Li et al., 2017). It gives the most accurate predictions for the following datasets: MacAdam (MacAdam, 1942), the Munsell Data (*Munsell Renotation Data*, 1967), and wide-range lightness (M. Fairchild & Chen, 2011); and a reasonably accurate prediction for the hue linearity data sets (Hung & Berns, 1995). JzAzBz is also known to be more accurate for HDR scenes with a better prediction in Blue-Yellow color ranges (Huang et al., 2019; Xu & Luo, 2019). This color space is available as a Matlab code for the adapting white-point of D65 (Safdar et al., 2017a).

b) Image segmentation

The iCAM06 color appearance model uses a *fast* version of the bilateral filter to separate the original image into a details layer containing all details and contours, and a base layer containing the large luminance values (Kuang, Johnson, et al., 2007; Paris & Durand, 2009).

The bilateral filter uses a local Gaussian filter on the areas which belong to a similar luminance range. It identifies edges when there is a large difference in luminance between neighboring pixels of an area, and thus preserves them by not applying any Gaussian blurring. Sometimes this also leads to creation of false edges where the grey levels vary within a similar boundary. This edge preserving Gaussian filter, though effective in edge characterization, creates small plateaus of local pixels at the edges, which follow the entire edge and thus creates a visible 'staircase' of plateaus (Buades et al., 2006; Hutchison et al., 2010). A guided filter is supposed to be an effective alternative to the bilateral filter derived from a local linear model. The guided filter computes the filtering output by considering the content of a *guidance* image, which can be the input image itself or another image (a binary mask).

Three possible iCAM06 modifications were established: iCAM06 default (called Mod A); iCAM06 with JzAzBz color space and Bilateral Filter (called Mod B); and iCAM06 with IPT color space and Guided Filter (called Mod C). The combination of both JzAzBz color space and Guided filter was not evaluated since the resulting images were found to be unacceptably dark and very saturated during preliminary tests.

5.2.1. Research Questions

- The use of iCAM06 as a TMO-HDR has been validated by the research team behind the creation of iCAM06. But is it sufficiently accurate also for application to complex vision through colored sunglasses?

- iCAM06 uses the bilateral filter for edge-sensitive image segmentation and the color corrected final image is treated with the IPT color space. Can the recent developments in image processing and colorimetry improve the color perception of the final color corrected images and bring them closer to reality?

5.2.2. Experimental methodology

a) Stimuli

A light booth setup was chosen for an indoor analysis of the complex scenes, the background of the light booth was covered with a plain white cloth of uniform reflectance (ρ=0,8). The top of the light booth was covered with a granular diffuser to allow a light source to illuminate the scene uniformly. An EIZO ColorEdge CG277 (see Table 11) display was used to present the captured and processed images to six observers who were experts in colorimetry (3 female, 3 male, age $\in$ (24,58)). The EIZO display was calibrated for dark surround and 190 cd/m^2 of luminance. The degree of chromatic adaptation in iCAM06 was fixed at D=0.9. The additional parameters for iCAM06 (which remain unchanged for the future experiments as well) were: overall contrast, *pval* set to 0,75 (default value for indoor scenes) and the surround factor parameter, *gval* set to 1,5 (dim surround) while using the image color gamut of Adobe RGB.

Table 11, Characteristics of the display device

Manufacturer	Model	Backlight	Size	Native Resolution	Brightness (max)	Contrast Ratio (typical)	Wide Gamut Coverage
EIZO	ColorEdge CG277	Wide-Gamut LED	27.0" / 68 cm	2560 x 1440 (16:9 aspect ratio)	300 cd/m2	1000:01:00	Adobe RGB: 99%, DCI-P3: 93%

For the stimuli, we aimed towards evaluating a complex scene but with basic familiar objects to moderate the difficulty of the experiment. A basket of plastic fruits and vegetables was prepared for this purpose containing, apples (red and green), chilies (red and green), eggplant, tomatoes, an orange and a lemon. A stem of blue orchids was also placed in the basket to add blue colors. To have a reference, a Macbeth color chart of 24 patches and a Spectralon were also added in the scene, see Figure 66.

Figure 66, Experimental scene

A side-by-side haploscopic visual field was chosen for evaluating the different iCAM06 modifications (on the screen) alongside the original scene (light-booth) as shown in Figure 67. Such a presentation method has been used in various comparison setups for its ease of use, reduced complexity and a simultaneous

visualization of two scenes that can be differently illuminated (Bao & Minchen, 2019; Bruno et al., 1997; M. Fairchild et al., 1994; Harter et al., 1974; Ohno et al., 2019; Ruttum & Von Noorden, 1984; Shevell et al., 1992). The sunglasses had just one lens on the left eye to visualize the light booth and covered the entire left eye, see Figure 67. The right lens had been removed so that the observers could compare the simulation of the sunglasses on the EIZO screen. The camera objective was placed at the approximate position of the observer's eye (see Figure 68) and it scanned the light booth from right to left. The image on the EIZO display was flipped horizontally for a mirrored effect. This way the observers could compare objects at the left edge of the light booth with their reproduction on the display without moving their eyes, thus facilitating their comparison. The complete schematic of the experimental setup is shown in Figure 68.

Figure 67, Stimuli presentation method (left) sunglass sample (right)

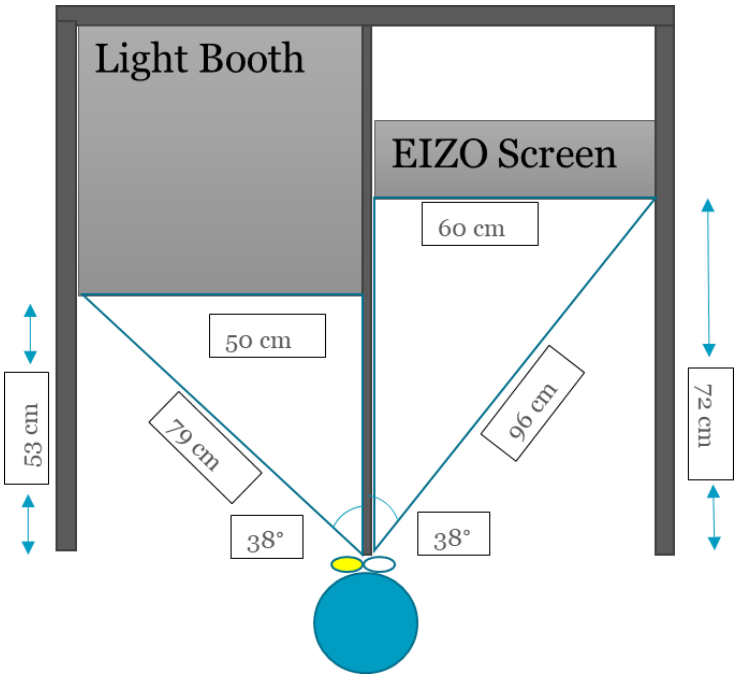

Figure 68, Schematic representation of the experimental setup

Two SPDs were created with the help of multivariable search algorithms to be metameric to CIE standards: P30 and D65 (Viénot et al., 2012). Metameric light sources have different shapes but matching cone-fundamental-based tristimulus values (XYZf10°) (CIE 170-2, 2015). One SPD was metameric to a Planckian spectrum at 3000K of CCT, named L3K; and the other was metameric to a daylight spectrum at 6900K, named L7K, see Figure 69. The light booth was illuminated with these SPDs one by one and the scene was captured by a hyperspectral imaging (HSI) system (SPECIM V10E).

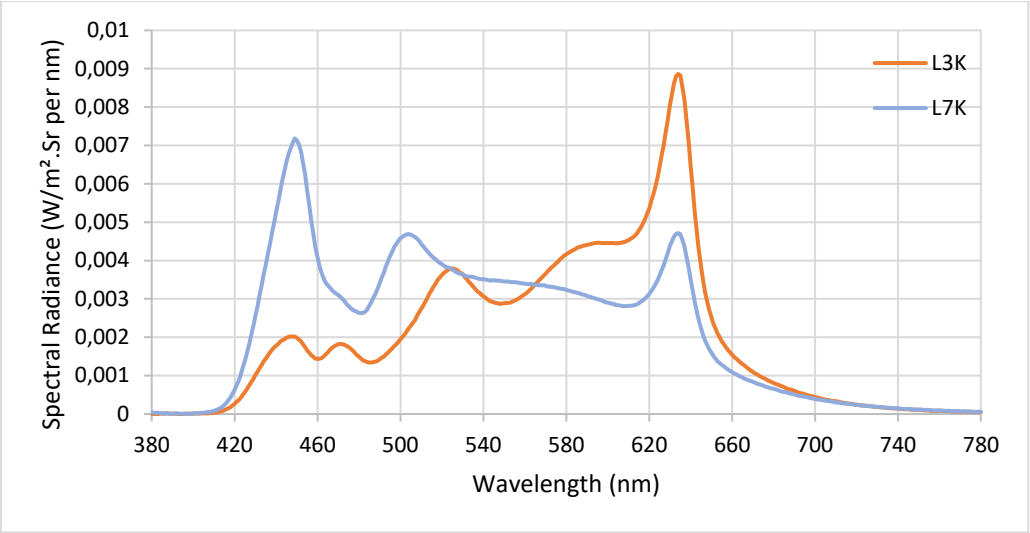

Figure 69, Test light sources, Experiment 1

Our objective was to evaluate the application of filters on complex images and compare their reproduction accuracy on a computer screen regarding colors and overall luminance perception. For this purpose, three sunglasses of ~15% transmittance (called PBC3, PBrC3 and PGGC3, see Figure 70) were applied to both the hyperspectral cubes (under the sources L3K and L7K). The chosen filters correspond to classic sunglasses that induce feeble chromaticity changes, with a low transmittance of visible light. The first 2-4 letters (everything before *C*) of the filter acronyms correspond to the proprietary name of the sunglass series. The last two characters of the filter acronyms correspond to the *category* of the filters (C0-C1-C2-C3-C4). The category of a filter determines the level of visible light transmission which is between 80-100% for C0 (clear tint), 43-80% for C1 (light tint), 18-43% for C2 (medium tint), 8-18% for C3 (heavy tint) and between 3-8% for C4 (very dark tint) (Essilor International, 1997). The filter acronyms follow the same nomenclature throughout this thesis.

Thus, the three sunglasses (Figure 70) were applied on the hyperspectral image under L3K and L7K, and treated with iCAM06 and its two modifications. An unfiltered image (called N100) under the two light sources was also included in the experiment. The effective colorimetric values, measured on the Spectralon, for every light source and filter combination, are presented in Table 12. Sample images for the three modifications are shown in Figure 71 for light source L7K and no-filter (N100). To give an idea about the color rendition of the filters, sample simulations for every tested filter under L7K with default iCAM06 are shown in Figure 72.

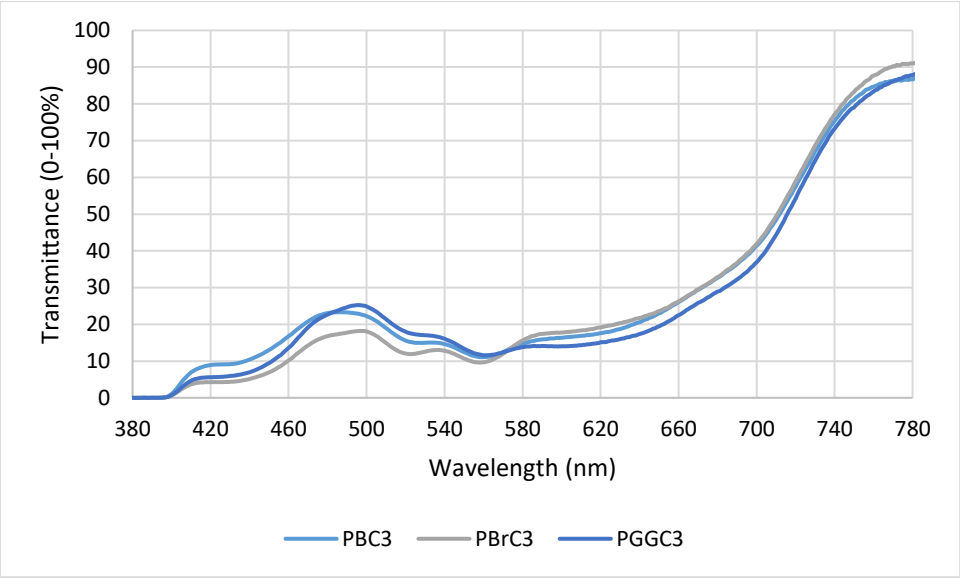

Figure 70, Spectral transmittances of the tested sunglasses, Experiment 1

Table 12, Colorimetric values for the two light sources and the four filters: Experiment 1

Scene	X	Y	Z	x	y	Luminance (cd/m²)	CCT(K)
L7K_N100	95	100	109	0,3136	0,3291	231	6458
L7K_PBC3	97	100	79	0,3514	0,3620	20	4810
L7K_PBrC3	98	100	82	0,3514	0,3574	10	4793
L7K_PGGC3	98	100	78	0,3557	0,3617	14	4664
L3K_N100	110	100	40	0,4405	0,4010	216	2919
L3K_PBC3	116	100	28	0,4741	0,4098	20	2495
L3K_PBrC3	117	100	29	0,4757	0,4062	10	2445
L3K_PGGC3	117	100	28	0,4787	0,4078	14	2421

Figure 71, Sample images under N100 for Experiment 1:
iCAM06 original (left), iCAM06 JzAzBz (center) and iCAM06 Guided filter (right)

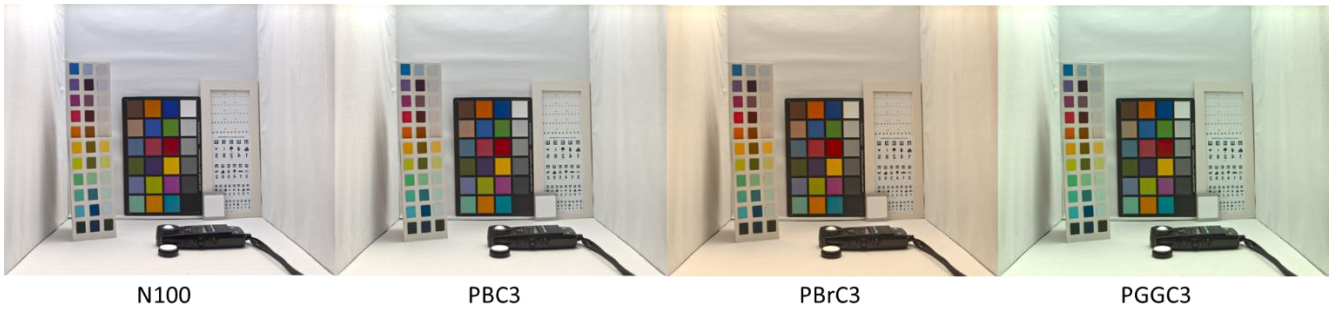

Figure 72, Images for each tested filter, simulated under L7K with default iCAM06 (D=0,3, bilateral filter, IPT): Experiment 1

b) Evaluation Method

A rating scale of 0-10 was chosen to evaluate the reproduction accuracy of the original scene (light booth) projected on the EIZO screen. A rating of 10 implied 'perfectly accurate color reproduction', while a rating of 0 meant 'not at all accurate reproduction'. The objects evaluated were: Tomato, Green apple, Flowers, Lemon, Orange (fruit), MCC Blue, MCC Green, MCC Red, MCC Yellow and MCC Orange (in order). A global color accuracy score was also asked at the beginning of the experiment.

A rating scale was chosen over magnitude estimation or ranking since rating is one of the simple forms of judgement (Kuang, Yamaguchi, et al., 2007). It has also been found to render similar precision as compared to ranking (Čadík et al., 2008; Kuang, Yamaguchi, et al., 2007), and is used widely in the color vision community (Cadik et al., 2006; Čadík et al., 2008; Kuang, Yamaguchi, et al., 2007; M. Luo & Lv, 2019; Suzuki et al., 1999; Yoshida et al., 2005).

The final 24 stimuli (2x4x3) consisted of a unique combination of one of the two SPDs (L3K and L7K); the four filters (N100, PBC3, PBrC3 and PGGC3); and the three iCAM06 versions (including the default version). The default iCAM06 model was also repeated without filter under L7K to test the repeatability of the experimental protocol. To objectively quantify the differences between the two versions, every image reproduced with the modified version of iCAM06 was compared against the default iCAM06 (bilateral filter and IPT) for colorimetric differences. Figure 73 shows the ΔE*ab of the versions that produced the maximum and the minimum color differences with the default iCAM06 for this experiment.

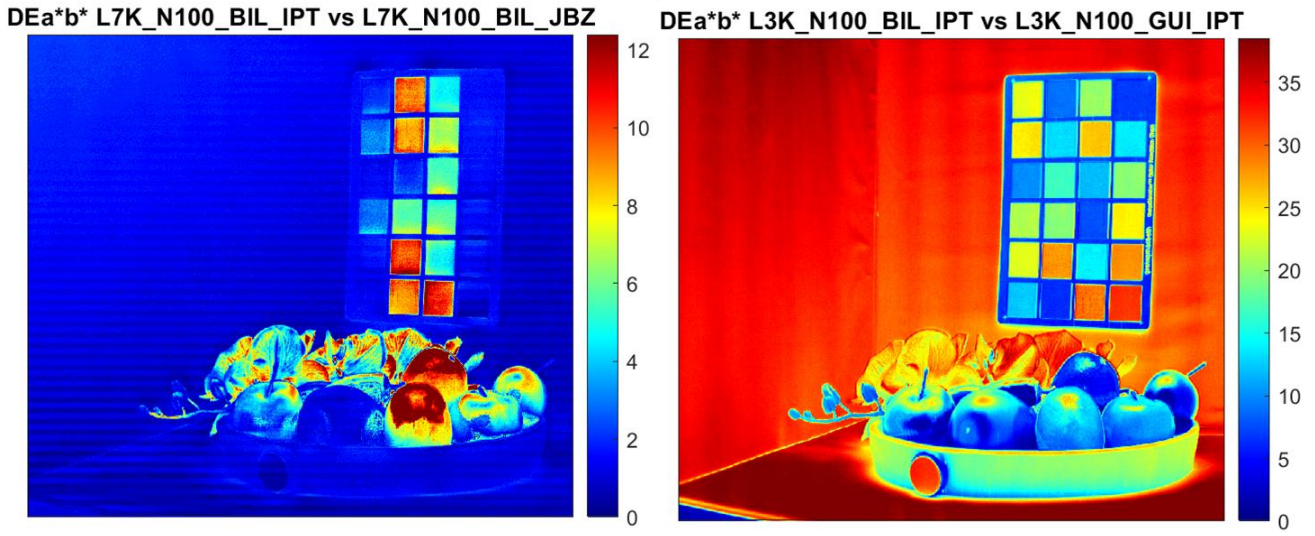

*Figure 73, Min ΔE*ab: L7K_N100: Bilateral IPT vs Bilateral JzAzBz (left) and Max ΔE*ab: L3K_N100: Bilateral IPT vs Guided IPT (right)*

The observers were given an introduction to the experiment and the instructions orally in French from an already prepared document (Annex II: Experimental Instructions). The total duration of the experiment

was nearly 2 hours, with a 5 minute pause after one hour. Before starting the experiment, the observers also did a 5 minute dark adaptation to ensure that the visual conditions before starting the experiment were comparable for every observer despite their previous environment's lighting conditions.

The images were flipped horizontally to present a mirrored vision of the real scene on the EIZO screen. The stimuli were presented in a Microsoft PowerPoint presentation using a controlled randomized sequence to avoid any position bias. Whenever there was a change in either the SPD or the colored filter, a 2 minute long chromatic adaptation was done during which the observer simply looked at the scene. For each combination of the SPD-colored filter, a 10s dark adaptation was done between changing iCAM06 modifications. After the adaptation period, the observers had as long as they wanted to rate each object's color reproduction accuracy.

5.2.3. Results

Repeatability

The iCAM06 default (bilateral filter, IPT color space) was repeated once under the L7K light source to test the repeatability of the protocol. The repetition was the last stimulus for half of the observers and the first stimulus for the rest. A median sign rank test (see Annex I: Statistical Definitions) was done on the two repeated evaluations and it revealed no significant difference (tested p-value >0,05, see Annex I: Statistical Definitions) between the two evaluations for each object/patch evaluated, see Table 13. The two ratings were thus averaged to have a single rating for the unfiltered scene under L7K.

Table 13, Repeatability median rank test, Experiment 1

Stimuli	Global	Tomato	Green Apple	Flowers	Lemon	Orange	MCC 13	MCC 14	MCC 15	MCC16	MCC17
Z-value	1,22	0,00	0,00	1,79	-0,41	0,41	0,89	-0,50	0,00	0,00	0,41
P-value	0,22	1,00	1,00	0,07	0,68	0,68	0,37	0,62	1,00	1,00	0,68

A Factorial ANOVA (see Annex I: Statistical Definitions) was conducted on all the ratings across all the color patches and observers, followed by a Tukey's HSD post-hoc test (see Annex I: Statistical Definitions). A factorial ANOVA was conducted as there are various independent variables (SPD, Filter, Mod and color patch) that can influence a single dependent variable (rating). It allows us to explore differences within a group and at the same time describe the interactions with other characteristics. The factorial ANOVA test can help us indicate if there are significant differences in the test group, but to identify which individual characteristic is significant, we need to conduct a post hoc test. For this purpose, a Tukey's HSD post hoc test was chosen as it is one of the most popular and powerful post hoc test.

The mean ratings for all the patches across different SPDs, filters and modifications are presented in Figure 74. An asterisk above the plotted value identifies significantly higher ratings for that particular SPDxFilterxMod combination, against the rest of the combinations, as per the posthoc test. While, an asterisk below the plotted value indicates significantly lower ratings of the particular SPDxFilterxMod combinations. The modifications are Mod A: iCAM06 with bilateral filter and IPT (original), Mod B: iCAM06 with bilateral filter and JzAzBz; and Mod C: iCAM06 with Guided filter and IPT.

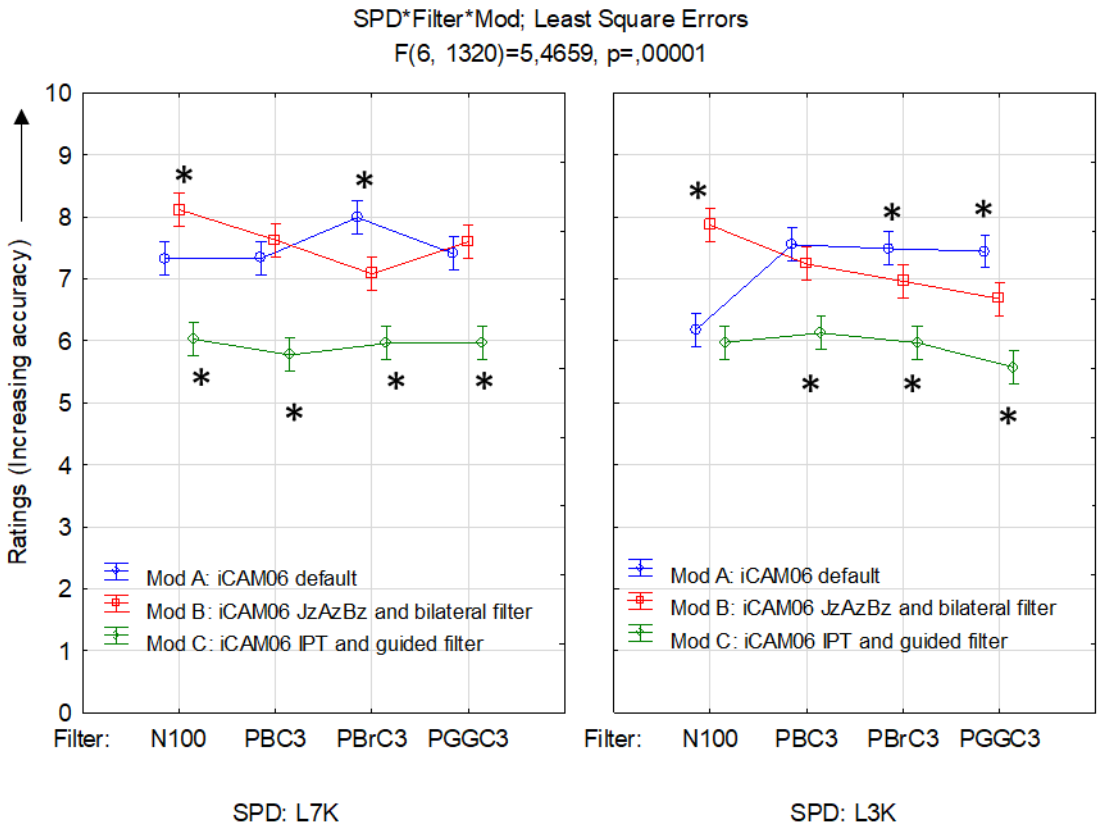

Figure 74, Statistical data (Error bars 95% C.I.): Source x Filter x Modification, Experiment 1

The above results show that Mod C (iCAM06 with IPT and Guided Filter) had the poorest ratings for all the stimuli, and with significance for almost all the instances. It is clear that the use of guided filter degrades the image color reproduction. Individual average ratings across the different patches/objects are presented in **Annex** IIIA.

In function of different filters, no-filter reproduction of colors was evaluated higher and with significance for the iCAM06 with JzAzBz (Mod B) than the default iCAM06 (Mod A) for both L7K and L3K SPDs. The filter PBC3, which is quite neutral, had no significant difference for either Mod A or Mod B. The filter PBrC3 (brownish tint) was rated higher with iCAM06 default for both the SPDs, but with significance only under L7K. The filter PGGC3 was rated without any difference for both modifications under L7K while there was a significant difference in favor of iCAM06 default under L3K. Average z-scores for each filter are presented in Annex IIIB.

5.2.4. Conclusion

The Guided filter gave universally and significantly lower reproduction accuracy for all SPDs, filters and patches. The use of JzAzBz seems much more ambiguous. **Vision without any filter has shown clear improvements in terms of color reproduction if we replace IPT with JzAzBz.** But for filtered vision this does not hold true, IPT is significantly better for PBrC3 in L7K and PGGC3 under L3K. PBC3 being more neutral than the other two filters, did not show any significant differences. It seems that for sunglasses that transmit only 10-15% of the light, IPT is a better or equivalent choice. But since JzAzBz has a better color reproduction accuracy for unfiltered scenes, maybe for sunglasses that are closer to unfiltered vision (glasses with higher transmittance: C0-C1-C2), JzAzBz might be a better choice. For this purpose, a supplementary test was run on high transmittance versions (~40-60%) of the same series of sunglasses. A paired comparison of the two color spaces in iCAM06 (IPT and JzAzBz) revealed that the observers (same as before) found the two images to be similar with no significant difference.

The results and their analysis indicate that the Bilateral filter implemented in iCAM06 is more suitable than a Guided filter for edge sensitive Gaussian image segmentation. Furthermore, the replacement of IPT by JzAzBz for filtered color vision was not found to be adapted and thus excluded from further experiments. Nevertheless, the use of JzAaBz in iCAM06 seems to improve unfiltered vision and should be investigated further, though it is out of scope for this thesis.

5.2.5. Corollary experiment: Experiment 1A

Many observers noticed that the images were too 'white' for all the filters. It was only for the no filter (N100) simulation under the cold light source (L7K) that they found the 'whiteness' of the scene acceptable. This 'whiteness' of images could perhaps be explained by the degree of chromatic adaptation D used in our application of iCAM06. It was kept fixed at 0.9 for the experiment since a two-minute chromatic adaptation was carried out. Furthermore, a D=0,9 was also recommended for real world scenes (Smet et al., 2014).

A corollary experiment was carried out to identify whether D=0,9 was really the optimal value of D in iCAM06 for a complete chromatic adaptation. We wished to compare image simulations of sunglasses for different degrees of adaptation (D = 0,5; 0,7 and 0,9) for image reproduction accuracy. The experimental setup (Figure 66) and the light sources (Figure 69) were the same as before. We wanted to include a large range of sunglasses under both L3K and L7K. Thus, six filters with different transmittances and chromatic characteristics, and one no-filter condition were chosen, see Figure 75. The effective colorimetric values of the sunglasses under the two light sources and their respective degree of chromatic adaptation as per CAT02 (for reference only) are presented in Table 14.

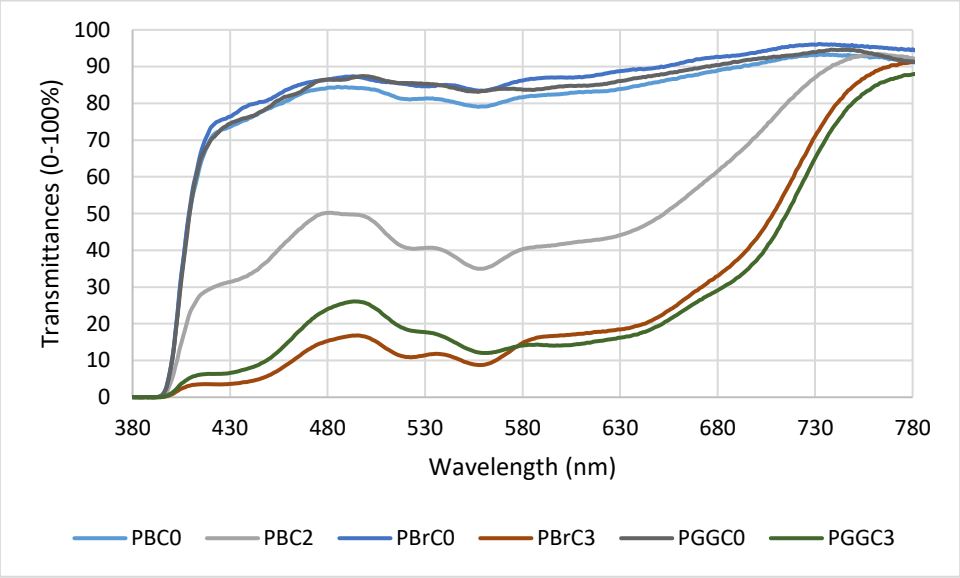

Figure 75, Spectral transmittances of the tested sunglasses, Experiment 1A

Table 14, Colorimetric values for the two light sources and the eight filters, Experiment 1A

SPD	Filter	X	Y	Z	x	y	Luminance (cd/m²)	CCT (K)	D (CAT02)
L3K	N100	110	100	40	0,4405	0,401	215,8	2919	0,85
L3K	PBC0	110	100	27	0,4648	0,4211	159,1	2711	0,98
L3K	PBC2	112	100	27	0,4686	0,4193	66,3	2644	0,97
L3K	PBrC0	110	100	27	0,4655	0,4217	165,6	2706	0,97
L3K	PBrC3	117	100	30	0,4757	0,4062	9,8	2445	0,91
L7K	N100	95	100	109	0,3136	0,3291	231	6458	0,82
L7K	PGGC0	92	100	69	0,351	0,3836	172,4	4896	0,99

L7K	PGGC3	98	100	78	0,3557	0,3617	13,9	4664	0,97

Three degrees of chromatic adaptation were chosen for each of the eight scenes: 0,5; 0,7 and 0,9. Sample images for the three degrees of adaptation for L3K without filter are shown in Figure 76. Other than the D-value, no other parameter was changed, they all were processed with the default iCAM06 framework. Thus, for each combination of SPD and filter, there were three versions of the scene reproduced using iCAM06.

Figure 76, Test images: L3K with N100 with D=0,5 (left), D=0,7 (center) and D=0,9 (right), Experiment 1A

Four participants from the six experts in colorimetry of the previous experiment participated in this experiment (2 female, 2 male, age $\in$ (19,58)). During this experiment, no ratings were given for simplicity as we wanted to see whether a change in the degree of chromatic adaptation would bring the images closer to the real scene. The attributes chosen for comparison were (eight in total): global color and luminance accuracy, and the color reproduction accuracy of the background and five objects: Tomato, Green Apple, Flowers, Lemon and the Orange fruit. Thus, the participants were shown the three images for every scene (on a Microsoft PowerPoint presentation) and were asked to identify the attributes in the image that seemed the closest to the real scene. Whenever there was a change in either the SPD or the colored filter, a 2 minute long chromatic adaptation was done during which the observer simply looked at the scene.

For each attribute in an image selected as the closest to the original scene, a score of 1 was given to that particular attribute (thus for the particular D value used for image creation). In cases where more than one image had equally accurate reproduction of the attributes, the score of 1 was divided among the images of the selected attributes. The total score for each attribute per image, per participant, was averaged at the end of the experiment, and multiplied by 100 to give a percentage value for each image to be selected as the closest to the real scene. These percentages of precision in image reproduction for the various attributes for image were compared for the different D-values. The percentages of precision were then averaged for all observers. They are presented in Figure 77 for the two SPDs combined with the different filters. Detailed results per attribute are available in Annex IV: Comprehensive object-wise results for Experiment 1.

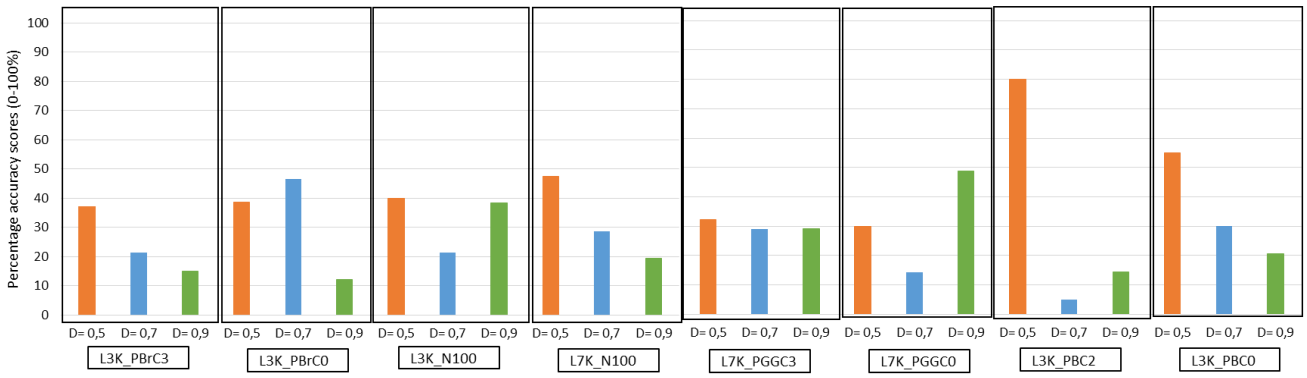

Figure 77, Mean percentage accuracy (over 8 attributes), for SPDxFilter, for three D values, Experiment 1A

As it can be seen above, no unique-value of D was found to be preferred by a majority of observers for the eight combinations of SPDs and Filters. This experiment reinforced the notion that the CAT02 D (~0,9) value is not the only suitable D value for image vision. For most scenes, the observers also expressed orally that the images were still too white and that going as low as D=0,5 was not enough for many filters, especially under the warm light source. It seems that the use of lower D-values might be required even when a complete chromatic adaptation is performed, as was done in this experiment. The results from the corollary experiment show a tendency that needs to be confirmed via a complete psychovisual experiment followed by a statistical analysis. This will be done in the next phase of experiments.

5.3. Tuning iCAM06 parameters: adapting D-value and white-point

The results from Experiment 1A in section 5.2.5 showed that the choice of degree of adaptation D required further testing for image vision through sunglasses. Thus, a full-scale experiment was conducted to identify the optimum value of D for our application.

As identified by the observers, the whiteness of the scenes was too pronounced even for a D as low as 0,5. An explanation for that among others could be the choice of white-point for the chromatic adaptation in iCAM06 or any other CAM for that matter. All the CAMs use Illuminant D65 (Daylight at 6500 K) or Illuminant E (Equi-Energy) as the adapting white point. Vision with sunglasses is quite different from daylight or other lighting conditions. As said earlier, sunglasses induce a drastic reduction in luminance, sometimes accompanied by strong color shifts. Our chromatically adapted vision with sunglasses may not be similar to a chromatic adaptation for a light source as cold as D65.

Keeping the above two points in mind, an experiment was designed to test the efficacy of: a) using lower D values, i.e. D=0,3-0,5-0,7 in addition to D=0,9 and b) using a modified white point that takes in account the effective tristimulus values of the light source filtered by the sunglasses.

This modified white point would be unique to each combination of sunglass and light source and would be adjusted to have the luminance (Y channel) of 100 cd/m^2. The calculation of the modified white point is explained hereafter:

If $\phi(\lambda)_f$ is the effective spectral radiance of the light source $\phi(\lambda)_o$ modified by the sunglass's transmittance τ_v and XYZ_{ref} are the effective XYZ tristimulus coordinates of the effective spectral radiance $\phi(\lambda)_f$, the CIE tristimulus coordinates of the modified white-point are calculated as shown below

$$XYZ_{ref} = k \int_{\lambda} \phi(\lambda)_{f(i,j)} \overline{xyz_{F10}}(\lambda) d\lambda \ldots (35a)$$

$$XYZ_{mod\_wp} = XYZ_{ref}./n \quad (35b)$$

Where, the rest of the symbols have usual meaning as described in chapter 2 and $n = 100/Y_{ref}$.

5.3.1. Research Questions

- A higher degree of chromatic adaptation corresponds to a complete chromatic adaptation. But is it the case also for filtered complex scenes? Perhaps a lower degree of adaptation can improve the color reproduction accuracy of the scenes?

- The default adapting white-point in iCAM06 is D65 which might not be optimum for filtered images. Can a change of adapting white point from D65 to the effective white-point of the light source filtered through a sunglass improve color reproduction accuracy for images?

5.3.2. Experimental methodology: Experiment 2

a) Stimuli

The light booth setup from the previous experiments (see Figure 66) continued to be the method of stimuli presentation to the six observers (experts in colorimetry), (3 female, 3 male, age $\in$ (24,58)), under the same light sources (L7K and L3K, see Figure 69). All the sunglasses tested before were presented together in this experiment. These sunglasses were: PBC0, PBC1, PBC2, PBC3; PBrC0, PBrC1, PBrC2, PBrC3; PGGC0, PGGC1, PGGC2 and PGGC3. Their spectral transmittances are shown in Figure 78 and their colorimetric values measured on Spectralon are shown in Table 15 for L3K and in Table 16 for L7K. A no filter (N100) image was also tested under both light sources.

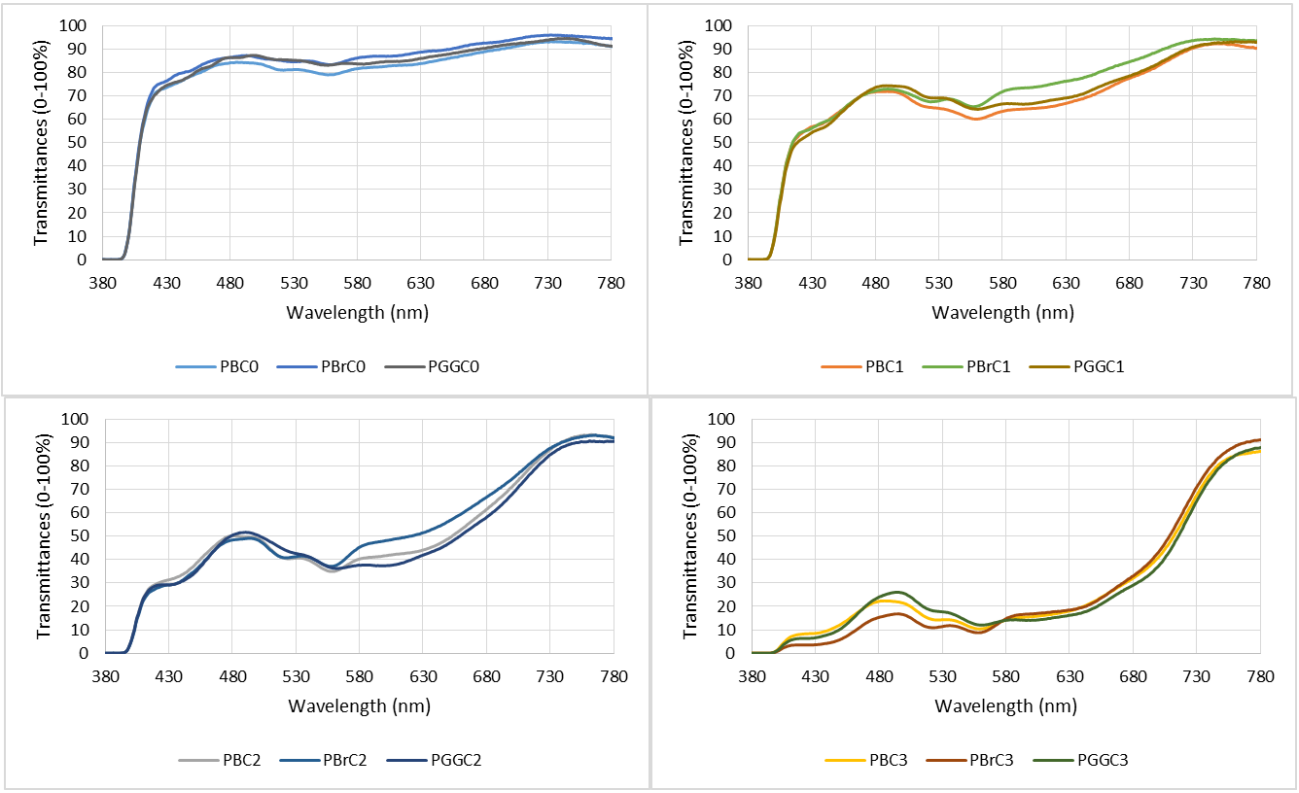

Figure 78, Spectral transmittances of the tested sunglasses, Experiment 2

Table 15, Colorimetric values for L7K filtered with the tested filters, Experiment 2

Filter	X	Y	Z	x	y	Luminance (cd/m²)	CCT
N100	95	100	109	0,3136	0,3291	231	6458
PBC0	92	100	74	0,3468	0,3756	167	5008
PBC1	92	100	70	0,3513	0,3807	132	4878
PBC2	93	100	72	0,3502	0,3756	69	4897
PBC3	100	100	80	0,3514	0,3620	20	4810
PBrC0	92	100	73	0,3480	0,3773	173	4974
PBrC1	93	100	70	0,3512	0,3819	135	4885
PBrC2	94	100	74	0,3489	0,3735	66	4934
PBrC3	100	100	80	0,3514	0,3574	10	4793
PGGC0	92	100	69	0,3510	0,3836	172	4896
PGGC1	93	100	70	0,3530	0,3816	128	4829
PGGC2	92	100	78	0,3418	0,3684	50	5164
PGGC3	100	100	79	0,3557	0,3617	14	4664

Table 16, Colorimetric values for L3K filtered with the tested filters, Experiment 2

Filter	X	Y	Z	x	y	Luminance (cd/m²)	CCT
N100	111	100	27	0,4405	0,4010	216	2919
PBC0	111	100	26	0,4648	0,4211	159	2711
PBC1	112	100	27	0,4679	0,4227	126	2681
PBC2	115	100	30	0,4686	0,4193	66	2644
PBC3	110	100	27	0,4741	0,4098	20	2495
PBrC0	110	100	25	0,4655	0,4217	166	2706
PBrC1	113	100	27	0,4676	0,4234	130	2691
PBrC2	120	100	30	0,4680	0,4184	63	2647
PBrC3	110	100	25	0,4757	0,4062	10	2445
PGGC0	111	100	25	0,4669	0,4248	165	2712
PGGC1	111	100	30	0,4695	0,4226	123	2659
PGGC2	114	100	29	0,4625	0,4170	47	2710
PGGC3	100	100	79	0,4787	0,4078	14	2421

As in the previous experiment, the different iCAM06 versions were compared against the default iCAM06 (D=0,3 and WP= D65) for objective color differences. One such example of the image versions with the minimum and maximum color difference is shown in Figure 79.

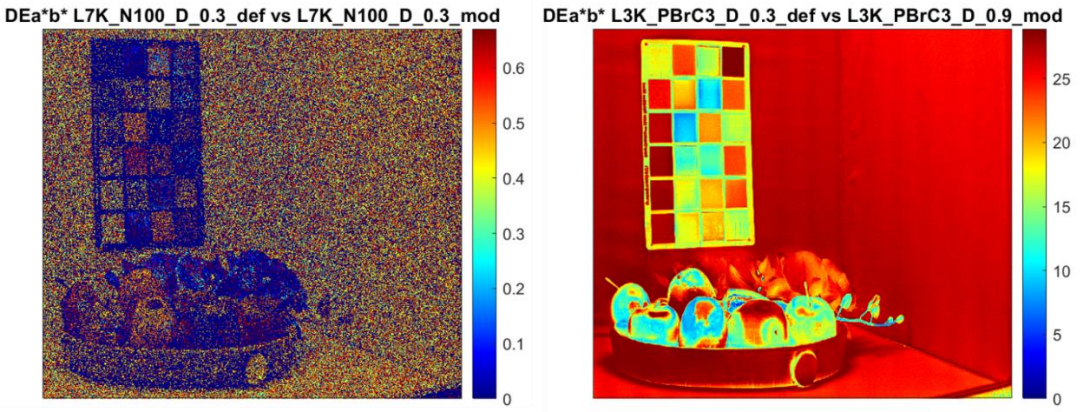

*Figure 79, Min ΔE*ab: L7K_N100: D_0.3_default WP vs D_0,3_modified WP (left) and Max ΔE*ab L3K_PBrC3: D_0.3_default WP vs D_0,9_modified WP (right)*

The modified white-point (mod) was applied only for images with a D=0,3 or D=0,9 to avoid testing too many versions of the same image which have no perceptual color differences. For most combinations of L3K and sunglasses, four D values (0,3; 0,5*; 0,7* and 0,9) and two adapting white-points (=D65 (def) or the modified white-point (mod)) were tested, totaling six images. An asterisk indicates that the particular D-value was not tested for each SPDxFilter combination. For certain sunglasses (PBC2, PBC3, PBrC3, PGGC2 and PGGC3) D=0,5* vs 0,3 and D=0,7* vs 0,9 produced visually and objectively (through ΔE*ab) indistinguishable images under L3K. Thus, only the images with D=0,3 and 0,9 were kept in the experiment to reduce the number of test images. For PBrC2, only D=0,7* was excluded while D=0,3-0,5 and 0,9 were tested. For the same reason, only D=0,3 and D=0,9 were tested for light source L7K (every filter), thus four images for each combination of light source and filter. The chromaticity difference (Δu'v') between the modified white points and D65 white-point is shown in Figure 80 for the two light sources. To give an idea about the color rendition of the filters, sample simulations for every tested filter under L7K with default iCAM06 are shown in Figure 81.

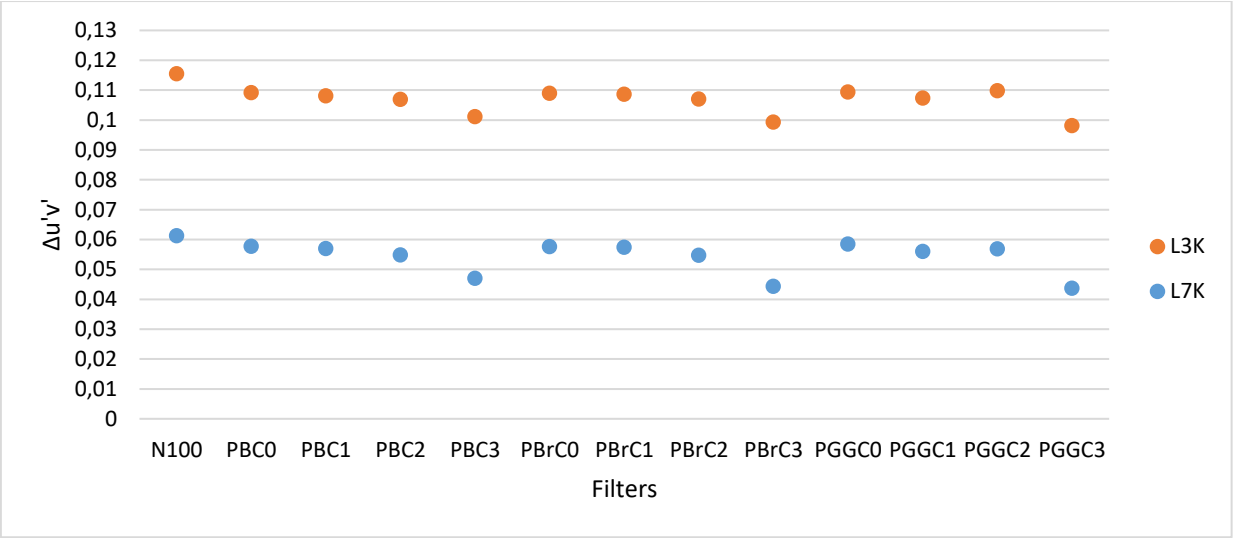

Figure 80, Δu'v' between D65 white-point and modified white-point, Experiment 2

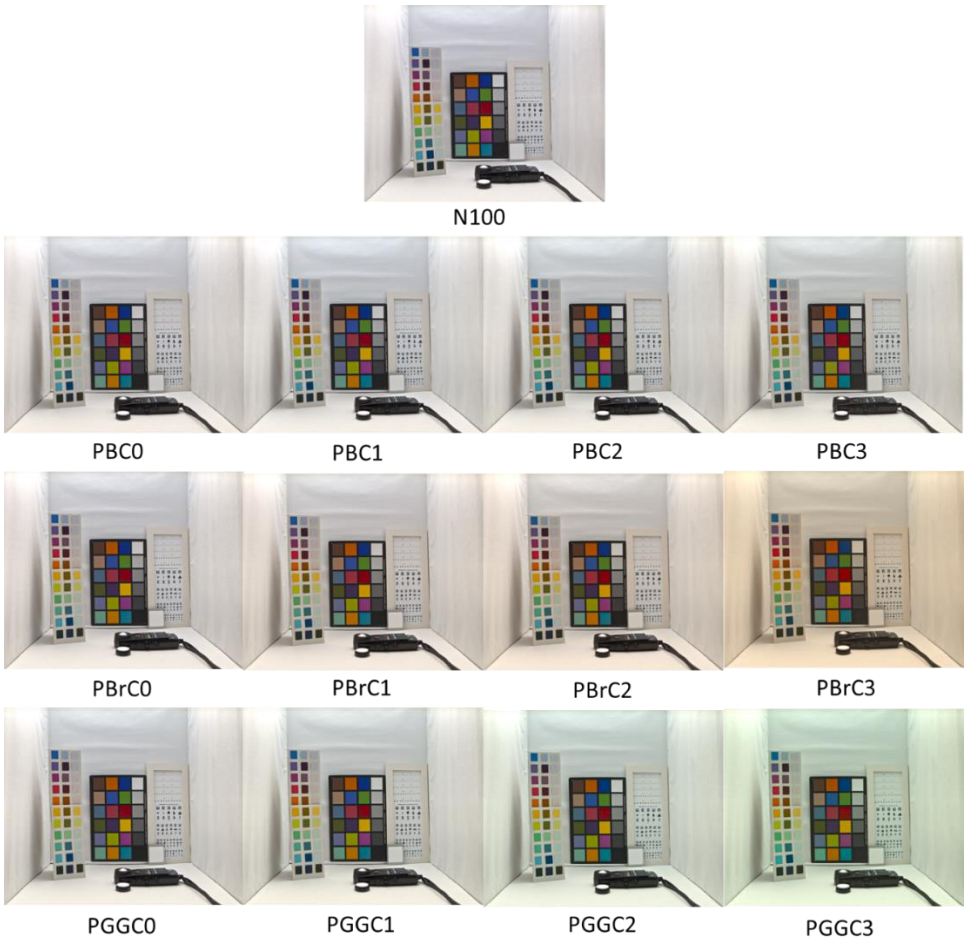

Figure 81, Images for simulated filters under L7K with default iCAM06 (D=0,3): Experiment 2

b) Evaluation Method

The evaluation method consisting of rating various objects in the image one by one was found to be long and laborious by the observers in the previous experiments. Furthermore, no statistical significance was found for different objects and MCC patches. Keeping these factors in mind, the evaluation methodology was modified to reduce the complexity of the task for the observers.

For this experiment, only global color reproduction accuracy ratings were asked from the observers. But before rating, they were asked to rank the images in a decreasing order of overall image accuracy in terms of color and luminance reproduction compared to the real scene, where both the attributes had the same importance. To rank the images, the observers had to rearrange the order of images directly in the Microsoft PowerPoint presentation where the images were displayed. There was no limit of time for this ranking process. Even though the ranks were not evaluated, the reordering of images made the rating process much simpler for the observers. Once the observers confirmed their ranking order, they were again shown the images in the selected order for a final confirmation. Then they gave ratings (0-10) to quantify the global color reproduction accuracy of the scene. A score of 10 meant that the image was perfectly accurate in color reproduction while 0 meant a complete lack of accuracy in color reproduction. The order of image presentation was randomized for every pair of sunglasses under each light source. At the beginning of the experiment, every observer did a dark adaptation during 5 minutes and then whenever there was a change in the light source or the sunglass, a 2 minute chromatic adaptation was completed.

5.3.3. Results

An ANOVA was conducted on the rating data obtained from the experiment. There were four variables that could impact the rating (0-10) for any image. They were: SPD (L3K and L7K), Filter (12 different sunglasses+N100), D-value (0,3; 0,5*; 0,7* and 0,9) and Adapting White-Point (WP=def or mod). A combination of four level interactions showed no significant impact on the rating for the image color reproduction accuracy (F(6, 5,08)=0,23; p=0,99). Furthermore, four combinations of three levels of interactions were evaluated. The combination of SPD*Filter*D (F(6, 10,21)=0,46; p=0,93) and Filter*D*WP (F(6,5)=0,22; p=0,99) showed no significant impact whereas the combination of SPD*Filter*WP (F(6 , 41,4)=1,89; p=0,03) and SPD*D*WP (F(6 , 27,08)=14,85; p=0,00*) had a significant impact on observer ratings. The average ratings for the combination of white point (def/mod) and D values (0,3;0,5*;0,7* and 0,9), for the two SPDs (L3K/L7K) are shown in Figure 82. The average ratings for the combination of Filters, and White-Points (def/mod) for the two SPDs (L3K/L7K) are shown in Figure 83. All the graphs have error bars representing a 95% confidence interval.

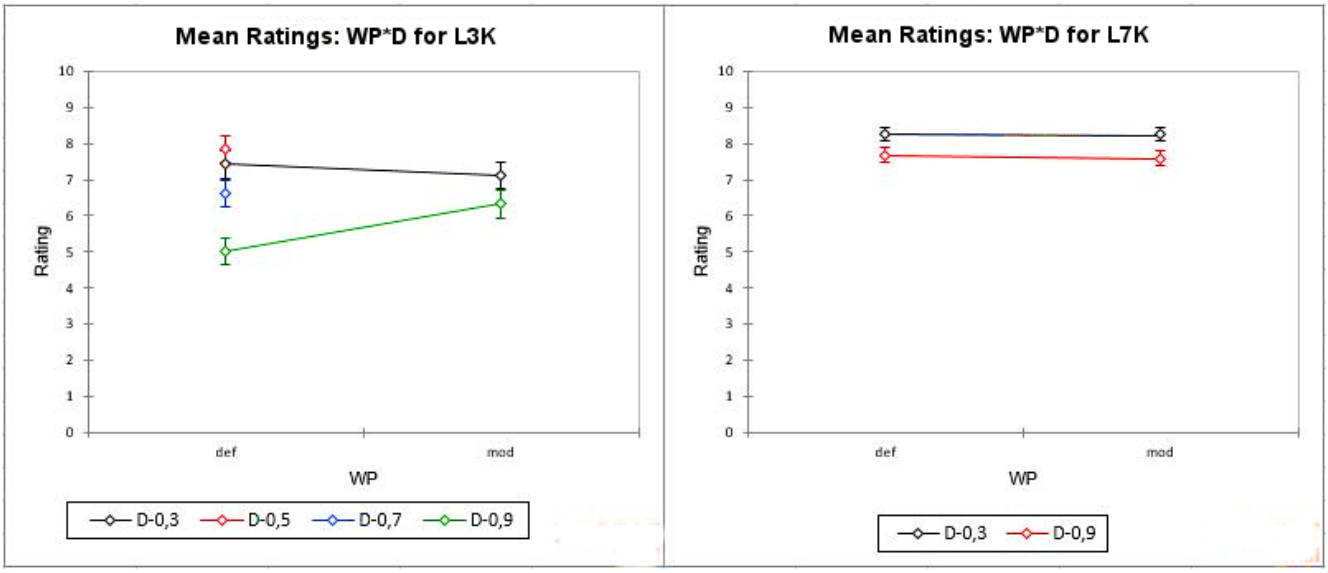

*Figure 82, Average ratings for SPD*D*WP with ANOVA = F(6 , 27,08)=14,85; p=0,00**

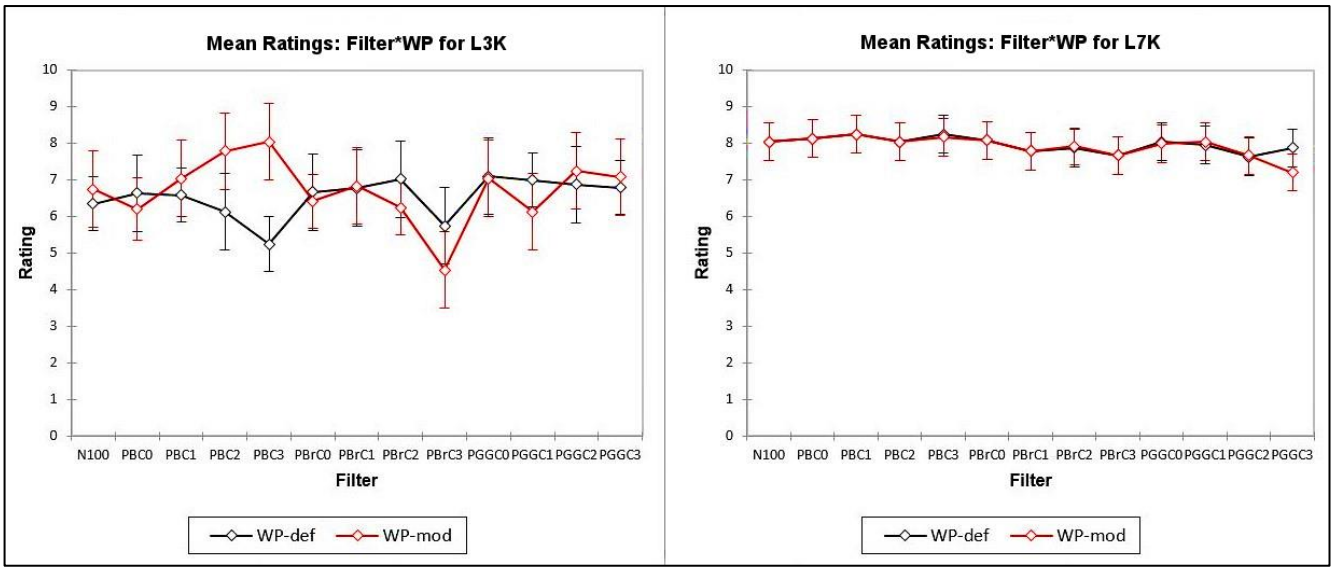

*Figure 83, Average ratings for SPD*Filter*WP with ANOVA = F(6 , 41,4)=1,89; p=0,03*

A Tukey's HSD posthoc was conducted on these ANOVA results to identify the variables that impact the ratings significantly. It was found that the degree of adaptation, D=0,9 and D=0,7 produced the lowest ratings for the accuracy of color reproduction for L3K SPD. Though a significant impact was identified only when using the default D65 as the white-point. It is to be noted that D=0,5 and D=0,7 were not applied to all the images due to perceptually imperceptible color differences with either D=0,3 or D=0,9, see section 5.3.2. Between D=0,3 and D=0,5, the average rating was higher for D=0,5 against that of D=0,3, but without any significance. For L7K SPD, with either WP, def (D65) or mod (modified), the average ratings were significantly lower at D=0,9 compared to D=0,3. It is inferable from the results in Figure 82 that a higher D-value produces lower ratings for color reproduction accuracy, especially if D is set at 0,9, a value which had the lowest ratings for either of the filter/SPD/white-point.

Only one filter (PBC3 under SPD L3K) had a significantly improved color reproduction accuracy when the white-point was changed from D65 to the modified white-point. Even though there is a general trend of improvement in ratings for all the filters of the PB series (greyish tint), no other significant impact was noticed on any filter or SPD for a change in adapting white-point. For the SPD L7K, the absence of any difference in ratings is less surprising since the adapting white-points (def vs mod) have a small (yet noticeable) chromaticity difference, with max $\Delta u'v' < 0{,}07$ (see Figure 80) for any filter. On the other hand, for the SPD L3K, the modified WP for any filter combination had a $\Delta u'v' \in (0{,}10;0{,}13)$ with D65. This is almost twice the one for L3K and 10 times the limit of the CIE Just Noticeable Differences of 0,0013 in u'v' coordinates (JNDs) (Ohno & Blattner, 2014).

Average ratings for all the filters, with all the combined modifications averaged together (D-value (0,3; 0,5*; 0,7* and 0,9); WP (def and mod) and two SPDs (L3K and L7K)) are shown in Figure 84. Only the filter PBrC3 (brownish tint with 15% transmittance) had significantly lower average rating when compared to PBC1, PBC2, PBC3, PGGC0 and PGGC2. All the other filters had a statistically similar accuracy in color reproduction. Average ratings for the other variables: D-value, SPD and WP are shown in Annex V: Individual variable wise ratings for Experiment 3.

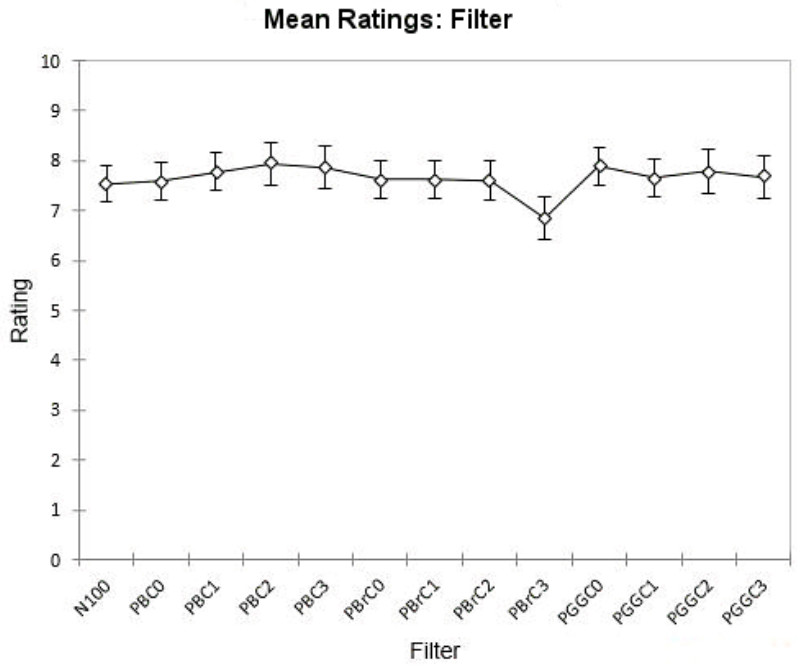

Figure 84, Average filter wise ratings for all the modifications: Experiment 2 (D-value (0,3; 0,5; 0,7* and 0,9); WP (def and mod) and two SPDs (L3K and L7K))*

5.3.4. Analysis

This Experiment 2 was conducted with the objective to test the change in image reproduction accuracy (color and luminance reproduction) induced by changing certain parameters of iCAM06. The tested parameters were the degree of chromatic adaptation 'D' and the adapting white-point 'WP'. Four different D-values (=0,3; 0,5*; 0,7* and 0,9) and two WPs (=D65 (def) and modified (mod)) were tested for color reproduction accuracy of twelve filters and one no-filter scene, under two light sources: L3K and L7K.

The results of the experiment were clear for the choice of D-value, a lower value of D=0,3 or D=0,5 improved the color reproduction accuracy with significance (except for modified WP under L3K). This confirmed that the use of the default degree of adaptation (D=0,9), closer to the value specified in CAT02, reduced the color reproduction accuracy significantly. Though the choice of D between 0,3 and 0,5 was still not clear, further tests on a larger population could be a possible method to answer this question. Despite the clearly significant difference between the use of D=0,9 vs D=0,3, it can be seen that the difference in average rating is less than 1 for L7K, see Figure 82. This shows that for light sources similar to L7K (for e.g. daylight), the use of D=0,3 is preferable though the use of D=0,9 will not drastically reduce the color reproduction accuracy. For L3K, the difference between the ratings of D=0,9 vs D=0,3 or D=0,5 is quite high, and thus D=0,9 is not suitable for indoor lightings that have lower CCTs.

The choice of white-point gave less clear results with the modified white-point improving the color accuracy (with significance) for only one filter (PBC3) under the warm light source (L3K). Under the cold light source (L7K), a change in white-point had no impact. The average ratings for the default WP and the modified WP for an unfiltered scene, for a light source metameric to D65 were also the same. This absence of impact of the white-point for the unfiltered image (N100) was expected as in this case, the modified WP and the default WP had the same tristimulus values. This further assured the repeatability of our experimental protocol. Even though a modified WP improved the color reproduction accuracy for only one filter (PBC3) under warm light, it was decided to continue testing the modified WP in our future experiments. This was done in order to eliminate any doubt if any other additional filters which have similar neutral greyish tints like PBC3 could benefit from a modified WP. Furthermore, the utility of a modified white-point should also be tested on sunglasses that impact the color perception of the scene more visibly than the filters tested so far.

5.3.5. Large population testing of altered iCAM06 parameters: Experiment 3

Following the results from the Experiment 2, it was deemed important to further test the color reproduction precision when using the XYZ tristimulus values of the light source and the filter taken together as the adapting white point.

The sunglasses tested in the previous experiments had very similar CCTs (for a particular SPD). To counter this tendency, it was decided to include filters with varying CCTs in the list of tested sunglasses. Thus, certain color enhancement filters (that modify the color perception) were added to the list of classic sunglasses tested so far. Their metameric pairs were also produced with different technologies and dyes, and integrated in the experiment to evaluate the effect of spectral transmission on color reproduction.

The previous experiments also highlighted the importance of lower D-values, which impacted the color precision differently for different light source and filter combinations. Certain filters showed a general change in trends, though without significance, especially for the use of a modified white-point, or the use of D=0,3 vs D=0,5 for warm light sources. To ensure more robust results, it was decided to conduct the experiment on a larger population, preferably with at least 30 participants.

5.3.6. Updated research questions

- A lower degree of chromatic adaptation of D=0,5 in iCAM06 seems to reproduce filtered images better. Perhaps an even lower degree of adaptation of D=0,3 can further improve the color reproduction accuracy of the images?

- The default adapting white-point in iCAM06 is D65 which might not be optimum for filtered images. Can a change of adapting white point from D65 to the effective white-point of the light source filtered through the sunglass improve color reproduction accuracy for images?

- Does the color reproduction accuracy of iCAM06 simulated images change with the distribution of the spectral transmission of filters, specifically the one of metameric filters ?

5.3.7. Experimental methodology

a) Stimuli

The experiment tested two parameters: the adapting white point (WP) and the degree of chromatic adaptation (D). Two values for each parameter were tested on 34 observers (13 female, 21 male, age $\in$ (19,58)), two WPs: default D65 (def) and modified (mod); and two D values: D=0,3 and D=0,5. Thus, for each SPD and filter combination, there were four iCAM06 versions to test.

In the previous experiment (Experiment 2), the ratings for the PGG series of filters was quite good (avg. rating~8), and was uniform among different categories (C0-C1-C2-C3). Thus, they were excluded from further experiments. On the other hand, the PB and PBr series had not so uniform results among different categories, especially for C3. So, it was decided to keep PBC3 and PBrC3 for further testing. Furthermore, 8 complex filters that either alter the chromaticity of the scene or alter the spectral transmission distribution of PBC3/PBrC3 were also added to the experiment. Thus, in this experiment, the filters tested were PBC3, PBrC3, their metameric pairs (PBC3M, PBrC3M) and a pair made from a different dye (PBC3D, PBrC3D). Four color enhancing filters (of C3, ~15% transmittances) were also incorporated in the experiments. They were KUB, KUG and their metameric pairs (KUBM, KUGM). An unfiltered scene (N100) was also included in the set of ten filters tested whose transmittances are shown in Figure 85.

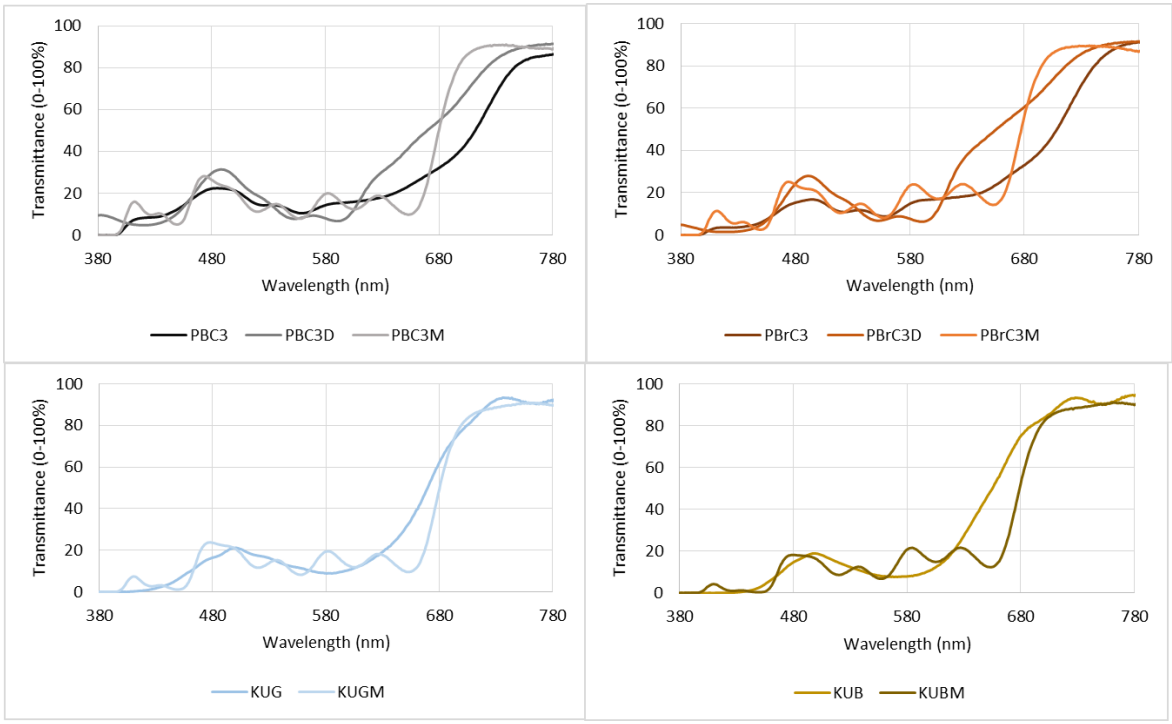

Figure 85, The set of 10 tested filters, Experiment 3

The previously used warm light source L3K (see Figure 69), when filtered through the color enhancement filters (KUG, KUGM, KUB, KUBM), produced a very warm scene (CCT~1700 K). When the hyperspectral image of the combination was treated with iCAM06, and with either the modified white-point or a D=0,3 (or both combined), the images were rendered falsely (purple shadows). To circumnavigate the problem, a less warm light source was used instead (L4K with a CCT of 4000K).

The light source L4K had a sufficiently low CCT to assess the working of our model in warm lights, and thus provide a reference for warm SPDs. And at the same time, it did not saturate the colors to the point where they became unreproducible by iCAM06. The images for L7K were captured with the SPECIM V10E HSI system, while the images for L4K were simulated. The previously tested L3K and L7K were measured consecutively, without moving the HSI device. Since it was not practically possible to obtain hyperspectral measurements under the source L4K, with exactly the same position of the camera as for L3K/L7K, a simulation was considered a simpler choice. To simulate L4K, the L7K hyperspectral image was converted from radiance to reflectance by dividing the radiance of the light source L7K from every pixel's radiance spectrum. Thereafter, the hyperspectral image containing reflectance data was multiplied with the single radiance spectrum of the L4K light source.

The validity of this method was confirmed by simulating a hyperspectral image with a CCT of 4000K from one pre-existing hyperspectral image at 6500K, see Figure 86, and then calculating the color difference (ΔE*ab) with a pre-existing hyperspectral image at 4000K. This process was repeated for a similar pre-existing hyperspectral image at 3000K, see Figure 86. The obtained color differences for either simulation were imperceptible with a ΔE*ab <3 for the majority of the image except for the edges, see Figure 87. Since either method gave similar ΔE*ab, (median ΔE*ab <0,6, mean ΔE*ab <1,3), the 6500K image was used as the reference hyperspectral data.

Figure 86, Reconstructed 4000K image from 3000K image (left), original 4000K image (middle) and reconstructed 4000K image from 6500K image (right)

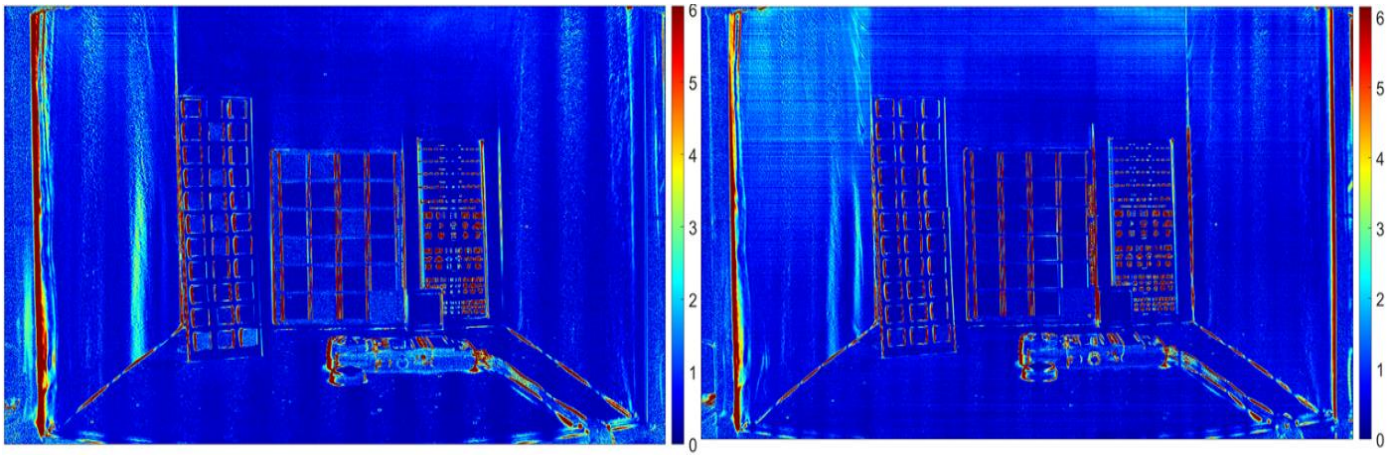

*Figure 87, ΔE*ab between the real 4000K HSI compared with a reconstruction from 3000K (left) and 6500K (right)*

Thus, the tested light sources were L4K (4000K) and L7K (6500K), which illuminated a light booth (same as in previous experiments) consisting of fruits, vegetables, flowers and a Macbeth 24 Color Checker Chart. The experimental scene and the SPDs are shown in Figure 88. The colorimetric values measured on Spectralon for the tested filters are shown in Table 17 for L4K and in Table 18 for L7K. As before, every version of the iCAM06 was compared against the default iCAM06 (D=0,3 and WP=D65) for colorimetric differences, the maximum and minimum differences are shown in Figure 89.

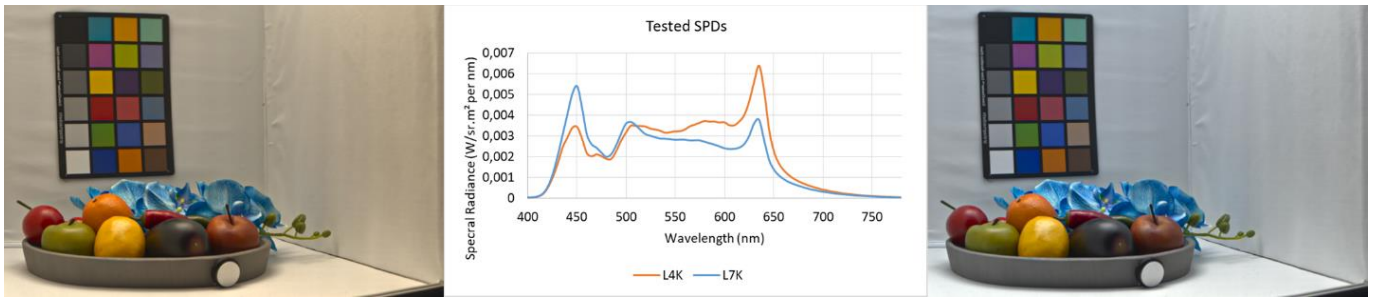

Figure 88, L4K test image (left), L7K test image (right) and their radiance curves (center)

Table 17, Colorimetric values for L4K and the tested filters, Experiment 3

SPD	Filter	X	Y	Z	x	y	Luminance (cd/m²)	CCT (K)
L4K	N100	101	100	68	0,3762	0,3718	274	4092
L4K	PBC3M	101	100	57	0,3901	0,3875	40	3836

L4K	PBC3	102	100	62	0,3855	0,3789	41	3891
L4K	PBC3D	103	100	62	0,3897	0,3773	41	3773
L4K	PBrC3M	109	100	38	0,4404	0,4045	44	2950
L4K	PBrC3	109	100	41	0,4360	0,4012	39	2997
L4K	PBrC3D	112	100	39	0,4462	0,3984	41	2803
L4K	KUGM	96	100	33	0,4199	0,4356	39	3535
L4K	KUG	94	100	39	0,4045	0,4288	38	3786
L4K	KUBM	110	100	22	0,4723	0,4310	37	2685
L4K	KUB	110	100	27	0,4646	0,4220	35	2721

Table 18, Colorimetric values for L7K and the tested filters, Experiment 3

SPD	Filter	X	Y	Z	x	y	Luminance (cd/m²)	CCT
L7K	N100	95	100	109	0,3135	0,3289	230	6464
L7K	PBC3M	91	100	86	0,3282	0,3606	33	5671
L7K	PBC3	93	100	98	0,3191	0,3445	35	6096
L7K	PBC3D	90	100	94	0,3164	0,3521	35	6192
L7K	PBrC3M	97	100	58	0,3815	0,3913	36	4076
L7K	PBrC3	98	100	65	0,3723	0,3815	32	4261
L7K	PBrC3D	95	100	59	0,3742	0,3929	33	4272
L7K	KUGM	85	100	48	0,3652	0,4301	32	4657
L7K	KUG	83	100	59	0,3414	0,4132	32	5246
L7K	KUBM	97	100	32	0,4226	0,4359	30	3489
L7K	KUB	94	100	41	0,4010	0,4254	29	3836

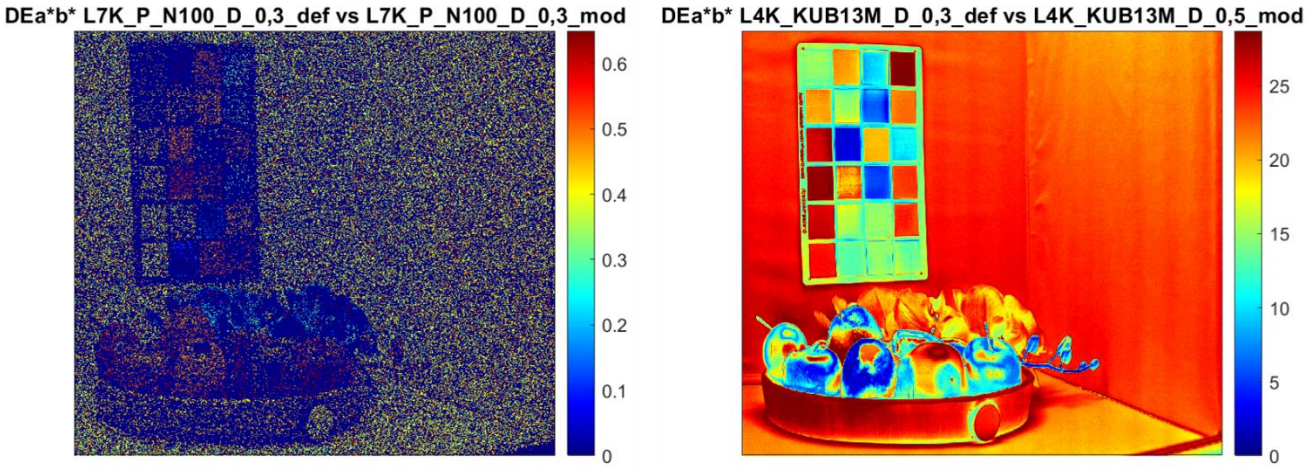

*Figure 89, Min ΔE*ab: L7K_N100: D_0.3_default WP vs D_0,3_modified WP (left) and Max ΔE*ab L4K_KUBM: D_0.3_default WP vs D_0,5_modified WP (right)*

The chromaticity difference (Δu'v') between the modified white points and D65 white-point is shown in Figure 90 for the two light sources. To give an idea about the color rendition of the filters, sample simulations for every tested filter under L7K with default iCAM06 are shown in Figure 91.

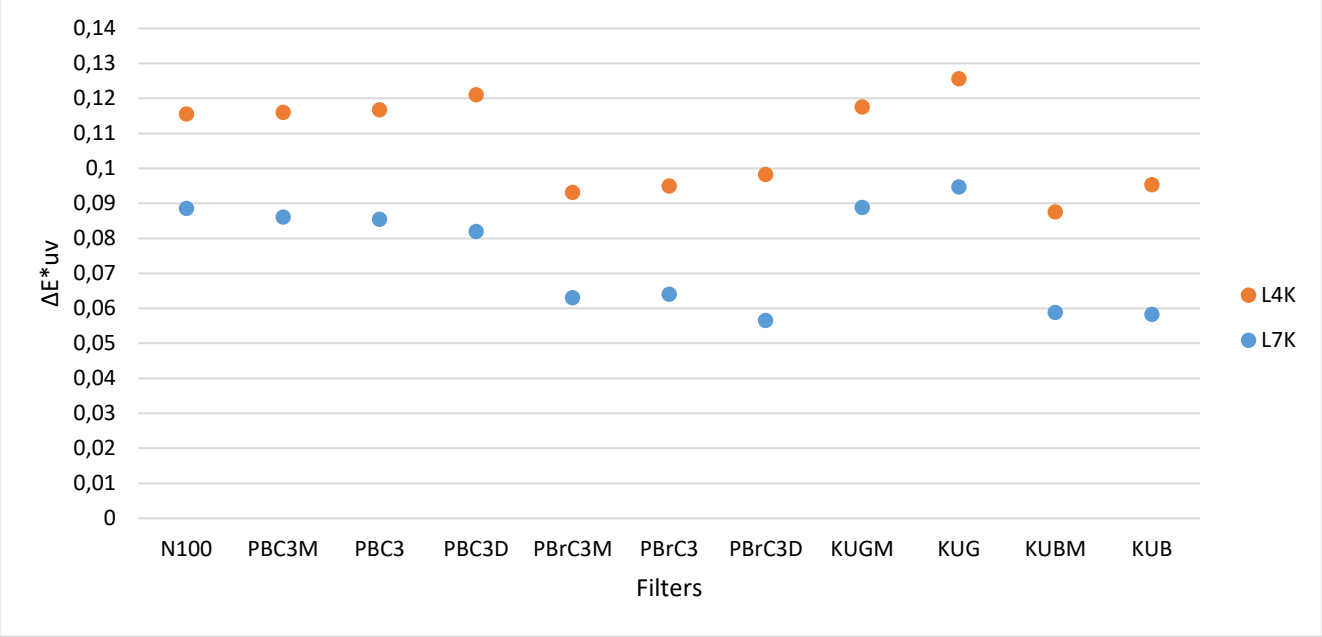

Figure 90, Δu'v' between D65 white-point and modified white-point, Experiment 3

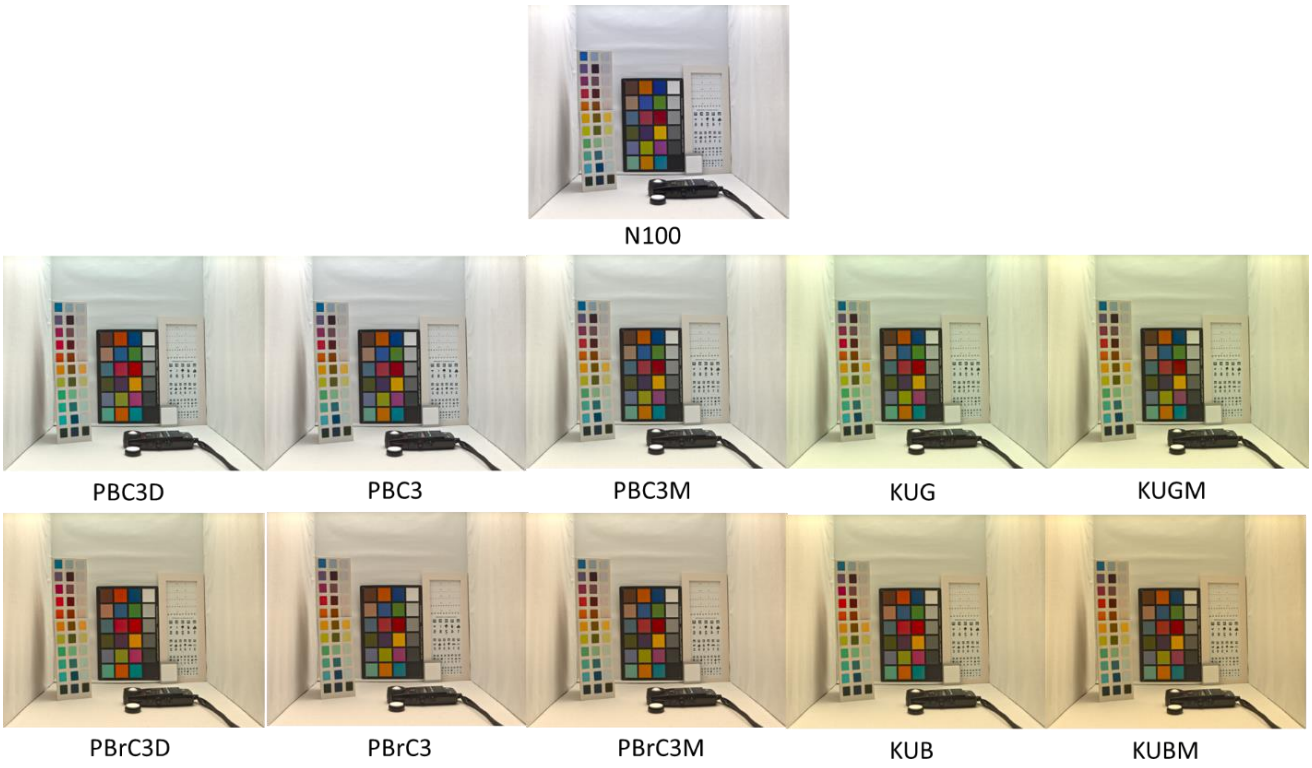

Figure 91, Images for simulated filters under L7K with default iCAM06 (D=0,3): Experiment 3

b) Evaluation Method

The protocol of the experiment remained the same as in the previous experiment (Experiment 2). The observer was seated in front of the light booth and the EIZO screen, separated by a cardboard covered with a black cloth, see Figure 92.

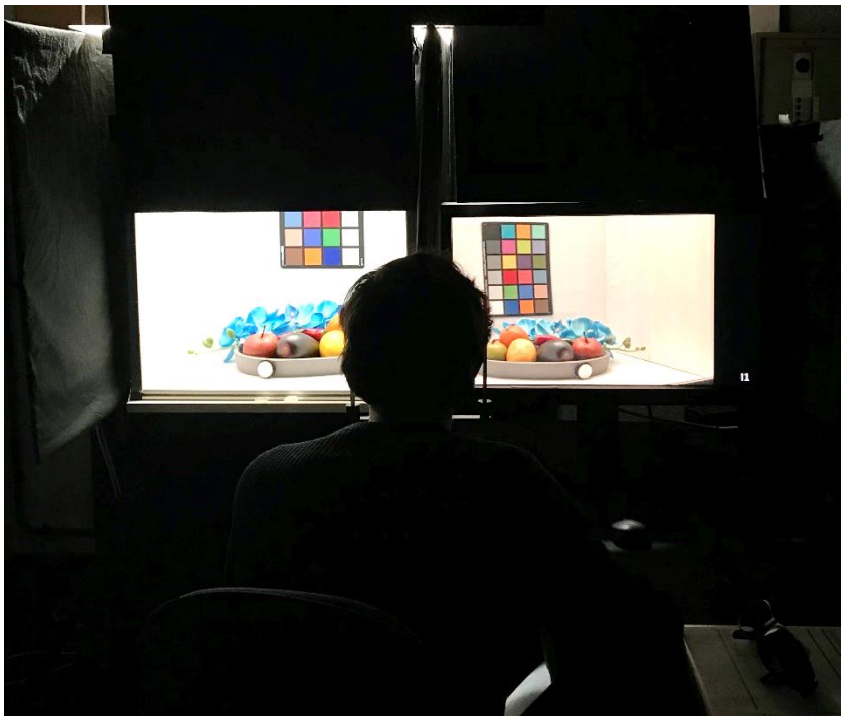

Figure 92, Experimental setup with an observer

Before the experiment began, a dark adaptation was done for 5 minutes followed by a reading of precise and written oral instructions. The sequence of the filter presentation was the same for all observers, while the first light source (L4K or L7K) depended on the parity of their serial number. Even numbered participants started the experiment with L4K while odd numbered participants started with L7K. The observers had 2 minutes of chromatic adaptation in front of the first of the four images, before visualizing the three others on PowerPoint. They had no limit of time to compare the four images with the real scene by the combined method of ranking and rating.

5.3.8. Results

The rating results for the 34 observers were grouped in a single table and a factorial ANOVA was conducted on them. Every rating score had four independent variables, namely the SPD, Filter, White point (WP) and the adapting D-value (D). The ANOVA results show that these four variables combined together, impact the rating score **significantly** ($F(10, 65{,}6)=3{,}12$, $p=,001$). Since a significance was found at the highest interaction level (all four variables), the lower interaction levels were not studied. To identify the pattern in which these groups of variables impact the rating results, a Tukey's HSD post-hoc test was conducted on the ANOVA. The ANOVA results are reported graphically in Figure 93 where ratings for the different D-values are compared for fixed white points, and Figure 94, where the ratings for the different white points are compared for fixed D-values. An asterisk (*) indicates that the difference between the two ratings is significant as per the post-hoc test.

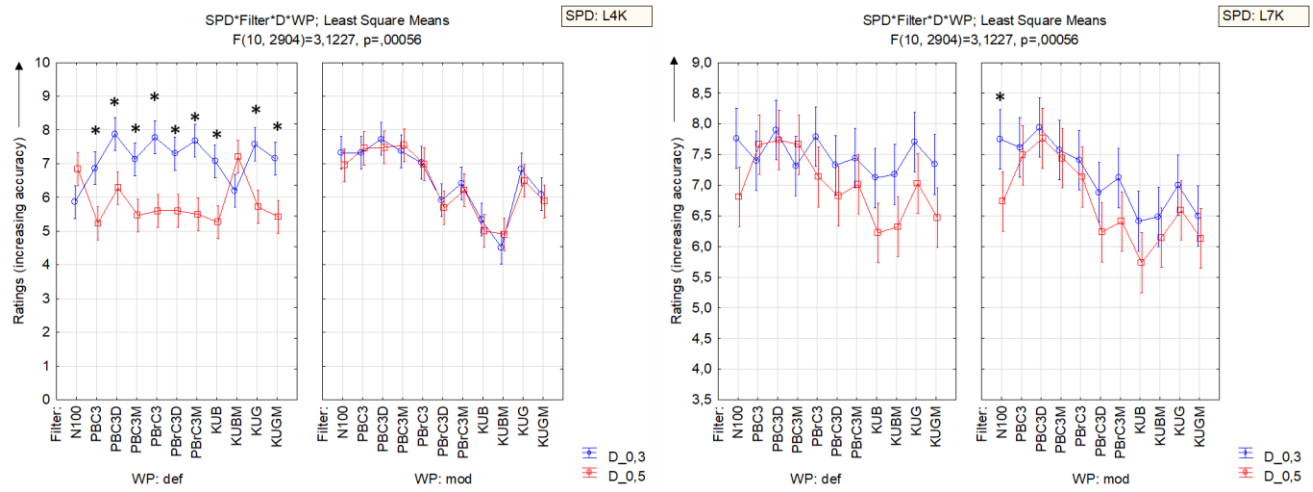

Figure 93, Average ratings for fixed white-points compared against changing D-values (Error bars represent 95% CI)

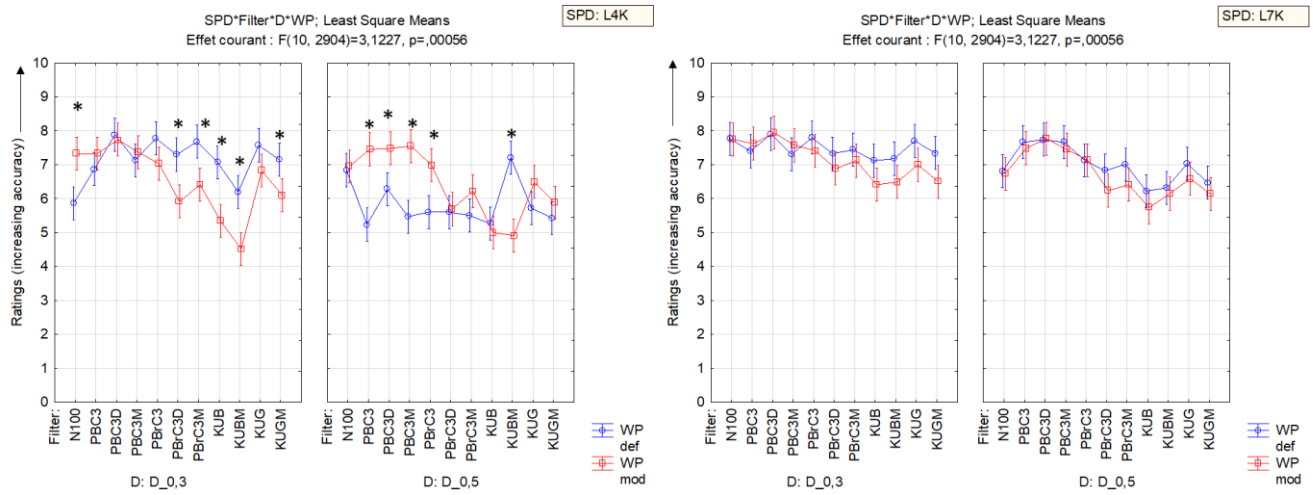

Figure 94, Average ratings for fixed D-values compared against changing white points (Error bars represent 95% CI)

The post-hoc analysis shows that different light sources and filters behave differently for different combinations of white points and D-values. These differences are explained in the following paragraphs.

Under the SPD L4K, a significant impact of the choice of D value is seen which is interdependent on the choice of white-point. When using the default white-point of D65, D=0,3 produces images that are either rated significantly higher than D=0,5 or at least the same. When using a modified white-point, no difference is obtained in ratings, see Figure 93.

When we look at the results from the point of view of white-point, see Figure 94, brown tinted filters with an exception of PBrC3 (i.e. **PBrC3M**, **PBrC3D**, **KUB** and **KUBM**) are reproduced more accurately with the default white point with D=0.3. The Black/Grey filters do not have any significant difference in ratings except for **KUGM**, which is reproduced better with the default white-point. The unfiltered scene is reproduced significantly better with a modified white point.

When the same scene is rendered with a D=0.5, the trend is no longer the same. With the exception of **PBrC3** (which is reproduced better with the modified white-point) none of the other Brown filters has significantly different ratings irrespective of the white-point choice. The Black/Grey filters produce significant differences for **PBC3**, **PBC3M** and **PBC3D** having improved ratings for modified white point, while KUG13 and KUG13M have no significant differences for any white point.

The SPD L7K produces consistently similar results for different white points and D-values. The only significant differences produced were for the unfiltered (**N100**) scene, where the modified white point with D=0.3 produced improved results compared to D=0.5. Though when comparing for a fixed D-value, the changing white points do not produce significantly different results.

A clear effect of SPD can be seen from the graph on the left to one on the right for both of the above figures. Indeed, the average ratings were significantly impacted by SPD ($F(1,2904)=129,3$, $p=0,0$*). It can be said that filter simulation with L4K gives significantly inferior results than L7K. For very warm light sources (similar to a combination of L4K and filters), a modified white-point can significantly improve results when a higher degree of adaptation D is used (D=0,5 in our case).

To further study the impact of filters that vary the CCT significantly, a correlation coefficient was calculated between the CCTs of the SPD-Filter combination and the respective ratings obtained (separately for L4K and L7K). An impact of the overall CCT of filter and SPD is present in the obtained results, and is shown in Figure 95. Filter and SPD combinations with a higher CCT have a **significantly** higher color reproduction accuracy for L4K (coefficient of correlation=0,71; p-value=0,036), which is even more **significant** for L7K (coefficient of correlation=0,78; p-value=0,004). This explains why we have poor ratings even with L7K for various color enhancing filters that have a CCT $<$ 4000K.

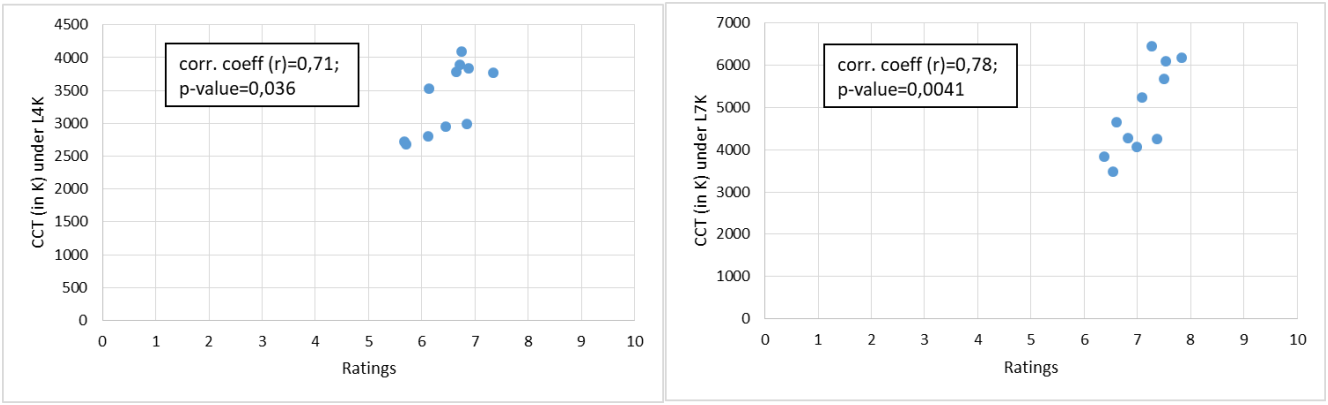

*Figure 95, Correlation between CCTs of SPD*Filter combination and mean ratings for L4K (left) and L7K (right)*

These results on L4K (and previously on L3K) enabled us to characterize the limits of simulating sunglasses in warm light sources that are mostly present in indoor scenes. They have shown that filtered images have a relatively lower color precision for warm light sources as compared to cold light sources. It can be said that iCAM06 is relatively less precise for color reproduction for CCT<4000 K. Since sunglasses are predominantly worn in outdoor settings (under daylight), the rest of the analysis (and future experiments) will focus on L7K simulations, that corresponds closely to daylight.

5.3.9. Further analysis on L7K and conclusion

The average ratings for the filters for the cold light source L7K, across all the modifications, are shown in Figure 96. Clearly, a significant effect of filter choice is visible on the average color reproduction accuracy ratings.

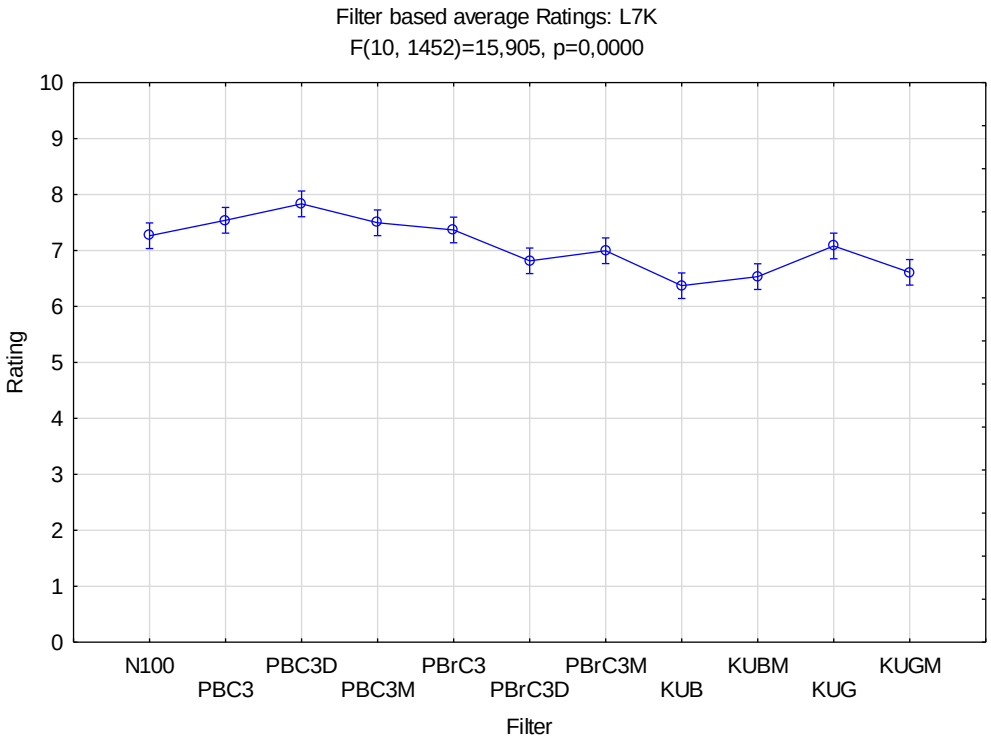

Figure 96, Average filter wise ratings for L7K

The above results were grouped based on their chromaticity coordinates. The chromaticity coordinates of all the filters under L7K are shown in Figure 97 (left) with the elliptical Venn diagrams representing filter groups that do not have significant differences among them Figure 97 (right).

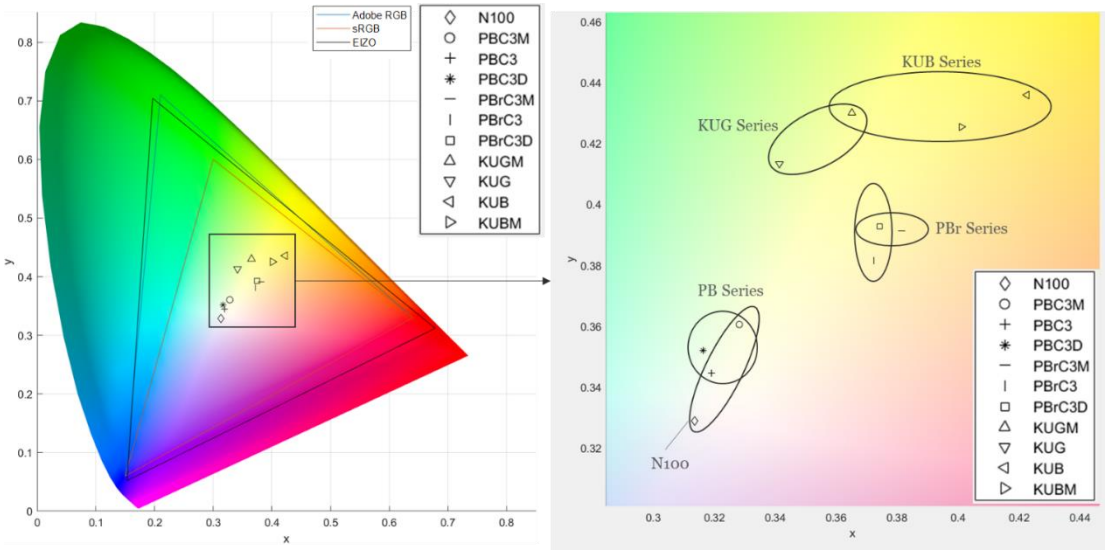

Figure 97, Chromaticity coordinates for all filters under L7K (left) and similar color reproduction accuracy-based Venn diagrams (right)

Among the following groups: PBC3/PBC3M/PBC3D; PBrC3/PBrC3M/PBrC3D; KUG/KUGM and KUB/KUBM, only the group of PBrC3 has a significant difference within the group. PBrC3 has a significantly higher average rating (mean=7,25) than PBrC3D (mean=6,7) though no significant difference is observed in PBrC3D/PBrC3M or PBrC3/PBrC3M.

To further understand the impact of iCAM06 on different filters, the chromaticity coordinates of six colored objects in the scene were plotted on the CIE xy chromaticity diagram for every major component of iCAM06. They were: xy from raw XYZ--> xy post chromatic adaptation-->xy post color space application-->xy final output, see section 2.6. The fixed parameters were D=0,3 and WP=D65, see Figure 98. The chromaticity diagrams correspond to the Red, Green, Blue, Yellow, Orange and White patches as seen under the L7K light source for the unfiltered scene (N100) and two filters (KUB and PBC3).

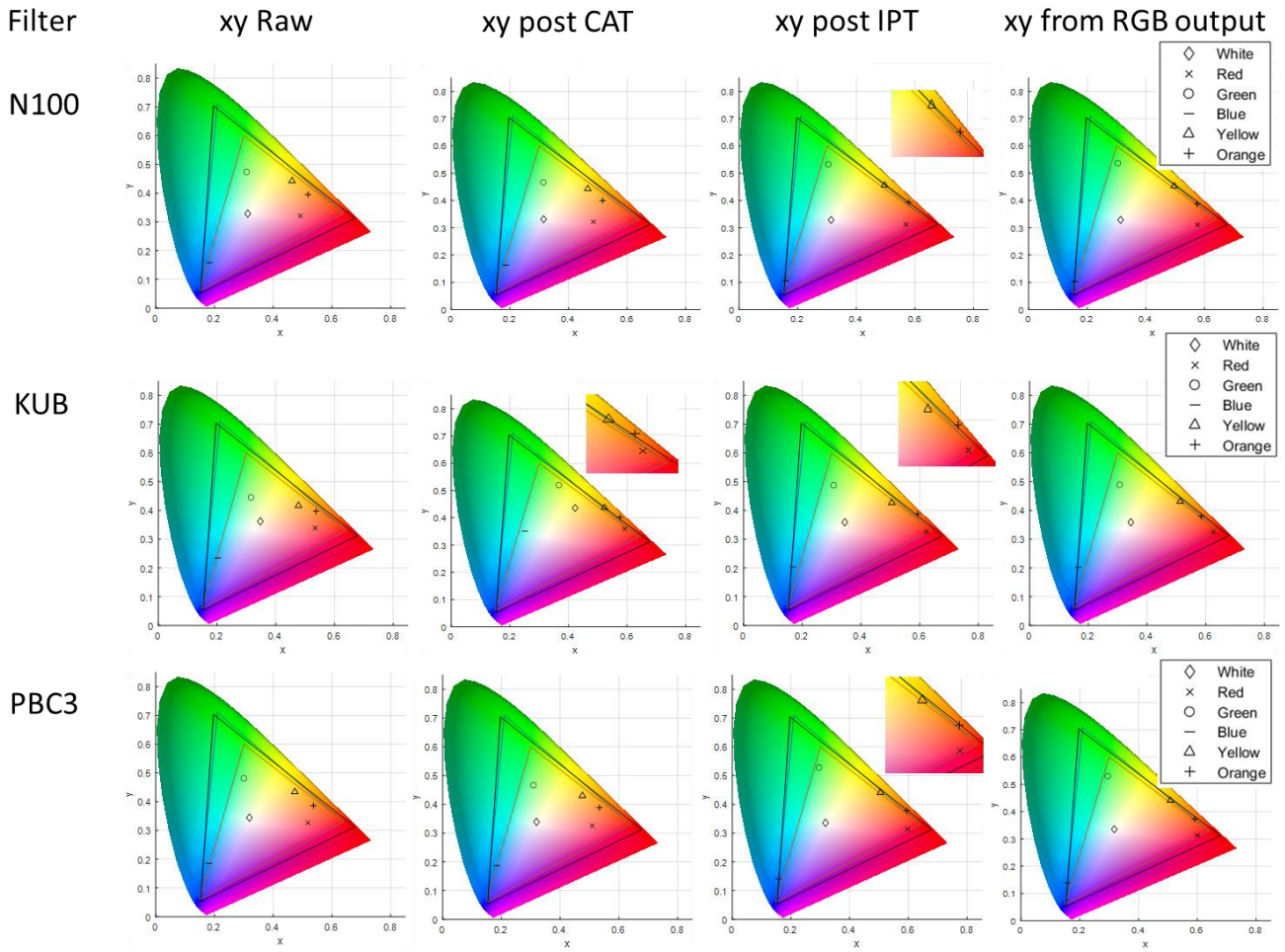

Figure 98, Evolution of chromaticity diagrams at different steps of iCAM06 for Red/Green/Yellow/Blue/Orange and White colored patches

These diagrams show that it is the application of the IPT color space (or CAT+IPT for KUB) that saturates the colors and shifts them on the peripheries of the gamut and not just for filters but for unfiltered images as well. Since iCAM06 doesn't have a gamut mapping algorithm, the colors which were outside the color gamut seems to have been clipped back inside to fit in the gamut. This further explains why certain color enhancing glasses (KUB, KUBM, KUG and KUGM) have comparatively lower average ratings when compared to classic glasses as apparently both IPT and CAT02 render the colors out of gamut for KUB.

The choice of the degree of chromatic adaptation in iCAM06 (D=0,3) seems to be well supported by the results of the experiment. It was important to study various D-values (0,9-0,7-0,5 and 0,3), since the only varying input in the calculation of the D-value is the luminance of the adapting white, see section 2.5. This value is also generally fixed at 20% of 100 cd/m^2. This leaves less room of optimization for filtered vision, where not only luminance but chromaticity is also an important factor.

In general, the use of a lower D-value of 0,3 against a D-value of 0,5 is shown to either significantly improve the color reproduction accuracy or maintain it. The results from Experiment 3 also confirm the results from Experiment 1A and Experiment 2.

The adapting white-point helps in maintaining the color constancy of objects despite the rendered output of the filtered light source. The default white-point, i.e. D65 sometimes renders the scene appearance colder than what it might be in reality for filtered vision. A modified white-point seems to be working for only a few filters, and the reason behind that might be that the modified white-point is sometimes too far from the Planckian curve and thus the rendered scenes do not maintain the concept of color constancy (chromatic adaptation) and rather saturates the colors.

The choice of white-point, although clearer than before, is not yet final. Images with a higher degree of chromatic adaptation (D=0,5) have a better reproduction accuracy for the modified white-point. Even though this experiment confirmed the choice of D=0,3 to be the optimum solution, further testing is still needed regarding the choice of white-point. Especially on highly chromatic sunglasses (red-green-blue etc.) and color enhancing sunglasses (KUB, KUG etc.) which are outside the sphere of classic sunglasses, perhaps with a WP that is closer to D65 then the modified WP.

5.4. Retrofitting iCAM06: non-linear CATs and modified white points

The observations resulting from Figure 98 are even more interesting from the point of view of highly chromatic sunglasses. If the application of iCAM06 saturates the colors for the not so chromatic sunglasses tested till now, the effect on highly chromatic glasses could be even more pronounced. With the current fashion trends, colorful sunglasses are more and more present on the market. Apart from the fashion perspective, chromatic sunglasses also find a place in the sports field where such sunglasses improve the object recognition of the wearer by improving the contrast of edges. For example, ski sunglasses have a high chromaticity in order to improve the detection of snow slopes and edges.

A recent study (Ma et al., 2019) pointed out that a modified version of CMCCAT97 was more suitable than the CIECAT02 for colored light sources (i.e. not white). The CMCCAT97 treats the L and M cones similarly to that of CIECAT02 while the S cones are modified through a power transform. This study conducted various experiments to identify the factors that could impact chromatic adaptation, and with the help of these results they proposed and evaluated three different models of chromatic adaptation based on CMCCAT97, named MA1, MA2 and MA3. The impact of colored sunglasses can be thought to be close to that of non-white light sources. In this sense, our application could also benefit from the use of a possibly improved CAT (Chromatic Adaptation Transform) for colored light sources.

Thus, the best performing model, MA3, from the three tested by Ma et al. was incorporated in iCAM06. To include a reference, the original CMCCAT97 (see section 2.5) was also incorporated in iCAM06. The MA3 model is presented below:

$$\begin{pmatrix} L_c \\ M_c \end{pmatrix} = \left[D \begin{pmatrix} \alpha & 0 \\ 0 & \beta \end{pmatrix} + 1 - D \right] \begin{pmatrix} L \\ M \end{pmatrix} \text{...(36a)}$$

$$S_c = (D\lambda + 1 - D)^p S \text{...(36b)}$$

$$p = \left(\frac{S_w}{S_{rw}}\right)^q = \left(\frac{1}{\lambda}\right)^q \text{...(36c)}$$

Where, $\alpha = \frac{L_{rw}}{L_w}$; $\beta = \frac{M_{rw}}{M_w}$ and $\lambda = \frac{S_{rw}}{S_w}$; $q = 0{,}2467$; while the subscripts w refers to the white point of the test illuminant and rw refers to the white point of the reference white source in $L, M, and\ S$ coordinates.

Apart from different chromatic adaptation transforms, the experiment continued to include the modified white-point from the previous experiments. Though this time three modified white points (WP 0-1-2) were tested, alongside D65, instead of just one effective white point of the light source and the filter (WP0). Two more white points (WP1 and WP2) were identified between D65 and WP0, which were closer to the Planckian curve than the WP0. To do this, the distance between the X and Z values of WP0 and D65 was divided by three and the two resulting intercepts became WP1 and WP2. The Y value was fixed at 100 for all the tested white-points. These intermediary white-points might prove to be a good compromise between completely white D65 and ultra-chromatic WP0. The concept can be further understood with the help of the illustrated white-points for the filter PBrC3 under the L7K light source in Figure 99.

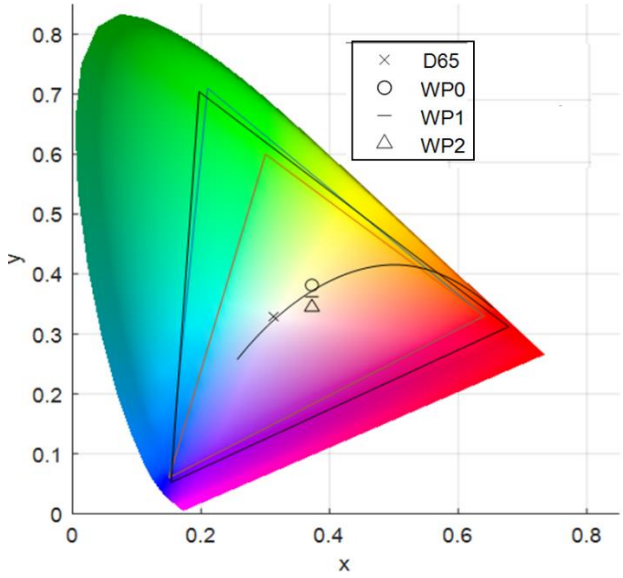

Figure 99, Illustration of different white-points

5.4.1. Research questions

- iCAM06 uses CAT02 as the chromatic adaptation transform, but is it the optimum solution for color vision simulation through filters? Can non-linear CATs (like CAT97 or modified CAT97) provide a better solution for filtered vision?

- The use of sunglasses creates a color shift, which raises questions on the use of D65 as the adapting white-point in iCAM06. Perhaps an effective white-point of light source and filter together would bring the colored vision closer to reality?

- Can the use of modified white points which are closer to the Planckian locus improve the reproduction accuracy for color vision simulation through filters?

5.4.2. Experimental methodology: Experiment 4

a) Stimuli

The experiment 4 tested two parameters, the choice of white point (WP0, WP1, WP2 and D65) and the chromatic adaptation transform (CAT02, CAT97 and MA3). Four filters tested previously were included in the experiment (PBC3D, PBrC3D, KUB and KUGM), see Figure 100. Five highly chromatic filters were added to the experiment (Red, Green, Blue, Yellow and Orange), see Figure 101. An unfiltered scene was also added for reference, thus bringing the total number of tested scenes to 10.

After a pre-test with the same protocol as the one in Experiment 3, and with 4 participants, only the WP2 (closest to the Planckian curve) and D65 were kept as part of the experiment. Though WP2 was tested only with CAT02 since the other CATs made the images too saturated. CAT97 and MA3 were thus tested with the default white-point of D65. To summarize, four iCAM06 versions were tested with the following parameters for CAT and WP: CAT02-WP2, CAT02-D65, CAT97-D65 and MA3-D65.

The scene (light booth) was the same as all the above experiments, see Figure 66, and was illuminated with the L7K light source only, see Figure 69. As explained during the analysis of Experiment 3, the previous experiments enabled us to identify the color reproduction accuracy of filtered images treated via iCAM06 for both warm and cold light sources (L3K and L7K). Since warm light sources correspond mostly to lighting in interior spaces, these experiments provided a reference accuracy of filtered indoor images. Sunglasses are mostly worn in outdoor settings and since we already have identified the reference accuracy for warm light sources, this experiment will study only the cold light source: L7K. Thus, in total, 10 filters (4+5+1) were tested under 1 light source (L7K) with 4 iCAM06 modifications (CAT02-D65, CAT97-D65,

MA3-D65 and CAT02-WP2). The chromaticity difference (Δu'v') between WP2 and D65 is shown in Figure 102, the chromaticity difference between WP0 and D65 is also visualized for reference purposes. Table 19 contains the colorimetric values and the reference white-points (WP0 and WP2) of every tested filter under L7K. Every modified version of iCAM06 was tested for objective color differences with the default iCAM06 (WP=D65 and CAT02), one such example of the maximum and minimum color difference is shown in Figure 103.

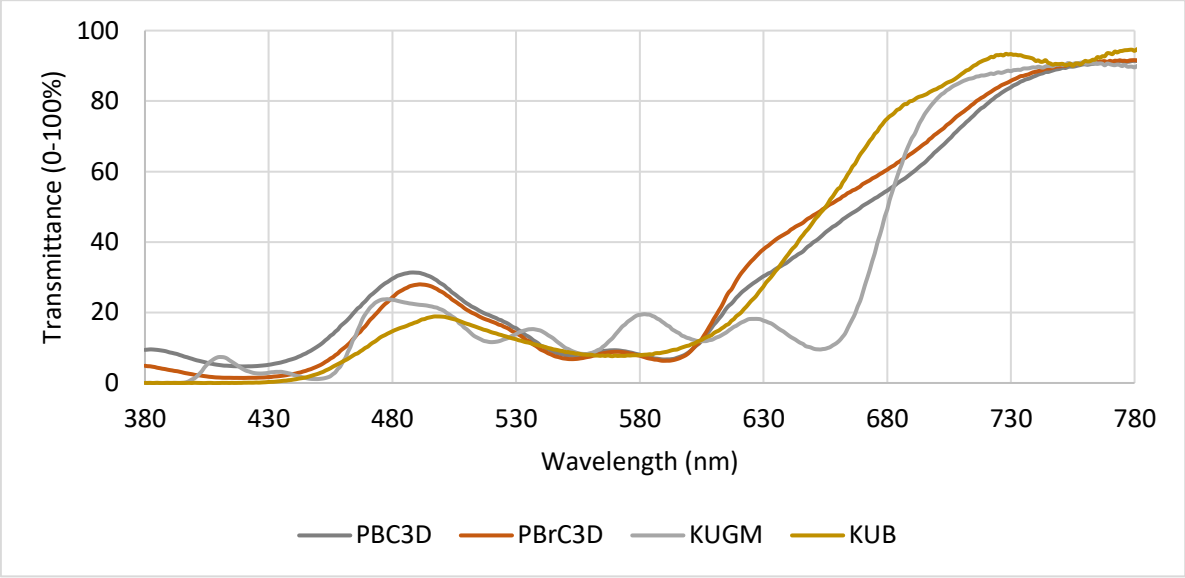

Figure 100, Tested Classic filters

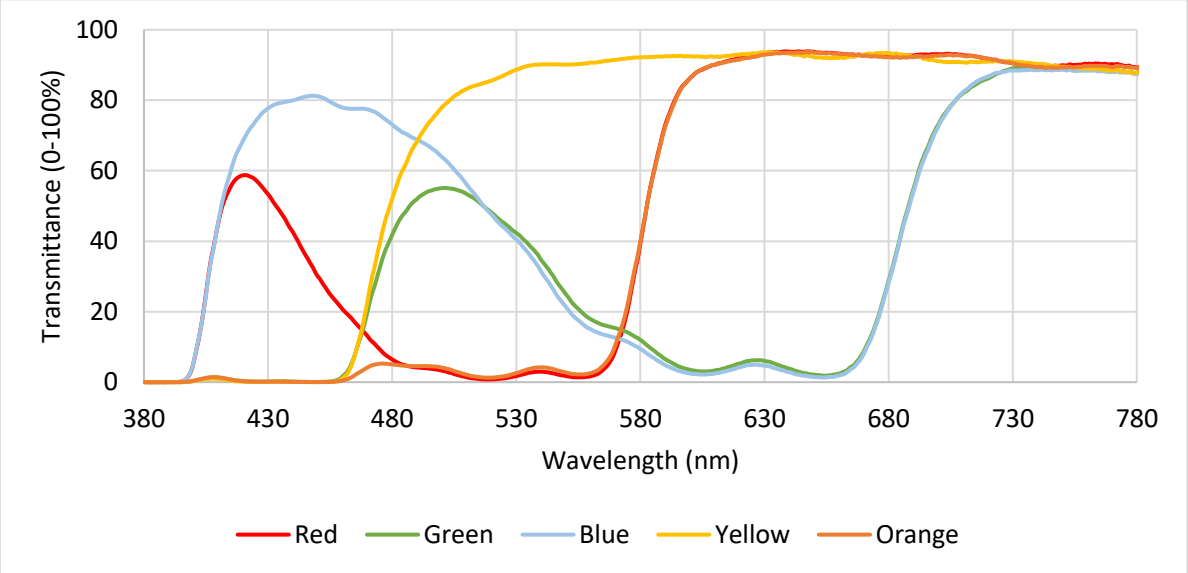

Figure 101, Tested Chromatic filters

Table 19, Colorimetric values for L7K and the tested filters, Experiment 4

Filter	X	Y	Z	X_wp2	Y_wp2	Z_wp2	x	y	Luminance (cd/m²)	CCT
N100	95	100	109	95	100	109	0,3135	0,3289	230	6464
KUGM	85	100	48	92	100	89	0,3652	0,4301	32	4657
KUB	94	100	41	95	100	86	0,4010	0,4254	29	3836
PBC3D	90	100	94	93	100	104	0,3164	0,3521	35	6192
PBrC3D	95	100	59	95	100	92	0,3742	0,3929	33	4272

Red	187	100	125	126	100	114	0,4534	0,2424	59	2671
Blue	76	100	288	89	100	169	0,1640	0,2153	68	241631
Green	39	100	31	76	100	83	0,2301	0,5886	58	7479
Yellow	86	100	12	92	100	77	0,4332	0,5065	192	3704
Orange	171	100	4	120	100	74	0,6216	0,3634	57	1820

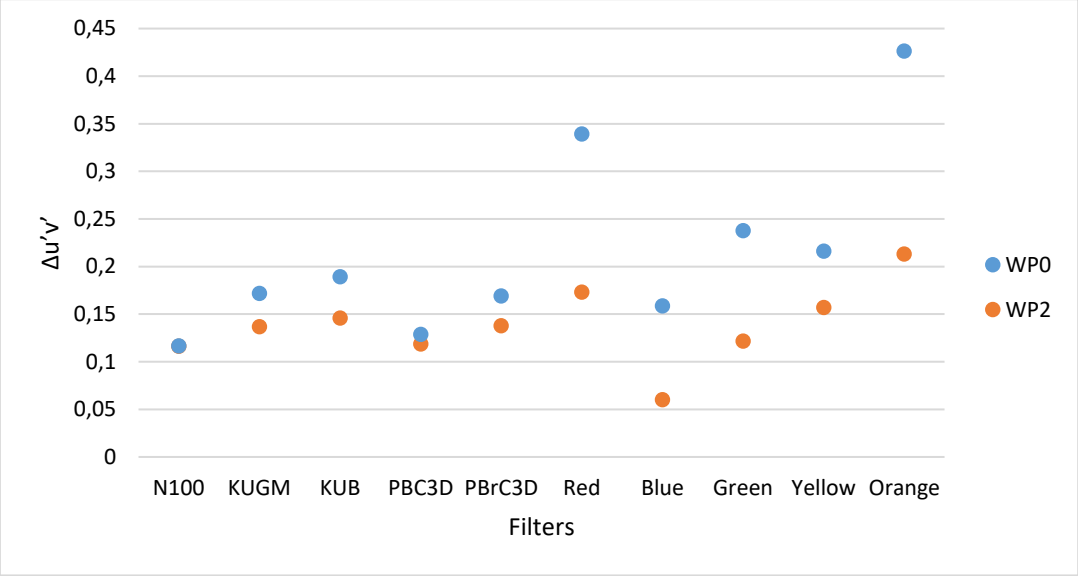

Figure 102, Δu'v between WPs': D65 vs WP0 and WP2, Experiment 4

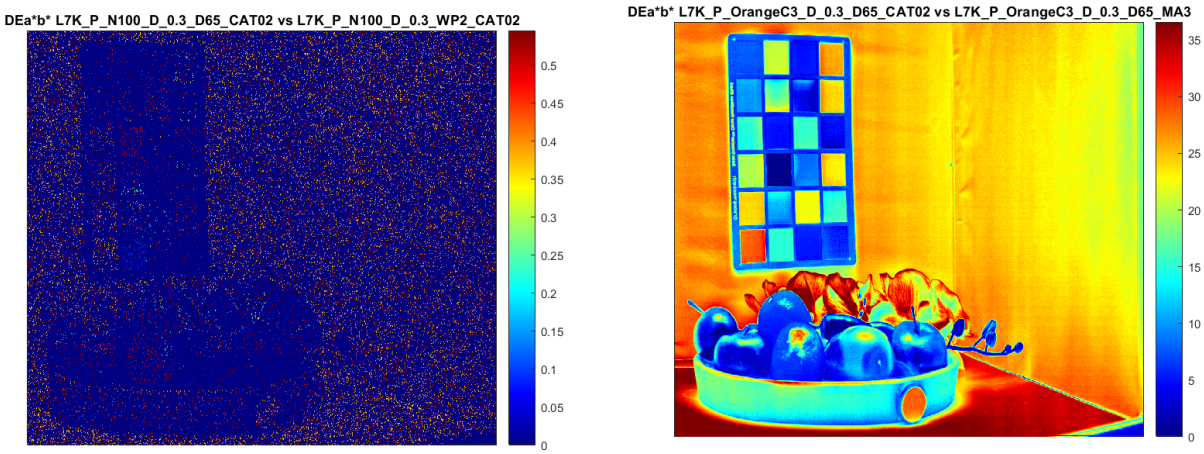

*Figure 103, Min ΔE*ab: L7K with N100: CAT02 with default WP vs CAT02 with WP2 (left) and Max ΔE*ab: L7K with Orange: CAT02 with default WP vs CAT97 with default WP (right)*

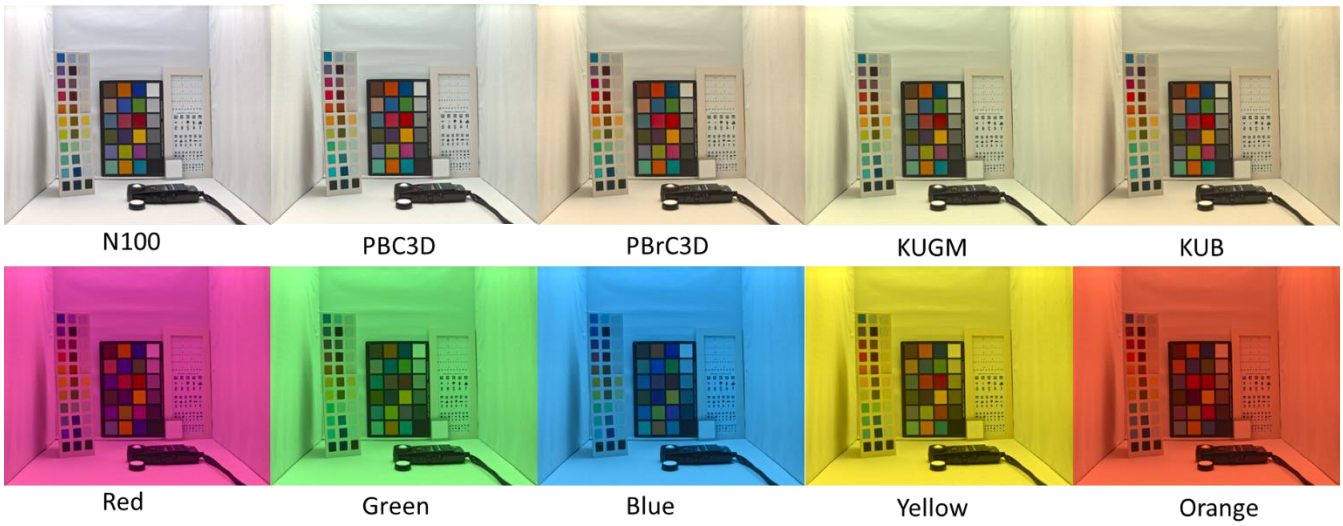

Figure 104, Images for filters simulated under L7K with default iCAM06 (D=0,3): Experiment 4

b) Evaluation Method

The evaluation method remained similar to the previous experiments. The observers did a 5-minute dark adaptation, and every time a filter was changed, a 2-minute chromatic adaptation was completed. A total of 20 observers (11 female, 9 male, age $\in$ (19,58)) participated to the experiment which lasted about 1 hour. Half of the observers started the experiment with the chromatic filters while the other half started with the classic filters. For each filter, the observers were asked to:

1. Rank the four images in a descending order in the Microsoft PowerPoint document (best to worst) as per the observed accuracy ("fidélité" in French) of the image's global color reproduction.

2. Once ranked, assign a score between 0-10 for each image's global color reproduction.

5.4.3. Results

A factorial ANOVA was conducted on the experimental data obtained from the 20 observers. A significance was obtained for the combination of the two variables tested (10 Filters and 4 Mods). The ANOVA results for Filters x Mod was $F(27,759)=4,59$, $p=0,00$*. A Tukey's HSD post hoc test was performed on the ANOVA results to identify the modifications that brought significant differences in the average ratings of the observers. The ANOVA results are shown graphically for the classic filters in Figure 105 and for chromatic filters in Figure 106, with an asterisk indicating significance as per the post-hoc results.

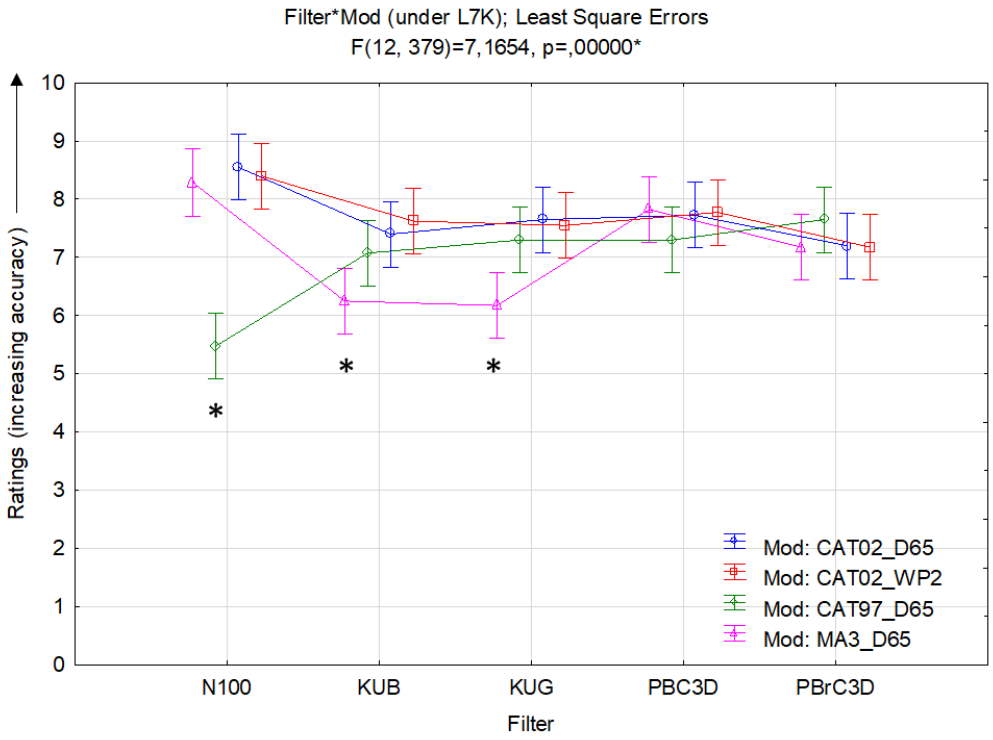

Figure 105, ANOVA results for classic filters

Figure 106, ANOVA results for chromatic filters

In the case of classic filters, most of the time, no modification had any significant difference on the average ratings per filter. For KUB and KUG the modification MA3-D65 of CAT97 was rated significantly lower than CAT02 (for either WP2 or D65). In the case of N100, the use of CAT97-D65 produced significantly lower ratings than any other modification. For either of the classic filters, the two WPs (WP2 and D65) produced similar results, despite very different adapting WPs, see Table 19 and Figure 102. For chromatic filters,

CAT02-WP2 had significantly lower ratings for the Red filter and CAT97-D65 had significantly lower ratings for the Blue filter. The Red filter, which is more pinkish in color (see Figure 104) is the only filter which showed different results for the use of D65 and WP2. No significant differences were obtained for the three other filters. In general, the use of D65 as WP produced the most uniform results for any tested filter.

The filter-wise average ratings (see Figure 107) show a significant difference for the Orange filter (lowest rating) compared to all the other filters. N100 and PBC3D had significantly higher ratings than Red, Green and Blue filters. No other significant difference was found in average ratings among the 10 (=9 filters +1 no-filter) filters. A strong correlation was found between the CCTs of Classic filters (under L7K) and the average ratings (coefficient of correlation=0,95; p-value=0,01) while no correlation was found between the CCTs of chromatic filters and the average ratings (coefficient of correlation=0,07; p-value=0,90), see Figure 108. This further corroborates the correlation results obtained in section 5.3.8 of Experiment 3 for neutral and color enhancing filters. Chromatic filters clearly do not follow this trend.

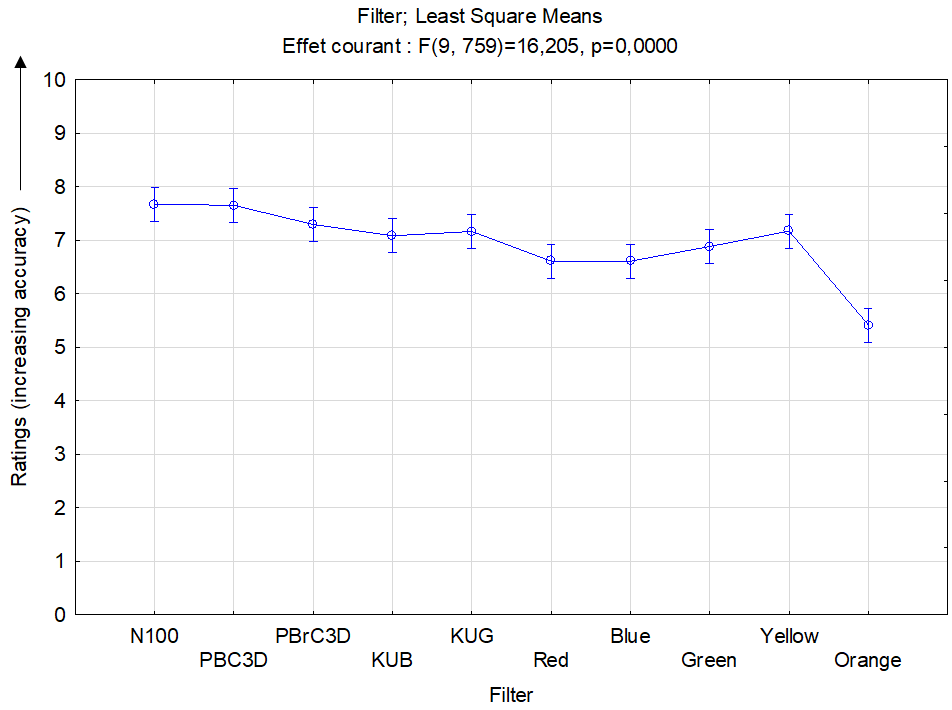

Figure 107, Average ratings for all the tested filters, Experiment 4

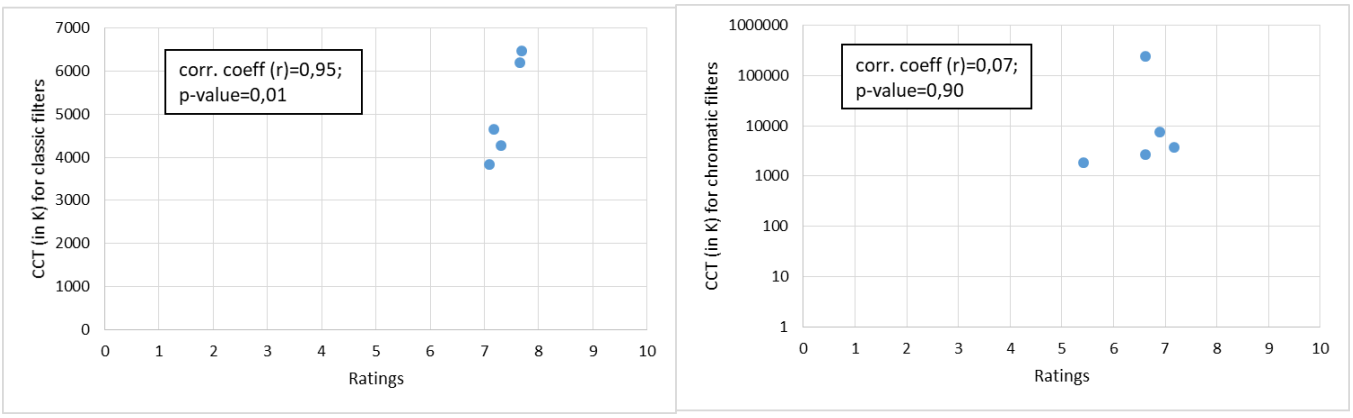

*Figure 108, Correlation between CCTs of L7K*Filter combination and mean ratings for classic filters (left) and chromatic filters (right)*

5.4.4. Conclusion

It can be concluded that the original iCAM06 with D65 as the white point either had equally good ratings as the other modifications or significantly higher. The results of the MA3 modification were surprising since this modification has been documented to improve the color reproduction for colored light sources (via color matching experiments on simple colored cubes). For the color enhancing filters (KUB and KUG) the average ratings were lowest for the MA3's modification even though these filters do not produce very strong color shifts (relative to chromatic filters). The CAT97 was shown to produce significantly lower ratings for N100 (other than the Blue filter) thus re-emphasizing the original need to use CAT02 as the CIE standard instead of CAT97. When comparing ratings obtained from D65 vs WP2 as white-point, only the Red filter produced significantly different ratings for the two WPs. This could be perhaps related to a general observation made by participants that the image with WP2, when applied to L7K combined with Red filter distorted the color of Orange and Lemon drastically (relative to other modifications). These objects were found in the center of the scene, and thus may have influenced the overall color reproduction accuracy of the scene more strongly. It is to be noted that the filter Red had a strong pinkish hue (almost magenta), and thus produced very strong reddish hues on orange and lemon, thus perhaps giving an impression of over-saturation.

To summarize, these series of experimentations have shown that the original iCAM06 has either the highest or similar color reproduction accuracy for filtered images (under the cold light source L7K), among the different modifications tested in chapter 5. The experiments established the need to use a lower value for D the degree of chromatic adaptation (=~0,3) than the CIECAT02 default value (=~0,9). It was also found that iCAM06 does not reproduce scenes similarly as per the CCT of the illuminant. Scenes lit with warm illuminants (for e.g. L3K or L4K) have a significantly lower color reproduction accuracy when compared to scenes lit with a cold illuminant (for e.g. L7K). The same goes for scenes that are reproduced with chromatic filters or filters that alter the effective 'neutral whiteness' of the scenes. The higher is the chromaticity of the filter, the lower is its average reproduction accuracy. This can be linked to the CCT for classic filters, but not for chromatic filters, which have extremely different chromaticities, even when compared with other chromatic filters. They almost approach the edges of the chromaticity diagrams (see Figure 109), and thus do not show any similar trend because of stark differences.

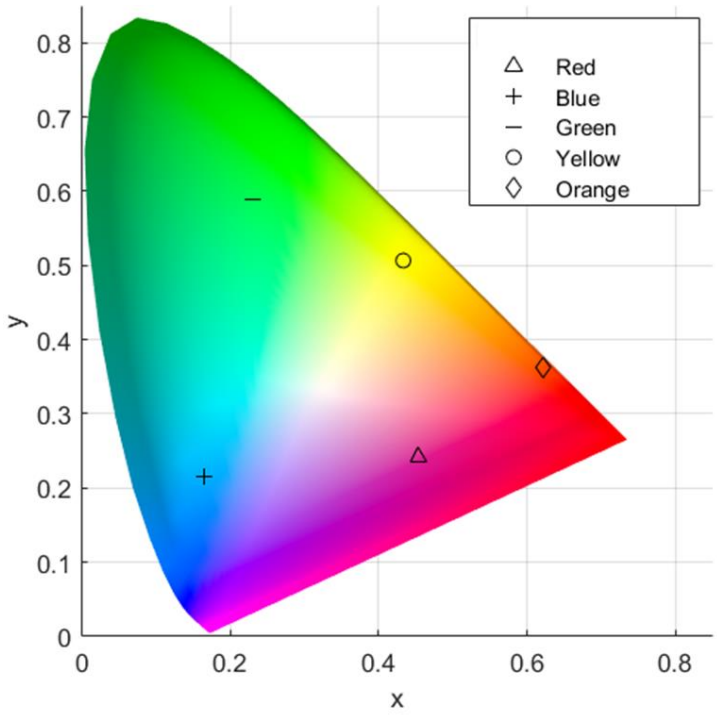

Figure 109, Chromaticity coordinates of chromatic filters

In terms of white-point, for interior scenes lit with a warm light source (L3K), when the degree of chromatic adaptation was fixed around D=0,5; the modified white point (WP Mod) produced significantly improved images. For the less warm L4K source, the images for unfiltered scene were significantly improved when using the WP mod. For the rest of the cases, the default WP of D65 produced either equally good or better images than any other tested white-point. The average ratings for the default iCAM06 coupled from all the previous experiments was found to be above 7 for any filter except the highly chromatic Orange filter. The average ratings for all the tested filters are shown in Figure 110 for classic filters and their metameric pairs (Part A) and Figure 111 for chroma-enhancement/chromatic filters (Part B). For each average rating, the number of observers (N) is also indicated in the graphs. These experiments have thus validated the use of iCAM06 for complex color vision simulation though sunglasses.

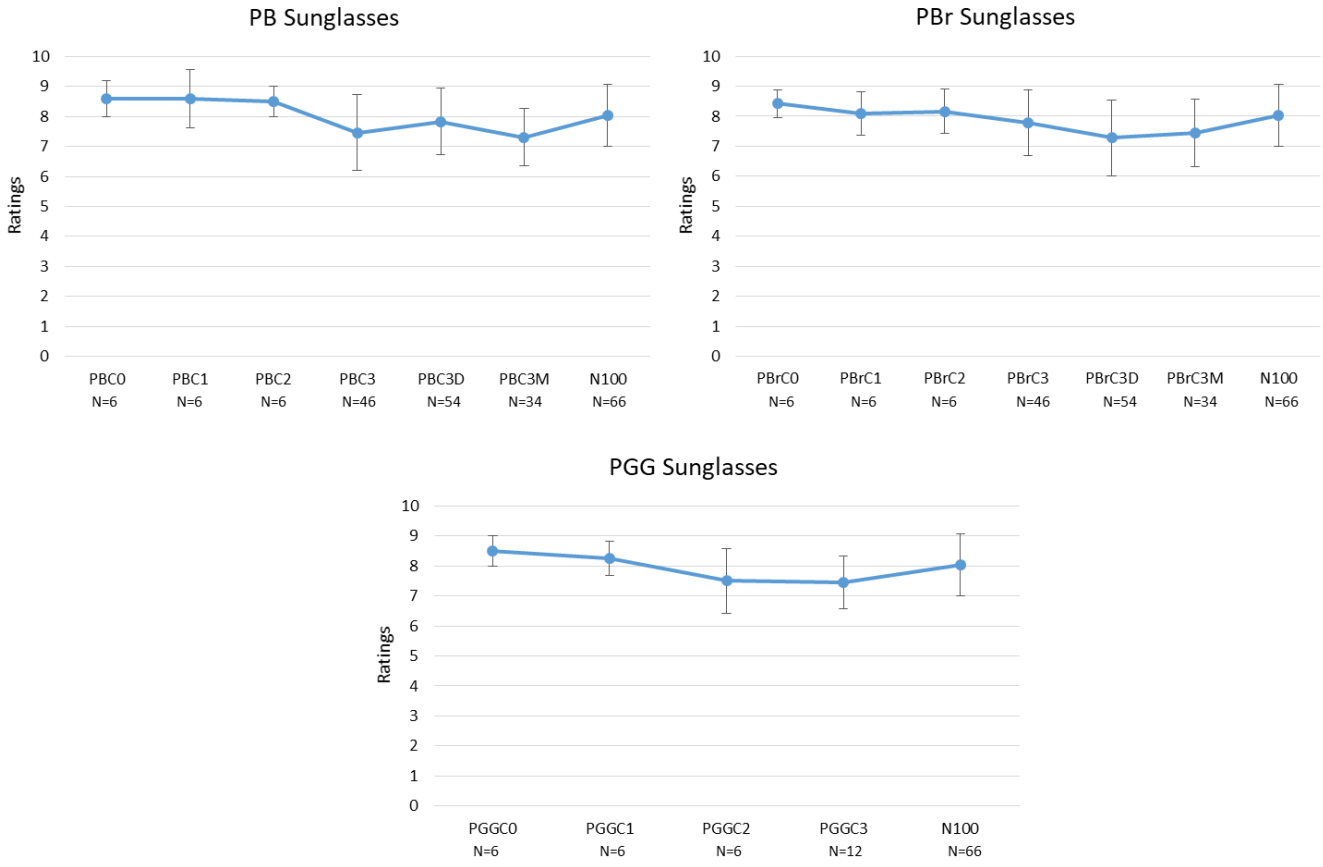

Figure 110, Average ratings for filters: Part A; with Std. Dev Errors

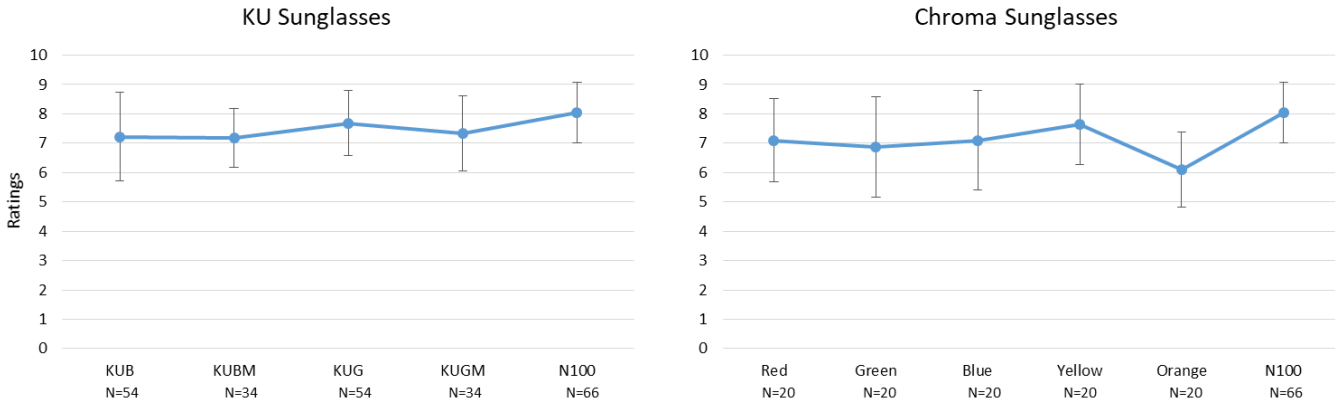

Figure 111, Average ratings for filters: Part B; with Std. Dev Errors

6. Characterization of color shift induced by sunglasses

The primary use of sunglasses is to prevent glare by reducing the amount of light transmitted to the eyes. This transmittance varies across the range of visible spectrum and can introduce important color shifts. These color shifts necessitate characterization by fast and reliable means. The simulation of sunglasses through the means of hyperspectral images and an image color appearance model (iCAM06) has been validated in chapter 5 for color reproduction accuracy. However, the objective effect of sunglasses on color vision is not easy to interpret from these simulated images. Thus, we need to characterize these color shifts through a streamlined process, providing simplified yet informative data. For this purpose, we propose to illustrate the effect of sunglasses by representing the resulting color shifts on a color graphic.

In this chapter, we will first do a literature review of certain color graphics presently used by researchers for color shift calculations of light sources. Next, we will describe a few currently existing methods to identify the color composition of a scene. Later on, we will describe a technique to automatically identify the dominant colors of the scene to enable color shift calculation. This methodology to calculate the dominant colors will be validated by a panel of observers through a psycho-visual experiment. Finally, with a working and duly validated dominant color descriptor technique, we will later describe its use as a color shift identifier with the help of a direct application on sunglasses. We will use the dominant colors of the image seen through the tinted film and compare it to the dominant colors of the original unfiltered image. The contents of this chapter were subject to one conference proceeding and two journal articles (Raza et al., 2021a, 2021b, 2020).

6.1. Literature review: Color Graphics

The use of visually illustrative tools to characterize color tone modifications has existed since the 1950s, for example to study the effects of chromatic adaptation (Sobagaki et al., 1974) and color shifts (Helson et al., 1979; Hunt, 1965). In the last ten years, such graphic tools have resurfaced, and are used more and more for color rendering characterizations. Notably, the color rendering vectors of van der Burgt et al. in the a*b* plane of CIELAB color space where color shifts are symbolized by vectors (van der Burgt & van Kemenade, 2010). It represents the color shifts of 215 color samples produced by a test source in comparison to a reference illuminant at the same Correlated Color Temperature (CCT) (Figure 112a).

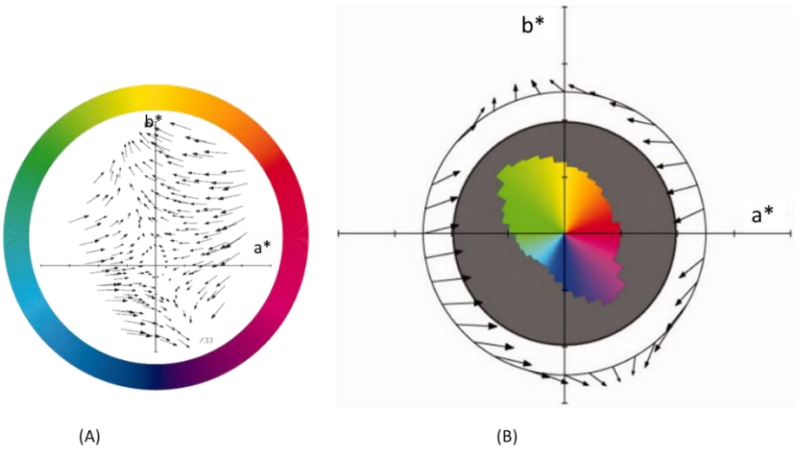

Figure 112, Color rendering vectors of van der Burgt (van der Burgt & van Kemenade, 2010)

The arrow base represents the reference color while the end point represents the modified color. The arrow-length corresponds to the magnitude of the color shift while its direction provides an estimate of the type of distortion. For example, an arrow pointing towards the origin means that the color has less chroma (with no change in hue) under the test source than under the reference. An arrowhead pointing outwards indicates the opposite. Radial deviations signify shifts in hue. Van der Burgt et al also introduced a color-rendering polar diagram (van der Burgt & van Kemenade, 2010) that provides averaged information on the color shifts in hue and relative chroma for 36 hue segments of 10 degrees each (Figure 112b). In this

graphic, the arrow-base of each vector is positioned on a circle representative of the hue under the reference illuminant with normalized values (maximum spectral radiance corresponds to 1). The significance of size, start/end-point of each arrow remains the same as in the graphic in Figure 112a.

Davis and Ohno (Davis & Ohno, 2005) continued using the CIELAB a*b* plot to represent color shifts for the 15 samples of the Color Quality Scale CQS (Figure 113a) and a color icon (Figure 113b). In their color icon, a white circle identifies the reference lighting while the colored surface shows the distorted colors due to a test lighting. A colored surface inside the white circle means a loss of chroma, a surface outside means a gain in chroma. This graphic has proved to be useful to interpret the results of scientific articles dealing with color rendition of lighting solutions (Dangol et al., 2015; Feng et al., 2017; Jost-Boissard et al., 2009b, 2015, 2016; Y. Lin et al., 2017; Wei et al., 2014).

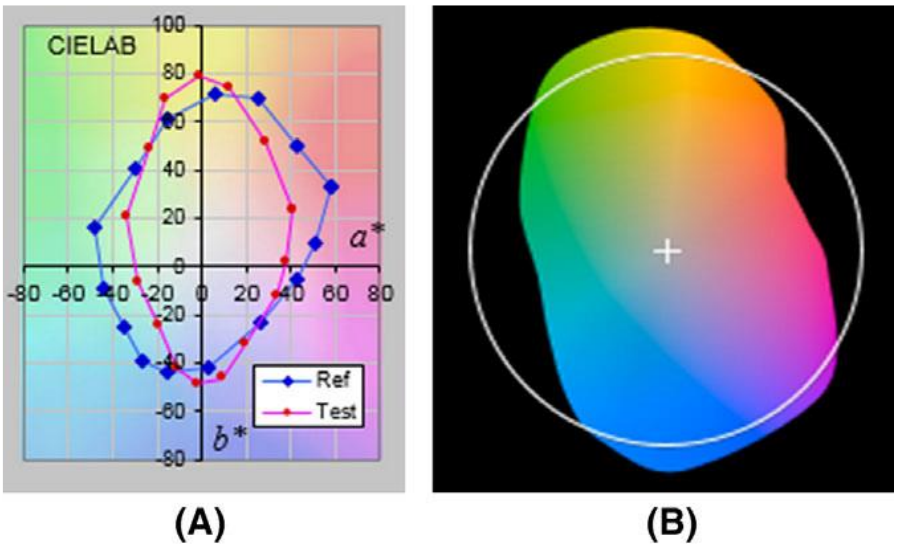

Figure 113, Color Quality Scale of Davis and Ohno (Davis & Ohno, 2005)

More recently, IES proposed a new color fidelity index to replace CIE Ra, as well as a color gamut index, and a set of graphical representations including a color vector graphic and a color distortion graphic (IES TM-30-15, 2015). The graphics in Figure 114 (a and b) show the IES color icon with the CIE F3 (fluorescent, CCT 3447 K) as a test source compared against a reference Incandescent source (CCT 3448 K). These graphs show the average color shifts of 99 samples divided into 16 hue bins (22.5 degrees each), in the a'b' plane of CAM02-UCS (M. R. Luo et al., 2006). Since their publication, they have become the reference to test the hypothesis of psychophysical experiments and to illustrate experimental results (Khanh et al., 2017; M. Royer et al., 2017; M. P. Royer, 2018; Wei, Houser, et al., 2017).

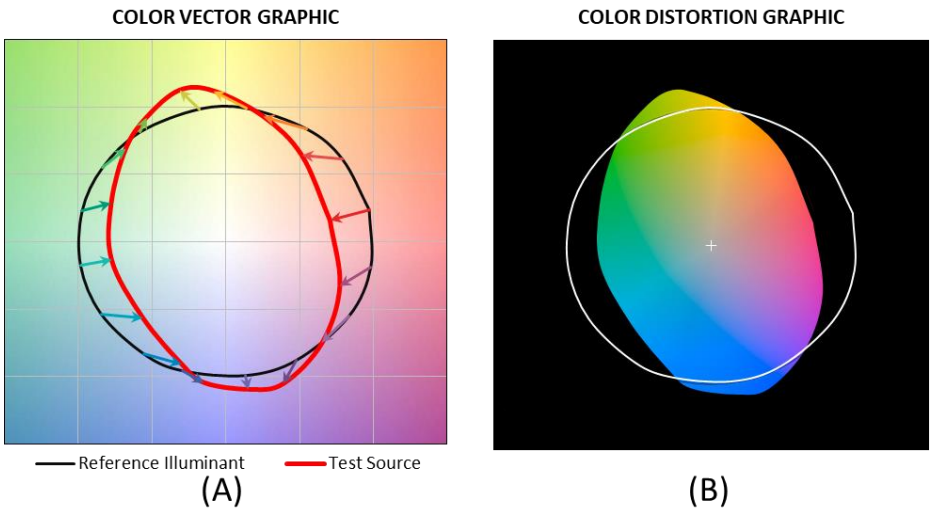

Figure 114, IES TM-30-15 color vector graphic and color icon (IES TM-30-15, 2015)

These graphics have made the characterizations more illustrative, thus easier to understand. They have been very helpful in the development of new color rendering tools. They also show the direction of the color shifts. In particular, they provide information on potential hue changes and indicate if the test source leads to a loss or gain in chroma compared to the reference one. The common point among all these color graphics is the use of predefined color patches and palettes, which provide a very extensive description of the possible color shift but does not address the color distortions due to the actual color content of the real scenes.

The color graphic (Figure 115) developed by Cauwerts and Jost follows a similar principle but addresses the actual colors present in a complex scene rather than a predefined color palette (Cauwerts & Jost-Boissard, 2018). Instead of the a*b* color plane, it uses the PT plane of the IPT color space while categorizing colors into distinct bins of six basic colors (purple, blue, green, yellow, orange and red). IPT color space is known to be homogenous and has a uniform hue representation. The color shift is identified by connecting the original reference colors with the modified color in the PT color space. Furthermore, there are histograms on the periphery of the graphic that indicate the percentage presence of pixels assigned to a particular color bin. This color graphic has an added contextualization and has shown to be effective for use in the analysis of color shift due to glazing and LED lightings (Cauwerts & Jost-Boissard, 2018).

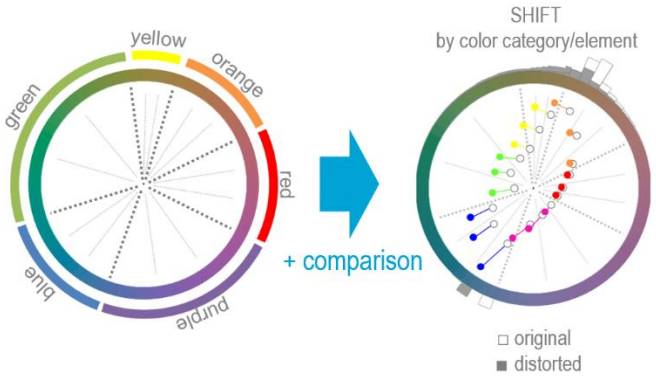

Figure 115, Cauwerts and Jost color graphic icon (Cauwerts & Jost-Boissard, 2018)

The approach of our study is to develop a color graphic that takes into account the contextualization of real scenes and the colors present in them. At the same time, to increase readability of the color graphics, this study aims to reduce the number of colors used to represent the color shifts and take in account only the

dominant colors of the real scene. This way, the color shifts will be calculated only for the most significant colors (and thus more perceptible) in the real scene. We also want to give standardized names to the retrieved colors thus increasing the comprehensibility of the graphic.

For this purpose, we aim to describe the color composition of the real scene after the application of sunglasses and image processing through iCAM06. The color composition of a scene (natural or artificial) represents the significant colors that will dictate the visual perception of the observers. The color that will dominate the visual cue of the image is the dominant color, and along with other significant colors, it forms the color composition of the image. Humans with normal color vision can easily identify the dominant colors in a scene whereas it is not such a simple task to do it computationally. The color composition of a scene is sometimes referred as its color palette, analogous to the physical color palette of artists and painters.

Many other domains benefit from the use of color palettes for different purposes. For example, in computer vision for Content Based Image Retrieval (Belongie et al., 1998; Datta et al., 2008; Gevers & Smeulders, 2000; Hui Yu et al., 2002; Jain & Vailaya, 1996; Mehtre et al., 1995; Smith & Chang, 1996), in cultural heritage management for artwork restoration (Bacci, 2006), in graphics industry for theme extraction (S. Lin & Hanrahan, 2013) and for certain image manipulations (Aksoy et al., 2017; Tan et al., 2016), and in photography and cinema for ensuring the color harmony of the scene (N. M. Kalmus, 1935).

6.2. Determining image color composition: existing methods

Numerous methods exist for determining the color composition of images, the most common being a color histogram (Gong et al., 1996; Lu et al., 1994; Sethi et al., 1997; Stricker & Orengo, 1995; Stricker & Swain, 1994; Yihong et al., 1994). A histogram is a mathematical function that counts the number of observations that fall into discrete categories (Delon et al., 2007). An image color histogram identifies the pixels in the image in terms of a probability density function of the pixel information, which are the color coordinates in a color space like RGB, HSV, XYZ etc. (Worring & Gevers, 2001).

The major issue with a histogram is the lack of complementary spatial information. In Figure 116, three different color spaces (RGB, HSV and XYZ) are used to plot the basic color histograms of a desert image. The histograms give an idea of the pixel color distribution but no clues regarding their spatial distribution, i.e. orange in the lower half and blue in the upper half. The lack of spatial information associated with pertinent color bins makes histograms less usable for complex images (Talib et al., 2013).

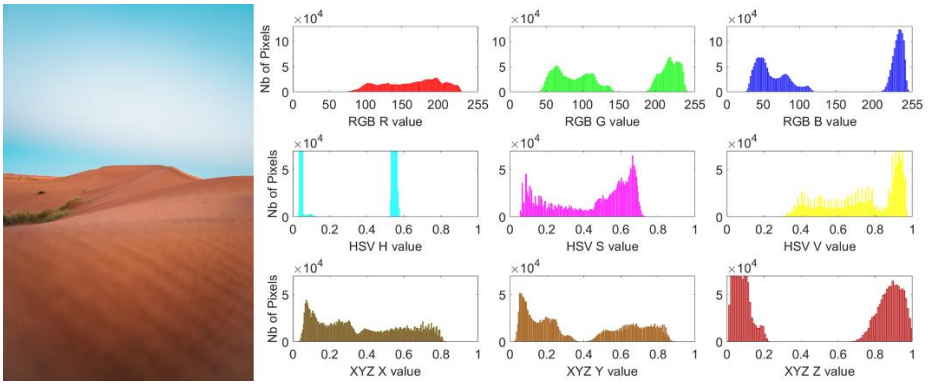

Figure 116, Image (open access) and it's RGB, HSV and XYZ color histograms

Apart from color histograms, other approaches exist for color based image description and dominant color retrieval. A brief description of a few prominent techniques is described hereafter.

Image segmentation techniques occupy a large share among other techniques to identify the image color composition. For example, region growing, in which initial 'seeds' (pixels) become a region by adding similar neighboring pixels if they clear the predetermined threshold (R. Adams & Bischof, 1994). Studies

have shown successful implementation of the region growing technique (Jianping Fan et al., 2001; Merzougui & Allaoui, 2019; Tremeau & Borel, 1997), though it suffers from a lack of global approach which poses a problem for complex scenes.

Combination of different techniques provides significant improvements in the final results by using techniques that complete each other, for example: image segmentation combined with histograms (Sural et al., 2002), or image segmentation combined with a 2-stage hierarchical artificial neural network map based on Kohonen Self organizing maps (Ong et al., 2002). The major problem with these approaches is their complexity which hinders their adaptation in different domains.

6.3. Dominant color descriptor algorithm

To identify the color composition of the scene, we decided to use image segmentation techniques. The idea was to be able to distribute the colors present in the scene into various clusters of similar colors and retrieve the dominant colors of the scene. We implemented the K-means++ algorithm for image segmentation to provide a simple but efficient color descriptor of a complex image (Arthur & Vassilvitskii, 2007).

The original K-means algorithm determines all the k seeds randomly without considering the distance between the different centroids. This sometimes leads to the initialization of far-away centroids that have no other data point, or the initialization of more than one centroid for a similar data group, leading to poor and lengthy clustering. K-means++ algorithm determines the first seed by random assignment but the rest of the seeds are carefully determined to maximize the distance between the centroids. This approach takes longer in initializing, but the clustering process has been proved to be faster than the original K-means clustering, thus globally reducing the time taken to converge the k clusters (Aubaidan, 2014).

The first step of the algorithm is to undo any gamma correction on the input image, thus the iCAM06 processed image is converted to a linear version. This linear image is further transformed into the CIELAB color space. CIELAB color space was chosen over other color spaces not only because of simple, homogeneous, and uniform color distribution but also because of the perceived effectiveness of CIELAB color differences. CIELAB color differences (ΔE^*, ΔH^* or ΔC^*) have been standardized and are easier to interpret than any other color difference calculations. The CIELAB color space requires the knowledge of the white point of the illuminant, this creates a problem for images with unknown illuminants. Various illuminant estimation methods exist that provide an approximation of the illuminant white-point from an image. The more common ones being the White Patch Retinex algorithm and the Gray world algorithm (Buchsbaum, 1980; Land, 1977). Both of the algorithms, though quite effective, are prone to large estimation errors (Hordley, 2006). Another method that exists, identifies the bright and dark pixels of the image as per their distance from the average color of the scene. It than performs Principal Component Analysis (PCA) on the bright and dark pixels. The first component of the PCA is thus the estimated illuminant. The PCA based illuminant estimation method has been shown to produce significantly better results than many other methodologies and thus was chosen to identify the illuminant white-point from an image (Cheng et al., 2014).

With the illuminant white-point, the linear RGB image is converted into a LAB image which is then treated with a low pass Gaussian filter (sigma (σ)= 8). A Gaussian blur is achieved by convolving an image with a Gaussian (bell-shaped) kernel (Mordinstov & K, 2013). The σ is the standard deviation of the distribution and controls the variance around a mean value of the Gaussian distribution. A blurring is essential for our approach to facilitate faster convergence of the K-means++ algorithm. Blurring with a relatively high sigma gives less importance to the edges and local differences and brings out the global color tendencies of the image. To visually interpret the impact of blurring and the eventual reduction in the spatial frequency of the image, a Discrete Fourier transform is applied on an image while progressively increasing the sigma. Figure 117 shows the effective reduction in the high frequency components of an image as the filter size increases (a large spread of the grey points suggests the presence of high frequency components). Thus,

frequency components below the threshold of the selected sigma are allowed to pass while the other frequencies are cut-off.

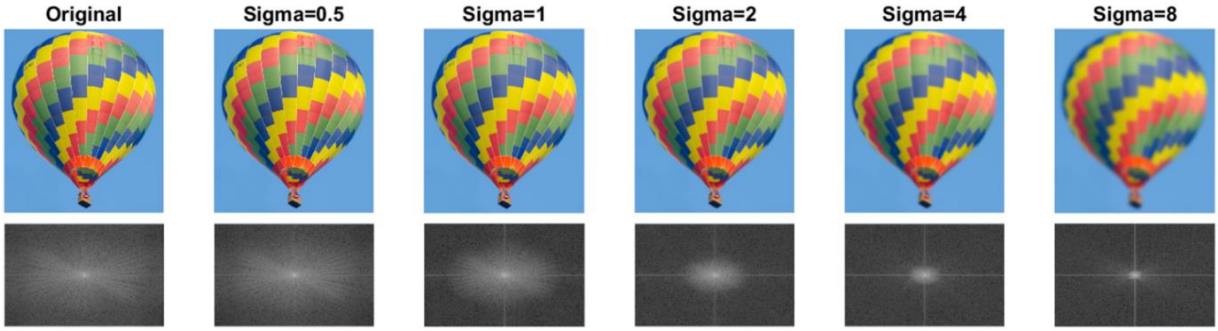

Figure 117, Gaussian blurs on the original image and their corresponding spatial frequency maps

The image is then ready for the clustering process and K-means++ with 6 initial seeds is applied on the blurred LAB image. The number of 6 seeds was determined empirically after various trials and the choice was validated a posteriori, further details can be found in section 6.6.1. The resulting 6 color clusters are used to identify the spatial location of the untouched color clusters and to calculate the pixel percentage distribution of each color cluster. A median sRGB triplet is calculated for each cluster for visualizing the color and then converted to LAB values (without any Gaussian blurring). These LAB triplets are then compared with the ISCC-NBS color palette for the closest color triplet and its name through the CIEDE2000 formula (Cobeldick, 2019; Judd & Kelly, 1939; Sharma et al., 2005). The ISCC-NBS color palette was chosen because it is a recognized standard color dictionary and it is based on the Munsell color system. It uses a three-level color naming system, where 13 basic color names form the first level, 29 intermediate color categories form a finer second level while 20 adjectives like vivid, dull, bright, moderate etc. form the finest third level. Each combination of basic color, intermediate color category complemented with adjectives for the hue and color, distinguishes between various categories of colorfulness. Since not all the adjectives are used for all the color categories, the final palette contains 267 distinct color names. Once the 6 color names are identified, they are checked for redundancy, i.e. whether color names appear more than once. This can happen in images which have an abundance of a particular hue, and thus lead to less than six actual clusters. The repeating clusters, if any, are merged to form a new cluster and the proportion of color distribution is updated. The regrouping is done only for exact same colors and not for colors that are close to each other. Most of the time, the application of sunglasses modifies a color without completely changing it, these enhancements will be ignored if similar colors are also regrouped. Figure 118 summarizes the entire process in a flowchart.

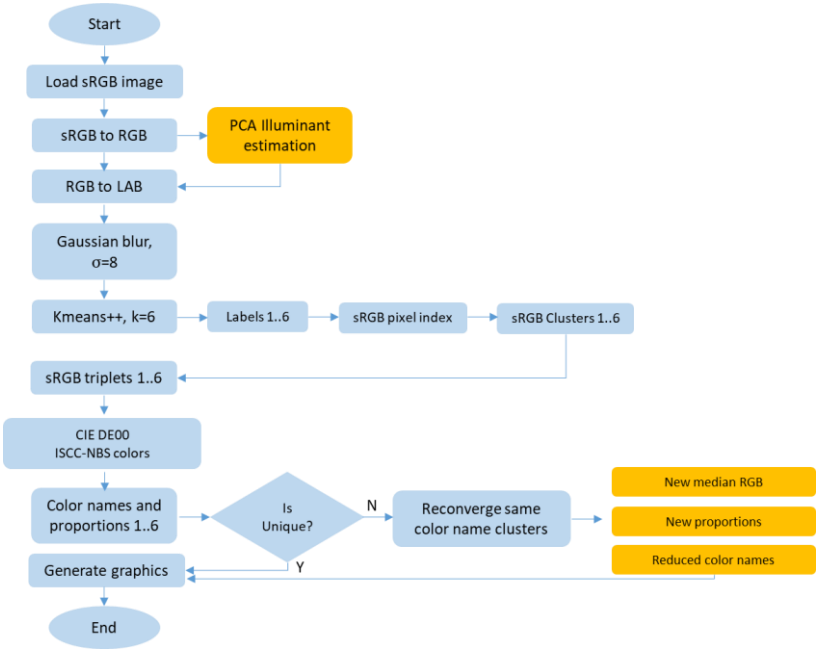

Figure 118, Flowchart of the dominant color descriptor algorithm

As output, the program gives 1) a labelled image per each color cluster, 2) a bar plot with the color names and proportions, 3) a CIE a*b* plot with color proportions and an MS Excel file with the CIELAB values, the color names and their proportions, see Figure 119.

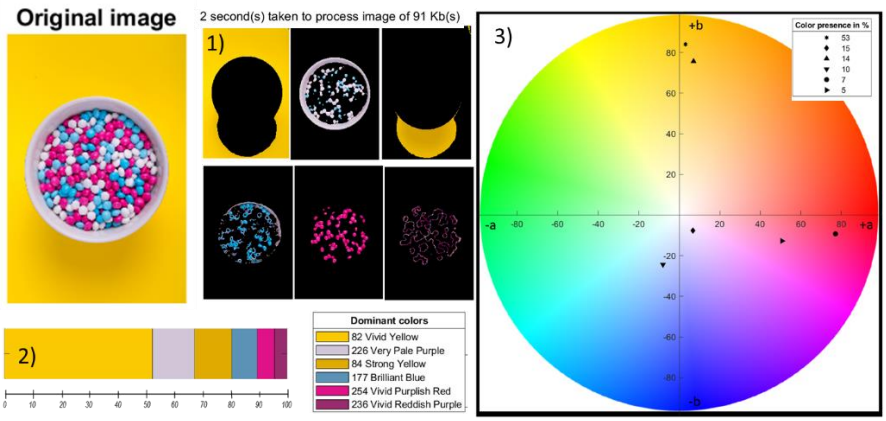

*Figure 119, Results: Dominant color descriptor algorithm and CIE a*b* chromaticity plot*

6.4. Validation

The validation process involved testing the resulting color palette for a visual coherence with the image, on a dataset of test images. This task was first performed by the author individually on a large dataset and was followed by a similar validation with the help of a panel of observers through a psycho-visual experiment on a smaller dataset.

The dominant color descriptor algorithm was tested on 50 open source no attribution required photos, and 50 photos from our own database. Figure 120 shows the color distribution obtained through our method on a few indoor/outdoor images which seem to be in harmony with the images. No impact of the source of the database was noticed, the results were in equal harmony for open source images and the author's dataset. Since the initial validation was positive, the next step was to validate the color palette through psycho-visual experimentation.

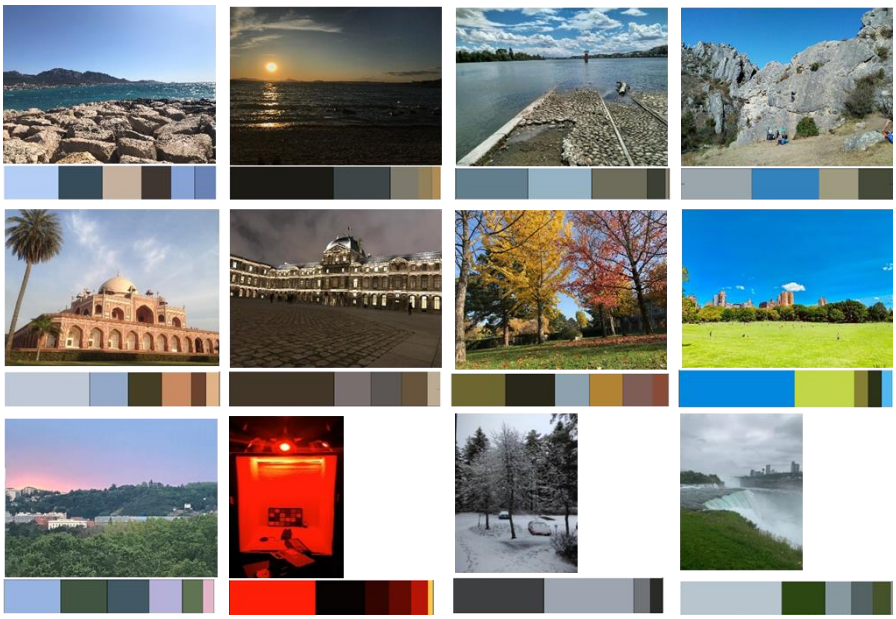

Figure 120, Results from the dominant color descriptor algorithm on various images

6.4.1. Experimental procedure

To further validate the results in terms of visual perception, the experimental data (observer responses) from a previously conducted psycho-visual experiment were retrieved (Cauwerts & Jost-Boissard, 2018). In this experiment, six images (five natural and one urban scene, Figure 121) were presented in a dark room, on a color calibrated monitor (EIZO ColorEdge CG277) in a controlled Latin square sequence. These images were acquired with the Specim V10E and converted in 2D via iCAM06 (*pval*=0,75; *gval*=1,5; F=1; D=0,9). The participants were asked to name the dominant colors in each image and list their proportions in order. They were further asked to allocate each color to a specific color category: Red, Green, Blue (historical primary colors), Purple, Yellow, Orange (associated secondary colors) and Black, White and Gray (neutral colors). The colors retrieved through our methodology were also similarly categorized. Twelve people (age ∈ [23,62]) with normal color vision, and normal-to-corrected vision participated in this experiment.

The filtered images used in this experiment (and the application in the next section) were retrieved from an already existing database, in which a D=0,9 was used for iCAM06 processing. Even though, in the section 5.4.4, a need to use a D=0,3 was established, at the same time it was also established that for cold light sources (L7K, Figure 69); D=0,9 reduced the accuracy ratings by only 1 point. Since the reduction in accuracy was not dramatic, and the usage here was only for demo purposes, the existing images were left untouched.

Figure 121, Images used for the psycho-visual experiment

6.4.2. Results

The objective and subjective results show coherence in the overall color distribution, and particularly in the dominant colors for all six images with a 93.2% correlation. Figure 122 illustrates the similarity/dissimilarity between the objective and the subjective results for each color category and image.

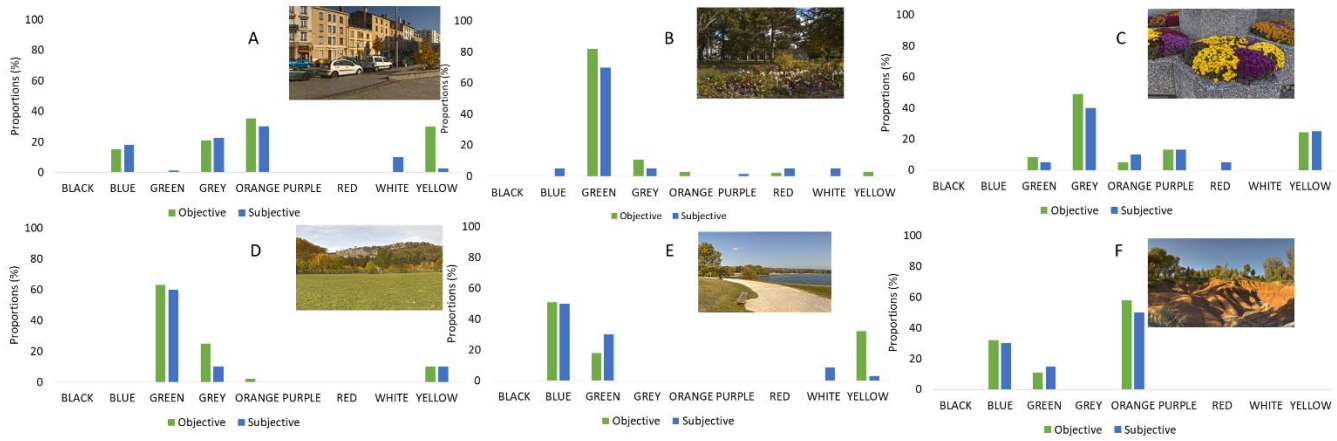

Figure 122, Objective results vs Subjective results on Color distribution of complex scenes

One inconsistency in the results is the distribution of white and yellow colors for image A and image E. The algorithm detects no pure white tones and many yellow tones. On the contrary, the subjective results obtained through the psychophysical experiment show a larger amount of white tones and less amount of yellow.

The images were treated with iCAM06, with the D-value for chromatic adaptation fixed at 0.9 for real world conditions (Smet & Hanselaer, 2015). Since the simulation of chromatic adaptation on the images was not complete, the strong sunlight was not completely discounted from the images. This leads to a yellow tint on neutral objects (white cars in image A, and the sand path in image E).

The effect of memory colors of familiar objects thus leads to the observers considering the yellowish objects as completely white (Smet et al., 2014), see Figure 123 (A) and (B). This effect is even stronger in image E, where a lot of grass is dried (and thus yellowish), see Figure 123 (C). Since grass is associated with a green color, the observers put it in the green color category. Thus, the algorithm correctly attributes the cars, the sand path and the dried grass in the yellow bin even though the participants classify them white/green.

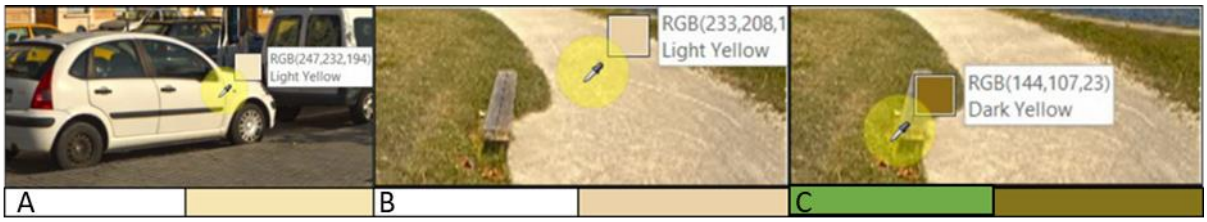

Figure 123, Actual color of the supposedly "white/green" objects in the images A and E

6.5. Application: Color shift identification due to sunglasses

Sunglasses reduce the amount of sunlight reaching the eyes with the help of low light transmission filters. But sometimes, the filters also add a colorful tint that modifies the color rendering of the external scene. This induces a shift in color perception of the original scene and thus requires a method to quantify these color shifts.

Our methodology to segment images into clusters based on their color distribution was used to calculate the hue shift and the chroma differences resulting from sunglass application. Two different sunglasses of Essilor were applied on the hyperspectral images of a day-lit urban scene, see Figure 125 (a). The spectral transmission of two colored sunglasses: KUB and PZBB (see Figure 124) were then multiplied with the hyperspectral image of the original scene to create the hyperspectral image of the scene as seen through the sunglasses. These hyperspectral images were then converted to XYZ tristimulus values and iCAM06 (*pval*=0,75; *gval*=1,5; F=1; D=0,9) was applied to render a 2D simulation of the original and tinted scenes, Figure 125 (b) and (c).

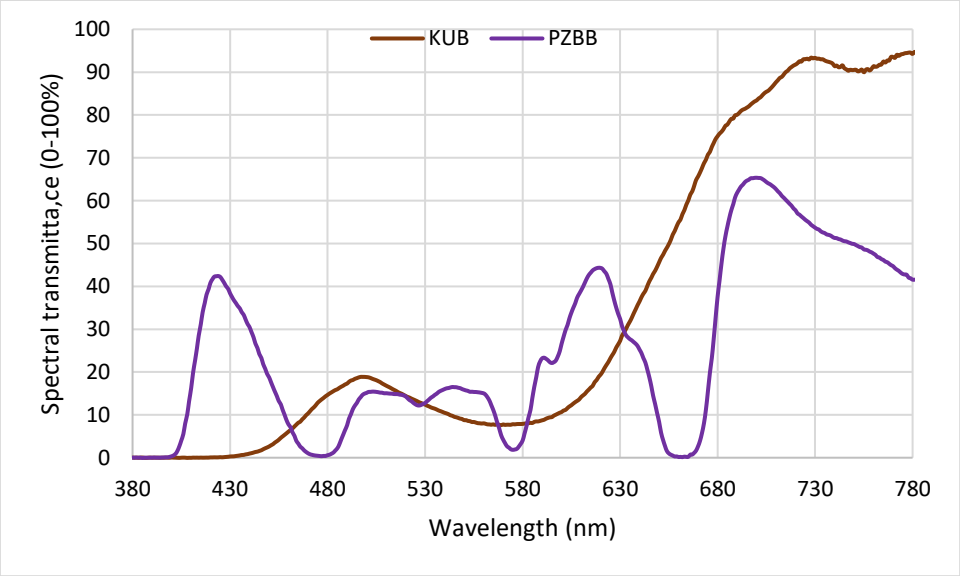

Figure 124, Spectral transmission of the simulated filters

Figure 125, (a) Original image, (b) Seen through KUB, (c) Seen through PZBB

The next step was to apply our algorithm on the original image to obtain the six clusters. Using the pixel locations of the original image's clusters, the median sRGB colors of the tinted images were calculated. The actual colors and modified colors are shown in Figure 126. The color segmentation methodology was not applied on filtered images, as the filter application changed the clusters. Certain colors which were part of the same cluster before, were separated in different clusters. This created a problem, as we wanted to analyze the color shift in dominant color composition of the original unfiltered scene. Thus, the clusters were identified only for the unfiltered image, and were used for color shift identification.

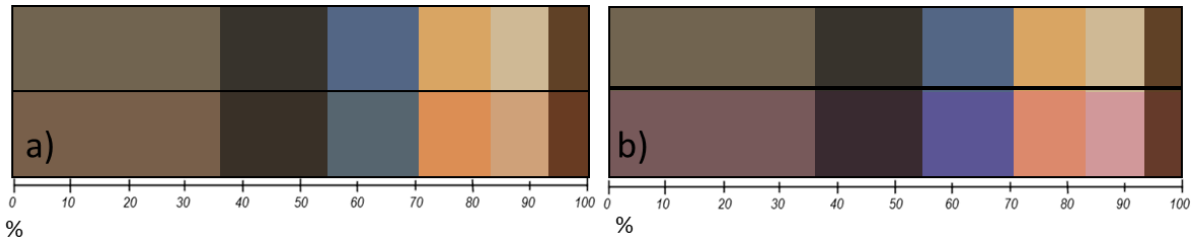

Figure 126, Original (top) and modified (bottom) color distributions of (a) KUB, (b) PZBB

These six original and modified colors were then converted to CIELAB. Using a technique similar to that of van der Burgt (van der Burgt & van Kemenade, 2010), arrows on the a*b* plane of the CIE LAB color space were used to identify the color shift, with the arrow starting at the original color and ending at the modified color. A measure of chroma difference (ΔC*) and hue difference (ΔH*) was also added to quantify the effects of the sunglasses, along with the percentage presence of the modified color in the image. The resulting color shift graphic is shown in Figure 127 ((a) for KUB and (b) for PZBB).

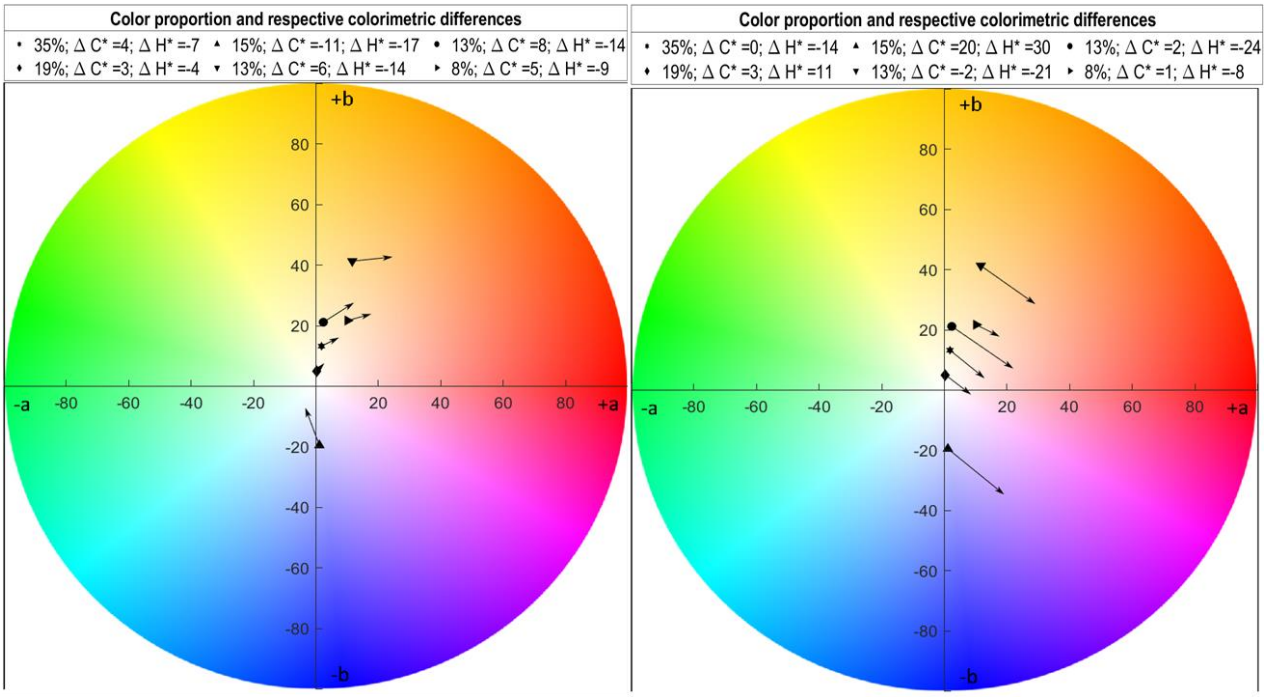

Figure 127, (a) Color shift due to KUB, (b) Color shift due to PZBB

As one would have imagined, the brownish KUB shifted the colors towards the yellow-orange-red hues, thus warming up the whole scene. Since the original scene had some amount of yellow tones already present in the scene, these tones got more accentuated and vivid. The blue tones (primarily the sky), became dull with a shift towards gray/neutral tones. In terms of overall color differences, the grey areas of the original image were less impacted ($\Delta C \in (3, 4)$; $\Delta H \in (-7,-4)$) than the blue sky or the other more colorful areas ($\Delta C \in (-11, 8)$; $\Delta H \in (-19,-9)$). The blue areas became visibly less chromatic with a negative chroma difference and a greyish hue shift.

The purplish PZBB added a colder tone to the scene with all the colors taking a very deep shift in the direction of the blue plane of the CIE a*b* color space. The grey/neutral colors took a purple hue while beige/brownish colors took a pinkish hue because of the shift in the deeper red region without any significant chroma shift. The blue sky became much more vivid and purplish. The color shift of PZBB is much stronger than KUB, with $\Delta H \in (-14,30)$ and the ΔC approaching 20 for the blue colors, though no other region showed any significant shift in chroma.

6.6. Discussion and conclusion

6.6.1. Dominant color descriptor

The aim of the developed algorithm was to propose a simplified methodology to automatically determine the color distribution of images. Our method achieves a reasonable precision by making the most of the available color data (from the images). In particular, the choice of CIELAB color space accentuates the results positively by bringing the clusters closer to human visual perception. A Gaussian blur improves the processing time and the accuracy of the clustering process. It removes the highest spatial frequencies and thus removes the details that do not represent the global color composition of the image. The results from the psycho-visual experiment are in good agreement with the results predicted by the algorithm. The K-means++ algorithm guarantees that the results are repeatable and that the image will be segmented in the same manner provided that no parameter is changed.

The processing time taken by our algorithm for 100 photos had a median of 1,16 seconds. The time taken and the size of the images is shown in Figure 128. The algorithm was developed on a Dell Precision 7520 computer, equipped with an Intel Xeon ER-1535M v6 processor and 32 Gb RAM.

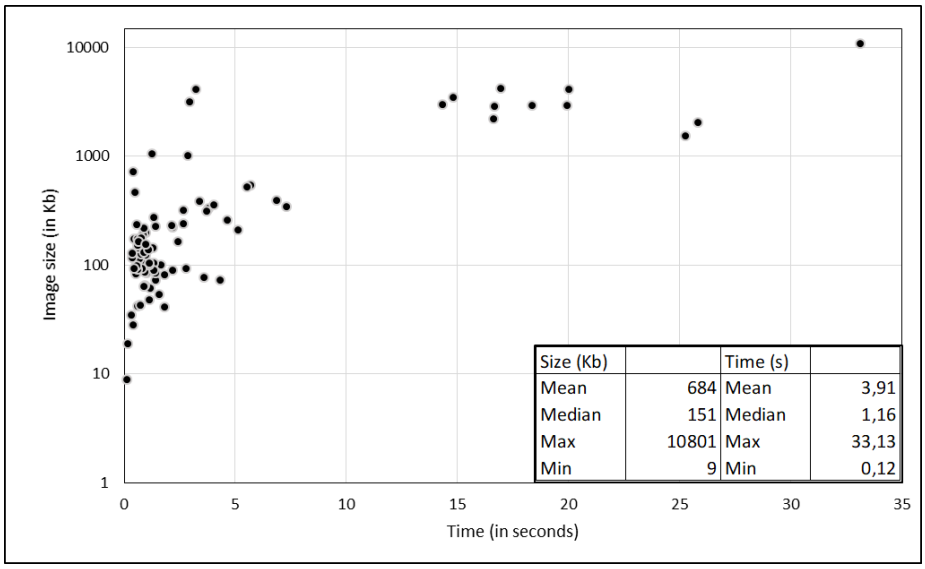

Figure 128, Image size vs Processing Time for 100 photos

A concern we have in our algorithm is the inability to determine the number of clusters as per the content of the image. We determined k=6 as an optimum seed value after various pre-tests. Evaluation methods like Silhouette index, Davies-Bouldin index, Calinski Harabasz index etc. exist to check if the number of seeds (k) is appropriate for the data sample or not (Caliński & Harabasz, 1974; Davies & Bouldin, 1979; Rousseeuw, 1987). But the evaluation process for images is long and power-hungry. It takes more than 5 minutes for a Calinski Harsbasz/Davies-Bouldin Evaluation for the image in Figure 125a, which also rendered the computer inaccessible for the duration of processing. The Silhouette Index method failed to converge even after 10 minutes of evaluation and 100 iterations. The possible k values tested $\in$ [3,8] and the optimum k from both Calinski Harsbasz and Davies-Bouldin Cluster Evaluation methods was found to be 6. Thus, our empirically determined value was validated a posteriori.

The algorithm provides a good solution for dominant color retrieval and image segmentation at the same time. Nevertheless, there are still about 10% of tested images that had different colored objects clustered together. This happens when the image has a lot of overlapping objects of different colors. This leads to inaccurate segmentation, even if the sRGB triplets correspond to the dominant visual perception. For example, in Figure 129, there is a coherence in the six dominant colors and the visual perception but it would have been better to have green and yellow in two separate clusters rather than one. With higher

values of k (as high as 10), similar blue and red colored objects are segmented into more than one cluster, producing even more incoherent results.

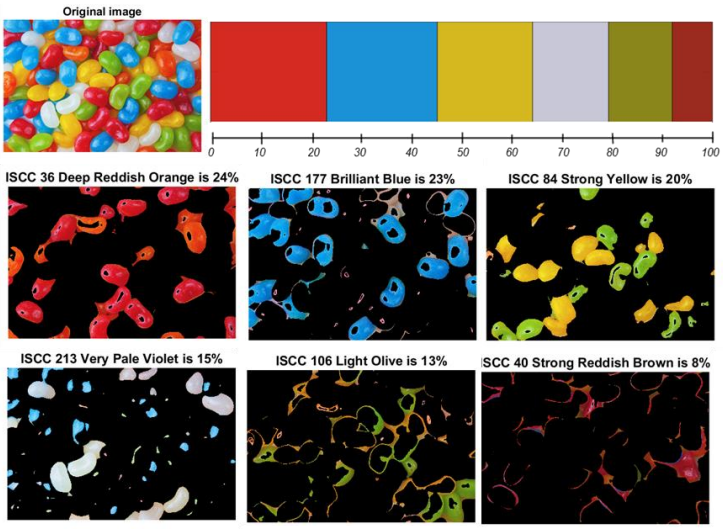

Figure 129, Example of inaccurate clustering but accurate color distribution

Nevertheless, the main objective, which is to automatically describe the color composition of an image, has been achieved despite the above problems. Overall, the algorithm works efficiently and rapidly to analyze colors for any image, and can be applied across various domains.

6.6.2. Color shift descriptor

The color shift descriptor is simple, fast and reliable enough for a quick colorimetric analysis of complex scenes and their rendering when seen through sunglasses. One major improvement our graphic tool brings is the increased readability and the direct comprehension of the changes in colors. Only the dominant colors of the scene are processed thus reducing the cluttering seen with other descriptors using a large number of fixed colors. We compared our results with that of the IES TM-30-15 which is currently one of the most used color vector graphics for comparing rendition of lightings (IES TM-30-15, 2015). The reference light source was daylight (D65) and the test source was daylight seen across the two sunglasses KUB (Figure 130) and PZBB (Figure 131).

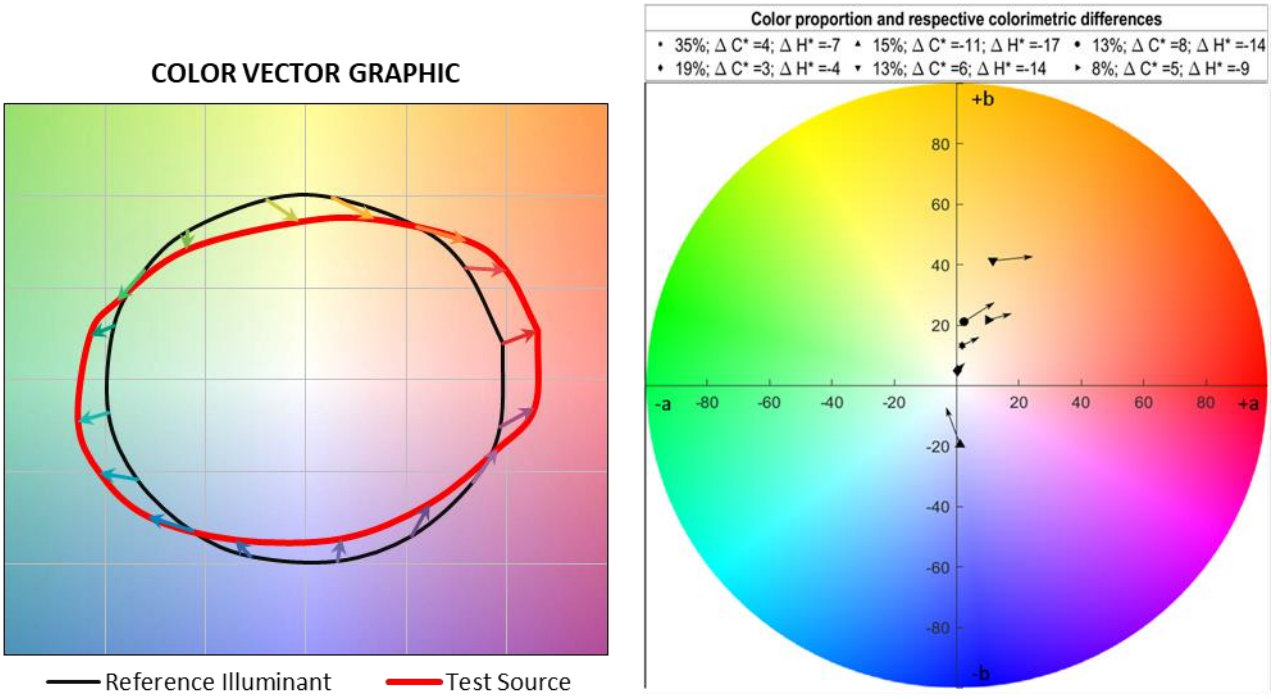

Figure 130, IES TM-30-15 color rendition of daylight vs our color shift descriptor: Urban scene in Figure 125 under KUB

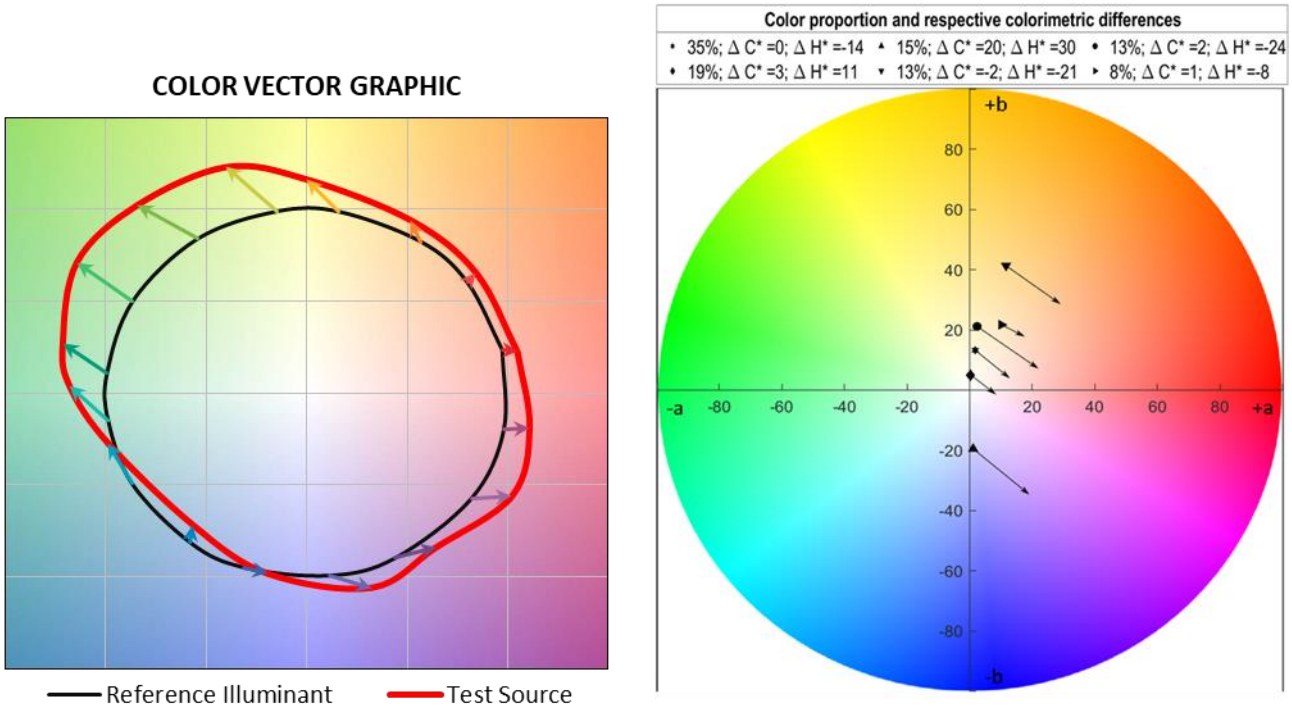

Figure 131, IES TM-30-15 color rendition of daylight vs our color shift descriptor: Urban scene in Figure 125 under PZBB

As it can be seen in Figure 130 and Figure 131, color rendering based on a generalized set of colors instead of the colors present in the target scene produces confusion. The purplish PZBB (Figure 124) is expected to produce stronger distortions in the favor of blue hues. The IES TM 30-15 does show these possible distortions in the blue region but shows a much stronger distortion for the green region. Except that, there is very little to no green present in the target scene (Figure 125a).

Another concern here could be the apparent reduction in the chroma content for yellow-orange colors for the brownish KUB. This is not the case in the image of the original scene seen through this sunglass, see Figure 125b. Our processing shows an enhancement of the chroma while the IES TM-30-15 predicts otherwise. The same issue is observed for the sky, which became visibly dull and grey while the IES TM-30-15 predicted an increase in chroma for blue colors. The chroma changes are visibly closer to visual perception with our color graphic, with a positive Delta C* for all colors except for the sky which has a Delta C* of -6, thus more coherent with the visual perception. The reason for this behavior could be that IES TM-30-15, or for that matter any color rendering metric, is built and trained on light sources. Comparing the two renditions of daylight, where one test source has about 85% less energy than the other, might produce incorrect predictions.

Another issue with the application of popular color rendition graphic tools, for example, the latest IES TM 30-18, is the inability to characterize radical changes in hue (IES TM-30-18, 2018). The IES TM-30-18 returned an error when PZBB under daylight (D65) was given as a test source. The filter was too chromatic for the calculation of CCT and other indices that the IES TM-30-18 provides.

Our method to quantify the color shift due to sunglasses is able to characterize all kinds of sunglasses even when they are too chromatic to be tested by traditional color rendering metrics. Our color shift graphic can be an important tool to objectively analyze the final rendered color of a scene under any sunglass. The direction of hue change can be identified with the change in dominant colors of the scene.

7. Summary and conclusion

The aim of this PhD thesis was to characterize and simulate color vision as perceived through sunglasses. In this chapter, we conclude the thesis with a summarized discussion of the work and we identify various directions for future work.

7.1. Recapitulation

Color vision is a complex process and scientists have been trying to properly characterize it with the help of mathematical models. The Trichromatic color theory of Helmholtz (Von Helmholtz, 1867), the opponent color theory of Herring (Hering, 1920) and the Chromatic adaptation theory of von Kries (von Kries, 1902) together form the basis of the color vision modelling as we know it today. While Helmholtz and Hering helped us understand the basic functions of the eye and the brain in processing color information, von Kries laid the foundation of color constancy. Further research carried out by various scientists in the early 1900s enabled direct application of these concepts. Even the most elementary color model requires the knowledge of CIE colorimetry, i.e. the CIE Color Matching Functions (CMFs) developed by grouping data from the experiments of Guild and Wright (Guild, 1931; Wright, 1929). The CIE CMFs and the CIE 1931 tristimulus values (XYZ) form the basis of color imaging. The basic CIE colorimetry, however helpful, still could not explain why colors with similar tristimulus values could appear differently in different situations. Since the development of the CIE tristimulus values, two major axes of color vision helped shape the future of colorimetry. The first axis involved scientists like Hunt, Stevens and others who tried to explain and simulate various color phenomena like Simultaneous contrast, Bartleson-Breneman effect, Spreading, Bezold-Brucke Hue shift, Steven's effect, Hunt effect etc. (Albers, 1963; Bartleson & Breneman, 1967; Chevreul, 1839; Hunt, 1965; Purdy, 1931; Stevens & Stevens, 1963). This led to a better understanding of these phenomena, which along with chromatic adaptation form the basis for any Color Appearance Model (CAM) today. The second axis is related to the development of Cartesian coordinate systems to identify colors, including the Munsell order of colors (Newhall, 1940) and the much later CIELAB color system (E. Q. Adams, 1942; CIE 15.2, 1986; McLAREN, 1976). Almost every device independent color space today is based on the standardized CIELAB color system using a channel for lightness (or value) and two others for redness-greenness and yellowness-blueness. The CIELAB system, despite having no chromatic adaptation transform, is considered by many as the first unofficial CAM. After the development of the CIELAB color space, the developments in the field of colorimetry accelerated with the release of various chromatic adaptation transforms (M. Fairchild & Reniff, 1995; Land, 1977; M. R. Luo & Hunt, 1998; Nayatani et al., 1981) leading to the very first official CIE CAM, CIECAM97 (CIE 131, 1998).

The CIECAM97 used the CMCCAT97 that modulated the S-cones with a non-linear factor. This created problems for the calculation of inverse CIECAM97 values. The CIE TC 8-01 later developed a completely linear CAT called CIECAT02 used in the current CIE standard: CIECAM02 (CIE 159, 2004). CIECAM02 is currently the most used CAM and predicts highly accurate color appearance correlates (Lightness, Brightness etc.). Despite being the current CIE standard, CIECAM02 has many unsolved problems like negative values of lightness that are caused due to a two-step chromatic and luminance adaptation in CIECAM02. This was corrected with the release of CAT16 and CAM16 in 2017 (C. Li et al., 2017) which are the current contenders to become the CIE official standards.

These developments still leave one area of study unanswered: the spatial context of vision. All the above CAMs and CATs treat the stimulus as a point and proceed with the calculation of color appearance correlates for a point stimulus related to its background. To solve this lack in CIECAM02, Fairchild and his team developed image CAMs, the most notable being iCAM06 (Kuang, Johnson, et al., 2007). iCAM06 takes as an input the entire image (CIE XYZ tristimulus) and treats the image spatially for chromatic adaptation, luminance adaptation and other color adjustments. iCAM06 also brings in two interesting concepts. The first being the edge-sensitive filtering to apply chromatic adaptation in a spatial context. And the second being a tone-compression algorithm that uses CIECAM02's chromatic adjustment and Hunt's achromatic signal adjustment to render iCAM06 as a High Dynamic Range-tone mapping operator as well. Tone mapping ensures a dynamic mapping of the color and luminance levels of a HDR scene to fit on a display

device with a smaller dynamic range, by conserving the perception of colors and luminance. This along-with the use of the IPT color space, which has an improved hue-linearity over CIELAB, makes iCAM06 a great candidate to simulate sunglasses.

To simulate sunglasses on complex scenes with the help of iCAM06, we first created hyperspectral images that were our stimuli. Acquiring, treating and analyzing hyperspectral images was a multi-step process that required precision. First and foremost, the hyperspectral data was calibrated to produce spectral radiances independently from the device's spectral sensitivity. For determining a protocol to calibrate a Hyper-Spectral Imaging (HSI) device, we chose to use the Specim FX10 whose specifications were described in section 3.2.1. To determine the spectral sensitivity of the HSI device, the spectral data from a reference device (spectroradiometer) was compared against the raw data of the HSI device. The raw data was treated for dark subtraction through a proprietary software of Specim before any comparison. The quotient of their division formed the spectral calibration curve. This curve, when divided by the raw spectral radiances from the hyperspectral radiances, produced calibrated data in SI units (W/m^2. per Sr. per nm). We did this comparison over a homogenous measurement area (a lambertian white object: Spectralon) with a uniform white light source (cold incandescent). The efficiency of this calibration curve was tested for spectral and colorimetric precision through the means of standardized metrics. Normalized Root Mean Square Deviation (NRMSD) was used for testing the spectral precision, and ΔE*ab for colorimetric precision (CIE 15.4, 2018; Foster & Amano, 2019). Scenes captured under light sources with different spectral properties have different reproduction accuracies. Thus, it was deemed important to identify the attainable precision of our calibration curve for different light sources (LED, Fluorescent and Incandescent). The objective of this precision study was to identify the device's range of errors. The Specim FX10, when calibrated with our methodology produced a mean NRMSD=4% (spectral), and a mean ΔE*ab=4 (colorimetric) on LED and fluorescent sources.

The calibration of hyperspectral data provides correct and standardized spectral measurements for any capture. However, other parameters may strongly influence the data accuracy if mismanaged. One example is the *exposure* decided for any particular scene. Many digital cameras come with a possibility to calculate this *exposure* automatically with the help of luminance sensors. Hyperspectral cameras unfortunately do not come with such a feature and *exposure* has to be selected manually. Nevertheless, the interface of the acquisition software provides information to identify saturation of the camera sensor by showing the overexposed pixels in red. Apart from over-exposure, under-exposure may also be an issue, as low exposure can lead to capturing noise instead of valuable data.

It is possible to predetermine the correct exposure for hyperspectral captures in function of the spectral radiance of the scene's illuminant. To do that, we can simulate the raw spectral response of the HSI device for multiple exposures and predetermine the exposure that produces either saturated or noisy data, thus ensuring the capture of correct hyperspectral data.

With this aim, we proceeded by simulating raw spectral radiance of Specim FX10 by simply multiplying a single reference spectral measurement (from a spectroradiometer) with the camera calibration curve. This simulated the raw radiance curve for the *exposure* chosen for the camera calibration (40 ms). We further identified the relation between the various exposures and their raw radiance values to simulate the raw radiance of not just one but multiple exposures. With the help of the earlier defined limits of the acquisition system, we were able to identify the exposures that crossed the threshold of measurable radiance of the system for a particular scene.

The properties discussed above helped us in characterizing and maximizing the data precision for one device (Specim FX10). Though, devices with different hardware and sensitivities, lead to different level of precisions. Certain devices are made for outdoor captures (Specim FX10) while some are more suitable for indoor captures (Specim V10E), see section 3.5 for further specifications. Then there is the question of pricing as well, hyperspectral cameras today can propose very sophisticated features, but these features come with high price tags. For example, the Specim V10E costs about four times the price of the portable Specim FX10. Though this compromise between portability and inexpensive price range vs data precision

is significant for Specim FX10. The data is less precise than Specim V10E, and sometimes outside the standardized limits of error metrics (see section 3.5.6).

An HSI device produces spectral radiance data which requires calibration. This calibrated hyperspectral data is multi-faceted, i.e. other forms of data can be derived from it. If the illuminant's radiance spectrum is known, the spectral radiances of a scene can be converted into reflectances. The spectral radiance values can also be converted into CIE XYZ tristimulus values to have absolute colorimetric and photometric information for the entire scene. With the help of the absolute colorimetric information of the illuminant, the XYZ tristimulus values can be converted into the CIELAB color space to obtain uniform colorimetric data for the entire scene. Apart from this, the CIE XYZ values can also be used to create color corrected images by applying CAMs (like iCAM06). Such versatile measuring devices should be characterized with separate metrics suitable for each aspect of use. This could allow the comparison of two different devices. Spectral (or radiometric) precision can be calculated for any device with a normalized metric like the Normalized Root Mean Square Deviation (Foster & Amano, 2019). It facilitates comparison between a reference measurement (spectroradiometer) and a test device by capping the maximum deviation. For photometric precision, a Mean Absolute Percentage Error can be helpful to identify the absolute differences in the measured luminance values for two different devices against the reference luminance values (Inanici & Galvin, 2004). Colorimetric precision can be quantified by a standard color difference formula like ΔE*ab that has well-defined and standardized perceptual limits (CIE 15, 2004). Image quality is a more subjective attribute and reference-less metrics like BRISQUE or NIQE can be used to identify the objective traits of an image based on the image statistics (Mittal et al., 2013, 2011).

To compare two HSI devices: the Specim FX10 and the Specim V10E, for all the above qualities, it was important to ensure that the measurement conditions were identical. The light source, the measurement scene and the reference measurement device had to be the same to exclude any protocol dependent errors. A uniform light booth with a Macbeth ColorChecker chart was chosen for these comparisons. Uniform ColorChecker charts have patches that mimic the colors of natural objects (skin, foliage, flowers etc.). For the choice of light source, tunable LEDs were found to be a good solution since they allow to simulate different kinds of light source temperatures with the same lighting fixture. This ensured that the two HSI devices could be compared for precision under light sources metameric to standard Planckian and Daylight light sources. These comparisons helped us identify the conditions where a certain kind of hyperspectral device was more suitable. For example, the Specim V10E was found to be the system with a significantly better precision for both, produced data (spectral: mean NRMSD=1,8%) and derived data (luminance: mean MAPE=4,3%, colorimetric: mean ΔE*ab=1.7). In terms of image quality after processing with iCA0M06, the Specim V10E produced images as good as those coming from a digital single-lens reflex camera (Canon EOS 5D Mark II), see Figure 132.

Figure 132, iCAM06 treated image in the light booth under EES light source: Specim V10E(left) and Canon EOS 5D (right)

The Specim FX10 had a decent spectral and photometric precision (mean NRMSD=4,5% and mean MAPE =4,5%) and a max ΔE*ab<6 (only for cold light sources), though the spectral and photometric data had significantly more noise for MCC Black patch. For warm light sources (CCT<3000K), it was found to have unacceptable color differences (ΔE*ab>6). In terms of image quality, even if the Specim V10E had significantly better metrics (mean BRISQUE=27, mean NIQE=3), the Specim FX10 produced acceptable images for indoor scenes with ambient illuminance of ~1800 lux (mean BRISQUE 37, mean NIQE 4). Since we wanted to create stimuli for indoor scenes with both warm and cold light sources, we chose the Specim V10E. The very different results of the tested metrics (detailed in section 3.5), highlight the importance of such tests before characterizing not just a HSI device, but any measurement device where the precision is of high importance.

For outdoor captures, the two cameras have different pros and cons. The Specim V10E produced sharp and crisp images but at the same time it was very bulky to transport. At least two people were needed when doing outdoor captures with the Specim V10E. The Specim FX10 produced relatively less sharp images but it was significantly easier to transport. A single person was enough for outdoor captures with the Specim FX10.

These comparisons helped us identify the suitable HSI device for psychovisual experiments (the Specim V10E) but further adjustments were possible in the acquisition parameters of the hyperspectral data to optimize output data for different needs. For example, with a few optimizations during data processing, it was possible to significantly reduce the size of hyperspectral data. The spectral resolution of a hyperspectral camera had a very strong impact on the data size. By processing and collecting data at reduced intervals (every 5,4 nm instead of every 1,3 nm or every 2,7 nm), it was possible to reduce the data size without impacting the precision of the measured data (insignificant differences in ΔE*ab, see section 4.1). Another parameter was the spectral range of the hypercube. Both Specim V10E and Specim FX10 measured data from UV to Near IR (400 nm-1000 nm). For our application, the spectral data was meant to be converted into images. Thus, the hypercube could be calculated only for the visible range of spectrum (400 nm-780 nm) instead of the entire measurable range of the hyperspectral camera. This further brought down the size of the hypercube without affecting the precision of the data, see section 4.2.

With every parameter for the stimuli creation defined in clear terms, the hyperspectral data was now ready to be used for simulating sunglasses on complex images. This was achieved by multiplying the spectral transmittances of Essilor filters with the spectral data of every pixel in the target scene. This spectral data was converted into the CIE XYZ color space to be used as an input for iCAM06. To ensure an exhaustive characterization of filters, a large range of target images were required for filter simulation. We created our own database of 50 hyperspectral images of urban, natural, and city landscapes containing buildings, vehicles and people. Our database also included day-lit indoor spaces, with or without people, see section 4.4. Even if it is worthwhile to create your own databases to have pertinent images acquired with appropriate parameters (spectral resolution etc.), various hyperspectral databases of indoor and outdoor scenes are available freely for research purposes. To cite a few: UEF spectral image database (UEF, n.d.), UGR spectral image database (Eckhard et al., 2015), UiT spectral image database (Prasad & Wenhe, 2015), BGU spectral image database (Arad & Ben-Shahar, 2016) and ENTPE spectral image database (Cauwerts & Jost-Boissard, 2019).

Hyperspectral data can be quantified with the help of objective metrics but the sunglass filtered 2D images, which have been further treated with iCAM06, cannot be so straightforwardly quantified for real world colorimetric precision. The objective of these filtered images is to simulate real perception through sunglasses as best as possible. For this purpose, psychovisual experiments are the optimum solution to identify how closely (or not) iCAM06 treated images from filtered hyperspectral data accurately reproduce real scenes with sunglasses.

These psychovisual experiments also provided an occasion to test iCAM06 as a CAM and not just a tone mapping operator. Furthermore, recent developments that have been made in the field of colorimetry and image processing (since iCAM06 was released) could also be tested.

One of the important developments was the creation of a new wide gamut color space: JzAzBz, which is suitable for HDR images and has a better uniformity than the IPT color space (Safdar et al., 2017b). Another candidate for improvement was the guided filter that applied a more informed edge-sensitive spatial filtering (Hutchison et al., 2010). They both were tested in the iCAM06 by replacing the IPT color space with JzAzBz color space and the bilateral filter with the guided filter. Certain basic filters with neutral grey/brown tints were simulated on a light-booth based test scene containing fruits, vegetables, flowers and a standard Macbeth chart. The experiment (Experiment 1) was conducted under a warm light (3000 K) and repeated for a cold light (6900 K). With the help of haploscopic comparison and ratings, the simulation of three colored filters was tested against the real scene as visualized through real filters. The JzAzBz color space improved the precision with which the scene was reproduced for unfiltered scenes, though no such benefit was found for filters. The guided filter on the other hand significantly reduced the color precision of the simulations for filtered and unfiltered scenes as well. Thus, this psycho-visual experiment allowed us to identify that neither of the two modifications were suitable for filter simulation.

The images were simulated for an almost complete chromatic adaptation via iCAM06, using a D value of 0,9, since the observers did adapt for 2 minutes. Theoretically, D values lie between 0-1 in function of the chromatic adaptation desired, though values below 0,3 are rarely used. Many observers however found that the images were too cold (bluish white) when compared to reality. This could have been due to the high degree of chromatic adaptation used for the image simulations. In a corollary experiment (Experiment 1A), it was found that lower degrees of chromatic adaptation (D=0,5 and D=0,7) improved the reproduction accuracy of the simulations.

The adapting white-point in iCAM06 was fixed at D65 in iCAM06. In the context of filter application, the resulting scene could sometimes have a color cast as per the chromaticity of the filter. For this purpose, another modification was introduced that replaced D65 with the effective white-point of the light source and the filter together, called modified white-point (mod). An experiment (Experiment 2) was conducted to test smaller degrees of adaptation (D=0,3-0,5-0,7 and 0,9), combined with a modified white-point. Filters with varying levels of transmittances were added to the experiment. The results showed a clear improvement in color reproduction with a reduction in the degree of chromatic adaptation. For certain filters, a modified white-point also improved color reproduction accuracy.

This prompted a large-scale study (Experiment 3), on a larger sample of population that tested two degrees of chromatic adaptation (D=0,3 and 0,5), and two white points (D65 and effective). All the tested filters had the same transmittance (~15%) but, this time, certain color enhancement filters were added to the classic filters to test the impact of filters that modify the chroma. To test the impact of spectral shape on color reproduction accuracy, these filters were accompanied by their metameric pairs. For both tested light sources (warm:3000K or cold:6900K), a lower D produced better images. A modified white-point improved the accuracy for a greyish filter and the unfiltered scene for the warm light source, though it reduced the precision for most of the brownish filters. Based on these results, the degree of chromatic adaptation D was fixed at 0.3. However, the choice of modified white-point was considered to be too chromatic and was altered for the next experiment (Experiment 4), see section 5.4.1 and section 5.4.2.

A recent publication had found that the color reproduction accuracy of CAMs for non-white light sources could be improved by using a modified version of the CMCCAT97 model instead of CIECAT02 (Ma et al., 2019). Since filtered vision can be considered to be closer to non-white light sources, this modification was implemented in iCAM06. To have a reference, the non-modified CMCCAT97 model was also implemented. Two white-points were tested in this experiment: D65 and a modified white-point that was closer to the Planckian curve (thus less chromatic) than the modified white-point tested in previous experiments, section 5.4.2 for details. A study (Experiment 4) was organized to test a modified white-point and D65 as white point for CIECAT02 images, and D65 as white point for the CMCCAT97's modified version and the

original one. The modified white-point was not applied to CMCCAT97 and its modified version since the resulting images were too saturated, see section 5.4.2. Intensely chromatic filters were tested alongside the filters from the previous experiments which had the best and worst reproduction accuracy. Results showed that the use of either the two CMCCAT97 models or a modified WP did not bring any significant improvement on the color reproduction accuracy of the filtered images. This experiment reinforced the use of CIECAT02 and D65 for either chromatic or white light sources when simulating complex images as seen through sunglasses.

Our methodology was validated under controlled and optimized viewing conditions, where there was a uniform distribution of light and the observers visualized this scene with sunglasses that covered the entirety of the visual field. This is in contrast with real outdoor situations where luminance levels may reach $\sim$25000 cd/m^2 on a bright sunny day, and the frames might not cover the entire field of view. Nevertheless, these experiments showed that, with carefully selected input parameters (WP and D-value), the original iCAM06 is the best (or equally best) solution for filter simulation on complex scenes among the other modifications tested in chapter 5. This validated the use of iCAM06 in haploscopic conditions with a maximum luminance dynamic of about 0,18-595 cd/m^2. The iCAM06 algorithm was originally validated on HDR scenes with a luminance dynamic as high as 0,74-99800 cd/m^2, with the help of memory based comparisons (see section 5.1).

Once the optimum candidate for filter simulation was assessed with exhaustive measures, characterization tools were developed to study the impact of sunglasses on vision, see chapter 6. Sunglasses induce shifts in colors, which require proper characterization to understand the impact of an existing or hypothetic filter. To this aim, a method of image dominant color descriptor was found to be ideal in terms of ease of understanding and ease of implementation. An image color descriptor can identify the colors present in a filtered hyperspectral image treated with iCAM06 by simplifying the color distribution. K-means++ based image segmentation techniques, with appropriate pretreatment of the images, can efficiently reduce the image into discrete bins of fewer colors that dictate the color perception of an observer (Arthur & Vassilvitskii, 2007).

An image color descriptor was developed using K-means++ that segmented the images into 6 bins of discrete colors, thus identifying the dominant colors of the scene. This color descriptor was found to be in accordance with human color perception when tested via a psychovisual experiment. When a similar discretization of colors was performed on a filtered image, and compared with an unfiltered image, we were able to identify the color shifts due to that particular filter. With the help of objective chroma and hue difference formulas, this color shift was further quantified for easy understanding.

The color shift descriptor could serve as an important tool for the sunglass industry which so far did not have any specific metrics to quantify the impact of colored filters on complex images.

7.2. Research answers

- iCAM06 was found to be similarly accurate for application to complex vision, with or without colored sunglasses.

- The recent developments in image processing and colorimetry (JzAzBz color space and guided filter) did not significantly improve the color perception of filtered iCAM06 images in testing conditions.

- A higher degree of chromatic adaptation in iCAM06 (D=0,9) might correspond to a complete chromatic adaptation but a lower degree of adaptation in iCAM06 improves the color reproduction accuracy of images, with or without filters.

- The default adapting white-point in iCAM06 is D65 which is also optimum for filtered images.

- Color reproduction accuracy of (default) iCAM06 simulated images did not change with a variation in the distribution of the spectral transmission of filters. However, it did diminish with a reduction in the Correlated Color Temperature of the scene visualized through the filter, for both warm and cold light sources.

- iCAM06 uses CAT02 as the chromatic adaptation transform, which is also the optimum solution for color vision simulation through filters. Non-linear CATs (like CAT97 or modified CAT97) did not significantly improve the filtered vision through iCAM06.

7.3. Conclusion

Sunglasses have become a daily use object not only to protect eyes from sunlight glare but also from harmful UV rays. With the continuous development of aesthetically pleasing frames and lenses, sunglasses have also become an essential fashion accessory. They are worn by young and old alike, and almost everywhere in the world. Today, the sunglass industry offers filters which are dedicated to specific tasks: playing sports (baseball, ski, etc.), night driving, professional car racing etc. Filters may also be designed with different objectives like reducing photo-sensitivity or lowering visual stress symptoms. Sunglasses originally offered neutral grey or brown tints, but today, highly chromatic sunglasses made with very selective dyes are commonplace.

Despite the aforementioned developments in sunglass features, there has been no development in the ability to virtually simulate the vision through sunglasses. There has been no research on the impact of sunglasses on chromatic adaptation either.

Currently sunglasses can only be simulated either on simple color patches or with the help of custom ICC color profiles on images. The filtered spectral radiance of simple color patches under standard light sources (like D65) can be used to calculate CIELAB values that can be converted to sRGB for visualization. Alternatively, filtered spectral radiances of an entire chart of simple color patches (Macbeth Digital Color SG with 100 patches) could be used to create ICC profiles using CIECAM02 correlates. This profile can then be applied on traditional unfiltered images to simulate the filter rendering. With the first method, there is no spatial simulation, so the spatial characteristics of human vision are ignored. In the second method, use of images adds a spatial perspective to the simulation, though the color correlates of CIECAM02 are applied without taking in account the structure of the target image, but as per the structure of the color chart.

The major reason why there is a lack of comprehensive tools for sunglass simulation is the fact that unlike the lighting industry, sunglasses are worn in specific conditions and represent a very small part of the color industry. There is less demand for such tools outside the sunglass industry to initiate large scale research in the color industry.

This PhD thesis proposed the ability to simulate complex vision as seen through sunglasses with the help of hyperspectral imaging. With the development of push broom scanners, hyperspectral cameras now offer high spectral and spatial resolutions. With increasing portability and advanced fore-optics of the hyperspectral imaging devices, it is now possible to capture the spectral information of the entire visual field with a high precision, in-situ. This more detailed hyperspectral data can be further multiplied with the spectral transmittance of the sunglasses to create filtered hyperspectral images.

This filtered hyperspectral data, when converted in a 2D space with the help of CIE colorimetry (XYZ), was used to apply iCAM06. The iCAM06 processed images, filtered through sunglasses, enabled us to take into account various spatial color appearance phenomena that are not part of standard CAMs. All these steps made the process a multi-fold task that required extensive testing and validation of parameters used at each and every step, from imaging device to color vision simulations. With the help of psycho-visual testing, we ensured the efficiency of our chosen method for the simulation of hyperspectral images via iCAM06.

We found that our chosen method was as efficient for sunglasses as it was for unfiltered daylight vision. However, the fidelity of reproduction accuracy of iCAM06 was not uniform as per the CCT of the illuminant

or the chromaticity of the filter. In contrast to cold light sources, iCAM06 simulated images had a lower precision when warm light sources were used. The use of IPT color space in iCAM06 also saturated warm colors and forced them outside the gamut of the screen. The current iCAM06 structure maintained the relative distance of colors inside the gamut of a screen, but not for colors outside the gamut. This effect was amplified when chromatic filters were applied, thus reducing their average reproduction accuracy. Though the modification of certain iCAM06 parameters/components did not change this accuracy, thus validating the use of default iCAM06 for filtered vision simulation.

7.4. Future work

The use of hyperspectral images with iCAM06 has been validated to simulate sunglasses on complex scenes. This use has been validated for luminance levels reaching 594 cd/m^2 and it can only be assumed that the same will hold true for outdoor luminance levels (outdoor luminance $\in$ (5000 cd/m^2 for a cloudy day-35000 cd/m^2 for a clear sunny day)). This still needs to be confirmed by further testing on high luminance levels and also for the application of iCAM06 on hyperspectral images of scenes with a high dynamic range of luminance (a minimum range of 0,05 cd/m^2-1000 cd/m^2). This can further assure the working of the model (with sunglasses) as a TMO on outdoor scenes, which are most of the time HDR in nature.

The currently used light booth, illuminated with three LED projectors, is already at its maximum possible light level for LED metameres of standard illuminants. To create indoor scenes with higher luminance levels would require new LED projectors offering a higher flux. A new display device with a higher luminance would also be required. Newer display devices now exist that can go as high as 1000 cd/m^2, like the EIZO Prominence CG3146 (our current EIZO screen has a max luminance of 300 cd/m^2). A display device going up to 1000 cd/m^2 could ensure simulation of filters with transmittance lower than 10% (C3…) with luminance levels around 10000 cd/m^2 close to sky luminance levels.

This thesis already tested CCT levels lower than daylight (6500 K) and it was found out that iCAM06 offers a relatively poor reproduction accuracy for these cases. Though a modified white-point for certain filters and warm light sources (see section 5.3.8), or the use of JzAzBZ color space for unfiltered scenes did improve this reproduction accuracy (see section 5.2.3). The next step could be testing filtered iCAM06 for light sources with a very high CCT (~10000K). This would also approach the CCT levels witnessed in snow laden ski domains (clear blue sky with no sun) which are an important segment of the sunglass industry.

The sunglass frame used for the experiments during the thesis covered the field-of-view completely. Though, this is not always the case in reality, majority of sunglass frames cover the field-of-view partially. Our next step could be using frames that cover only a part of visual field, and thereby modelling a chromatic adaptation transform better suited for sunglass frames.

One interesting observation in the experiments with color enhancing filters (see section 5.3.9) was the apparent gamut clipping of colors due to the application of IPT color space. An opportunity to improve the current iCAM06 model for filtered vision could be the use of gamut mapping algorithms that fit the out of gamut objects perceptually closer to the real colors, while staying in the gamut of the display device. This way, we could reduce the discrepancies observed between the real and simulated appearances of saturated colors, which are simply gamut clipped as per the current method. Since the use of a gamut mapping algorithm will further increase the complexity of the method, further testing will be required to test its performance for color reproduction accuracy. The use of a more recent version of IPT, the $I_gP_gT_g$ color space, could also perhaps solve this issue or at least reduce the extent of gamut clipping as it performs better than IPT in terms of hue-linearity (Hellwig & Fairchild, 2020).

The introduction of CAM16 in the iCAM06 framework might also help us to improve the current ratings observed in section 5.4.4, which stay between (7-8,5) for classic filters and between (6-8) for color enhancing and chromatic filters. The major complication would be to merge the separate chromatic adaptation and the tone compression steps of iCAM06 to fit the one-step CAM16 model. Though, this seems to be possible, since a solution has already been proposed that permits the use of CAT16 as a stand-alone

CAT after the removal of the Y_w parameter introduced in CAM16 (relative luminance of the adapting white), see section 2.5 (Smet & Ma, 2020).

Our methodology opens the door for various other applications, not just in the sunglass industry but also in the lighting industry. For example, it can also be used to simulate the appearance of a room (via its hyperspectral image) when illuminated with a new lighting fixture (with a known spectral radiance). With the help of the color shift tool, one can also identify the eventual color shifts induced by the new lighting fixture. Certain new modifications could potentially improve the accuracy of our method. Nevertheless, as it is, we have a robust methodology to spatially capture spectral radiances of a scene. With the help of these spectral images, we were able to create high fidelity images for a variety of sunglasses (different transmittances, chromaticities and spectral distribution), thus concluding this thesis.

8. Bibliography

Adams, E. Q. (1942). X-Z Planes in the 1931 ICI System of Colorimetry1. *Journal of the Optical Society of America*, *32*(3), 168. https://doi.org/10.1364/JOSA.32.000168

Adams, R., & Bischof, L. (1994). Seeded region growing. *IEEE Transactions on Pattern Analysis and Machine Intelligence*, *16*(6), 641–647. https://doi.org/10.1109/34.295913

Aksoy, Y., Aydin, T. O., Smolić, A., & Pollefeys, M. (2017). Unmixing-based soft color segmentation for image manipulation. *ACM Transactions on Graphics (TOG)*, *36*(2), 1–19.

Albers, J. (1963). *Interaction of color* (50th anniversary edition ; 4th edition). Yale University Press.

Arad, B., & Ben-Shahar, O. (2016). Sparse Recovery of Hyperspectral Signal from Natural RGB Images. In B. Leibe, J. Matas, N. Sebe, & M. Welling (Eds.), *Computer Vision – ECCV 2016* (pp. 19–34). Springer International Publishing.

Arthur, D., & Vassilvitskii, S. (2007). *k-means++: The advantages of careful seeding*. 1027–1035.

Aubaidan. (2014). COMPARATIVE STUDY OF K-MEANS AND K-MEANS++ CLUSTERING ALGORITHMS ON CRIME DOMAIN. *Journal of Computer Science*, *10*(7), 1197–1206. https://doi.org/10.3844/jcssp.2014.1197.1206

Bacci, M. (2006). NON-INVASIVE INSTRUMENTATION FOR DETECTION AND COLOUR CONTROL OF PAINTINGS AND ART W ORKS. *Archeometriai Műhely*, 46–50.

Baillet, G., Bourdoncle, B., Harrar, M., & Vienot, F. (2008). *Evaluation quantitative d'un filtre coloré* (Patent No. FR2905007 A1).

Bao, W., & Minchen, W. (2019). EFFECT OF LIGHT LEVEL ON COLOR PREFERNECE AND SPECIFICAITON OF LIGHT SOURCE COLOR RENDITION. *PROCEEDINGS OF the 29th Quadrennial Session of the CIE*, 241–250. https://doi.org/10.25039/x46.2019.OP35

Bartleson, C. J., & Breneman, E. J. (1967). Brightness Perception in Complex Fields. *Journal of the Optical Society of America*, *57*(7), 953. https://doi.org/10.1364/JOSA.57.000953

Belongie, S., Carson, C., Greenspan, H., & Malik, J. (1998). Color- and texture-based image segmentation using EM and its application to content-based image retrieval. *Sixth International Conference on*

Computer Vision (IEEE Cat. No.98CH36271), 675–682. https://doi.org/10.1109/ICCV.1998.710790

Biggs, W. (2004). *Perceptual accuracy of tone mapping algorithms*.

Black, P. (2018). Progressive thinking. *Optician Select*, *2018*(7), 176186–1. https://doi.org/10.12968/opti.2018.7.176186

Bodrogi, P., Brückner, S., Khanh, T. Q., & Winkler, H. (2013). Visual assessment of light source color quality. *Color Research & Application*, *38*(1), 4–13. https://doi.org/10.1002/col.20726

Bodrogi, P., Csuti, P., Hotváth, P., & Schanda, J. (2004). *Why does the CIE colour rendering index fail for white RGB LED light sources?* CIE expert symposium on LED light sources: Physical measurement and visual and photobiological assessment.

Brill, M. H. (2006). Irregularity in CIECAM02 and its avoidance. *Color Research & Application*, *31*(2), 142–145. https://doi.org/10.1002/col.20193

Brill, M. H., & Mahy, M. (2013). Visualization of mathematical inconsistencies in CIECAM02. *Color Research & Application*, *38*(3), 188–195. https://doi.org/10.1002/col.20744

Brill, M. H., & Süsstrunk, S. (2008). Repairing gamut problems in CIECAM02: A progress report. *Color Research & Application*, *33*(5), 424–426. https://doi.org/10.1002/col.20432

Brown, T. M., Tsujimura, S., Allen, A. E., Wynne, J., Bedford, R., Vickery, G., Vugler, A., & Lucas, R. J. (2012). Melanopsin-Based Brightness Discrimination in Mice and Humans. *Current Biology*, *22*(12), 1134–1141. https://doi.org/10.1016/j.cub.2012.04.039

Bruno, N., Bernardis, P., & Schirillo, J. (1997). Lightness, equivalent backgrounds, and anchoring. *Perception & Psychophysics*, *59*(5), 643–654. https://doi.org/10.3758/BF03206012

Buades, A., Coll, B., & Morel, J.-M. (2006). The staircasing effect in neighborhood filters and its solution. *IEEE Transactions on Image Processing*, *15*(6), 1499–1505. https://doi.org/10.1109/TIP.2006.871137

Buchsbaum, G. (1980). A spatial processor model for object colour perception. *Journal of the Franklin Institute*, *310*(1), 1–26.

Bullough, J. D., Radetsky, L. C., Besenecker, U. C., & Rea, M. S. (2014). Influence of Spectral Power Distribution on Scene Brightness at Different Light Levels. *LEUKOS*, *10*(1), 3–9. https://doi.org/10.1080/15502724.2013.827516

Cadik, M., Wimmer, M., Neumann, L., & Artusi, A. (2006). *Image Attributes and Quality for Evaluation of Tone Mapping Operators*.

Čadík, M., Wimmer, M., Neumann, L., & Artusi, A. (2008). Evaluation of HDR tone mapping methods using essential perceptual attributes. *Computers & Graphics*, *32*(3), 330–349. https://doi.org/10.1016/j.cag.2008.04.003

Cai, H., & Chung, T. (2011). Improving the quality of high dynamic range images. *Lighting Research & Technology*, *43*(1), 87–102. https://doi.org/10.1177/1477153510371356

Calabria, A. J., & Fairchild, M. (2001). *Herding CATs: A comparison of linear chromatic-adaptation transforms for CIECAM97s*. *2001*(1), 174–178.

Caliński, T., & Harabasz, J. (1974). A dendrite method for cluster analysis. *Communications in Statistics*, *3*(1), 1–27. https://doi.org/10.1080/03610927408827101

Cao, D., Chang, A., & Gai, S. (2018). Evidence for an impact of melanopsin activation on unique white perception. *Journal of the Optical Society of America A*, *35*(4), B287. https://doi.org/10.1364/JOSAA.35.00B287

Cauwerts, C., Jost, S., Raza, A., & Deroisy, B. (2019). HDR versus hyperspectral images for applied colour and lighting research. *IS&T Color Imaging Conference (CIC)-Material Appearance Workshop*.

Cauwerts, C., & Jost-Boissard, S. (2018). A color graphic informing on the impact of electric lighting and coated glazing in complex architectural scenes. *Color Research & Application*, *43*(6), 885–898. https://doi.org/10.1002/col.22267

Cauwerts, C., & Jost-Boissard, S. (2019). Color rendering of window glass: Analysis of landscape content with hyperspectral imaging. *Proceedings of the International Colour Association (AIC) Conference 2019, Buenos Aires, Argentina*. AIC 2019. https://www.entpe.fr/en/ressources-p2e

Chae, S., Lee, S., & Sohng, K. (2013). Color correction for preserved saturation and hue in HDR images. *CES-CUBE 2013, ASTL*, *25*, 29–32.

Chakrabarti, A., & Zickler, T. (2011). Statistics of real-world hyperspectral images. *CVPR 2011*, 193–200. https://doi.org/10.1109/CVPR.2011.5995660

Cheng, D., Prasad, D. K., & Brown, M. S. (2014). Illuminant estimation for color constancy: Why spatial-domain methods work and the role of the color distribution. *Journal of the Optical Society of America A*, *31*(5), 1049. https://doi.org/10.1364/JOSAA.31.001049

Chevreul, E. (1839). *De la loi du contraste simultané des couleurs et de l'assortiment des objets colorés*. Chez Pitois-Levrault.

CIE 13.3. (1995). *Method of measuring and specifying colour rendering properties of light sources*. Commission Internationale de l'Eclairage.

CIE 15 (Ed.). (2004). *Colorimetry* (3. ed). CIE, Central Bureau.

CIE 15.2, 1986. (1986). *CIE 015:1986 Colorimetry, 2nd Edition*. International Commission on Illumination (CIE). https://doi.org/10.25039/TR.015.2018

CIE 15.4. (2018). *CIE 015:2018 Colorimetry, 4th Edition*. International Commission on Illumination (CIE). https://doi.org/10.25039/TR.015.2018

CIE 131 (Ed.). (1998). *THE CIE 1997 INTERIM COLOUR APPEARANCE MODEL (SIMPLE VERSION) CIECAM97S*. CIE Central Bureau.

CIE 159 (Ed.). (2004). *A colour appearance model for colour management systems: CIECAM02*. CIE Central Bureau.

CIE 170-1 (Ed.). (2006). *Fundamental chromaticity diagram with physiological axes. Pt. 1: ...* CIE Central Bureau.

CIE 170-2. (2015). *Fundamental Chromaticity Diagram with Physiological Axes—Part 2: Spectral Luminous Efficiency Functions and Chromaticity Diagrams* (Vol. 41). http://doi.wiley.com/10.1002/col.22020

CIE 177 (Ed.). (2007). *Colour rendering of white LED light sources*. CIE Central Bureau.

CIE 208. (2014). *Effect of stimulus size on colour appearance*. CIE Central Bureau.

CIE 224. (2017). *CIE 2017 colour fidelity index for accurate scientific use*. CIE Central Bureau.

Cobeldick, S. (2019). *Convert between RGB and Color Names* (4.0.1) [Computer software]. MATLAB Central File Exchange. https://www.mathworks.com/matlabcentral/fileexchange/48155-convert-between-rgb-and-color-names

Cohen-Tannoudji, D., Barrau, C., Villette, T. P., Sahel, J.-A., Picaud, S., Arnault, E., Plessis, C., & Conte, D. (2014). *Ophthalmic filter*.

Crizal Prevencia. (2013). *Crizal Prevencia*.

Crizal Sapphire+. (2017). *CRIZAL® SAPPHIRE+*. https://www.essilor.fr/nos-verres/crizal/crizal-sapphire

Csuti, P., & Schanda, J. (2008). Colour matching experiments with RGB-LEDs. *Color Research & Application*, *33*(2), 108–112. https://doi.org/10.1002/col.20385

Csuti, P., & Schanda, J. (2010). A BETTER DESCRIPTION OF METAMERIC EXPERIENCE OF LED CLUSTERS. *Light & Engineering*, *18*(1).

Dangol, R., Bhusal, P., & Halonen, L. (2015). Performance of colour fidelity metrics. *Lighting Research & Technology*, *47*(8), 897–908. https://doi.org/10.1177/1477153514555721

Datta, R., Joshi, D., Li, J., & Wang, J. Z. (2008). Image retrieval: Ideas, influences, and trends of the new age. *ACM Computing Surveys*, *40*(2), 1–60. https://doi.org/10.1145/1348246.1348248

Davidoff, J. B. (1991). *Cognition through color*. MIT Press.

Davies, D. L., & Bouldin, D. W. (1979). A Cluster Separation Measure. *IEEE Transactions on Pattern Analysis and Machine Intelligence*, *PAMI-1*(2), 224–227. https://doi.org/10.1109/TPAMI.1979.4766909

Davis, W., & Ohno, Y. (2005). *Toward an improved color rendering metric* (I. T. Ferguson, J. C. Carrano, T. Taguchi, & I. E. Ashdown, Eds.; p. 59411G). https://doi.org/10.1117/12.615388

De Valois, R. L., Abramov, I., & Jacobs, G. H. (1966). Analysis of Response Patterns of LGN Cells*. *Journal of the Optical Society of America*, *56*(7), 966. https://doi.org/10.1364/JOSA.56.000966

Delahunt, P. B., & Brainard, D. H. (2000). Control of chromatic adaptation: Signals from separate cone classes interact. *Vision Research*, *40*(21), 2885–2903. https://doi.org/10.1016/S0042-6989(00)00125-5

Delon, J., Desolneux, A., Lisani, J.-L., & Petro, A. B. (2007). A Nonparametric Approach for Histogram Segmentation. *IEEE Transactions on Image Processing*, *16*(1), 253–261. https://doi.org/10.1109/TIP.2006.884951

Derrington, A. M., Krauskopf, J., & Lennie, P. (1984). Chromatic mechanisms in lateral geniculate nucleus of macaque. *The Journal of Physiology*, *357*(1), 241–265. https://doi.org/10.1113/jphysiol.1984.sp015499

Dubail, M., Jost-Boissard, S., & Cauwerts, C. (2020). *Method for filter selection* (Patent No. US20200166780A1).

Dubuc, B. (2013). *The brain from top to bottom*. https://thebrain.mcgill.ca/flash/d/d_02/d_02_cl/d_02_cl_vis/d_02_cl_vis.html

Durand, F., & Dorsey, J. (2002). Fast bilateral filtering for the display of high-dynamic-range images. *Proceedings of the 29th Annual Conference on Computer Graphics and Interactive Techniques - SIGGRAPH '02*, 257. https://doi.org/10.1145/566570.566574

Ebner, F., & Fairchild, M. (1998). *Development and testing of a color space (IPT) with improved hue uniformity*. *1998*(1), 8–13.

Eckhard, J., Eckhard, T., Valero, E. M., Nieves, J. L., & Contreras, E. G. (2015). Outdoor scene reflectance measurements using a Bragg-grating-based hyperspectral imager. *Applied Optics*, *54*(13), D15. https://doi.org/10.1364/AO.54.000D15

Essilor Eyezen. (2015). *EYEZEN*. https://www.essilor.fr/nos-verres/eyezen

Essilor International. (1997). CAHIERS D'OPTIQUE OCULAIRE. In *CAHIERS D'OPTIQUE OCULAIRE*.

Essilor SunSolution. (2018). *Essilor SUN SOLUTION*. https://www.essilor-sunsolution.com/

Essilor Xperio. (2009). *XPERIO®*. https://www.essilor.fr/nos-verres/protection-solaire/xperio

Evans, R. M. (1943). Visual Processes and Color Photography*. *Journal of the Optical Society of America*, *33*(11), 579. https://doi.org/10.1364/JOSA.33.000579

Evans, R. M. (1974). *The Perception of Color* (Vol. 2). John Wiley and Sons.

Fairchild, M. (1992a). Chromatic adaptation and color constancy. *Advances in Color Vision Technical Digest*, *4*, 112–114.

Fairchild, M. (1992b). Chromatic adaptation to image displays. *TAGA Proc. Rochester*, *2*, 803–823.

Fairchild, M. (2004). ICAM framework for image appearance, differences, and quality. *Journal of Electronic Imaging*, *13*(1), 126. https://doi.org/10.1117/1.1635368

Fairchild, M. (2013). *Color appearance models* (Third edition). John Wiley & Sons, Inc.

Fairchild, M. (1993a). *Chromatic adaptation in hard copy/soft copy comparisons*. *1912*, 47–61.

Fairchild, M. (1993b). *RLAB: A color appearance space for color reproduction* (R. J. Motta & H. A. Berberian, Eds.; pp. 19–30). https://doi.org/10.1117/12.149061

Fairchild, M. & Chair. (1995). *CIE TC 1-34 Testing Colour-Appearance Models*.

Fairchild, M., & Chen, P.-H. (2011). *Brightness, lightness, and specifying color in high-dynamic-range scenes and images* (S. P. Farnand & F. Gaykema, Eds.; p. 786700). https://doi.org/10.1117/12.872075

Fairchild, M. D. (2002). *Status of CIE color appearance models* (R. Chung & A. Rodrigues, Eds.; p. 550). https://doi.org/10.1117/12.464726

Fairchild, M., & Johnson, G. M. (2003). *Image appearance modeling* (B. E. Rogowitz & T. N. Pappas, Eds.; p. 149). https://doi.org/10.1117/12.477370

Fairchild, M., & Johnson, G. M. (2002). *Meet iCAM: A next-generation color appearance model*. *2002*(1), 33–38.

Fairchild, M., Pirrotta, E., & Kim, T. (1994). Successive-ganzfeld haploscopic viewing technique for color-appearance research. *Color Research & Application*, *19*(3), 214–221. https://doi.org/10.1002/col.5080190309

Fairchild, M., & Reniff, L. (1995). Time course of chromatic adaptation for color-appearance judgments. *Journal of the Optical Society of America A*, *12*(5), 824. https://doi.org/10.1364/JOSAA.12.000824

Fairchild, M., & Wyble, D. R. (2007). *Mean observer metamerism and the selection of display primaries*. *2007*(1), 151–156.

Faris Belt, A. (2012). *The Elements of Photography: Understanding and Creating Sophisticated Images* (0 ed.). Routledge. https://doi.org/10.4324/9780240815169

Feng, X., Xu, W., Han, Q., & Zhang, S. (2017). Colour-enhanced light emitting diode light with high gamut area for retail lighting. *Lighting Research & Technology*, *49*(3), 329–342. https://doi.org/10.1177/1477153515610621

Fischer, C., & Kakoulli, I. (2006). Multispectral and hyperspectral imaging technologies in conservation: Current research and potential applications. *Studies in Conservation*, *51*(sup1), 3–16. https://doi.org/10.1179/sic.2006.51.Supplement-1.3

Foster, D. H., & Amano, K. (2019). Hyperspectral imaging in color vision research: Tutorial. *Journal of the Optical Society of America A*, *36*(4), 606. https://doi.org/10.1364/JOSAA.36.000606

Foster, D. H., Amano, K., & Nascimento, S. M. C. (2006). Color constancy in natural scenes explained by global image statistics. *Visual Neuroscience*, *23*(3–4), 341–349. https://doi.org/10.1017/S0952523806233455

Fotios. (2006). Chromatic adaptation and the relationship between lamp spectrum and brightness. *Lighting Research & Technology*, *38*(1), 3–14. https://doi.org/10.1191/1365782806li149oa

Gegenfurtner, K. R., & Kiper, D. C. (2003). Color Vision. *Annual Review of Neuroscience*, *26*(1), 181–206. https://doi.org/10.1146/annurev.neuro.26.041002.131116

Gevers, T., & Smeulders, A. W. M. (2000). PicToSeek: Combining color and shape invariant features for image retrieval. *IEEE Transactions on Image Processing*, *9*(1), 102–119. https://doi.org/10.1109/83.817602

Ghadiyaram, D., & Bovik, A. C. (2016). Massive Online Crowdsourced Study of Subjective and Objective Picture Quality. *IEEE Transactions on Image Processing*, *25*(1), 372–387. https://doi.org/10.1109/TIP.2015.2500021

Giannos, S. A., Kraft, E. R., Lyons, L. J., & Gupta, P. K. (2019). Spectral Evaluation of Eyeglass Blocking Efficiency of Ultraviolet/High-energy Visible Blue Light for Ocular Protection. *Optometry and Vision Science*, *96*(7), 513–522. https://doi.org/10.1097/OPX.0000000000001393

Gill, G. W. (2008). *A solution to CIECAM02 numerical and range issues*. 327–331.

Giraudet, G. (2010). *Coloured ophthalmic lenses for people with dyslexia*.

Goetz, A. F., Vane, G., Solomon, J. E., & Rock, B. N. (1985). Imaging spectrometry for earth remote sensing. *Science*, *228*(4704), 1147–1153.

Gong, Y., Chuan, C. H., & Xiaoyi, G. (1996). Image indexing and retrieval based on color histograms. *Multimedia Tools and Applications*, *2*(2), 133–156. https://doi.org/10.1007/BF00672252

Graham, D. M., & Wong, K. Y. (1995). Melanopsin-expressing, Intrinsically Photosensitive Retinal Ganglion Cells (ipRGCs). In H. Kolb, E. Fernandez, & R. Nelson (Eds.), *Webvision: The Organization of the Retina and Visual System*. University of Utah Health Sciences Center. http://www.ncbi.nlm.nih.gov/books/NBK27326/

Grunsby, R. (2012, June 18). *Scientific CMOS (sCMOS) Technology: An Overview*. https://www.photonicsonline.com/doc/scientific-cmos-scmos-technology-an-overview-0001#:~:text=Conventional%20CMOS%20cameras%20offer%20very,view%20simultaneously%20in%20one%20image.

Guild, J. (1931). The colorimetric properties of the spectrum. *Philosophical Transactions of the Royal Society of London. Series A, Containing Papers of a Mathematical or Physical Character*, *230*(681–693), 149–187. https://doi.org/10.1098/rsta.1932.0005

Guth, S. L. (1991). Model for color vision and light adaptation. *Journal of the Optical Society of America A*, *8*(6), 976. https://doi.org/10.1364/JOSAA.8.000976

Hall, R. (1999). *Color Perception*. https://web.mst.edu/~rhall/web_design/color_perception.html

Harter, M. R., Seiple, W. H., & Musso, M. (1974). Binocular summation and suppression: Visually evoked cortical responses to dichoptically presented patterns of different spatial frequencies. *Vision Research*, *14*(11), 1169–1180. https://doi.org/10.1016/0042-6989(74)90213-2

Hartong, D. T., Berson, E. L., & Dryja, T. P. (2006). Retinitis pigmentosa. *The Lancet*, *368*(9549), 1795–1809. https://doi.org/10.1016/S0140-6736(06)69740-7

Hellwig, L., & Fairchild, M. D. (2020). Using Gaussian Spectra to Derive a Hue-linear Color Space. *Color and Imaging Conference*, *2020*(28), 244–251. https://doi.org/10.2352/J.Percept.Imaging.2020.3.2.020401

Helson, H., Wilson, M., & Judd, D. (1979). Color rendition with fluorescent sources of illumination. *Contributions to Color Science*, *13*, 422.

Hering, E. (1920). *Outlines ofa Theory ofthe Light Sense (trans. By LM Hurvich and D. Jameson)*.

Herzog, M. H., & Clarke, A. M. (2014). Why vision is not both hierarchical and feedforward. *Frontiers in Computational Neuroscience*, *8*. https://doi.org/10.3389/fncom.2014.00135

Hordley, S. D. (2006). Scene illuminant estimation: Past, present, and future. *Color Research & Application*, *31*(4), 303–314. https://doi.org/10.1002/col.20226

Hordley, S. D., Finalyson, G., & Morovic, P. (2004). A multi-spectral image database and its application to image rendering across illumination. *Third International Conference on Image and Graphics, ICIG 2004, Hong Kong, China, December 18-20, 2004*, 394–397. https://doi.org/10.1109/ICIG.2004.10

Huang, H.-P., Wei, M., Xiao, K., Ou, L.-C., & Xue, P. (2019). UNIQUE HUE JUDGMENTS UNDER LIGHT SOURCES WITH DIFFERENT CHROMATICITIES. *PROCEEDINGS OF the 29th Quadrennial Session of the CIE*, 515–520. https://doi.org/10.25039/x46.2019.OP70

Hui Yu, Mingjing Li, Hong-Jiang Zhang, & Jufu Feng. (2002). Color texture moments for content-based image retrieval. *Proceedings. International Conference on Image Processing*, *1*, 929–932. https://doi.org/10.1109/ICIP.2002.1039125

Hung, P.-C., & Berns, R. S. (1995). Determination of constant Hue Loci for a CRT gamut and their predictions using color appearance spaces. *Color Research & Application*, *20*(5), 285–295. https://doi.org/10.1002/col.5080200506

Hunt, R. W. G. (1952). Light and Dark Adaptation and the Perception of Color*. *Journal of the Optical Society of America*, *42*(3), 190. https://doi.org/10.1364/JOSA.42.000190

Hunt, R. W. G. (1965). Measurement of Color Appearance. *Journal of the Optical Society of America*, *55*(11), 1540. https://doi.org/10.1364/JOSA.55.001540

Hunt, R. W. G. (1982). A model of colour vision for predicting colour appearance. *Color Research & Application*, *7*(2), 95–112. https://doi.org/10.1002/col.5080070207

Hunt, R. W. G. (1987). A model of colour vision for predicting colour appearance in various viewing conditions. *Color Research & Application*, *12*(6), 297–314. https://doi.org/10.1002/col.5080120605

Hunt, R. W. G. (1991). Revised colour-appearance model for related and unrelated colours. *Color Research & Application*, *16*(3), 146–165. https://doi.org/10.1002/col.5080160306

Hunt, R. W. G. (1995). *The reproduction of colour* (5th ed). John Wiley & Sons.

Hurvich, L. M., & Jameson, D. (1957). An opponent-process theory of color vision. *Psychological Review*, *64*(6, Pt.1), 384–404. https://doi.org/10.1037/h0041403

Hutchison, D., Kanade, T., Kittler, J., Kleinberg, J. M., Mattern, F., Mitchell, J. C., Naor, M., Nierstrasz, O., Pandu Rangan, C., Steffen, B., Sudan, M., Terzopoulos, D., Tygar, D., Vardi, M. Y., Weikum, G., He, K., Sun, J., & Tang, X. (2010). Guided Image Filtering. In K. Daniilidis, P. Maragos, & N. Paragios (Eds.), *Computer Vision – ECCV 2010* (Vol. 6311, pp. 1–14). Springer Berlin Heidelberg. https://doi.org/10.1007/978-3-642-15549-9_1

IES TM-30-15. (2015). *IES TM-30-15, IES Method for Evaluating Light Source Color Rendition*. Illuminating Engineering Society of North America.

IES TM-30-18. (2018). IES method for evaluating light source color rendition. *IES TM-30-18*.

Imai, F. H., Wyble, D. R., Berns, R. S., & Tzeng, D.-Y. (2003). A feasibility study of spectral color reproduction. *Journal of Imaging Science and Technology*, *47*(6), 543–553.

Inanici, M., & Galvin, J. (2004). *Evaluation of High Dynamic Range Photography as a Luminance Mapping Technique* (LBNL--57545, 841925; p. LBNL--57545, 841925). https://doi.org/10.2172/841925

ISO 13666 QSignals. (2019). *ISO 13666*. https://www.iso.org/obp/ui/#iso:std:iso:13666:ed-3:v1:en

Jacobs, G. H., Neitz, J., & Krogh, K. (1996). Electroretinogram flicker photometry and its applications. *Journal of the Optical Society of America A*, *13*(3), 641. https://doi.org/10.1364/JOSAA.13.000641

Jain, A. K., & Vailaya, A. (1996). Image retrieval using color and shape. *Pattern Recognition*, *29*(8), 1233–1244. https://doi.org/10.1016/0031-3203(95)00160-3

Jiang, F., Fairchild, M., & Masaoka, K. (2019). Perceptual Estimation of Diffuse White Level in HDR Images. *Color and Imaging Conference*, *2019*(1), 195–200. https://doi.org/10.2352/issn.2169-2629.2019.27.35

Jiang, J., Wang, Z., Luo, M. R., Melgosa, M., Brill, M. H., & Li, C. (2015). Optimum solution of the CIECAM02 yellow-blue and purple problems. *Color Research & Application*, *40*(5), 491–503. https://doi.org/10.1002/col.21921

Jianping Fan, Yau, D. K. Y., Elmagarmid, A. K., & Aref, W. G. (2001). Automatic image segmentation by integrating color-edge extraction and seeded region growing. *IEEE Transactions on Image Processing*, *10*(10), 1454–1466. https://doi.org/10.1109/83.951532

Jindrova, H. (1998). Vertebrate phototransduction: Activation, recovery and adaptation. *Physiological Research*, *47*, 155–168.

Jost-Boissard, S., Avouac, P., & Fontoynont, M. (2015). Assessing the colour quality of LED sources: Naturalness, attractiveness, colourfulness and colour difference. *Lighting Research & Technology*, *47*(7), 769–794. https://doi.org/10.1177/1477153514555882

Jost-Boissard, S., Avouac, P., & Fontoynont, M. (2016). Preferred Color Rendition of Skin under LED Sources. *LEUKOS*, *12*(1–2), 79–93. https://doi.org/10.1080/15502724.2015.1060499

Jost-Boissard, S., Fontoynont, M., & Blanc-Gonnet, J. (2009a). Perceived lighting quality of LED sources for the presentation of fruit and vegetables. *Journal of Modern Optics*, *56*(13), 1420–1432. https://doi.org/10.1080/09500340903056550

Jost-Boissard, S., Fontoynont, M., & Blanc-Gonnet, J. (2009b). Perceived lighting quality of LED sources for the presentation of fruit and vegetables. *Journal of Modern Optics*, *56*(13), 1420–1432. https://doi.org/10.1080/09500340903056550

Juan, L., & Luo, M. (2000). New magnitude estimation data for evaluating colour appearance models. *Colour and Visual Scales*, 3–5.

Judd, D. B., & Kelly, K. L. (1939). Method of designating colors. *Contributions to Color Science*, 219–230.

K. Shevell, S. (1982). Color perception under chromatic adaptation: Equilibrium yellow and long-wavelength adaptation. *Vision Research*, *22*, 279–292. https://doi.org/10.1016/0042-6989(82)90128-6

Khanh, T., Bodrogi, P., Vinh, Q., & Stojanovic, D. (2017). Colour preference, naturalness, vividness and colour quality metrics, Part 1: Experiments in a room. *Lighting Research & Technology*, *49*(6), 697–713. https://doi.org/10.1177/1477153516643359

Kim, D.-H. (1997). New Weighting Functions for the Modified CIELAB Colour-Difference Formulae. *Textile Coloration and Finishing*, *9*.

Kim, H.-G., & Lee, S.-H. (2013). Separate Color Correction for Tone Compression in HDR Image Rendering. *IEICE Transactions on Fundamentals of Electronics, Communications and Computer Sciences*, *E96.A*(8), 1752–1758. https://doi.org/10.1587/transfun.E96.A.1752

Knight, R., Buck, S. L., Fowler, G. A., & Nguyen, A. (1998). Rods affect S-cone discrimination on the Farnsworth–Munsell 100-hue test. *Vision Research*, *38*(21), 3477–3481. https://doi.org/10.1016/S0042-6989(97)00414-8

Krauskopf, J., Williams, D. R., & Heeley, D. W. (1982). Cardinal directions of color space. *Vision Research*, *22*(9), 1123–1131. https://doi.org/10.1016/0042-6989(82)90077-3

Kuang, J., Johnson, G. M., & Fairchild, M. (2007). iCAM06: A refined image appearance model for HDR image rendering. *Journal of Visual Communication and Image Representation*, *18*(5). https://doi.org/10.1016/j.jvcir.2007.06.003

Kuang, J., Johnson, G. M., & Fairchild, M. (2006). ICAM for high-dynamic-range image rendering. *Proceedings of the 3rd Symposium on Applied Perception in Graphics and Visualization - APGV '06*, 151. https://doi.org/10.1145/1140491.1140528

Kuang, J., Yamaguchi, H., Liu, C., Johnson, G. M., & Fairchild, M. (2007). Evaluating HDR rendering algorithms. *ACM Transactions on Applied Perception*, *4*(2), 9-es. https://doi.org/10.1145/1265957.1265958

Land, E. H. (1977). The retinex theory of color vision. *Scientific American*, *237*(6), 108–129.

Land, E. H. (1986). An alternative technique for the computation of the designator in the retinex theory of color vision. *Proceedings of the National Academy of Sciences*, *83*(10), 3078–3080.

Land, E. H., & McCann, J. J. (1971). Lightness and Retinex Theory. *Journal of the Optical Society of America*, *61*(1), 1. https://doi.org/10.1364/JOSA.61.000001

Larson, G. W., Rushmeier, H., & Piatko, C. (1997). A visibility matching tone reproduction operator for high dynamic range scenes. *IEEE Transactions on Visualization and Computer Graphics*, *3*(4), 291–306. https://doi.org/10.1109/2945.646233

Ledda, P., Chalmers, A., & Seetzen, H. (2004). A psychophysical validation of tone mapping operators using a high dynamic range display. *Proceedings of the 1st Symposium on Applied Perception in Graphics and Visualization - APGV '04*, 159. https://doi.org/10.1145/1012551.1012581

Lee, B. B., Martin, P. R., & Valberg, A. (1988). The physiological basis of heterochromatic flicker photometry demonstrated in the ganglion cells of the macaque retina. *The Journal of Physiology*, *404*(1), 323–347. https://doi.org/10.1113/jphysiol.1988.sp017292

Lewis, E., Schoppelrei, J., Lee, E., & Kidder, L. (2008). Near-infrared chemical imaging as a process analytical tool. *Process Analytical Technology*, 187.

Li, C., Ji, C., Luo, R., Melgosa, M., & Brill, M. H. (2015). CAT02 and HPE triangles. *Color Research & Application*, *40*(1), 30–39. https://doi.org/10.1002/col.21859

Li, C., Li, Z., Wang, Z., Xu, Y., Luo, M. R., Cui, G., Melgosa, M., Brill, M. H., & Pointer, M. (2017). Comprehensive color solutions: CAM16, CAT16, and CAM16-UCS. *Color Research & Application*, *42*(6), 703–718. https://doi.org/10.1002/col.22131

Li, C., Luo, M. R., Rigg, B., & Hunt, R. W. G. (2002). CMC 2000 chromatic adaptation transform: CMCCAT2000. *Color Research & Application*, *27*(1), 49–58. https://doi.org/10.1002/col.10005

Li, C., Luo, M. R., & Sun, P.-L. (2013). A Modification of CIECAM02 Based on the Hunt-Pointer-Estevez Matrix. *Journal of Imaging Science and Technology*, *57*(3). https://doi.org/10.2352/J.ImagingSci.Technol.2013.57.3.030502

Li, C., Luo, M. R., & Wang, Z. (2014). Different matrices for CIECAM02. *Color Research & Application*, *39*(2), 143–153. https://doi.org/10.1002/col.21765

Li, J., Hanselaer, P., & Smet, K. (2019). PILOT STUDY ON COLOR MATCHING ACCURACY USING DIFFERENT PRIMARIES. *PROCEEDINGS OF the 29th Quadrennial Session of the CIE*, 1010–1018. https://doi.org/10.25039/x46.2019.PO038

Liang, H. (2012). Advances in multispectral and hyperspectral imaging for archaeology and art conservation. *Applied Physics A*, *106*(2), 309–323. https://doi.org/10.1007/s00339-011-6689-1

Lin, S., & Hanrahan, P. (2013). *Modeling how people extract color themes from images*. 3101–3110.

Lin, Y., Wei, M., Smet, K., Tsukitani, A., Bodrogi, P., & Khanh, T. (2017). Colour preference varies with lighting application. *Lighting Research & Technology*, *49*(3), 316–328. https://doi.org/10.1177/1477153515611458

Linhares, J. M. M., Pinto, P. D., & Nascimento, S. M. C. (2008). The number of discernible colors in natural scenes. *Journal of the Optical Society of America A*, *25*(12), 2918. https://doi.org/10.1364/JOSAA.25.002918

LPR 60. (2017, March). *Application of CIE 2015 Cone-Fundamental Based CIE Colorimetry*. *60*. http://files.cie.co.at/LpR%2060%20CIE%20RESEARCH%20Special%20-%20Cone-Fundamental-Based%20CIE%20Colorimetry.pdf

Lu, H., Ooi, B.-C., & Tan, K.-L. (1994). Efficient Image Retrieval By Color Contents. In W. Litwin & T. Risch (Eds.), *Applications of Databases* (Vol. 819, pp. 95–108). Springer Berlin Heidelberg. https://doi.org/10.1007/3-540-58183-9_43

Luo, M., & Hunt, R. (1998). A chromatic adaptation transform and a colour inconstancy index. *Color Research & Application: Endorsed by Inter-Society Color Council, The Colour Group (Great Britain), Canadian Society for Color, Color Science Association of Japan, Dutch Society for the Study of Color,*

The Swedish Colour Centre Foundation, Colour Society of Australia, Centre Français de La Couleur, *23*(3), 154–158.

Luo, M., & Lv, X. (2019). LED SIMULATORS FOR THE REPRODUCTION OF THE NEW CIE STANDARD LED SOURCES. *PROCEEDINGS OF the 29th Quadrennial Session of the CIE*, 93–100. https://doi.org/10.25039/x46.2019.OP16

Luo, M. R. (1996). *LLAB model for color appearance and color difference evaluation* (J. Bares, Ed.; pp. 261–269). https://doi.org/10.1117/12.236975

Luo, M. R., Clarke, A. A., Rhodes, P. A., Schappo, A., Scrivener, S. A. R., & Tait, C. J. (1991). Quantifying colour appearance. Part I. Lutchi colour appearance data. *Color Research & Application*, *16*(3), 166–180. https://doi.org/10.1002/col.5080160307

Luo, M. R., Cui, G., & Li, C. (2006). Uniform colour spaces based on CIECAM02 colour appearance model. *Color Research & Application*, *31*(4), 320–330. https://doi.org/10.1002/col.20227

Luo, M. R., Gao, X. W., Rhodes, P. A., Xin, H. J., Clarke, A. A., & Scrivener, S. A. R. (1993). Quantifying colour appearance. Part IV. Transmissive media. *Color Research & Application*, *18*(3), 191–209. https://doi.org/10.1002/col.5080180309

Luo, M. R., & Hunt, R. W. G. (1998). Testing colour appearance models using corresponding-colour and magnitude-estimation data sets. *Color Research & Application*, *23*(3), 147–153. https://doi.org/10.1002/(SICI)1520-6378(199806)23:3<147::AID-COL6>3.0.CO;2-Q

Luo, M. R., & Pointer, M. (2018). CIE colour appearance models: A current perspective. *Lighting Research & Technology*, *50*(1), 129–140. https://doi.org/10.1177/1477153517722053

M. Stone. (2012). In Color Perception, Size Matters. *IEEE Computer Graphics and Applications*, *32*(2), 8–13. https://doi.org/10.1109/MCG.2012.37

Ma, S., Hanselaer, P., Teunissen, K., & Smet, K. A. G. (2019). Evaluation and modification of von Kries chromatic adaptation transform. *Color and Imaging Conference*, *2019*(1), 23–27. https://doi.org/10.2352/issn.2169-2629.2019.27.6

MacAdam, D. L. (1942). Visual Sensitivities to Color Differences in Daylight*. *Journal of the Optical Society of America*, *32*(5), 247. https://doi.org/10.1364/JOSA.32.000247

MacAdam, D. L. (1961). A nonlinear hypothesis for chromatic adaptation. *Vision Research*, *1*(1–2), 9–41. https://doi.org/10.1016/0042-6989(61)90020-7

MacAdam, D. L. (1993). *Selected papers on colorimetry-fundamentals* (Vol. 77). Society of Photo Optical.

MacDonald, L. W., Vitorino, T., Picollo, M., Pillay, R., Obarzanowski, M., Sobczyk, J., Nascimento, S., & Linhares, J. (2017). Assessment of multispectral and hyperspectral imaging systems for digitisation of a Russian icon. *Heritage Science*, *5*(1), 41. https://doi.org/10.1186/s40494-017-0154-1

Mansurov, N. (2020, April 6). *Understanding Aperture in Photography*. https://photographylife.com/what-is-aperture-in-photography#:~:text=What%20is%20Aperture%3F-,Aperture%20can%20be%20defined%20as%20the%20opening%20in%20a%20lens,the%20lens%20or%20the%20camera.

Marmion, M. (2016). *The Top 10 Questions about Hyperspectral Imaging (Part 2 of 2)*. https://www.specim.fi/the-top-10-questions-about-hyperspectral-imaging-part-2-of-2/

Martin, D., Fowlkes, C., Tal, D., & Malik, J. (2001). A database of human segmented natural images and its application to evaluating segmentation algorithms and measuring ecological statistics. *Proceedings Eighth IEEE International Conference on Computer Vision. ICCV 2001*, *2*, 416–423. https://doi.org/10.1109/ICCV.2001.937655

Martínez-Domingo, M. Á., Melgosa, M., Okajima, K., Medina, V. J., & Collado-Montero, F. J. (2019). Spectral Image Processing for Museum Lighting Using CIE LED Illuminants. *Sensors*, *19*(24), 5400. https://doi.org/10.3390/s19245400

Masuda, O., & Nascimento, S. M. C. (2013). Best lighting for naturalness and preference. *Journal of Vision*, *13*(7), 4–4. https://doi.org/10.1167/13.7.4

McLAREN, K. (1976). The Development of the CIE 1976 (L* a* b*) Uniform Colour Space and Colour-difference Formula. *Journal of the Society of Dyers and Colourists*, *92*(9), 338–341. https://doi.org/10.1111/j.1478-4408.1976.tb03301.x

Mehtre, B. M., Kankanhalli, M. S., Desai Narasimhalu, A., & Chang Man, G. (1995). Color matching for image retrieval. *Pattern Recognition Letters*, *16*(3), 325–331. https://doi.org/10.1016/0167-8655(94)00096-L

Merzougui, M., & Allaoui, A. E. (2019). Region growing segmentation optimized by evolutionary approach and Maximum Entropy. *Procedia Computer Science*, *151*, 1046–1051. https://doi.org/10.1016/j.procs.2019.04.148

Meyer, G. W. (1988). Wavelength selection for synthetic image generation. *Computer Vision, Graphics, and Image Processing*, *41*(1), 57–79. https://doi.org/10.1016/0734-189X(88)90117-X

Millington, E. C. (1942). History of the Young-Helmholtz theory of colour vision. *Annals of Science*, *5*(2), 167–176. https://doi.org/10.1080/00033794200201421

Mittal, A., Moorthy, A. K., & Bovik, A. C. (2011). Blind/Referenceless Image Spatial Quality Evaluator. *2011 Conference Record of the Forty Fifth Asilomar Conference on Signals, Systems and Computers (ASILOMAR)*, 723–727. https://doi.org/10.1109/ACSSC.2011.6190099

Mittal, A., Soundararajan, R., & Bovik, A. C. (2013). Making a "Completely Blind" Image Quality Analyzer. *IEEE Signal Processing Letters*, *20*(3), 209–212. https://doi.org/10.1109/LSP.2012.2227726

Mokrzycki, W., & Tatol, M. (2011). Color difference Delta E - A survey. *Machine Graphics and Vision*, *20*, 383–411.

Montagner, C., Linhares, J. M. M., Vilarigues, M., & Nascimento, S. M. C. (2016). Statistics of colors in paintings and natural scenes. *Journal of the Optical Society of America A*, *33*(3), A170. https://doi.org/10.1364/JOSAA.33.00A170

Mordinstov, A., & K, A. (2013). *Smoothing Images*. https://opencv-python-tutroals.readthedocs.io/en/latest/py_tutorials/py_imgproc/py_filtering/py_filtering.html

Munsell Renotation Data. (1967). https://www.rit.edu/cos/colorscience/rc_munsell_renotation.php

N. M. Kalmus. (1935). Color Consciousness. *Journal of the Society of Motion Picture Engineers*, *25*(2), 139–147. https://doi.org/10.5594/J05386

Nascimento, S. M. C. (2011). *Seeing colors in real scenes* (M. F. Costa, Ed.; p. 800102). https://doi.org/10.1117/12.888633

Nascimento, S. M. C., Amano, K., & Foster, D. H. (2016). Spatial distributions of local illumination color in natural scenes. *Vision Research*, *120*, 39–44. https://doi.org/10.1016/j.visres.2015.07.005

Nascimento, S. M. C., & Masuda, O. (2014). Best lighting for visual appreciation of artistic paintings—Experiments with real paintings and real illumination. *Journal of the Optical Society of America A*, *31*(4), A214. https://doi.org/10.1364/JOSAA.31.00A214

Nayatani, Y. (1995). Revision of the chroma and hue scales of a nonlinear color-appearance model. *Color Research & Application*, *20*(3), 143–155. https://doi.org/10.1002/col.5080200304

Nayatani, Y. (1997a). A simple estimation method for effective adaptation coefficient. *Color Research & Application: Endorsed by Inter-Society Color Council, The Colour Group (Great Britain), Canadian Society for Color, Color Science Association of Japan, Dutch Society for the Study of Color, The Swedish Colour Centre Foundation, Colour Society of Australia, Centre Français de La Couleur*, *22*(4), 259–268.

Nayatani, Y. (1997b). Examination of adaptation coefficients for incomplete chromatic adaptation. *Color Research & Application: Endorsed by Inter-Society Color Council, The Colour Group (Great Britain), Canadian Society for Color, Color Science Association of Japan, Dutch Society for the Study of Color, The Swedish Colour Centre Foundation, Colour Society of Australia, Centre Français de La Couleur*, *22*(3), 156–164.

Nayatani, Y., Hashimoto, K., Takahama, K., & Sobagaki, H. (1987). A nonlinear color-appearance model using estévez-hunt-pointer primaries. *Color Research & Application*, *12*(5), 231–242. https://doi.org/10.1002/col.5080120504

Nayatani, Y., Sobagaki, H., & Hashimoto, K. (1994). Existence of two kinds of representations of the helmholtz-kohlrausch effect. I. the experimental confirmation. *Color Research & Application*, *19*(4), 246–261. https://doi.org/10.1002/col.5080190405

Nayatani, Y., Takahama, K., & Sobagaki, H. (1981). Formulation of a Nonlinear Model of Chromatic Adaptation. *Color Research & Application*, *6*(3), 161–171. https://doi.org/10.1002/col.5080060308

Nayatani, Y., Takahama, K., & Sobagaki, H. (1986). Prediction of color appearance under various adapting conditions. *Color Research & Application*, *11*(1), 62–71. https://doi.org/10.1002/col.5080110112

Newhall, S. M. (1940). Preliminary Report of the OSA Subcommittee on the Spacing of the Munsell Colors. *Journal of the Optical Society of America*, *30*(12), 617. https://doi.org/10.1364/JOSA.30.000617

Oakley Prizm. (2018). *Oakley Prizm*. https://www.oakley.com/en-eu/PRIZM

Ohno, Y., & Blattner, P. (2014). CIE Chromaticity difference specification for light sources. *International Commission on Illumination, Tech. Rep. CIE TN*, *1*, 2014.

Ohno, Y., Kawashima, Y., Oh, S., & Kwak, Y. (2019). VISUAL EVALUATION OF CIE 2015 CONE FUNDAMENTAL-BASED 10° COLOUR MATCHING FUNCTIONS FOR LIGHTING APPLICATIONS. *PROCEEDINGS OF the 29th Quadrennial Session of the CIE*, 505–514. https://doi.org/10.25039/x46.2019.OP69

Oicherman, B., Luo, M. R., Rigg, B., & Robertson, A. R. (2008). Effect of observer metamerism on colour matching of display and surface colours. *Color Research & Application*, *33*(5), 346–359. https://doi.org/10.1002/col.20429

Ong, S. H., Yeo, N. C., Lee, K. H., Venkatesh, Y. V., & Cao, D. M. (2002). Segmentation of color images using a two-stage self-organizing network. *Image and Vision Computing*, *20*(4), 279–289. https://doi.org/10.1016/S0262-8856(02)00021-5

Paris, S., & Durand, F. (2009). A Fast Approximation of the Bilateral Filter Using a Signal Processing Approach. *International Journal of Computer Vision*, *81*(1), 24–52. https://doi.org/10.1007/s11263-007-0110-8

Párraga, C. A., Brelstaff, G., Troscianko, T., & Moorehead, I. R. (1998). Color and luminance information in natural scenes. *Journal of the Optical Society of America A*, *15*(3), 563. https://doi.org/10.1364/JOSAA.15.000563

Petrulis, A., Vitta, P., Aglinskaitė, J., Vaicekauskas, R., & Žukauskas, A. (2017). Metameric Light Sources: A Recent Paradigm for Functional Lighting. *Proceedings of the Latvian Academy of Sciences. Section B. Natural, Exact, and Applied Sciences.*, *71*(5), 366–371. https://doi.org/10.1515/prolas-2017-0062

Pinto, P. D., Linhares, J. M. M., Carvalhal, J. A., & Nascimento, S. M. C. (2006). Psychophysical estimation of the best illumination for appreciation of Renaissance paintings. *Visual Neuroscience*, *23*(3–4), 669–674. https://doi.org/10.1017/S0952523806233340

Pinto, P. D., Linhares, J. M. M., & Nascimento, S. M. C. (2008). Correlated color temperature preferred by observers for illumination of artistic paintings. *Journal of the Optical Society of America A*, *25*(3), 623. https://doi.org/10.1364/JOSAA.25.000623

Prasad, D. K., & Wenhe, L. (2015). Metrics and statistics of frequency of occurrence of metamerism in consumer cameras for natural scenes. *Journal of the Optical Society of America A*, *32*(7), 1390. https://doi.org/10.1364/JOSAA.32.001390

Purdy, D. McL. (1931). Spectral Hue as a Function of Intensity. *The American Journal of Psychology*, *43*(4), 541. https://doi.org/10.2307/1415157

Ramanath, R. (2009). Minimizing observer metamerism in display systems. *Color Research & Application*, *34*(5), 391–398. https://doi.org/10.1002/col.20523

Raza, A., Jost-Boissard, S., & Dubail, M. (2020). *Dominant color and Image color composition retrieval from complex images*. 378–382. https://aic2020.org/wp-content/uploads/2021/03/AIC2020_PROCEEDINGS_20210318-final.pdf

Raza, A., Jost-Boissard, S., Dubail, M., & Dumortier, D. (2021a, 02). Automatic colour segmentation and colour palette identification of complex images. *Journal of International Colour Association*, 11–21. https://www.aic-color.org/resources/Documents/jaic_v26_02.pdf

Raza, A., Jost-Boissard, S., Dubail, M., & Dumortier, D. (2021b). Categorizing color shifts due to tinted glazing via dominant colors of the scene. *Color Research & Application*, *46*(3), 623–634. https://doi.org/10.1002/col.22629

Raza, A., Jost-Boissard, S., Dubail, M., & Dumortier, D. (2019). SIMPLIFIED HYPERSPECTRAL CAMERA CALIBRATION FOR ACCURATE RADIOMETRIC MEASUREMENTS. *PROCEEDINGS OF the 29th Quadrennial Session of the CIE*, 636–646. https://doi.org/10.25039/x46.2019.OP92

Reinhard, E., & Devlin, K. (2005). Dynamic Range Reduction Inspired by Photoreceptor Physiology. *IEEE Transactions on Visualization and Computer Graphics*, *11*(01), 13–24. https://doi.org/10.1109/TVCG.2005.9

Reinhard, E., Stark, M., Shirley, P., & Ferwerda, J. (2002). Photographic tone reproduction for digital images. *ACM Transactions on Graphics*, *21*(3), 267–276. https://doi.org/10.1145/566654.566575

Rousseeuw, P. J. (1987). Silhouettes: A graphical aid to the interpretation and validation of cluster analysis. *Journal of Computational and Applied Mathematics*, *20*, 53–65. https://doi.org/10.1016/0377-0427(87)90125-7

Royer, M. P. (2018). Comparing Measures of Average Color Fidelity. *LEUKOS*, *14*(2), 69–85. https://doi.org/10.1080/15502724.2017.1389283

Royer, M., Wilkerson, A., Wei, M., Houser, K., & Davis, R. (2017). Human perceptions of colour rendition vary with average fidelity, average gamut, and gamut shape. *Lighting Research & Technology*, *49*(8), 966–991. https://doi.org/10.1177/1477153516663615

Rushton, W. A. H. (1972). Visual Pigments in Man. In H. J. A. Dartnall (Ed.), *Photochemistry of Vision: Vol. 7 / 1* (pp. 364–394). Springer Berlin Heidelberg. https://doi.org/10.1007/978-3-642-65066-6_9

Ruttum, M., & Von Noorden, G. K. (1984). The Bagolini striated lens test for cyclotropia. *Documenta Ophthalmologica*, *58*(1), 131–139. https://doi.org/10.1007/BF00140911

Safdar, M., Cui, G., Kim, Y. J., & Luo, M. R. (2017a). *MATLAB code for forward and reverse models of Jzazbz uniform color space*.

Safdar, M., Cui, G., Kim, Y. J., & Luo, M. R. (2017b). Perceptually uniform color space for image signals including high dynamic range and wide gamut. *Optics Express*, *25*(13), 15131. https://doi.org/10.1364/OE.25.015131

Sarkar, A., Blondé, L., Callet, P. L., Autrusseau, F., Morvan, P., & Stauder, J. (2010). *Toward reducing observer metamerism in industrial applications: Colorimetric observer categories and observer classification*. *2010*(1), 307–313.

Saylor, R. (2015). *Eyewear and lenses with multiple molded lens components.* (Patent No. WO 2015179538 A1).

Schanda, J. (Ed.). (2007). *Colorimetry: Understanding th CIE system*. Wiley.

Semmelroth, C. C. (1970). Prediction of Lightness and Brightness on Different Backgrounds. *Journal of the Optical Society of America*, *60*(12), 1685. https://doi.org/10.1364/JOSA.60.001685

Sethi, I. K., Coman, I. L., Day, B., Jiang, F., Li, D., Segovia-Juarez, J., Wei, G., & You, B.-M. (1997). *Color-WISE: A system for image similarity retrieval using color* (I. K. Sethi & R. C. Jain, Eds.; pp. 140–149). https://doi.org/10.1117/12.298438

Sharma, G., Wu, W., & Dalal, E. N. (2005). The CIEDE2000 color-difference formula: Implementation notes, supplementary test data, and mathematical observations. *Color Research & Application*, *30*(1), 21–30. https://doi.org/10.1002/col.20070

Shevell, S. K. (1978). The dual role of chromatic backgrounds in color perception. *Vision Research*, *18*(12), 1649–1661. https://doi.org/10.1016/0042-6989(78)90257-2

Shevell, S. K., Holliday, I., & Whittle, P. (1992). Two separate neural mechanisms of brightness induction. *Vision Research*, *32*(12), 2331–2340. https://doi.org/10.1016/0042-6989(92)90096-2

Shevell, S. K., & Humanski, R. A. (1988). Color perception under chromatic adaptation: Red/green equilibria with adapted short-wavelength-sensitive cones. *Vision Research*, *28*(12), 1345–1356. https://doi.org/10.1016/0042-6989(88)90066-1

Shi, S., Gong, X., Mu, Y., Finch, K., & Gamez, G. (2018). Geometric super-resolution on push-broom hyperspectral imaging for plasma optical emission spectroscopy. *J. Anal. At. Spectrom.*, *33*(10), 1745–1752. https://doi.org/10.1039/C8JA00235E

Sliney, D. H. (2001). Photoprotection of the eye – UV radiation and sunglasses. *Journal of Photochemistry and Photobiology B: Biology*, *64*(2–3), 166–175. https://doi.org/10.1016/S1011-1344(01)00229-9

Smet, K., & Hanselaer, P. (2015). Impact of cross-regional differences on color rendition evaluation of white light sources. *Optics Express*, *23*, 30216. https://doi.org/10.1364/OE.23.030216

Smet, K., & Hanselaer, P. (2016). Memory and preferred colours and the colour rendition of white light sources. *Lighting Research & Technology*, *48*(4), 393–411. https://doi.org/10.1177/1477153514568584

Smet, K., Lin, Y., Nagy, B. V., Németh, Z., Duque-Chica, G. L., Quintero, J. M., Chen, H.-S., Luo, R. M., Safi, M., & Hanselaer, P. (2014). Cross-cultural variation of memory colors of familiar objects. *Optics Express*, *22*(26), 32308. https://doi.org/10.1364/OE.22.032308

Smet, K., & Ma, S. (2020). Some concerns regarding the CAT16 chromatic adaptation transform. *Color Research & Application*, *45*(1), 172–177.

Smet, K., Ryckaert, W. R., Pointer, M. R., Deconinck, G., & Hanselaer, P. (2011). Correlation between color quality metric predictions and visual appreciation of light sources. *Optics Express*, *19*(9), 8151. https://doi.org/10.1364/OE.19.008151

Smet, K., Ryckaert, W. R., Pointer, M. R., Deconinck, G., & Hanselaer, P. (2012). A memory colour quality metric for white light sources. *Energy and Buildings*, *49*, 216–225. https://doi.org/10.1016/j.enbuild.2012.02.008

Smet, K., Whitehead, L., Schanda, J., & Luo, R. M. (2016). Toward a Replacement of the CIE Color Rendering Index for White Light Sources. *LEUKOS*, *12*(1–2), 61–69. https://doi.org/10.1080/15502724.2014.994747

Smet, K., Zhai, Q., Luo, M. R., & Hanselaer, P. (2017). Study of chromatic adaptation using memory color matches, Part I: neutral illuminants. *Opt. Express*, *25*(7), 7732–7748. https://doi.org/10.1364/OE.25.007732

Smith, J. R., & Chang, S.-F. (1996). *Tools and techniques for color image retrieval* (I. K. Sethi & R. C. Jain, Eds.; pp. 426–437). https://doi.org/10.1117/12.234781

Sobagaki, H., Yamanaka, T., Takahama, K., & Nayatani, Y. (1974). Chromatic-adaptation study by subjective-estimation method. *Journal of the Optical Society of America*, *64*(6), 743. https://doi.org/10.1364/JOSA.64.000743

Stabell, B., & Stabell, U. (1974). Chromatic rod-cone interaction. *Vision Research*, *14*(12), 1389–1392. https://doi.org/10.1016/0042-6989(74)90013-3

Stevens, J. C., & Stevens, S. S. (1963). Brightness Function: Effects of Adaptation*. *Journal of the Optical Society of America*, *53*(3), 375. https://doi.org/10.1364/JOSA.53.000375

Stiles, W. S., & Burch, J. M. (1959). N.P.L. Colour-matching Investigation: Final Report (1958). *Optica Acta: International Journal of Optics*, *6*(1), 1–26. https://doi.org/10.1080/713826267

Stockman, A., & Sharpe, L. T. (2000). The spectral sensitivities of the middle- and long-wavelength-sensitive cones derived from measurements in observers of known genotype. *Vision Research*, *40*(13), 1711–1737. https://doi.org/10.1016/S0042-6989(00)00021-3

Stricker, M. A., & Orengo, M. (1995). *Similarity of color images* (W. Niblack & R. C. Jain, Eds.; p. 381). https://doi.org/10.1117/12.205308

Stricker & Swain. (1994). The capacity of color histogram indexing. *Proceedings of IEEE Conference on Computer Vision and Pattern Recognition CVPR-94*, 704–708. https://doi.org/10.1109/CVPR.1994.323774

Sural, S., Gang Qian, & Pramanik, S. (2002). Segmentation and histogram generation using the HSV color space for image retrieval. *Proceedings. International Conference on Image Processing*, *2*, II-589-II–592. https://doi.org/10.1109/ICIP.2002.1040019

Suzuki, S., Shimizu, M., & Semba, S. (1999). High-accuracy Color Reproduction (Color Management Systems). *FUJITSU Sci. Tech. J*, 240–247.

Talib, A., Mahmuddin, M., Husni, H., & George, L. (2013). Efficient, Compact, and Dominant Color Correlogram Descriptors for Content-based Image Retrieval. *MMEDIA 2013 - 5th International Conferences on Advances in Multimedia*.

Tan, J., Lien, J.-M., & Gingold, Y. (2016). Decomposing images into layers via RGB-space geometry. *ACM Transactions on Graphics (TOG)*, *36*(1), 1–14.

Tremeau, A., & Borel, N. (1997). A region growing and merging algorithm to color segmentation. *Pattern Recognition*, *30*(7), 1191–1203. https://doi.org/10.1016/S0031-3203(96)00147-1

Tulet, O., Larabi, M.-C., & Fernandez-Maloigne, C. (2008). Image Rendering Based on a Spatial Extension of the CIECAM02. *2008 IEEE Workshop on Applications of Computer Vision*, 1–6. https://doi.org/10.1109/WACV.2008.4544030

UEF. (n.d.). *Joensuu spectral image database*. https://sites.uef.fi/spectral/databases-software/spectral-image-database/

van der Burgt, P., & van Kemenade, J. (2010). About color rendition of light sources: The balance between simplicity and accuracy. *Color Research & Application*, NA-NA. https://doi.org/10.1002/col.20546

Varilux RoadPilot. (2017). *VARILUX® ROADPILOT*. https://www.essilor.fr/nos-verres/varilux/tous-les-verres-progressifs-varilux#roadpilot

Varilux Sport. (2008). *VARILUX® SPORT*. https://www.essilor.fr/nos-verres/varilux/tous-les-verres-progressifs-varilux#activites

Vienot, F., Benhalima, F., & Brettel, H. (2002). *Procédé pour l'obtention d'une gamme de couleurs* (Patent No. FR2826450 B1).

Viénot, F., Brettel, H., Dang, T.-V., & Le Rohellec, J. (2012). Domain of metamers exciting intrinsically photosensitive retinal ganglion cells (ipRGCs) and rods. *Journal of the Optical Society of America A*, *29*(2), A366. https://doi.org/10.1364/JOSAA.29.00A366

Vilaseca, M., Schael, B., Delpueyo, X., Chorro, E., Perales, E., Hirvonen, T., & Pujol, J. (2014). Repeatability, reproducibility, and accuracy of a novel pushbroom hyperspectral system. *Color Research & Application*, *39*(6), 549–558. https://doi.org/10.1002/col.21851

Vitorino, T., Casini, A., Cucci, C., Gebejesje, A., Hiltunen, J., Hauta-Kasari, M., Picollo, M., & Stefani, L. (2015). Accuracy in Colour Reproduction: Using a ColorChecker Chart to Assess the Usefulness and Comparability of Data Acquired with Two Hyper-Spectral Systems. In A. Trémeau, R. Schettini, & S. Tominaga (Eds.), *Computational Color Imaging* (Vol. 9016, pp. 225–235). Springer International Publishing. https://doi.org/10.1007/978-3-319-15979-9_21

Von Helmholtz, H. (1867). *Handbuch der physiologischen Optik: Mit 213 in den Text eingedruckten Holzschnitten und 11 Tafeln* (Vol. 9). Voss.

von Kries, J. (1902). *Chromatic Adaptation, Festschrift der Albercht-Ludwig-Universität*.

Walraven, J. (1976). Discounting the background—The missing link in the explanation of chromatic induction. *Vision Research*, *16*(3), 289–295. https://doi.org/10.1016/0042-6989(76)90112-7

Walraven, J., Enroth-Cugell, C., Hood, D. C., MacLeod, D. I. A., & Schnapf, J. L. (1990). The control of visual sensitivity: Receptoral and postreceptoral processes. In *Visual perception: The neurophysiological foundations.* (pp. 53–101). Academic Press.

Wang, X., Zhang, Y., Ma, X., Xu, T., & Arce, G. R. (2018). Compressive spectral imaging system based on liquid crystal tunable filter. *Optics Express*, *26*(19), 25226–25243. https://doi.org/10.1364/OE.26.025226

Wang, Y., Lv, X., Wei, M., & Luo, M. (2019). PROPOSAL OF A NEW WHITENESS FORMULA BASED ON CAM16-UCS. *PROCEEDINGS OF the 29th Quadrennial Session of the CIE*, 521–524. https://doi.org/10.25039/x46.2019.OP71

Wang, Z., Li, Z., Luo, R., Zhang, X., & Li, C. (2016). Can the Problems of CIECAM02 Be Overcome without Losing Predicting Accuracy? *Electronic Imaging*, *2016*(20), 1–4. https://doi.org/10.2352/ISSN.2470-1173.2016.20.COLOR-322

Webster, M. (2015). Environmental Influences on Color Vision. In R. Luo (Ed.), *Encyclopedia of Color Science and Technology* (pp. 1–6). Springer Berlin Heidelberg. https://doi.org/10.1007/978-3-642-27851-8_76-3

Webster, M. A., & Mollon, J. D. (1994). The influence of contrast adaptation on color appearance. *Vision Research*, *34*(15), 1993–2020. https://doi.org/10.1016/0042-6989(94)90028-0

Wei, M., Houser, K., David, A., & Krames, M. (2017). Colour gamut size and shape influence colour preference. *Lighting Research & Technology*, *49*(8), 992–1014. https://doi.org/10.1177/1477153516651472

Wei, M., Houser, K. W., Allen, G. R., & Beers, W. W. (2014). Color Preference under LEDs with Diminished Yellow Emission. *LEUKOS*, *10*(3), 119–131. https://doi.org/10.1080/15502724.2013.865212

Wei, M., Ma, S., Wang, Y., & Luo, M. R. (2017). Evaluation of whiteness formulas for FWA and non-FWA whites. *Journal of the Optical Society of America A*, *34*(4), 640. https://doi.org/10.1364/JOSAA.34.000640

Westland, S., Ripamonti, C., & Cheung, V. (2012). *Computational colour science using MATLAB* (2nd ed). Wiley.

Worring, M., & Gevers, T. (2001). INTERACTIVE RETRIEVAL OF COLOR IMAGES. *International Journal of Image and Graphics*, *01*(03), 387–414. https://doi.org/10.1142/S0219467801000244

Wright, W. D. (1929). A re-determination of the trichromatic coefficients of the spectral colours. *Transactions of the Optical Society*, *30*(4), 141–164. https://doi.org/10.1088/1475-4878/30/4/301

Wyszecki, G., & Stiles, W. S. (1982). *Color science* (Vol. 8). Wiley New York.

Wyszecki, G., & Stiles, W. S. (2000). *Color science: Concepts and methods, quantitative data, and formulae* (Wiley classics library ed). John Wiley & Sons.

Xu, Q., & Luo, M. (2019). EXTENSION OF COLOUR DIFFERENCE FORMULAE FOR HDR APPLICATIONS. *PROCEEDINGS OF the 29th Quadrennial Session of the CIE*, 151–156. https://doi.org/10.25039/x46.2019.OP25

Yihong, G., Hongjiang, Z., & Chuan, C. H. (1994). An image database system with fast image indexing capability based on color histograms. *Proceedings of TENCON'94 - 1994 IEEE Region 10's 9th Annual International Conference on: "Frontiers of Computer Technology,"* 407–411. https://doi.org/10.1109/TENCON.1994.369269

Yoshida, A., Blanz, V., Myszkowski, K., & Seidel, H.-P. (2005). *Perceptual evaluation of tone mapping operators with real-world scenes* (B. E. Rogowitz, T. N. Pappas, & S. J. Daly, Eds.; p. 192). https://doi.org/10.1117/12.587782

Young, T. (1802). II. The Bakerian Lecture. On the theory of light and colours. *Philosophical Transactions of the Royal Society of London*, *92*, 12–48. https://doi.org/10.1098/rstl.1802.0004

Zele, A. J., Feigl, B., Adhikari, P., Maynard, M. L., & Cao, D. (2018). Melanopsin photoreception contributes to human visual detection, temporal and colour processing. *Scientific Reports*, *8*(1), 3842. https://doi.org/10.1038/s41598-018-22197-w

Zheng, H., Cheng, T., Li, D., Zhou, X., Yao, X., Tian, Y., Cao, W., & Zhu, Y. (2018). Evaluation of RGB, Color-Infrared and Multispectral Images Acquired from Unmanned Aerial Systems for the Estimation of Nitrogen Accumulation in Rice. *Remote Sensing*, *10*(6), 824. https://doi.org/10.3390/rs10060824

Annexes

Annex I: Statistical Definitions

Significance: The results of a statistical hypothesis being significant implies that the tested dataset/population have a difference that is not a random occurrence, and is ascertained by a measure of probability: p-value$<$0,05. A p-value $>$0,05 suggests an absence of significant difference.

Null hypothesis: A null hypothesis is a typical conjecture used during statistical analysis that shows that the compared population/dataset have no significant differences. The alternative hypothesis proposes that there is a difference.

Wilcoxon signed rank test: The Wilcoxon signed rank test compares the sample median against a hypothetical median. The null hypothesis for this test is that the medians of two samples are equal. The advantage of using this test for repeatability is that it does not require normal distribution of data, which is rare for the size of data compared in the repeatability test for one condition.

ANOVA: ANOVA or Analysis Of Variance is a test that helps us identify if there are significant differences between the tested groups. It tests the data for the null hypothesis that the test groups belong to a same population and rejects the null hypothesis at a p$<$0,05 when the tested groups have significant differences in a statistic (mean, median etc).

Factorial ANOVA: A Factorial ANOVA is a special type of ANOVA that performs ANOVA on multiple factors (2 or more) and at the same times studies the interactions between each independent factor.

Tukey's HSD posthoc test: The results of ANOVA/Factorial ANOVA ascertain the presence of a significant difference among tested groups and variables. A Tukey's HSD (Honest Significant Difference) posthoc test identifies these groups and variable. It identifies the specific groups, which have a significant difference in their mean values.

Annex II: Experimental Instructions

Instructions pour l'expérience

Avant de rentrer dans la pièce, je tiens à vous prévenir de ne pas lever les yeux vers la source de lumière pour éviter les effets de la fatigue oculaire et de l'éblouissement qui rendraient l'expérience impossible.

Je vous demanderais de vous asseoir sur la chaise en face de moi (dans le noir).

Dans cette expérience, vous allez comparer la reproduction des couleurs d'une scène projetée sur un écran d'ordinateur à la scène réelle (référence) située juste à côté de l'ordinateur, avec ou sans lunettes teintées.

En fonction de la combinaison de scènes, vous serez équipé de l'une des trois montures de verre qui n'ont qu'une lentille pour un œil.

Le côté de la monture équipé d'une lentille permet de visualiser la scène réelle (la cabine lumineuse), tandis que la partie sans lentille permet de voir l'écran sur lequel le filtre est déjà appliqué.

La scène est composée de fruits, de légumes, de fleurs pour vous permettre de juger de la fidélité de la reproduction des couleurs.

Vous allez comparer la fidélité de reproduction des couleurs sur une échelle de 0 à 10, avec un pas de 0,5 pour différentes combinaisons d'éclairage et de lentilles, appelées ici stimulus.

Pour chaque stimulus, il vous sera demandé de comparer la fidélité de couleur de différents objets dans la scène, ainsi que de toute la scène. La séquence d'objets vous sera lue au cours de l'expérience et vous devrez exprimer le classement souhaité (entre 0 et 10). Une note de 0 suggère que l'objet en question n'est pas du tout reproduit avec précision (pas du tout fidèle), tandis qu'une note de 10 suggère que l'objet est reproduit avec précision (tout à fait fidèle). Vous avez autant de temps que vous le souhaitez pour évaluer le stimulus, mais la durée d'évaluation préférée est inférieure à 30 secondes. Il n'y a pas de bonne ou de mauvaise évaluation, seule la perception réelle de vos yeux est nécessaire.

Avant de vous demander le classement, vous aurez de 30 secondes à 2 minutes pour observer la scène réelle et l'image sur l'écran en posant votre menton sur la mentonnière fournie.

Vous n'êtes pas autorisé à bouger votre tête, mais un léger mouvement des yeux est autorisé pour se concentrer correctement sur la scène. Je vous rappelle de ne pas regarder la source lumineuse vers le haut, mais de rester concentrer sur la scène et l'image à l'écran.

Je vous demande de ne pas vous focaliser sur la réalité perçue, la naturalité, la qualité de l'image et les distorsions résultant d'un point de vue différent.

Le seul critère est la fidélité de la reproduction des couleurs.

Maintenant, tournez-vous, ajustez la hauteur de votre fauteuil et posez votre menton sur la mentonnière (et mettez ces lunettes de soleil).

Maintenant, vous allez voir la première image. Veuillez regarder les deux scènes sans bouger la tête, mais vous pouvez bouger vos yeux.

Cliquez sur la flèche droite et lancez le chronomètre de 30 secondes.

Q.1 Evaluez la fidélité de la reproduction des couleurs entre 0 et 10 pour :

a. La scène entière (des remarques particulières ?)

b. La grosse tomate rouge (des remarques particulières ?)

c. La pomme verte (des remarques particulières ?)

d. Les fleurs bleues (des remarques particulières ?)

e. Le citron jaune (des remarques particulières ?)

f. Le fruit orange (des remarques particulières ?)

g. Le carré bleu sur la 2ème ligne verticale du graphique, en bas. (des remarques particulières ?)

h. Le carré vert dans la même ligne, juste au-dessus du carré bleu. (des remarques particulières ?)

i. Le carré rouge dans la même ligne, juste au-dessus du carré vert. (des remarques particulières ?)

j. Le carré jaune dans la ligne, juste au-dessus du carré rouge. (des remarques particulières ?)

k. Le carré orange, juste à côté du carré bleu. (des remarques particulières ?)

Si un changement d'éclairage/filtre :

Merci, maintenant, s'il vous plaît, retirez les lunettes et maintenez-les sur la position indiquée, puis tournez-vous pendant que je change de décor.

Retournez-vous s'il vous plaît, mettez ces lunettes et posez votre menton sur la mentonnière. Je vais vous montrer la prochaine image…

Merci, c'était la dernière image, vous pouvez maintenant retirer votre menton de la mentonnière (et les lunettes).

Avez-vous des remarques particulières sur la facilité de l'expérience ou des remarques sur certains objets ?

Merci pour le temps passé et bonne journée.

Annex IIIA: Individual Colored object ratings for Experiment 1

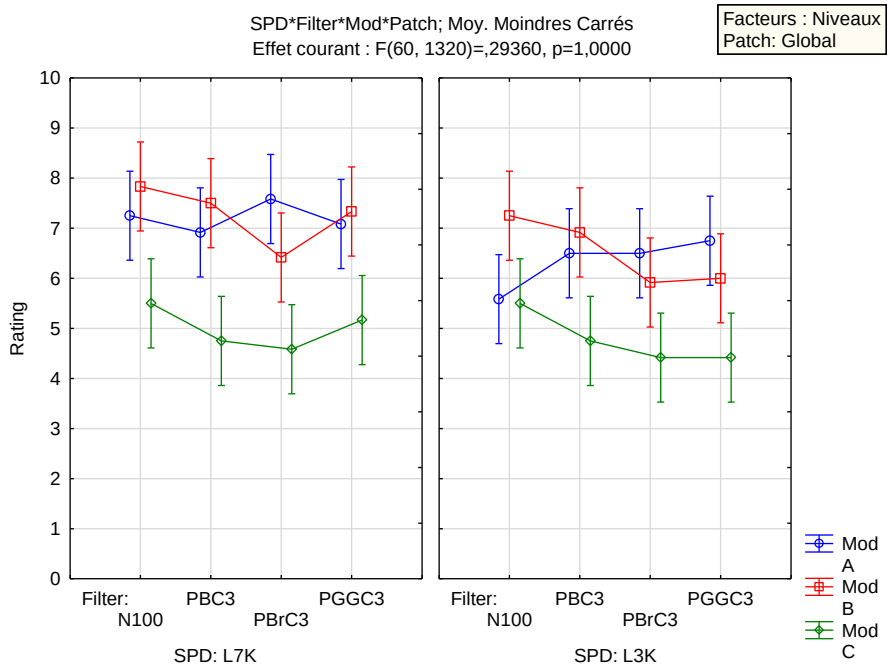

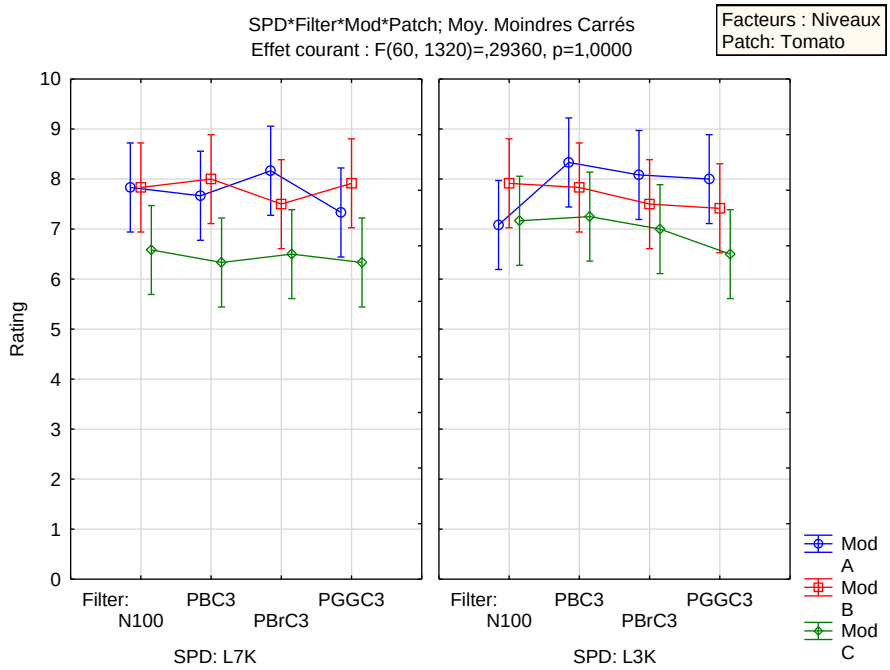

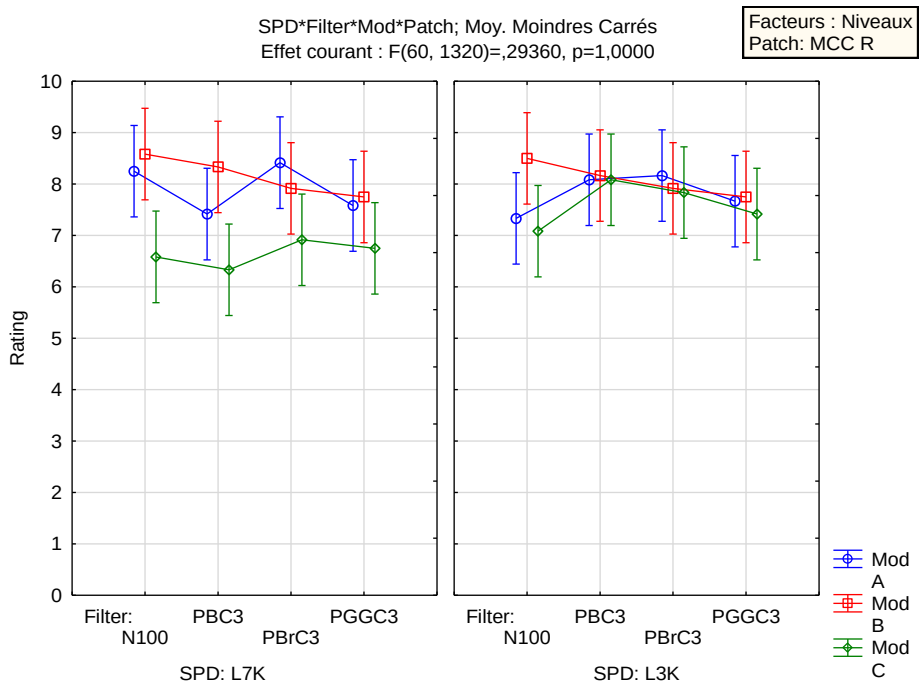

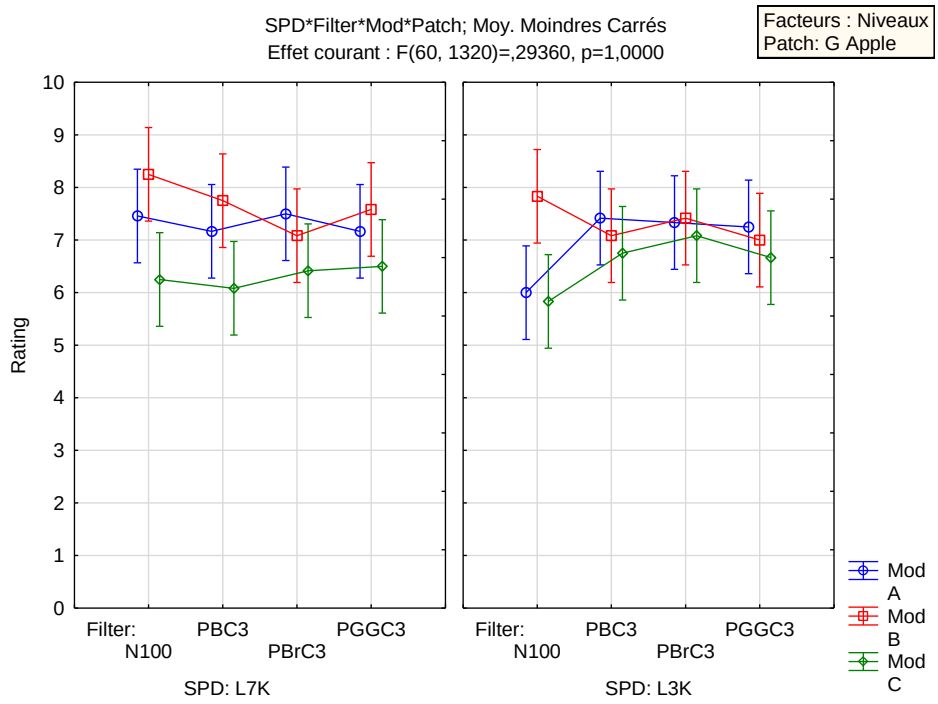

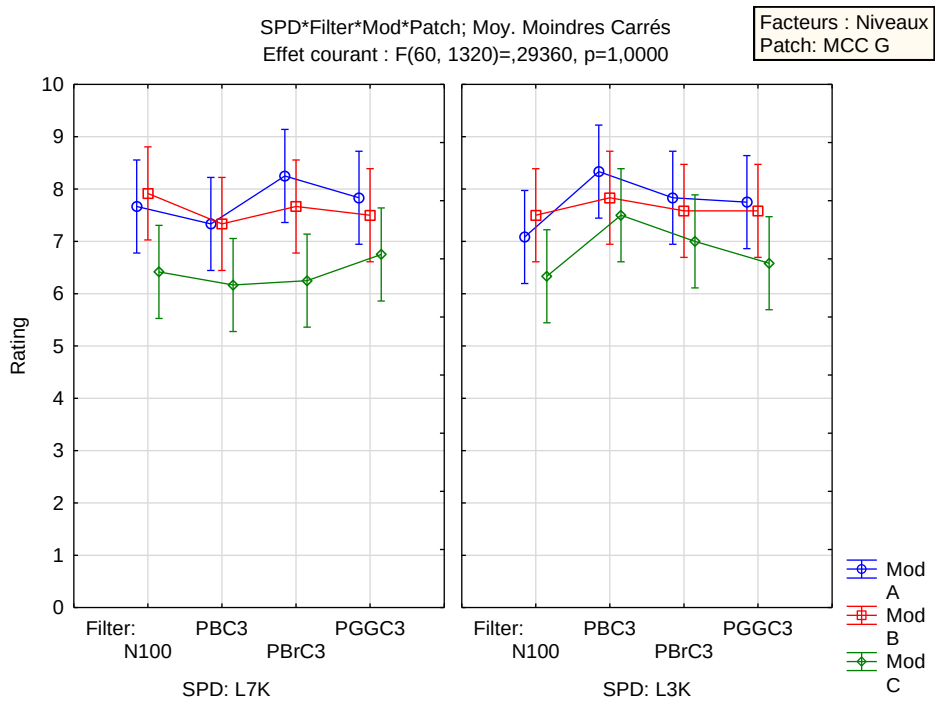

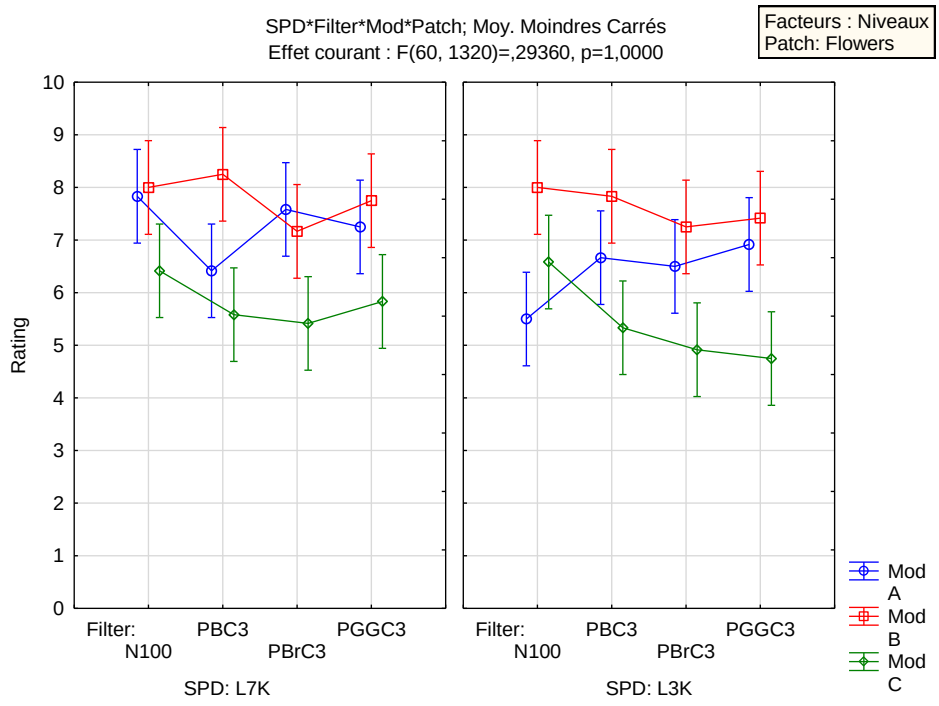

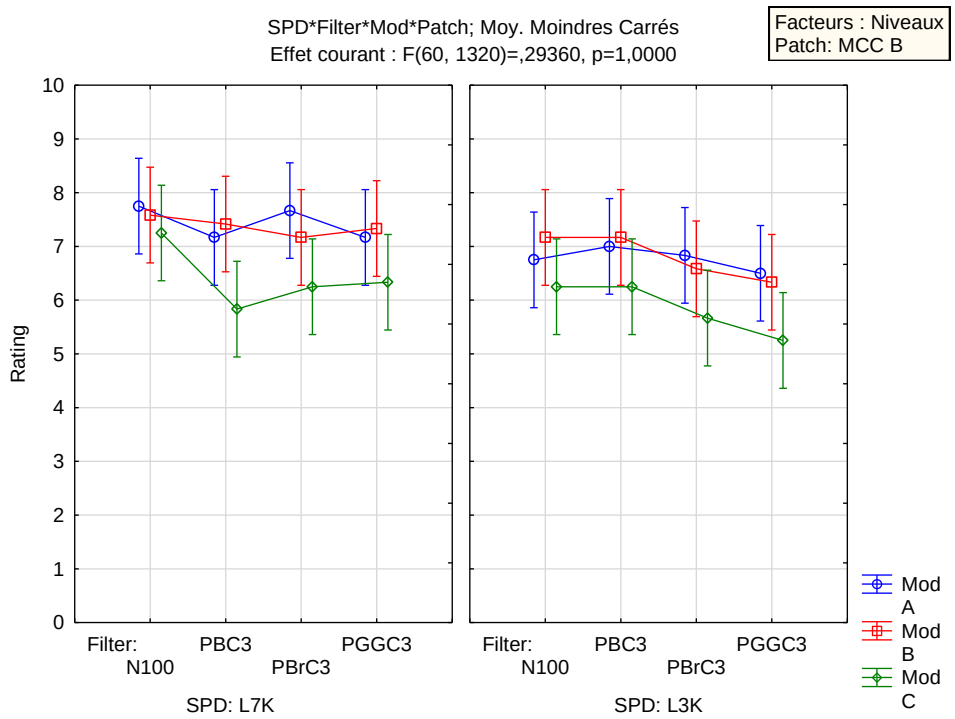

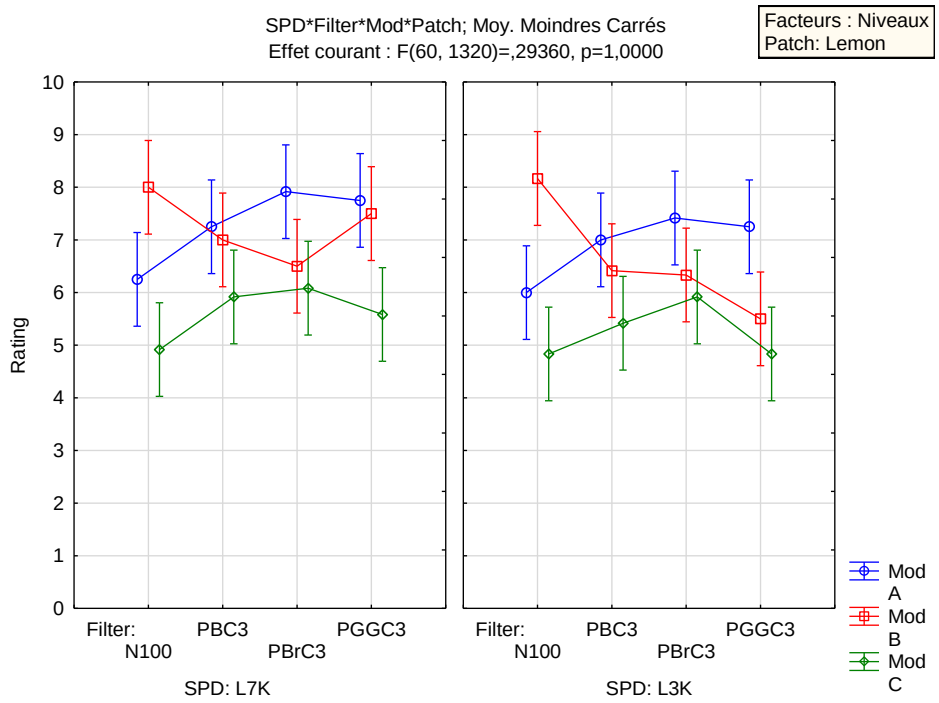

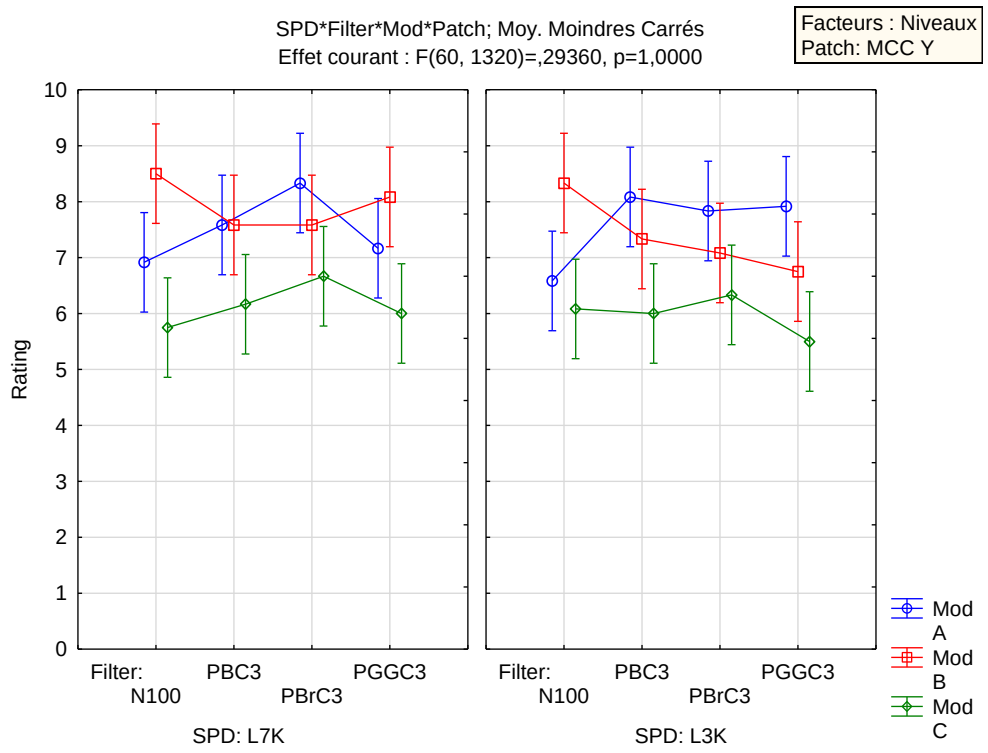

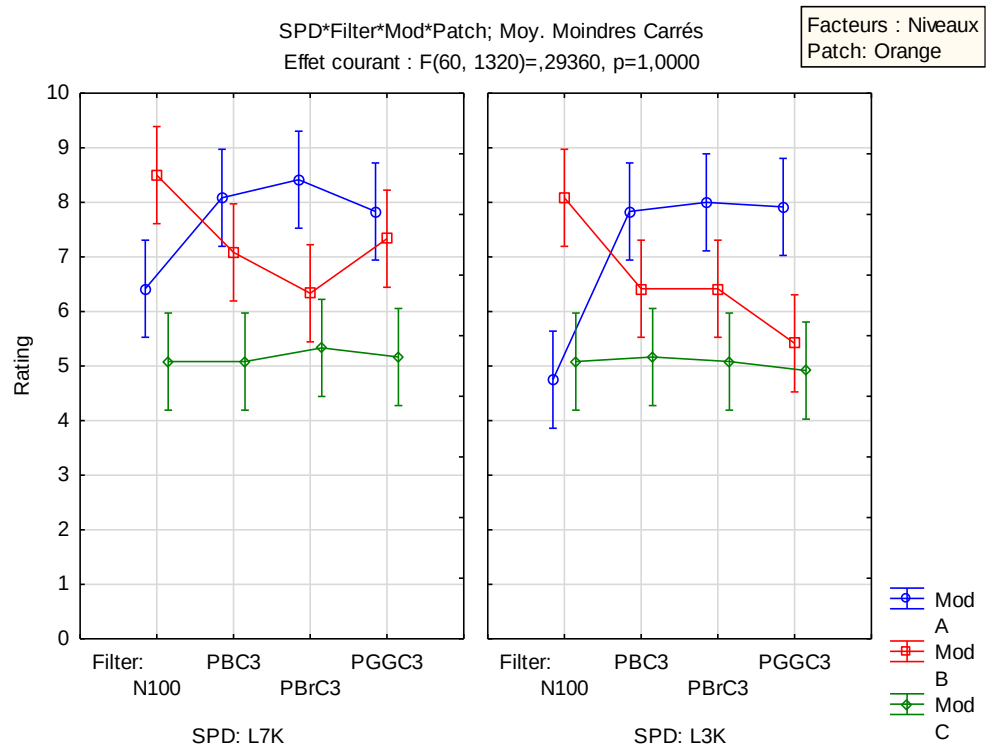

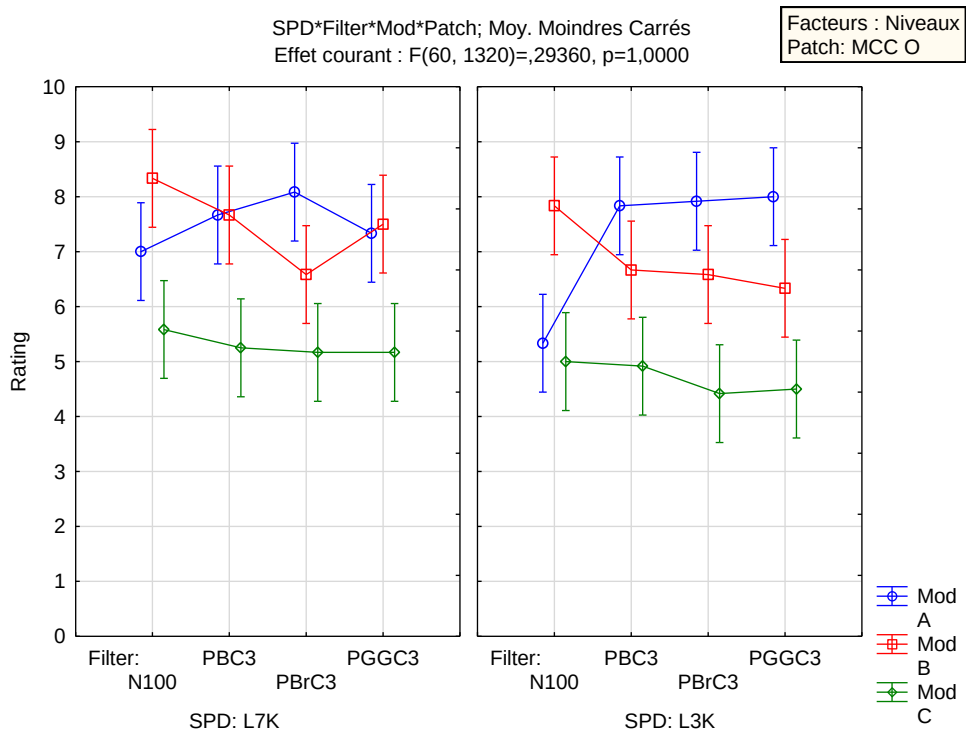

Annex IIIB: Individual filter wise ratings for Experiment 1

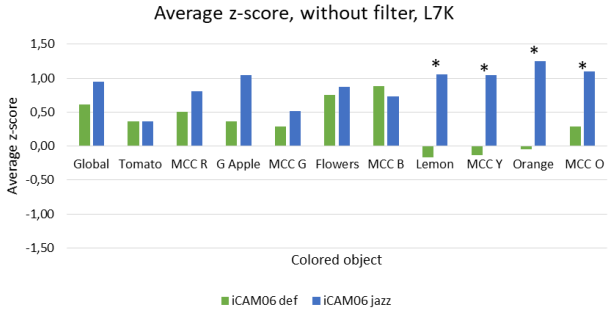

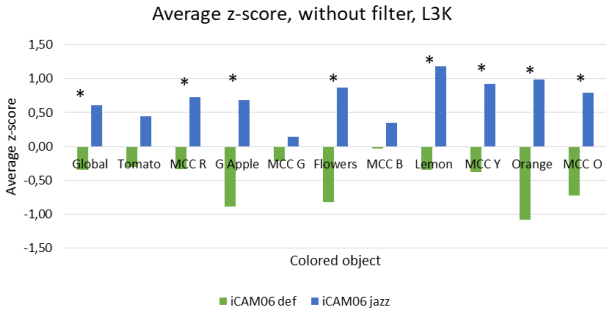

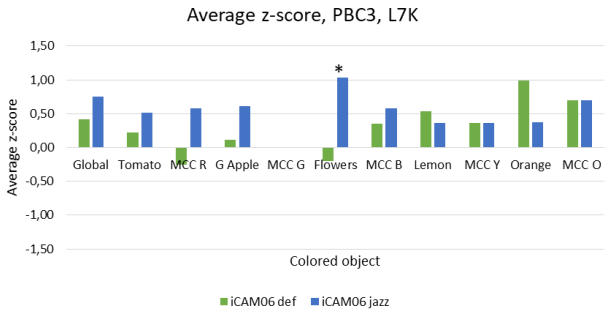

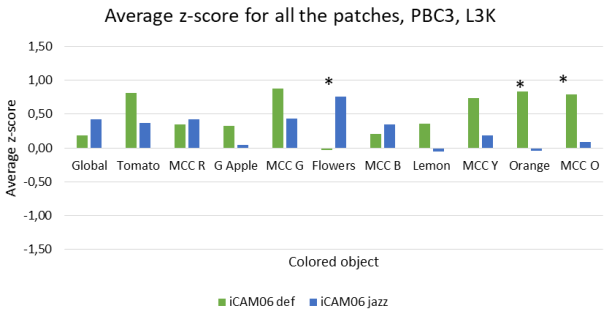

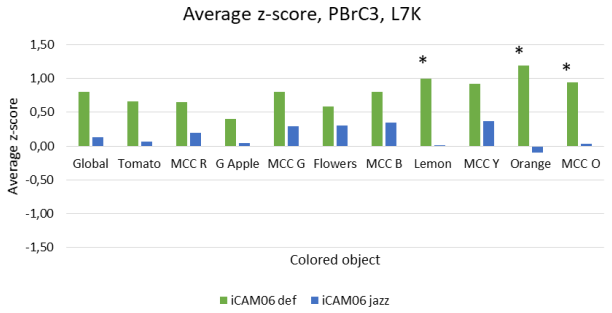

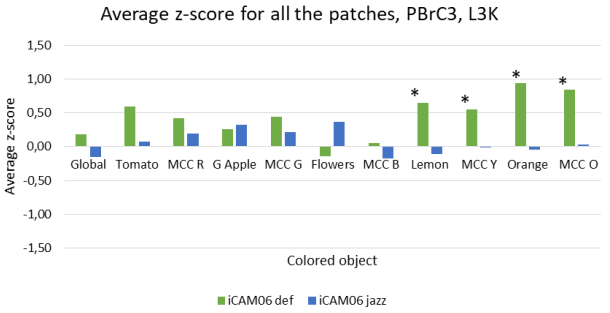

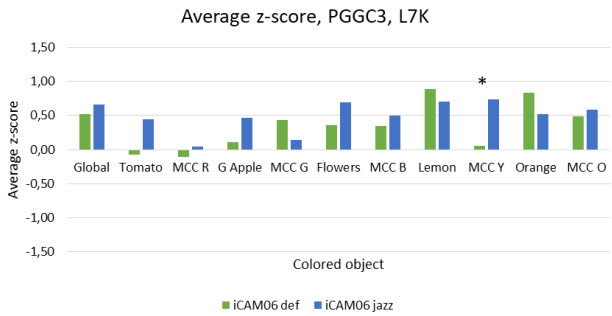

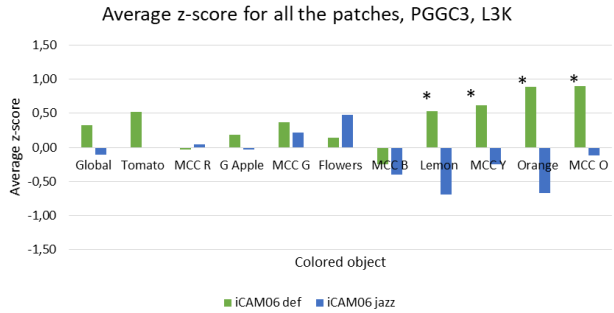

Annex IV: Comprehensive object-wise results for Experiment 1A

Scene	x	y	Y	CCT	D	Score Y	Score W	Score Global	Score Red	Score Green	Score Blue	Score Yellow	Score Orange	D	Total %	D selected
'L3K_PBrC3'	0,48	0,41	10	2445	0,5	65	65	40	15	40	40	15	15	0,5	37	<0,5
					0,7	15	15	15	40	15	15	15	40	0,7	21	
					0,9	15	15	15	15	15	15	15	15	0,9	15	
'L3K_PBrC0'	0,47	0,42	166	2706	0,5	37,5	57,5	37,5	57,5	0	62,5	25	32,5	0,5	39	0,5-0,7
					0,7	12,5	32,5	62,5	32,5	87,5	37,5	50	57,5	0,7	47	
					0,9	50	7,5	0	7,5	0	0	25	7,5	0,9	12	
'L3K_N100'	0,44	0,40	216	2919	0,5	12,5	50	50	57,5	25	75	25	25	0,5	40	0,5/0,9
					0,7	62,5	25	0	7,5	25	0	25	25	0,7	21	
					0,9	25	25	50	32,5	50	25	50	50	0,9	38	
'L7K_N100'	0,31	0,33	231	6458	0,5	62,5	75	40	40	52,5	15	47,5	47,5	0,5	48	0,5
					0,7	37,5	25	40	40	27,5	15	22,5	22,5	0,7	29	
					0,9	0	0	15	15	15	65	22,5	22,5	0,9	19	
'L7K_PGGC3'	0,36	0,36	14	4664	0,5	30	30	47,5	30	30	30	30	30	0,5	32	-
					0,7	30	30	22,5	30	30	30	30	30	0,7	29	
					0,9	30	30	22,5	30	30	30	30	30	0,9	29	
'L7K_PGGC0'	0,35	0,38	172	4896	0,5	50	50	22,5	32,5	22,5	25	22,5	15	0,5	30	0,9
					0,7	0	0	22,5	7,5	22,5	0	22,5	40	0,7	14	
					0,9	25	50	47,5	57,5	47,5	75	47,5	40	0,9	49	
'L3K_PBC2'	0,47	0,42	66	2644	0,5	100	100	75	57,5	50	100	75	82,5	0,5	80	0,5
					0,7	0	0	0	7,5	0	0	25	7,5	0,7	5	
					0,9	0	0	25	32,5	50	0	0	7,5	0,9	14	
'L3K_PBC0'	0,46	0,42	159	2711	0,5	50	75	50	32,5	75	50	50	57,5	0,5	55	0,5
					0,7	25	25	50	32,5	25	25	25	32,5	0,7	30	
					0,9	25	0	0	32,5	50	25	25	7,5	0,9	21	

Annex V: Individual variable wise ratings for Experiment 3